First principles calculations of surfaces and layered materials

Thesis submitted by

FABIO EDUARDO MACHADO CHARRY

to apply for the Degree of Doctor at the
Universitat Autònoma de Barcelona
in the Theoretical and Computational Chemistry Program

Supervisors:

Dr. Pablo Ordejón Rontomé

Dr. Enric Canadell Casanova

Institut de Ciència de Materials de Barcelona
Consejo Superior de Investigaciones Científicas
Campus de la UAB
08193 Bellaterra, Barcelona

Universitat Autònoma de Barcelona
Departament de Química
08193 Bellaterra, Barcelona

Institut Català de Nanotecnologia
Campus de la UAB
Facultat de Ciències
Edifici CM7
08193 Bellaterra, Barcelona

El Dr. Pablo Ordejón Rontomé,
Profesor de Investigación (CSIC)
y
el Dr. Enric Canadell Casanova,
Profesor de Investigaciòn (CSIC)

CERTIFICAN:

Que **Fabio Eduardo Machado Charry**, licenciado en Física por la Universidad Nacional de Colombia, ha realizado bajo su dirección el trabajo que lleva por título "**First principles calculations of surfaces and layered materials**", el cual se recoge en esta memoria para optar al grado de Doctor por la Universitat Autónoma de Barcelona.

Y para que conste, firman el presente certificado.

Bellaterra, Septiembre de 2007

Dr. Pablo Ordejón Rontomé

Dr. Enric Canadell Casanova

A mis padres.

A José Luis D.E.P.

Agradecimientos

A Pablo Ordejón, mi primer co-director. Ya sabe él de sobra como me cuesta escribir. Vaya que lo sabe. Y por tanto entenderá que me ha sido imposible encontrar las palabras que expresaran todo mi agradecimiento hacia él. Gracias por tu infinita paciencia para con este mortal. Otros en su puesto habrían tirado la toalla. Tuve una gran suerte de haberlo tenido como uno de mis directores, por lo anteriormente expuesto, pero más por su gran calidad y visión científica. Creo que he quedado endeudado para con él hasta el día del juicio final.

A Enric, mi segundo co-director. Quisiera destacar el profundo placer que ha sido estar bajo su supervisión debido a su forma tan elegante y sencilla de explicar las cosas, y sobre todo, esa infinita alegría que tiene al trabajar. Le agradezco profundamente la confianza que me ha dado, aunque realmente no creo merecerla. Gracias Enric por ese empujón final que me has dado, yo era el que casi tiraba la toalla. Pero más que todo te agradezco haberme transmitido ese placer de hacer ciencia.

Deseo agradecer a Eduardo Hernandez y Aldo Romero, por haber hecho esto posible. Pero sobre todo por la amistad que me han brindado.

Mi gratitud para con Alfredo Segura y Julio Pellicer en la Universidad de Valencia, por haberme dado la oportunidad de trabajar con ellos en algunos de los interesantes proyectos en lo que están involucrados.

A Riccardo Rurali, por su amistad y sus siempre muy claras y directas opiniones. Este hombre si que no tiene pelos en la lengua. Gracias a mi excompañero y amigo el Dr. Gerard Tobias, por todo sus oportunos auxilios.

Durante estos años siempre he podido contar con la desinteresada y certera ayuda de Manuel Cobian. Gracias Manu, ya lo sabes.. no te debo una, te debo un millón!. Al profesor Alberto Garcia quien siempre esta ahí dispuesto a escuchar. A Xavier Torrelles con quien estoy aun en deuda.

A Javier Rubio, quien además de haber estado dispuesto a ayudarme siempre y haberme salvado de unas graves, me ha dado su amistad. A Nacho (el serio) y a Marco *Antonio* los Hombres de Blanco.

A toda la gente que hacen del ICMAB un sitio tan humano y tan cálido. A Mary, cuida mucho ese brazo!!, Palmira, y Eva (la guapisima), Josep y Jose. A Maria, Montse, Pili, Rebeca y Patricia. Especial reconocimiento a Trini y Vicente. A Rosa Juan y Sandra Domene en el ICN, que siempre me han logrado robar una sonrisa en momentos críticos.

A Cecilia y Monica, las gemelas fantásticas. Gracias por vuestros super oportunos concejos, este pesado no se olvidara de vosotras.

A mis compañeros, a mis amigos: A Sandra por el cafe y las útiles enseñanzas

para la vida, a George el tierno gris, y a mi Caro por cuidar de mi barriga, y de nuevo, a Manu.

A aquellos que han sido muy importantes para mi por el solo hecho de ser y estar muy muy cerca de mi corazón. Mis amigos Annita, Xavi, el Marquez pepon, Cristian, Eva, la partner Lluisa y Elba.

Especial agradecimiento a Albert Figueres y Jordi Pascual por el gran empujón final que me han dado.

Agradezco al Consejo Superior de Investigaciones Cientificas y al Institut Català de Nanotecnologia por la ayuda económica para la realización de esta tesis.

Por ultimo, a las personas que son mi vida, a mi padres, mis hermanas, mis niñas y mi princesa. Todo por ellos, sin ellos nada.

A todos ellos gracias de nuevo y gracias a todos aquellos a los cuales mi vetusta memoria ha relegado a una ingratitud inmerecida.

Contents

Contents **I**

Introduction **1**

1 Methodology and Computational Details **5**
1.1 Introduction . . . 5
1.1.1 Density Functional Theory Framework . . . 5
1.1.2 The Hohenberg-Kohn Theorems . . . 6
1.1.3 The Kohn-Sham Ansatz . . . 7
1.1.4 SIESTA Implementation . . . 10
1.1.5 Pseudopotentials . . . 10
1.1.6 Basis Sets . . . 11

2 Reactivity of Barrier Layers **13**
2.1 Introduction and Motivation . . . 13
2.2 Computational Details . . . 16
2.3 Results and Discussions . . . 18
2.3.1 Structure of Bulk Metals and Surfaces . . . 18
2.3.2 Structure of Cu(hfac)(tmvs) and its Disproportiontion Reaction 19
2.3.3 Chemisorption of CF_3 on Ta(001) Surfaces . . . 19
2.3.4 Passivation of Ta Surfaces with N_2 . . . 21
2.3.5 First-Principles Molecular Dynamics Simulations of Cu(hfac)(tmvs) at Ta(001) and TaN(111) Surfaces . . . 26
2.4 Titanium and Tungsten Surfaces . . . 28
2.5 Concluding Remarks . . . 30

3 Structure of C_{60} on Ge(111) in the $\sqrt{13} \times \sqrt{13}\,R14^\circ$ Phase **33**
3.1 Introduction and Motivation . . . 33
3.2 Computational Details . . . 38
3.2.1 Optimization of Coordinates . . . 40
3.2.2 Energetic Analysis . . . 42

3.2.3 Electronic Properties 43
3.3 Concluding Remarks 55

4 Charge Density Wave phase in $Rb_{0.3}MoO_3$ 57
4.1 Introduction and Motivation 57
4.2 Crystal Structure 60
4.3 Computational Details 61
4.4 Bulk Band Structure 62
4.5 Surface Structure 64
4.5.1 Electronic Properties 64
4.5.2 Experimental Evidence 67
4.5.3 Discussion 68
4.6 Analysis of the Simulated STM Images 71
4.7 Concluding Remarks 72

5 Layered III-VI Semiconductors under Pressure 75
5.1 Introduction and Motivation 75
5.2 Crystal Structure 77
5.3 Computational Details 79
5.4 Results and Discussion 81
5.4.1 γ-InSe 81
5.4.2 γ-GaSe and ε-GaSe 89
5.4.3 GaS 99
5.5 Concluding Remarks 104

6 A Tetragonal Phase of InSe 109
6.1 Introduction and Motivation 109
6.2 Computational Details 112
6.3 The Monoclinic Phase of InSe 112
6.4 High Pressure Structure and Phase Transition 114
6.5 Electronic Structure of the Tetragonal InSe High Pressure Phase . . . 120
6.6 Concluding Remarks 124

7 Electronic Structure of Cubic GaS 125
7.1 Introduction and Motivation 125
7.2 Computational Details 129
7.3 Results and Discussion 129
7.3.1 Rock-salt and Zinc-blende Structures 130
7.3.2 A Zinc-blende Structure based on Cubane 132
7.3.3 Hydrogen-containing Phases 134
7.4 Concluding Remarks 138

A Articles and Patents **141**
A.1 Articles and Proceedings 141
A.1.1 Directly related with the Present Thesis 141
A.1.2 Not directly related with this Work 142
A.2 Patents 142

Bibliography **152**

Introduction

Due to the extended presence of surfaces in nature, the understanding of their phenomena has always attracted much research effort. Apart from the basic science point of view, the knowledge of the surface structures and their properties has been very important for many industrial applications, as for example adhesion, corrosion, catalysis, friction e.t.c.

Nowadays, the great interest in taking advantage of the properties discovered and predicted by the emerging nanoscience makes the surface and interface science a key research area. The main reason of this is that typically a surface is nothing else than the template on which some nanomaterials are constructed. Therefore surfaces are the laboratory where research at nanoscale can been done. Thus, the fundamental understanding of the atomic-scale processes taking place at surfaces, as well as their intrinsic properties, are key factors for nanoscience and nanotechnology. Moreover, all this technology motivation has also promoted the development of new experimental methods that now allow the study of the phenomena that emerge with the small size and low dimensionality.

Surfaces are typical examples of low dimensional systems. However, there are many other systems exhibiting low dimensional behavior. Indeed, these systems often have very rich and unusual physics and have been the focus of much attention. For instance, low dimensional metals frequently exhibit structural modulations related to the appearance of charge density waves (CDW). There have been many attempts to use scanning tunneling microscopy (STM) methods to see if the modulations occurring at the surface of the material differ from those occurring in the bulk. These studies have often led to puzzling results which are difficult to understand without a detailed knowledge of the electronic structure near the Fermi level. The study of layered semiconductors under pressure is another field related with low dimensionality that is the subject of much interest. In particular, the study of the pressure dependence of the optical properties of these materials is not only interesting from a basic point of view but has also a strong technological potential. In this work we have considered several problems related with both of these systems

The goal of this work has been to obtain insight, from *ab-initio* simulations, on the properties and phenomena of surface and layered materials. Particulary, we have concentrated our efforts on systems with relevance and importance for experimental groups. In this sense, along this work we have established strong collaborations with experimental groups in order to achieve better comprehension of phenomena occurring in these systems.

Let us briefly describe the systems considered in this work, as well as their relevance and the motivation to study them.

The deposition of Cu films on transition metal barrier layers by chemical vapor deposition (CVD) is a critical step in circuit fabrication processes. Experimentally, it has been observed poor adhesion characteristics of the grown Cu films when organometallic molecules are used as precursors in the CVD process. We have carried out an extensive study, in collaboration with Air Products and Chemicals, Inc, of the reactivity of tantalum and tantalum nitride surfaces towards an organometallic precursor commonly used in CVD industrial processes. The observed poor adhesion was interpreted in terms of the strong reactivity of the surfaces toward the precursors, which decompose spontaneously upon contact with the surface leading to contamination of the interface. We propose a passivation procedure to circumvent this adhesion problem. This study is presented in Chapter 2.

Another area of great interest in the field of nanotechnology is the possible application of C_{60} molecules. In this line, numerous studies have been done on the understanding of its interaction with surfaces. Chapter 3 describes our contribution to the determination of the structure and properties of C_{60} on germanium surfaces. This is a collaboration with experimental groups with the aim of interpreting their results and verifying the reliability of proposed structural models of the $\sqrt{13} \times \sqrt{13}\,R14^\circ$ phase.

The study of the properties of low dimensional systems is particulary interesting in condensed matter physics. Many quasi one dimensional systems present transitions at low temperature to a CDW phase. Recently, high resolution STM images at ultra-high vacuum have been obtained for the CDW phase of the rubidium Blue Bronze ($Rb_{0.3}MoO_3$). The interpretation of these images has brought some interesting questions. In collaboration with the experimental group at *Laboratoire of Photonique et Nanostructures-CNRS*, we studied this system. Our results, presented in Chapter 4, have provided a clear understanding of the nature of the experimentally observed STM images.

In Chapter 5 we present a complete study about the effects of pressure on the structural and optical properties of III-VI layered semiconducting compounds. We attempt to provide some understanding about the structural behavior of these compounds under pressure. In addition, we will describe the effect of pressure on the band structure and gap. This work has been done in strong collaboration with the experimental group of *Altas Presiones* in the *Universitat de València*.

As a consequence of this work on the III-VI semiconducting compounds, we have also been involved in the interpretation of the experimental results about the effect of pressure on the high pressure and high temperature monoclinic phase of InSe. From our theoretical study it has been possible to solve the nature of the structure of a new tetragonal phase of InSe. This research is presented in Chapter 6.

In another collaboration with the experimental group of *Altas Presiones* in the *Universitat de València* we study in Chapter 7 the electronic structure of a metastable cubic form of gallium sulphide, experimentally grown by CVD. We dis-

cuss about the reliability of its semiconducting character and present alternatives to interpret the experimental results.

All the simulations done in this work have been carried out with SIESTA (Spanish Initiative for Electronic Structure with Thousand of Atoms) method and the corresponding code. One of the characteristics of SIESTA is the use of numerical atomic-like orbitals as basis set. This characteristic has been crucial in our research due to the large number of atoms taken into account in order to have good descriptions of the systems considered.

Some results obtained along this work have been already published. A detailed list of these publications may be found in Appendix A.

Chapter 1

Methodology and Computational Details

In this chapter we describe the theory framework, and its computational implementation, used along this work to study the physical properties of our systems of interest.

1.1 Introduction

In this work we adopted the Density Functional Theory (DFT) as a tool for the calculation of the electronic structure of our systems. It is not the objective of our work to give a detailed explanation of DFT. However, a short description of its fundamental ideas, the approximations done and its limitations will be useful to understand our results, discussions and conclusions. Hundreds of reviews, articles and books have been written about DFT. A detailed mathematical and physical description of this theory can be found in the Ref.[1]. However, I strongly recommend the accessible and complete introduction given by Richard Martin in his book, see Ref. [2].

1.1.1 Density Functional Theory Framework

The main goal of any *ab-initio* computational method is, given the chemical composition and the geometrical structure of a system, to calculate its properties as accurately as possible by solving the electronic Schrödinger equations. In this way, these methods do not make use of any empirical information or free parameters.

However, the problem of solving Schrödinger equations to find the quantum ground state description of the electrons in a condensed system is a correlated many body problem, which at present can be solved only approximately.

Density Functional Theory, among the *ab-initio* methods, is now one of the most widely used approaches to the many body electron problem. It is, in principle, an exact theory for interacting electrons, but in practice, it is an approximate methodology in terms of single electron equations.

1.1.2 The Hohenberg-Kohn Theorems

P. Hogenberg and W. Kohn [3] formulated the basis of this theory in 1964. They established that any property of a system of many interacting particles, in an external potential $V_{ext}(\boldsymbol{r})$, can be seen as a functional of the density of particles in its ground state $n_0(\boldsymbol{r})$. In this way, given this functional of $n_0(\boldsymbol{r})$, it is possible, in principle, to get all the information of the system.

Strictly speaking, the Density Functional Theory is based on only two theorems:

- For any system of interacting particles in an external potential $V_{ext}(\boldsymbol{r})$, the potential $V_{ext}(\boldsymbol{r})$ is determined uniquely, except for a constant, by the ground state density $n_0(\boldsymbol{r})$.
- For any particular $V_{ext}(\boldsymbol{r})$, the exact ground state energy of the system is the global minimum value of the energy functional $E[n]$, and the density $n(\boldsymbol{r})$ that minimizes the functional is the exact ground state density $n_0(\boldsymbol{r})$.

These can be expressed in this alternative form: the density of particles in the ground state uniquely determines the external potential $V_{ext}(\boldsymbol{r})$ acting on them, and vice-versa. Hence, all the properties of the system, including the ground state wave function Ψ_o (and also the excited states) and all derived observables are uniquely determined by $n_o(\boldsymbol{r})$.

In this way, the total energy of the ground state of a system of n interacting electrons in an external potential can be obtained from the minimization of the Hohenberg-Kohn electronic total energy functional $E_{HK}[n]$

$$E_{HK}[n] = \int dr V_{ext}(\boldsymbol{r}) n(\boldsymbol{r}) dr + F[n], \tag{1.1}$$

where the functional $F[n]$ is the sum of a kinetic term and an interaction between electrons term

$$F[n] = T[n] + V[n]. \tag{1.2}$$

These expressions are basically the expectation value of the many body hamiltonian rewritten in a functional manner. For a system made of atoms, which contain electrons and nuclei, the external potential felt by the electrons contains the electron-nuclei interaction, and an additional, classical term E_{II} describing the interaction between nuclei must be added to the total energy in equation 1.1.

In this formulation, we still have the problem of evaluating the functional $F[n]$, for which we do not have an explicit form. Obtaining this form is equivalent to solving the original many-body problem, something which is only possible for systems with very few particles, very far from real and interesting systems like molecules, crystals or surfaces. The fact that transformed DFT in a primary practical tool for electronic calculations, was the proposal of the Kohn-Sham ansatz in 1965[4].

1.1.3 The Kohn-Sham Ansatz

In this ansatz, Kohn-Sham [4] assume that the exact ground state density of the original interacting system is equal to that of a fictitious non-interacting system. Then the ground state density of n electrons can be rewritten in the form

$$n_0(\boldsymbol{r}) = \sum_{i=1}^{N} \psi_i^*(\boldsymbol{r})\psi_i(\boldsymbol{r}), \tag{1.3}$$

where ψ_i are the occupied ground state wave functions of each independent electron (a more complete formulation must account for the electron spin), i.e., are eigenstates of the equation

$$(H_{KS} - \epsilon_i)\psi_i(\boldsymbol{r}) = 0 \tag{1.4}$$

where H_{KS} is the one particle Hamiltonian, which reads:

$$H_{KS} = -\frac{\nabla^2}{2} + \hat{V}_{eff}. \tag{1.5}$$

Atomic units are used throughout this chapter. $\hat{V}_{eff}$ is now an operator describing the effective potential in which one electron is embedded. In order to get the correct form of this effective potential we have first to describe the functional form of the energy taken by Kohn-Sham in their approach. At first, they took into account the classical Coulomb potential created by the electronic distribution. This is known as the Hartree potential, having the form

$$V_{Hartree} = \int \frac{n(\boldsymbol{r}')}{|\boldsymbol{r} - \boldsymbol{r}'|} d\boldsymbol{r}' \tag{1.6}$$

From here, the Hartree energy functional is defined as the self-interaction energy of the density $n(\boldsymbol{r})$ treated as a classical charge density

$$E_{Hartree}[n] = \int V_{Hartree}(\boldsymbol{r})n(\boldsymbol{r})d\boldsymbol{r} = \frac{1}{2}\int \frac{n(\boldsymbol{r})n(\boldsymbol{r}')}{|\boldsymbol{r} - \boldsymbol{r}'|} d\boldsymbol{r}d\boldsymbol{r}' \tag{1.7}$$

The ground state energy functional in the Kohn-Sham formulation has the form

$$E_{KS} = T_S[n] + \int V_{ext}(\boldsymbol{r})n(\boldsymbol{r})d\boldsymbol{r} + E_{Hartree}[n] + E_{XC}[n]. \tag{1.8}$$

The term $T_S[n]$ is the kinetic energy of this fictitious system of non-interacting electrons with the same density as the interacting one. In this way we have displaced all the complexity coming from electron interactions into a new term: the exchange-correlation functional E_{XC}.

With the purpose of gaining understanding about the meaning of E_{XC} we compare the Hogenberg-Kohn and Kohn-Sham expressions, equations 1.1 and 1.8 respectively, getting the expression

$$E_{XC}[N] = \langle T \rangle - T_S[n] + \langle V \rangle - E_{Hartree}[n]. \tag{1.9}$$

In this expression we see that E_{KS} is, in fact, the difference of the kinetic and the interaction energies between the true interacting many body system and the fictitious independent particle system with the electron-electron interaction replaced by the Hartree energy[2]. In other words, we recover here what we lost assuming a independent particle framework. The definition *exchange-correlation*, in this manner, is not fully appropriate, because E_{XC} contains, in addition to the exchange and correlation energies, a correction to the fictitious kinetic energy. In the above interpretation of E_{XC}, an exact analytical form of this functional is still unknown.

In essence, the Kohn-Shawn approach transforms the problem of n interacting electrons into the simpler problem of solving n independent Schrödinger equations for n non-interacting electrons moving in an effective potential. The effective potential is usually assumed to be local, and takes the form:

$$\begin{aligned} V_{eff}(\boldsymbol{r}) &= V_{ext}(\boldsymbol{r}) + \frac{\delta E_{Hartree}}{\delta n(\boldsymbol{r})} + \frac{\delta E_{XC}}{\delta n(\boldsymbol{r})} \\ &= V_{ext}(\boldsymbol{r}) + V_{Hartree}(\boldsymbol{r}) + V_{XC}(\boldsymbol{r}). \end{aligned} \tag{1.10}$$

Therefore, the many body effects are described by the exchange-correlation potential V_{XC}, related with the XC energy functional, equation 1.9. If the exact form of the E_{XC} functional is known, the exact ground state energy and density of the interaction system could be found by solving these Kohn-Sham equations in a self-consistent way.

It is important to note that the one particle Kohn-Sham wave functions ψ_i have nothing to do with the true many body ground state wave function Ψ_o of the interaction system, except that both define the same ground state density $n_0(\boldsymbol{r})$. This warning is also valid for the eigenvalues in the equation 1.4, which can not, strictly speaking, be considered as excitation energies. In spite of this, and the known

deficiencies in the description of the gap energies (see text below), it has been customary to adopt this interpretation, since more accurate methods, such as the GW approximation [5], are much more expensive than plain DFT.

Thus, with the help of the Kohn-Sham ansatz, the DFT theory becomes a practical methodology. However, we still have to deal with the problem of the unknown exact form of E_{XC}. Approximate expressions to this functional have been proposed in order to be able to solve the n non-interacting Kohn-Sham equations.

There are two standard approximations for the $E_{xc}[n]$ functional, the Local Density Approximation (LDA) and the Generalized Gradient Approximation (GGA). In the LDA [4] the energy density at each point $\boldsymbol{r}$ depends only on the particle density at that point $n(\boldsymbol{r})$, and so the total XC energy is expressed as:

$$E_{XC}^{LDA}[n(\boldsymbol{r})] = \int d\boldsymbol{r}\ n(\boldsymbol{r})\ \epsilon_{XC}(n(\boldsymbol{r})), \tag{1.11}$$

where $\epsilon_{XC}(n)$ is the exchange correlation energy density of an uniform electron gas of density n. Behind the expression 1.11 is the assumption that each volume element $d\boldsymbol{r}$ has a contribution to the exchange-correlation energy equal to what a homogeneous electron gas with the same density n would have. $\epsilon_{XC}(n)$ is a function which can be obtained as a parametrisation of the results obtained using more elaborate computational methods like quantum Monte Carlo. The most commonly used parametrisation, and our choice for LDA, is the Perdew and Zunger (PZ) [6] to the Ceperley-Alder (CA) [7] energies for the uniform electron gas, obtained from Monte Carlo calculations.

From its definition, the LDA is expected to work very well for systems with an electronic density close to a homogeneous gas, but it is not justified a priori for very inhomogeneous cases like atoms. However, even in very inhomogeneous cases, in practice LDA has shown to work remarkably well in a variety chemical and physical situations, including strongly inhomogeneous systems.

However, the LDA has some deficiencies that must be kept in mind. It has the tendency to underestimate the lattice constants and bond lengths, and to overestimate the cohesive energies and bulk moduli. In the other hand, LDA frequently underestimates energy gaps, if the eigenvalues are interpreted as excitation energies.

The GGA has been proposed as a way to overcome some of the deficiencies of LDA. Recognizing the failure of the LDA expression to describe the dependence of the energy density on spatial variations of the particle density, GGA [8] includes the dependence on the gradient (and further derivatives) of the density. In this way the total exchange-correlation energy is now expressed in a generalized form as

$$E_{XC}^{GGA}[n(\boldsymbol{r})] = \int d\boldsymbol{r}\ n(\boldsymbol{r})\ \epsilon_{XC}^{GGA}(n(\boldsymbol{r}), \nabla n(r), ...), \tag{1.12}$$

There are several different parametrisations of the GGA. Among them, there are

some semi-empirical and others are made from first principles. The parametrisation of GGA adopted by us, when it is the case, is the one proposed by Perdew, Burke, and Ernzerhof [8] from first principles calculations.

GGA has been shown to improve dissociation energies and bond lengths of small molecules [9, 10]. However, in spite of the gradient correction, the applications of GGA to solids have shown the tendency to over-correct the deficiencies of LDA. For instance, the lattice constants tend to be overestimated while bulk modulus is underestimated [11, 12]. Also, it is not able to correct the problem of the gap. However, GGA calculations are usually more reliable than LDA ones.

1.1.4 SIESTA Implementation

The solution of the Kohn-Sham equations, for systems of many atoms, in a numerical way is the goal of practical DFT formulations. The good results provided by these formulations have made them increasingly used by the scientific community. At the same time, the number of codes developed to perform these calculations, and their capabilities and efficiency, has increased dramatically, making them available for an increasingly wider community of DFT practitioners.

In our case, all the calculations done in this work have been carried out using the SIESTA method and the corresponding code (Spanish Initiative for Electronic Structure with Thousand of Atoms)[13, 14]. Our group is strongly involved in its continuous development and improvement, as well as its application on different fields of materials science, as we did here.

Again, we are not going to give a detailed description of the method, its implementation, or its abilities. This description can be found in the Reference [13], as well as in other papers describing the method [15, 16, 17, 18, 19] and its applications [20, 21]. We are going to give a brief description of some features commonly used in our calculations.

1.1.5 Pseudopotentials

The electrons in an atom can be divided in two groups, core and valence electrons. Core electrons reside in the deeper shells and are strongly bonded to the nuclei. As a consequence, the core electrons are not strongly affected by the chemical environment in which the atom is embedded, and they usually do not participate in the chemical bonding. However, from the numerical point of view, these core electrons represent a very high computational cost. Besides increasing the number of orbitals to be computed, the effect of the presence of the core electrons is also to impose the presence of nodes in the valence wave functions. This comes from the required orthogonality between the valence and core wave functions. The description of these nodes makes the calculations more expensive from the computational point of view.

For instance, in plane wave calculations, a huge number of plane waves would be required to describe these nodes near the core.

To reduce the numerical cost the pseudopotentials approximation was proposed. In this approximation, the strong nuclear potential and the core electrons are replaced by an effective ionic potential acting on the valence electrons.

Once these pseudopotentials have been generated, a condition that they must fulfill is their transferability, i.e., the results of pseudopotentials calculations have to differ by only a small amount from all-electron calculations, on diverse atomic configurations differing from the starting one.

Some general characteristics defining the pseudopotentials we used in this work: (a) We used norm conserving pseudopotentials, in which the norm of the pseudowave function is the same as the one of the true wave function [22, 23]. (b) The use of cutoff radii: these radii define the region beyond which the pseudo-charge density as well the pseudo valence orbitals are equal to the real ones. (c) The use of core-corrections [24]: these corrections account, at least partially, for the nonlinearity in the exchange and correlation potential in the charge density. Its use it strongly recommended when there is a large overlap between valence an core charge, e.g., in the transition metals. With this correction the true core charge is replaced by a fictitious and smoother charge which is added to the valence charge. (d) They are fully separable: they are formed by a local part, common for all angular momentum, and non-local part, which depend on each angular momentum following the method proposed by Kleinman and Bylander [25].

1.1.6 Basis Sets

In order to solve the one-electron KS problem numerically, the wave functions ψ_n are represented by a linear combination of basis set orbitals:

$$\psi_i(\boldsymbol{r}) = \sum_{\mu=1}^{p} c_{i\mu}\phi_\mu(\boldsymbol{r}). \tag{1.13}$$

There is broad variety of functions that can be chosen as basis set, e.g., plane waves, augmented plane waves, muffin-tin orbitals, gaussians, Slater-type orbitals, numerical radial atomic-like orbitals, real space grids, etc. The SIESTA method uses a localized basis scheme; specifically, the basis set are numerical atomic-like orbitals of finite range.

As a general description, a local atomic orbital basis is a set of orbitals $\phi_\mu(r-R_I)$, each associated with an atom at position R_I. Commonly, the orbital is factorized in two terms, one describing the radial dependence, and a spherical harmonic which takes into account the angular dependence. Localized orbitals bases are highly efficient and accurate, since the shape of the orbitals describes properly the effect of

the nuclear potential on the wave functions, However, unlike plane waves, the shape of the orbital must be optimized for each particular atomic species, and systematic convergence with respect to basis set is not easy to achieve. Also, there is a problem of "overcompleteness" if one attempts to go to convergence [2].

The common notation, in the field of localized orbitals, is that multiple radial functions for the same l, m are denoted "multiple-zeta". For example DZ (double-ζ) basis have two radial functions for each angular momentum shell. In order to have in account the nonsymmetric environment around an atom in a molecule or solid, it is customary to introduce higher angular momenta than the minimal basis in the atom. This extra functions are called polarization functions, and are normally denoted by a "P" letter.

Chapter 2

Reactivity of Barrier Layers of Ta and TaN toward Organometallic Precursors for deposition of Cu films

In this chapter we analyze the reactivity of barrier layers of tantalum and tantalum nitride towards the organometallic precursor Cu-hexafluoracetylacetonato-trimethylvinylsilane (Cu(hfac)-(tmvs)) in a chemical vapor deposition (CVD) process. We propose a procedure to avoid the contamination of the barrier by the organic fragments from the precursor. We also consider the case of barriers of tungsten and titanium, obtaining similar conclusions.

2.1 Introduction and Motivation

As the microelectronics industry evolves into ultra-large-scale integration (ULSI), the intrinsic properties of typical metallization materials emerge as the limiting factor in advanced circuit design and manufacture [26, 27]. Aluminum, which was commonly used as the interconnect metal up to the end of the last decade, suffers from several disadvantages such as its relatively high bulk electrical resistivity and susceptibility to electromigration, which may reduce its usefulness [28, 29]. Other metallization materials, such as tungsten and molybdenum, provide a high migration resistance but also have a high electrical resistivity, in such a way that it is not possible to have an integrated circuit based on them with high speed characteristics [27, 30]. Because of its low electrical resistivity and enhanced resistance to electromigration, copper is an attractive material for high-speed integrated circuits [27, 30]. Other candidates have been considered for use as a metallization material,

including platinum, cobalt, nickel, palladium, ruthenium, rhodium, iridium, gold, silver, and their alloys [27, 30].

Some of these metallic elements considered for interconnector material, like copper, show a high diffusivity into the semiconductor, which causes very negative effects on the functioning of the device. The typical solution to this problem is to use an intermediate layer (so-called "barrier layer") of another metal with low diffusivity into silicon, on which the metallic film is subsequently deposited. Ideal barrier materials include metals, such as titanium, tantalum, tungsten, chromium, molybdenum, zirconium, and vanadium, and carbides, nitrides, carbonitrides, silicon carbides, silicon nitrides, and silicon carbonitrides of these metals where they constitute a stable composition.

Numerous methods such as ionized metal plasma (IMP), physical vapor deposition (PVD), chemical vapor deposition (CVD), atomic layer deposition (ALD), plasma-assisted chemical vapor deposition (PACVD), plasma-enhanced chemical vapor deposition (PECVD), electroplating, and electroless plating have been used to deposit metal films on surfaces. Among them, CVD and ALD methods using one or more organometallic precursors are the most promising ones because they provide excellent step coverage for high aspect ratio structures and good via filling characteristics [31, 32, 33].

Several organometallic precursors have been developed to deposit low electrical resistivity copper films by the mentioned processes, particularly CVD or ALD. There has been special attention to two families of copper CVD precursor, the Cu(I) and Cu(II) β-diketonates [34, 35] [1]. The Cu(II) precursors require the use of an external reducing agent such as hydrogen or alcohol to deposit copper films that are largely free of impurities, whereas Cu(I) precursors can deposit pure copper films via a bimolecular disproportionation reaction that produces a Cu(II) β-diketonate as a volatile byproduct [34, 35]. The β-diketonate ligand most often present in these precursors is hexafluoroacetylacetonate, so called the hfac anion, $[OC(CF_3)CHC(CF_3)O]^-$.

1,1,1,5,5,5-hexafluoro-2,4-pentanedionato-copper(I) trimethylvinylsilane (with the acronym Cu(hfac)(tmvs)) is a particularly effective CVD copper precursor. This precursor, with trade name CupraSelect ®[36], is synthesized by Air Products and Chemicals, INC. As a copper thin film precursor, this compound undergoes the disproportionation reaction depicted in Fig. 2.1 upon deposition on the surface.

In some instances, the initial deposition of CVD or ALD metal or copper film on the barrier layer may function as a seed layer, e.g., an adhesive, conducting layer to facilitate further deposition of a subsequent metal layer such as copper by electrochemical plating, electroless plating, or by PVD, CVD, or ALD methods to complete

[1] According to IUPAC nomenclature of inorganic chemistry, copper(I) and copper(II) have in the molecule an oxidation state Cu^+ and Cu^{2+}, respectively.

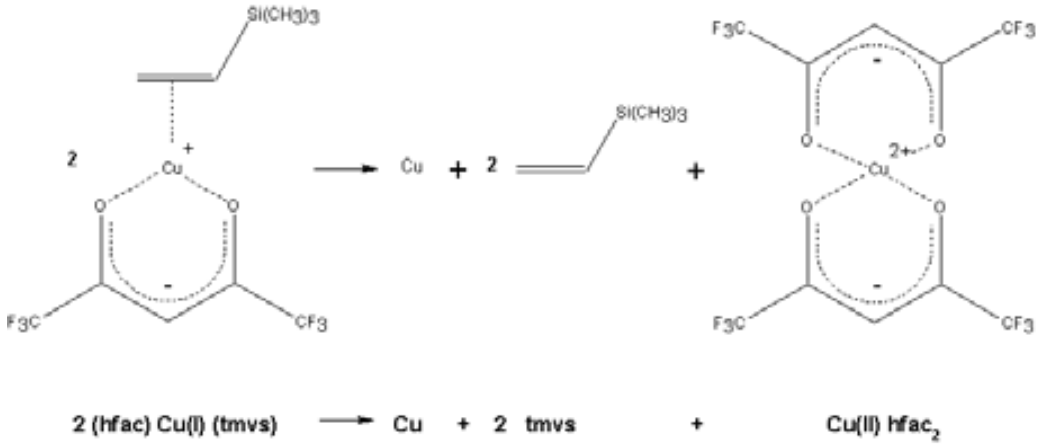

Figure 2.1: Disproportionation reaction

the thin-film interconnect [31, 32, 33]. Despite the foregoing developments, the integrated circuit (IC) industry has experienced some difficulties forming adherent metal or copper films on diffusion barrier layer materials. The metal substrates as barrier layers for copper deposition have been found to react with the organometallic precursors commonly used for Cu growth, resulting in spontaneous decomposition of the precursors at the surfaces [34, 35]. This gives rise to contamination of the barrier layers with the organic fragments of the ligands of the precursor chemisorbed on the surface, in addition to the desired adsorption on copper atoms.

In particular, it has been experimentally observed that Cu(hfac)(tmvs) [37] precursor suffers a decomposition upon deposition on barrier layer materials, such as Ta and Ti, instead of taking the desired disproportionation reaction path. Numerous attempts to adjust the deposition conditions to improve the copper adhesion have been made with limited success and a significant amount of fragments of the ligands was always found on surfaces [34, 38, 35, 37].

A variety of solutions to this problem have been proposed. For example, Gandikota et al. [38] have proposed to improve adhesion (a) depositing a copper flash layer on the barrier layer by physical vapor deposition (PVD) prior to chemical vapor deposition or (b) annealing the CVD copper layer after deposition [37]. Unfortunately, these methods are not readily acceptable to the IC industry because they add to the equipment requirements for the copper deposition step. In addition, annealing, particularly at elevated temperatures, can have harmful effects on the overall circuit.

The work presented here is the result of a collaboration with Air Products and Chemicals, INC to understand the adhesion problems when Cupraselect® is used to form copper thin films. We have done a series of theoretical studies based on first-principles calculations. Our results have elucidated the underlying mechanisms

that dictate the interaction between Cu(hfac)(tmvs) and the barrier materials. The results related in this Chapter correspond to the use of tantalum as barrier material. However, we also have studied systems in which the barrier surface is made by Ti and W, which we only shortly describe here.

In addition, we have proposed a surface passivation methodology to reduce the surface reactivity toward the copper precursor. The basic idea is to prevent the ligands of the precursor from interacting with the barrier layer via chemical bonding while maintaining strong adhesion of copper upon deposition. We have found that by forming a nitride film on the barrier layer, in which the top layer of the film is fully saturated with nitrogen, the barrier layer is passivated. Moreover, it can indeed give rise to strong adsorption to copper while repelling the organic ligands away from the surface. As a consequence, the disproportionation reaction can readily occur on the barrier layer without surface contamination due to the chemisorption of the fragmentation species of ligands.

2.2 Computational Details

In order to evaluate the reactivity of the barrier layers toward either the Cu(hfac)(tmvs) precursor or its constitutive parts, we have done structural optimizations and molecular dynamics (MD) simulations. The structural optimizations of small molecules exposed to the surfaces allow us to get insight about the nature of the interaction between them, the activation barrier of the reaction, the possible absorption sites and the absorption energies. The use of MD simulations of the large Cu(hfac)(tmvs) atop the surfaces gives a qualitative comprehension of the overall reaction along time under typical experimental conditions. Using these MD simulations we studied the interaction process of Cu(hfac)(tmvs) under different initial conditions like the velocity with which it is thrown toward the surface, and its orientation. The molecular velocities used correspond to temperatures in the range of from 100 to 200°C and the typical MD time was around 1 ps, sufficient to extract qualitative conclusions from the observed processes. Most of the molecular dynamics simulations were done at a constant temperature using the Nose thermostat technique [39, 40]. We also performed MD simulations in the microcanonical (constant energy) ensemble, but no appreciable qualitative differences in the conclusions from both types of simulations were found.

The structural optimizations and reaction and absorption energies were obtained using a rather complete split-valence double-ζ plus polarization basis set, as obtained with an energy shift of 0.004 Ry [13]. However, due to the large system sizes involved and the length of the simulations, the MD calculations presented here were performed using small basis sets, a single-ζ as obtained with an energy shift of 0.02 Ry. Some test MD runs were done using double-ζ plus polarization basis sets, and

		valence structure				core correction
H	*Occ*	$1s^1$	$2p^0$	$3d^0$	$4f^0$	
	r	1.25	1.25	1.25	1.19	-
C	*Occ*	$2s^2$	$2p^2$	$3d^0$	$4f^0$	
	r	1.25	1.25	1.25	1.25	-
N	*Occ*	$2s^2$	$2p^3$	$3d^0$	$4f^0$	
	r	1.29	1.29	1.29	1.29	-
O	*Occ*	$2s^2$	$2p^4$	$3d^0$	$4f^0$	
	r	1.14	1.14	1.14	1.14	-
F	*Occ*	$2s^2$	$2p^5$	$3d^0$	$4f^0$	
	r	1.19	1.19	1.09	1.09	-
Si	*Occ*	$3s^2$	$3p^2$	$3d^0$	$4f^0$	
	r	2.05	2.05	1.9	1.9	-
Cu	*Occ*	$4s^1$	$4p^0$	$3d^10$	$4f^0$	
	r	2.5	2.6	2.0	1.9	2.0
Ta	*Occ*	$6s^2$	$6p^0$	$5d^3$	$4f^0$	
	r	3.1	3.0	1.9	2.2	3.0

Table 2.1: Pseudopotentials configurations. *Occ*=Occupation, *r*=cutoff radii (Bohr).

the results were in qualitative agreement with those of the single-ζ calculations.

The generalized gradients approximation (GGA) in the form proposed by Perdew, Burke, and Ernzerhof [8] was used in this work for the structural optimizations and the calculation of reaction and adsorption energies. For the MD simulations, the local density approximation (LDA), in particular, the Perdew-Zunger [6] parametrization of the Ceperley and Alder quantum Monte Carlo data [7] was used. The atomic configuration, cutoff radii and core corrections of the pseudopotentials, generated according to the Troullier-Martins scheme [23], in the Kleinman-Bylander [25] separable form, for each species are collected in Table 2.1. The energy cutoff of the real space integration mesh, for GGA calculations, was 300 Ry for systems in which the surface material is tantalum, and 150 Ry for systems with tantalum nitride surfaces. For LDA calculations, the energy cutoff values are slightly smaller.

Those simulations involving interaction between an impinging molecule and a surface were done using slabs in a supercell geometry in which each surface substrate is modeled by four atomic layers. During the dynamics, the two lower layers of the slab were kept fixed. The lateral size of the cell was large enough to avoid direct interactions between periodic images of the molecules. This yields supercells with around eighty atoms, when small molecules were considered, and up to around one hundred atoms, when the Cu(hfac)(tmvs) molecule were included in MD simulation.

Due to the large size of these supercells, it was sufficient to use the Γ point for sampling the Brillouin zone.

2.3 Results and Discussions

2.3.1 Structure of Bulk Metals and Surfaces

Before we started with the study of reactivity of Cu(hfac)(tmvs) on the chosen barrier substrates, we have checked how well the bulk properties of materials in consideration are described in our calculations, to set up reliable models, which compare with available experimental data, of the surfaces of the solids of interest. An initial step needed to reach this is to have a good description of the respective solids.

The most common crystalline phase of Ta takes the bcc (Im3m) structure. Our calculations, in the GGA approximation, using a $(21 \times 21 \times 21)$ Monkhorst-Pack [41] grid in reciprocal space, predict a lattice constant of 3.30 Å, in excellent agreement with the experimental value of 3.3013 Å[42].

Tantalum forms nitrides with a wide range of stoichiometries. Here, we have restricted ourselves to the case of the stoichiometric TaN compounds, since these are the most common nitrides for copper barrier layers [43, 44]. TaN is found both in the NaCl phase [45] and in an hexagonal phase [42]. The cubic NaCl phase is the one commonly obtained by CVD, PVD, and sputtering [46, 47]. For this phase, we obtained a lattice constant, in the GGA approximation, of 4.45 Å (with a $(26 \times 26 \times 26)$ Monkhorst-Pack grid), which compares well with the experimental value of 4.331 Å. For the hexagonal phase (with a $(17 \times 17 \times 29)$ Monkhorst-Pack grid), our results for the two independent lattice parameters (5.25 and 2.96 Å) also compare very well with the experimental values (5.19 and 2.91 Å).

Concerning the surfaces of these metals, we have considered the (001) orientation for bcc-Ta. Experimentally, the Ta (001) surface does not show any reconstruction, and the first interlayer spacing is contracted by 11% with respect to the bulk value [48]. Our calculations for this surface also yield an unreconstructed surface, with a contraction of the first layer of 16%, in reasonable agreement with the experiment.

There is not much experimental information available about the surface structure of the Ta nitrides. In thin films, the preferred surface orientation depends on the method of growth and the preparation conditions. Here, we are mostly interested in the nitride surfaces in which the top surface layer contains only N atoms, because these are expected to be less reactive toward the organic ligands of the precursor molecules. Therefore, we have chosen the (111) orientation of cubic TaN. This surface termination can be experimentally obtained, for instance, by means of PVD growth. We performed a surface relaxation with no reconstruction being observed.

2.3.2 Structure of Cu(hfac)(tmvs) and its Disproportionation Reaction

Cu(hfac)(tmvs) exhibits a rather unique electronic structure. The bonding structure of this molecule can be viewed as the following: hexafluoracetylacetonato (hfac) serves as an anion that binds with Cu(I) via electron donation from the lone-pairs of the oxygen atoms to the empty 4s orbital of copper, forming a flat six-membered ring geometric structure due to the π-bonding. The two -CF_3 groups on the ring effectively reduce the charge transfer from oxygen atoms to copper, making the Cu-O bonds considerably weak. Trimethylvinylsilane is used here to prevent further oxidation of copper by pushing its π-electrons in the olefin to the empty 4s-orbital of copper. The C-CF_3 bond in the ligand ring is expected to be weaker than the common C-C bond found in organic molecules since upon the bond breaking the CF_3 species is a relatively stable radical and the other remaining radical fragment can be stabilized via the π-delocalization in the ring. We thus anticipate that this radical species can come off the precursor readily upon contact with the highly reactive metal surfaces, leading to the contamination of the barrier layer. We can therefore use the $\cdot CF_3$ radical species as a probe to study the surface reactivity. The higher reactivity results from more exothermic chemisorption of $\cdot CF_3$, which often leads to decomposition of the radical species at the surface.

Upon the CVD process at the surface, it is desired that two Cu(hfac)(tmvs) molecules undergo a disproportionation reaction process to deposit a copper on the surface while another copper is oxidized to form $Cu(hfac)_2$. The bonding structure between copper and hfac in $Cu(hfac)_2$ is similar to Cu(hfac)(tmvs) with slightly stronger strength due to the higher oxidation state of copper. Copper adopts a square planar electronic configuration, yielding an essentially flat geometric structure for the molecule.

The fully optimized structures of Cu(hfac)(tmvs) and $Cu(hfac)_2$ are shown in Fig. 2.2. For the disproportionation reaction, we estimate from our calculations that this process would be very endothermic in the gas phase with a reaction energy of 1.44 eV. However, this process becomes highly exothermic with a reaction energy in the range between -2.5 and -4.39 eV, depending on the surfaces and the specific sites on which copper is adsorbed. It is therefore clear that the key step for the disproportionation reaction is the adsorption of Cu(hfac)(tmvs).

2.3.3 Chemisorption of CF_3 on Ta(001) Surfaces

As the first step toward the understanding of the interaction of Cu(hfac)(tmvs) with the barrier layer, we utilized $\cdot CF_3$ as the probe to explore the surface reactivity. This $\cdot CF_3$ radical species could be present during the deposition process, as one of the decomposition products of Cu(hfac)(tmvs). We first performed extensive studies

Figure 2.2: Relaxed structures of Cu(hfac)(tvms), $Cu(hfac)_2$, and (tvms) in left, center, and right panels, respectively. In the image the H, C, O, F, Si and Cu atoms are shown as white, brown, red, gray, cyan and yellow balls, respectively

on the interaction of $\cdot CF_3$ with the Ta(001) surface. Initially, the $\cdot CF_3$ radical was placed about 5 Å above the surface, with different initial orientations. Starting from these configurations, we allowed the system to evolve to minimize the energy, using a conjugate gradients algorithm. In all cases, we found that the radical rapidly approaches the surface and is decomposed completely upon interacting with the barrier layer atoms. The decomposition of $\cdot CF_3$ yields strongly chemisorbed carbide and fluoride species on the metal surface. The initial structures and the fully optimized surface structures of two selected cases are shown in Fig. 2.3. The chemisorption process is extremely exothermic (12.61 eV in both cases) and the decomposition takes place spontaneously, with virtually no activation barrier. The extraordinarily high chemisorption energies arise from the charge transfer from Ta atoms to C and F atoms, since the d-electrons of Ta are chemically very active. It is therefore obvious that the ligands on Cu(hfac)(tmvs) or any other copper precursor will not be able to survive at the highly reactive Ta surface, and adhesion/contamination problems may occur due to the instantaneous decomposition of the precursor. This is the fundamental reason that efforts in the past few years to deposit highly adhesive copper films on Ta surfaces via a CVD process have shown limited success. We have performed similar calculations for $\cdot CF_3$ on W(001) and Ti(001) surfaces and found without exception that spontaneous decomposition of $\cdot CF_3$ will take place on both surfaces. We also have made calculations involving other organic radicals, like CH_3, finding a similar behaviour. Thus we conclude that no organic ligand would survive on any of the above metal surfaces without suffering its spontaneous decomposition.

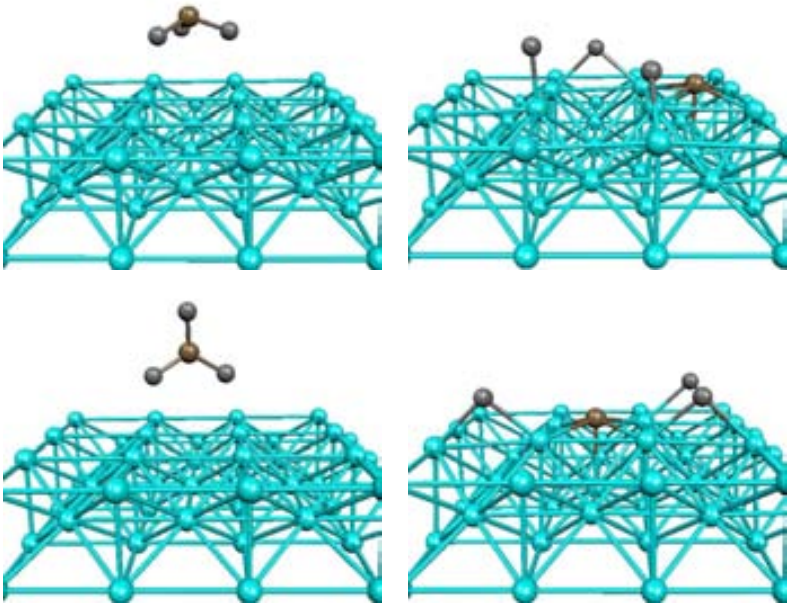

Figure 2.3: View of the initial (left) and final (right) structures for two simulations (up and down) of the $\cdot CF_3$ decomposition on a Ta (001) surface.

2.3.4 Passivation of Ta Surfaces with N_2

Clearly, the results shown in Section 2.3.3 suggest that the surfaces of virgin early transition metals are chemically too reactive toward $\cdot CF_3$ and other organic based ligand systems. Although this study was focused on deposition of copper films using a fluorine-containing organometallic complex such as Cu(hfac)(tmvs) because of its widespread experimental use, a nonfluorinated copper precursor would also undergo degradation on nascent Ta and Ti surfaces. Pretreatment of surfaces to reduce the reactivity is necessary prior to the deposition of copper film. In the present work, we consider using N_2 to passivate the metal surfaces, which is expected to yield nitride layers on top of the metal. The feasibility to form surface nitrides can be readily demonstrated by studying the dissociative chemisorption behavior of N_2 on the metal surfaces. For simplicity, we again selected the Ta(001) surface.

We examined two initial orientations of N_2 on the Ta(001) surface as shown in Fig. 2.4. In both cases, N_2 is located about 5 Å above the surface and approximately perpendicular to the surface normal; in one case, the molecule is placed above the hollow site, and in another, it is above the atop site. Upon energy minimization, the molecule is spontaneously decomposed and surface nitrides are readily formed. The final optimized structures are also shown in Fig. 2.4. The optimization pro-

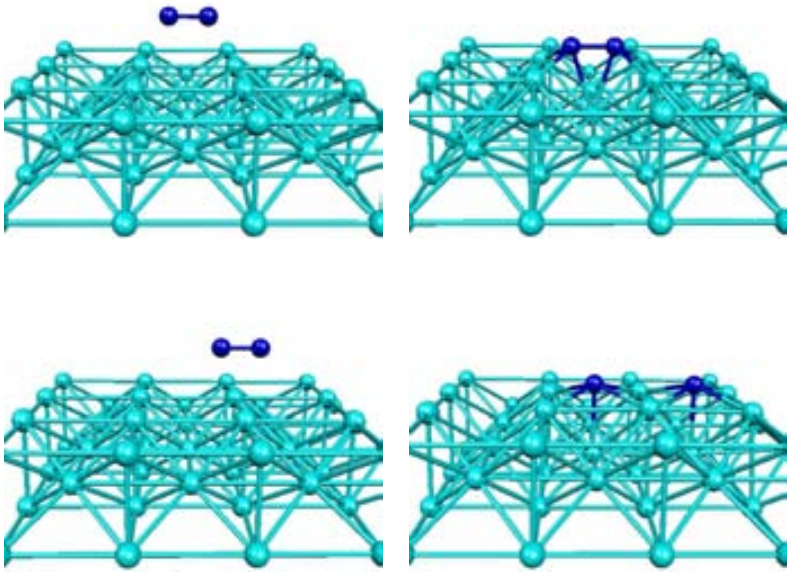

Figure 2.4: View of the initial (left) and final (right) structure for two simulations (up and down) of the adsorption of N_2 on a Ta(001) surface.

cess is nearly barrierless, indicating that the nitride formation process is extremely favorable energetically. Indeed, the calculated chemisorption energies for the above two cases are -3.86 and -6.69 eV, respectively, with the atop site for chemisorption being energetically more favorable. We thus conclude that surface nitriding with N_2 is highly feasible and metal nitride layers can be readily formed. It is worth noting that, with one of the highest bond energies, N_2 is still torn apart on the virgin early transition metal surface. We thus anticipate that no ordinary organic species will be able to survive on the surface without spontaneous decomposition as well.

To find out whether the surfaces of metal nitrides are indeed passivated toward $\cdot CF_3$, we once again examined the adsorption properties of this species on TaN surfaces. Here we assume the stoichiometry of the nitride layer to be 1:1 for simplicity. It will be clear later that this assumption is not necessary and the conclusions made from the present work are also applicable to any other stoichiometry with a richer nitrogen content. We first study $\cdot CF_3$ adsorption on the TaN(001) surface. The top layer of the TaN(001) surface contains both Ta and N atoms. The metal atoms are exposed to the incoming adsorption species. We chose two different orientations of $\cdot CF_3$ initially located at about 5 Å above the surface, one with F atoms tilting away from the surface and another with F atoms facing down the surface. Upon energy

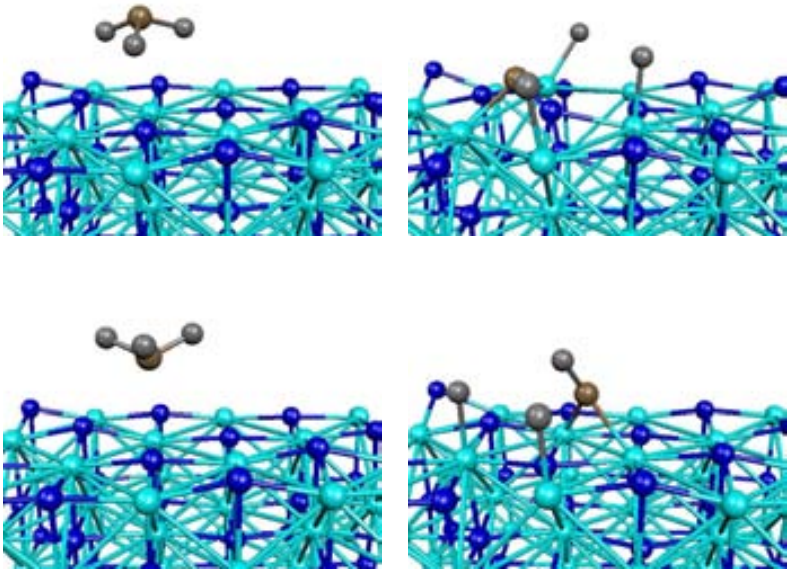

Figure 2.5: View of the initial (left) and final (right) structure for two simulations (up and down) of the adsorption of $\cdot CF_3$ on a TaN(001) surface.

minimization, the $\cdot CF_3$ species is observed decomposed to form surface carbides and fluorides as shown in Fig. 2.5, similar to what happened to the virgin metal surfaces. However, the calculated chemisorption energies are significantly reduced to 6.03 and 8.33 eV, respectively, with the configuration obtained starting with an orientation with F atoms facing down the surface being energetically more favorable, since it results in the formation of an extra Ta-F bond.

It is clear that nitriding on the metal surfaces reduces the surface reactivity toward the incoming precursors. However, the above results show that it is still insufficient to prevent $\cdot CF_3$ from dissociation upon surface contacts as long as the top layer surface contains exposed metal atoms. An interesting question thus arises: can we further passivate the metal nitride surfaces, in that case with N_2, to fully shield the top layer metal atoms from direct contact with the precursors? To address this issue, we took another step to further investigate the adsorption behavior of N_2 on the TaN(001) surface. Indeed, as shown in Fig. 2.6, continuing nitriding with N_2 on the TaN(001) surface is possible. In fact, the calculated adsorption energies show that the chemisorption process is still energetically highly exothermic. The figure shows two initial orientations of N_2 approximately parallel to the surface, one aligned with two neighboring Ta-Ta atoms and another located above an atop

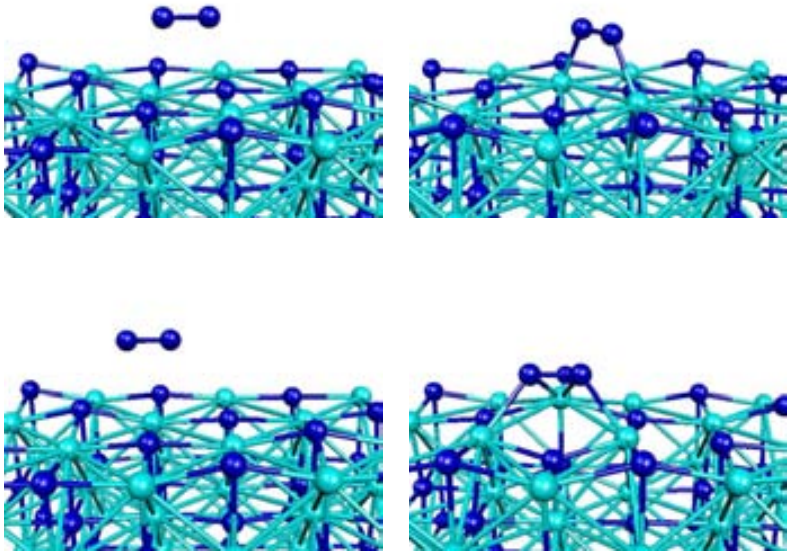

Figure 2.6: View of the initial (left) and final (right) structure for two simulations (up and down) of the adsorption of N_2 on a TaN(001) surface.

site of a Ta atom. Both are about 5 Å above the surface. Energy minimization in both cases yields a chemisorption energy of 1.02 and 1.80 eV, respectively, with the initial N_2 location above the atop site being energetically more favorable. The optimization path is essentially downhill, indicating that the chemisorption process is both kinetically and thermochemically favorable. The results suggest that in general any TaN surface with metal atoms exposed to N_2 molecules can be further nitrided. In other words, the results of the first-principles calculations imply that under N_2-rich environment, TaN surfaces should all be covered with N atoms.

Two important issues immediately following the formation of nitride surfaces are whether the surfaces are properly passivated and whether copper films can be formed on top of the surfaces. We already showed that the top layer of the TaN surfaces should be formed by N atoms under N_2-rich atmosphere. Therefore, for simplicity, we select the TaN(111) surface as the surface model of TaN since the top layer of the surface contains only N atoms. Once again, we consider the adsorption behavior of $\cdot CF_3$ on this surface. Several initial configurations, all with $\cdot CF_3$ species about 5 Å above the surface, are placed above the hollow, bridge and atop sites, respectively. However, upon energy minimization, the $\cdot CF_3$ species is landed at the atop site in all cases, forming a strong covalent C-N bond on the surface (see Fig. 2.7). Two final

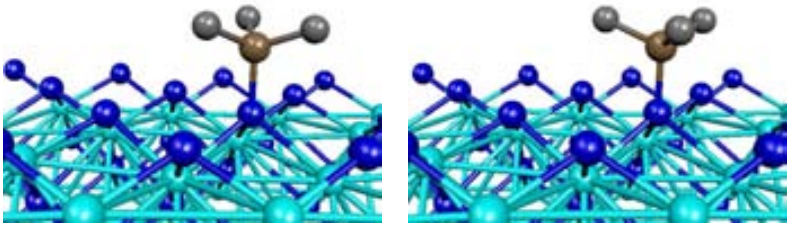

Figure 2.7: View of the final structures for two simulations of the adsorption of $\cdot CF_3$ on a TaN(111) surface.

	hollow	**bridge**	**atop**
Cu on Ta(001)	5.57	4.46	3.58
Cu on TaN(111)	4.44	4.04	3.03

Table 2.2: Adsorption energies (in eV) for a Cu atom on different sites of the Ta(001) and TaN(111) surfaces

configurations with different orientations of the CF bonds relative to the surface normal are obtained. However, the energies of these configurations are almost the same: 3.15 and 3.22 eV, respectively. In contrast to the $\cdot CF_3$ chemisorption on the virgin metal surface and the TaN surface with exposed metal atoms, the most striking feature in the present case is that $\cdot CF_3$ is not decomposed upon interacting with the surface and the calculated chemisorption energies are much lower than those in previous cases. The results indicate that the surface reactivity toward the precursor has been significantly reduced. The fact that $\cdot CF_3$ binds to the surface by means of a covalent bond simply indicates the radical character of this group but does not imply a stability problem on the surface, as we observed in the case of the pure metal and nitride surfaces with Ta atoms exposed.

To address the issue of the adhesion strength of the copper film on the nitride surface, we examined copper adsorption at three possible sites on both Ta(001) and TaN(111) surfaces. The calculated adsorption energy is displayed in Table 2.2. On both surfaces, we find that absorption on the hollow site is the most favorable, followed by the bridge site and last the atop site. However, at all sites, the adsorption energies are considerably large, indicating that the adhesion of the copper film will be very strong for both virgin metal surfaces and metal nitride surfaces. Therefore, surface passivation via nitriding would not significantly reduce the adhesion strength of the copper film. We also note that the driving force for the adhesion of copper

for the virgin metal surfaces and the metal nitride surfaces are completely different. In the former case, the adhesion occurs via metal-metal bonding, whereas in the later case, it is dictated by the charge transfer from copper to the nitrogen atoms in contact.

2.3.5 First-Principles Molecular Dynamics Simulations of Cu(hfac)(tmvs) at Ta(001) and TaN(111) Surfaces

Using $\cdot CF_3$ to probe the surface reactivity toward the copper precursors, we have shown in previous sections that surfaces of virgin metals as well as the surfaces of metal nitride with the metal atoms exposed will react strongly with the copper precursors, and that proper surface passivation with nitrogen can greatly reduce the reactivity. To gain a comprehensive understanding on the reaction mechanisms for Cu(hfac)(tmvs) at Ta surfaces and to ensure that the Ta surfaces are indeed properly passivated, we further carried out first principles molecular dynamics simulations to investigate the dynamic behavior of Cu(hfac)(tmvs) upon contact with Ta(001) and TaN(111) surfaces.

We start with the pure metallic tantalum surfaces and performed MD simulations under various initial conditions. In all cases, we found that Cu(hfac)(tmvs) spontaneously decomposes upon contact with the virgin early transition metal surfaces regardless of the initial orientations of the molecule with respect to the surface, its velocity, direction of impact, and other technical parameters, although the details of the final configurations depend on the initial conditions. Fig. 2.8 shows a few snapshots of Cu(hfac)(tmvs) on the Ta(001) surface during one of the MD runs. The simulation was run for 0.5 ps, keeping the system temperature at 373°K with a Nose thermostat. The molecule is disassembled very rapidly as it approaches the surface. The copper atom is released from the ligands and is adsorbed strongly at the hollow site. However, the ligands also break up as soon as they contact the metal surface, yielding H, F, and C atoms and other fragment species chemically attached to the top metal layer. Consequently, the metal surface becomes contaminated with various undesired chemical species, most probably leading to adhesion problems. The MD simulation nicely explains the experimental observation that carbide, oxide, and fluoride species are all formed upon deposition of Cu(hfac)(tmvs) on Ta surfaces. It is worth noting that, despite the fact that the present simulation is done only for Cu(hfac)(tmvs) on a Ta surface, other organometallic precursors will undoubtedly undergo similar instantaneous decomposition on Ta surfaces as well if the surfaces are not properly passivated.

Our extensive MD simulations of Cu(hfac)(tmvs) interactions with TaN(111) surface give a completely different picture. Fig. 2.9 displays a few snapshots of one of the MD runs, which was performed at 473°K for 1.0 ps. Initially, the pre-

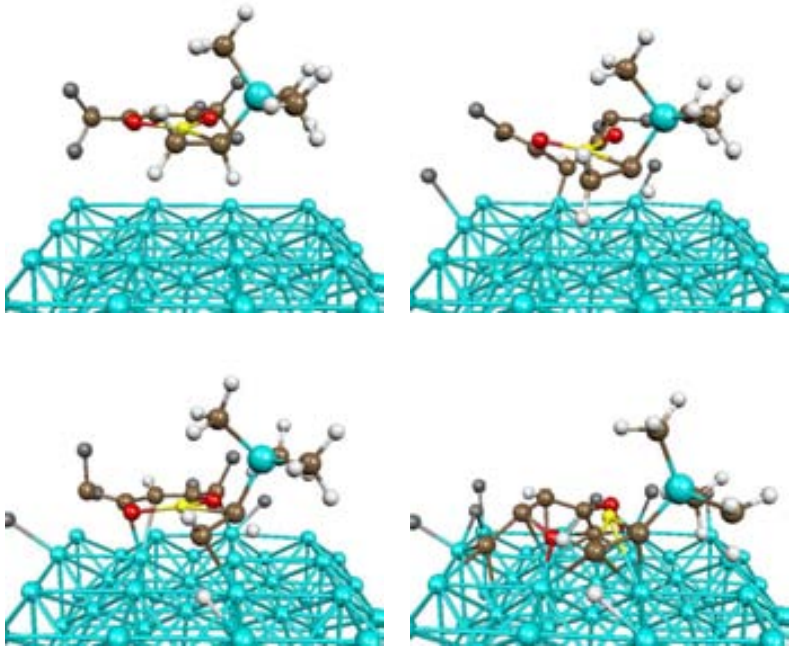

Figure 2.8: Snapshots of four configurations during a MD simulation on the decomposition of Cu(hfac)(tmvs) on a Ta (001) surface.

cursor was placed at about 5 Å above the surface with a vertical speed of 0.067 Å/fs downward. Note that the top layer of the surface is covered entirely by N atoms. Both the O-Cu bond and the Cu-olefin bond are gradually loosen up upon Cu(hfac)(tmvs) approaching the surface. At the end of the simulation, the Cu atom lands on the hollow site formed by 4 neighboring N atoms; however, both (hfac) and (tvms) remain loosely bonded with copper. This is because formally the Cu atom is still positively charged and disproportionation reaction has to occur to completely liberate the ligands. It is particularly remarkable that both (hfac) and (tvms) are now repelled from the nitride surface, in sharp contrast to the situation on pure virgin metal surfaces or incompletely passivated surfaces on which metal atoms are still exposed to the precursor. Qualitatively, the repulsion between the surface and ligands of the precursor should be expected since they are both electron rich. The other MD runs present similar general features, with Cu interacting attractively with the surface, and the ligands remaining intact and being repelled from the surface. These results indicate that surfaces fully covered with N atoms are indeed well passivated and can serve as the diffusion barrier layer for deposition of copper film. They underscore the fundamental importance of surface passivation for copper deposition at transition metal surfaces via CVD.

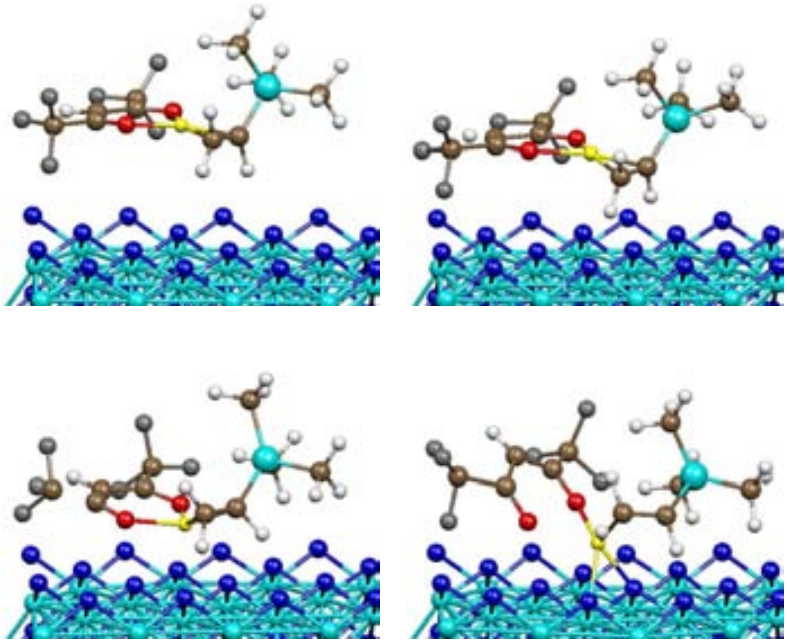

Figure 2.9: Snapshots of four configurations during a MD simulation on the deposition of Cu(hfac)(tmvs) on a TaN (111) surface.

2.4 Titanium and Tungsten Surfaces

In this section we briefly summarize the results for barrier layers of Ti and W. Following the same methodology as for Ta, several MD runs were performed, in which the Cu(hfac)(tmvs) molecule was thrown at the surface with a given initial velocity and orientation.

All the MD simulations of Cu(hfac)(tmvs) precursor with the pure, clean metallic Ti and W surfaces show clearly a decomposition of the precursor upon contact with the surfaces. This behavior is independent of the initial orientation of the molecule with respect to the surface, its velocity and other technical parameters. As an example, Fig. 2.10(a) shows the configuration at 1 ps of the MD runs for Cu(hfac)(tmvs) on the (001) surface of W. The details of the final configurations depend on the initial conditions. However, in all cases the surface ends up covered by a disordered ensamble of chemisorbed hydrogen, carbon, oxygen, and fluorine atoms.

For the nitrogen passivated surfaces, we considered surfaces in which the termination is such that only N atoms are exposed, as in the TaN case we observed that the presence of metal atoms exposed on the surface still leads to high reactivity. For TiN, we considered the (001) surface of the known cubic NaCl bulk phase [49]. For

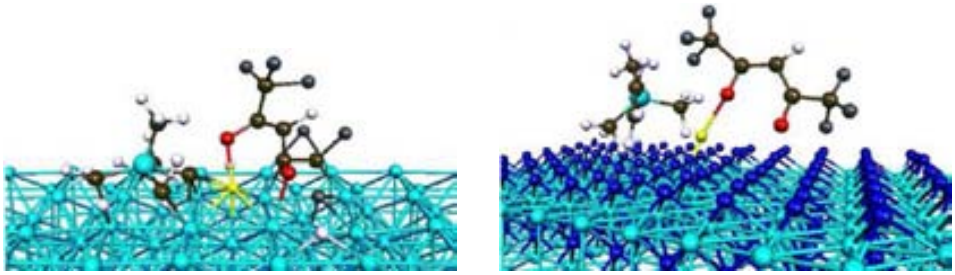

(a) (b)

Figure 2.10: Configuration at 1 ps from MD simulations of the interaction of: (a) Cu(hfac)(tmvs) with W(001) and (b) Cu(hfac)(tmvs) with a hexagonal-WN(100)

WN, we considered two possible crystalline structures reported in the literature: a hexagonal and a cubic NaCl phase [50]. For these two phases, the surfaces fully covered by N are the (001) and the (111), respectively. However, our calculations show that the N- covered (111) surface of the cubic phase undergoes a strong relaxation of the first two surface layers, which shift with respect to the underlying planes, in such a way that the stacking order at the surface is changed into one very similar to that of the (001) surface of the hexagonal phase. Therefore, the atomic structure of the N-covered surfaces of both crystalline phases are very similar, which leads to very close properties of reactivity toward the Cu(hfac)(tmvs) precursor. Therefore, we will only show here results for the (001) surface of the hexagonal WN phase.

Figure 2.10(b) shows a configuration at 1 ps from MD simulations of the interaction of Cu(hfac)(tmvs) with the N-covered (001) surface of WN. As we observed for the case of Ta, the nitrogen passivated surface of W shows that the surface is selectively interacting with the precursor. During the simulation, we can observe that the Cu atom binds to the surface, while breaking its bond with the olefin group of (tmvs). For the remaining part of the simulation, the Cu atom remains bonded to the surface and to the (hfac) group. In all our simulations for WN, we observed similar trends, with no reactivity of the ligands with the surface.

For the case of TiN, the situation is in general similar: the precursor does not decompose upon contact with the surface, and Cu bonds to the surface layer. However, in some of our simulations we have observed some interaction of the olefin group of (tmvs) with the surface (results not shown). The binding energy of this group on the TiN surface is around 4 eV.

2.5 Concluding Remarks

Chemical vapor deposition of copper film on a virgin or improperly passivated early transition metal diffusion barrier layer is a critical step for the production of a new generation microelectronic devices and has presented a challenge due to the persistence of adhesion difficulties with currently available deposition precursors. Direct deposition of copper films via CVD or ALD is accompanied by the formation of undesired organic fragments on surfaces, leading to poor adhesion properties. Using first-principles methods based on Density Functional Theory, we carried out extensive calculations to understand the deposition mechanisms and, most importantly, proposed a practical solution to solve the adhesion problems by passivating the transition metal surfaces with nitrogen. Our calculations were performed with one of the most important CVD precursors, Cu(hfac)(tmvs), with tantalum as the barrier material.

Using $\cdot CF_3$ as a probe to test the surface reactivity toward the precursor, we show that this radical species will undergo spontaneous decomposition on the Ta(001) surface (one of the most close-packed and, presumably, least reactive surface orientations), with extremely favorable dissociative chemisorption energies. The chemisorption process is facilitated by the electron transfer from the Ta atoms to C and F upon surface contact. It thus becomes obvious that the metal surface must be passivated prior to the deposition of any organometallic precursors. We show that this can be done by reacting N_2 with the metal surfaces to form the nitride layers. It was found that N_2 will readily decompose into atomic form upon contact with the metal surfaces and will further react with the exposed metal atoms on the nitride layers whenever possible via a dissociative chemisorption process until the top layer is fully covered with N atoms. Our results indicate that the surface reactivity in this case is greatly reduced and the barrier layer is properly passivated. We subsequently performed a series of molecular dynamics simulations to gain comprehensive understanding on the deposition mechanisms for the copper precursor, Cu(hfac)(tmvs), on Ta(001) and TaN(111) surfaces under typical deposition conditions. We show that Cu(hfac)(tmvs) will decompose spontaneously upon contact with the Ta(001) surface. The ligands on the precursor undergo rapid decomposition as the molecule approaches the surface. In addition to the copper deposition, the fragments of the ligands are also adsorbed on the metal surface, forming carbides, oxides, fluorides, and other undesirable species. The simulation has reproduced what was previously observed in experiments, and adds a microscopic explanation to these observations. The first-principles MD simulation on Cu(hfac)(tmvs) at TaN(111) surface yields a completely different picture. The copper atom is now firmly adsorbed at the hollow site formed by four neighboring N atoms. The ligands loose up their bonds with the Cu atom and are repelled from the surface due to the repulsion between the ligands, which are negatively charged (hfac) and electron-rich (tvms), and the electron-rich

N layer of the TaN(111) surface. In the entire course, the ligands are stable and will remain slightly above the surface until the disproportionation reaction occurs, in which they are liberated and returned to the vapor phase.

The first-principles computational results presented here underscore the critical importance of metal surface passivation for deposition of copper films on transition metal surfaces. Although we mainly presented the results for Cu(hfac)(tmvs) on Ta(001) and TaN(111) surfaces here, the same conclusions are applicable to other transition metals such as Ti and W (as we have presented here), and possibly to other organometallic precursors and other metals. One practical solution to the materials contamination issue is to passivate the metal surfaces with either N_2 or NH_3 to reduce the surface reactivity. By covering the entire top layer of the surfaces with N atoms, it is possible to obtain a copper film with good uniformity. Experiments on CVD on the passivated metal surfaces are being carried out and the preliminary results have confirmed the theoretical predictions.

Chapter 3

Structure of C_{60} on Ge(111) in the $\sqrt{13} \times \sqrt{13}\,R14°$ Phase

In this chapter we analyze a recent determination of the structure for the $\sqrt{13} \times \sqrt{13}\,R14°$ phase of C_{60} deposited on a Germanium(111)-c(2×8) surface. We present a detailed study about the interaction of C_{60} with the surface Germanium (Ge) atoms.

3.1 Introduction and Motivation

The carbon fullerene C_{60} is a molecule with spherical structure, first found by Kroto et al. in 1985 [51], which presents fascinating properties such as superconductivity [52] and photoconductivity [53] and unique potentialities for applications. Review of the work done on this molecule is available in the Refs. [54],[55]. However, to get advantage of its characteristics in potential electronic or mechanical devices, a prior step is to have a good knowledge of interaction between this molecule and different materials, since it is expected that its bonding will strongly influence its intrinsic properties. One research line has focused on the grown of thin C_{60} films on metallic or semiconductor host materials. Its main goal is to obtain stable C_{60} films on these substrates, keeping the original characteristics of C_{60} itself and its films. To reach this, a great effort has been done in revealing the properties of two dimensional single layers of C_{60} molecules adsorbed on single crystal surfaces. The reason for doing this is the common belief that chemical bonding effects due to substrate-C_{60} interactions appear only to be important for the C_{60} molecules in direct contact with the surface [56].

The understanding of the interaction of C_{60} with elemental semiconductor surfaces receives an intense interest due to its potential industrial applications. Studies have been done especially on silicon [57, 58, 59, 60, 61], germanium [62, 63, 64, 65, 66]

and gallium arsenide [67, 68].

In the particular case of the C_{60} adsorption on Ge(111), three different phases are known to form at the interface as the annealing temperature is increased, namely:

- For temperatures between 300° and 400°C, a 'bulk-like' C_{60} hexagonal single layer phase, with a C_{60}-C_{60} distance around 10 Å [62].
- For temperatures between 400° and 550°C, the close packed $3\sqrt{3} \times 3\sqrt{3}\,R30°$ phase, where the C_{60}-C_{60} distance is ∼10.4 Å [64].
- For temperatures between 550° and 650°C, the $\sqrt{13} \times \sqrt{13}\,R14°$ phase, with a C_{60}-C_{60} distance of ∼14.42 Å [66, 63].

These three phases are not reconstructions of the clean germanium surface; they correspond to the periodicity observed for the whole interface when the monolayer of C_{60} has been adsorbed on the Ge substrate.

Full C_{60} desorption occurs at $\sim$ 700°C, a temperature above which the Ge surface reconstructs back to its original c(2×8) structure. In the Ge(111)-c(2×8) reconstruction [69] the top bilayer is decorated with 1/4 monolayer of adatoms arranged into double rows running along the $[\bar{1}10]$ direction (upper part of the left image in Fig. 3.1). Each Ge adatom bonds to three atoms in the first layer, thus saturating three-fourths of the ideal surface dangling bonds.

The work presented in this chapter is the result of a collaboration with the *Surface and Interface Science Group* from the *European Synchrotron Radiation Facility* and the *Crystallography and X-ray diffraction laboratory* in the *Institut de Ciència de Materials de Barcelona*. The aim of this work has been to get a reliable model of the surface structure for the $\sqrt{13} \times \sqrt{13}\,R14°$ phase[1] and to describe its electronic structure as well as the interaction between the C_{60} and the Ge substrate. Using information from Low Energy Electron Diffraction (LEED), Scanning Tunneling Microscopy (STM) and surface high energy x-ray diffraction experiments, the above mentioned groups have proposed a model for this phase (see Torrelles *et al.* [70]). Before making a detailed description of this model, we will describe another model previously proposed by Xu *et al.* [66] for the same phase.

The scheme of the model proposed by Xu *et al.* is presented in Fig. 3.1(b). In this model there is a reconstruction of the virgin Ge(111)-c(2×8) surface structure characterized by a change in the position of the adatoms, in such a way that each C_{60} molecule is supported by three adatoms. All the adatoms are sandwiched in between the C_{60} molecules and the first Ge layer. Based on their Scanning Tunneling Microscope (STM) experiments, Xu *et al.* were not able in to determine the orientation of

[1] $\sqrt{13}$ means that the magnitude of the $\boldsymbol{a}$ and $\boldsymbol{b}$ is related with the lattice parameter $\boldsymbol{a}_{\mathrm{Ge}}$ of an ideal Ge(111) surface by the equation $|\boldsymbol{a}| = |\boldsymbol{b}| = \sqrt{13} * |\boldsymbol{a}_{\mathrm{Ge}}|$. $R14°$ refers to a rotation of $\boldsymbol{a}$ relative to $\boldsymbol{a}_{\mathrm{Ge}}$ by 14°.

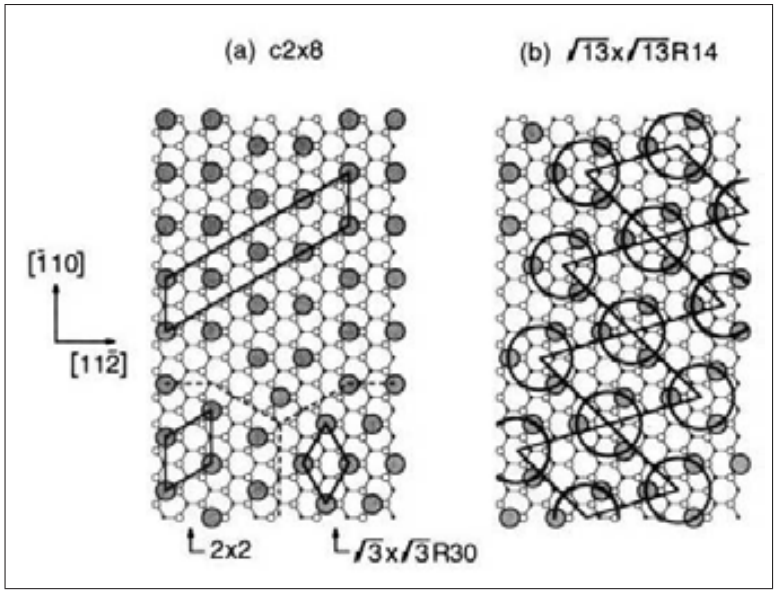

Figure 3.1: a) Top view of the clean Ge(111)-c(2×8) reconstruction. Shaded circles represent Ge adatoms. b) the $\sqrt{13} \times \sqrt{13}\,R14°$ model from Xu *et al.* [66]. The C_{60} molecules are represented by 10 Å large open circles scaled in proportion to the Ge(111) bilayer, shown in small open and solid circles in descending order. Image taken from Ref. [66].

the molecule relative to the surface. In the same manner the nature of the C_{60}-Ge interaction could not be explored. However, it was speculated that, due to the high electron affinity of the C_{60} molecule, there would be a localized charge transfer from the Ge atoms to the triply degenerate lowest empty orbitals of the C_{60}. Hence this ionic bonding would explain the structural flexibility demonstrated by the monolayer of the C_{60} which exhibits the above mentioned ordered phases depending of the annealing temperature. However, Goldoni *et al.* [64], from the analysis of C 1*s* core level and valence band photoemission spectra of the $3\sqrt{3} \times 3\sqrt{3}\,R30°$ phase, have proposed a primarily covalent nature of the bonding between the C_{60} and the Ge atoms.

Let us now describe the model proposed by Torrelles *et al.* [70] for the $\sqrt{13} \times \sqrt{13}\,R14°$ phase. From the LEED analysis, the symmetry of the system was determined; this phase follows a *p3* symmetry, which implies the presence of three 3-fold axes at $(\mathbf{a}, \mathbf{b})$,$(\frac{1}{3}\mathbf{a}, \frac{2}{3}\mathbf{b})$ and $(\frac{2}{3}\mathbf{a}, \frac{1}{3}\mathbf{b})$. From the best fitting to the x-ray diffraction spectra, Torrelles *et al.* have proposed a set of C and Ge atomic positions for this phase. Their resulting structure for the two first Ge bilayers and the C_{60} is shown in Fig. 3.2. It has two main characteristics. First, there are six Ge atoms missing from the uppermost Ge (111) bilayer thus forming a nanopit in the substrate around the

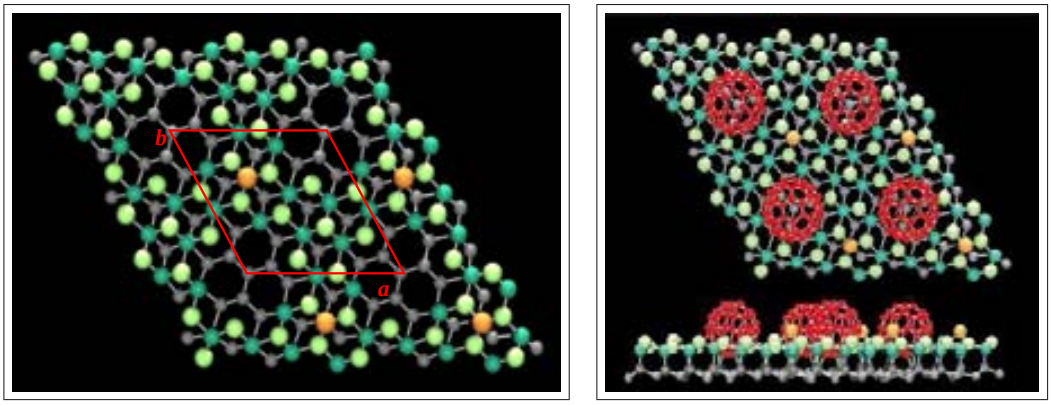

Figure 3.2: Left side: Two bilayers of Ge substrate. Orange spheres indicate the adatom and green first Ge bilayer. Right side: Including the C_{60}. Image designed by X. Torrelles.

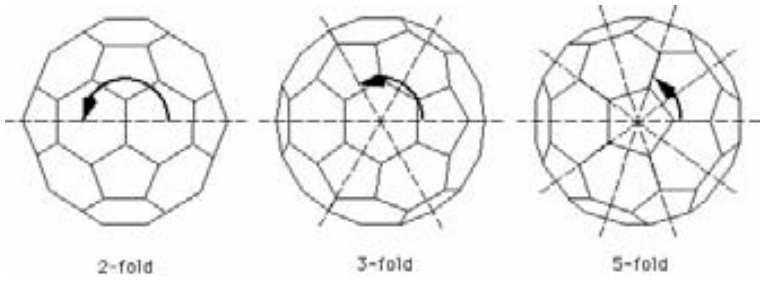

Figure 3.3: Top view of the C_{60} molecule, from each of the symmetry axes.

origin at the $(\mathbf{a}, \mathbf{b})$ fold axis. Second, in each nanopit there is localized a fullerene molecule constrained as well to the *p3* symmetry. In this way the C_{60} is partially buried in the substrate, in clear contrast with the previous model of Xu *et al.*

The possible orientations of the spherical C_{60} molecule with respect to the surface are limited by the observed *p3* symmetry. The isolated C_{60} molecule has an I_h point group symmetry [71], in which there are three kinds of rotation axes (2, 3 and 5-fold), see Fig. 3.3. When the C_{60} is oriented along a 3-fold axis, this axis goes through the center of two facing hexagons. Thus, according to the *p3* symmetry, the C_{60} must be placed on the nanopit with a hexagonal carbon ring parallel to the surface. However, to complete the structural model it is also necessary to especify the rotation around the 3-fold axis of the C_{60} inside the nanopit, with respect to the substrate. From their analysis, Torrelles *et al.* have found that two rotations of the C_{60} could exist, both in good agreement with x-ray diffraction data. The relationship between both, from now on *model I* and *model II*, is a 60° rotation around the 3-fold axis, Fig. 3.4.

Finally, we describe an additional structural characteristic observed by Torrelles

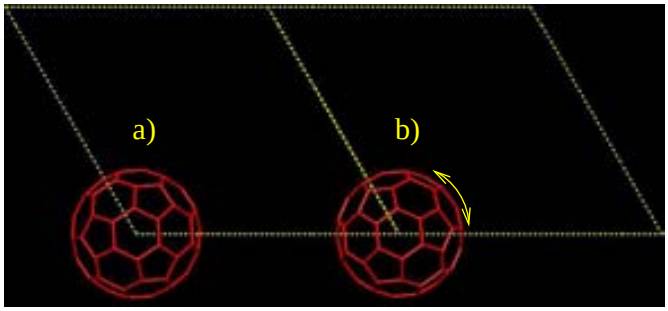

Figure 3.4: The two possible C_{60} orientations respect to the surface unit cell. a) *Model I* and b) *model II*. For clarity, only one hemisphere of C_{60} is shown.

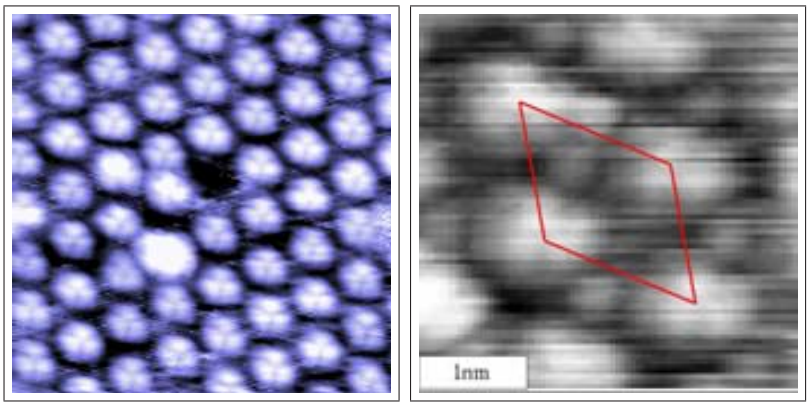

Figure 3.5: a) A constant current STM image of about 10×10 nm^2 of the $\sqrt{13} \times \sqrt{13}\,R14°$ phase, obtained using a sample bias of +1 eV and a constant current of 0.05nA. b) An enlarged image [70, 72]

et al. They have found that a model including an extra Ge atom on the top of the Ge substrate also can agree with the x-ray diffraction data with a good degree of confidence. This extra Ge atom, from now on *adatom*, is localized at the $(\frac{1}{3}\mathbf{a}, \frac{2}{3}\mathbf{b})$ position of the unit cell (orange spheres in Fig 3.2), saturating three Ge dangling bonds from the first layer. The inclusion of this adatom in the model was stimulated mainly by some evidence of its presence in STM images of the system at +1 eV, Fig. 3.5.

From the above description we can conclude that the Torrelles *et al.* model for the $\sqrt{13} \times \sqrt{13}\,R14°$ phase is in fact a set of four possible structural models, everyone in agreement with the experimental information. These four models are explicitly '*model I* with adatom', '*model II* with adatom', '*model I* without adatom' and '*model II* without adatom'.

		valence structure			
H	*Occ*	$1s^1$	$2p^0$	$3d^0$	$4f^0$
	r	1.49	1.25	1.25	1.19
C	*Occ*	$2s^2$	$2p^2$	$3d^0$	$4f^0$
	r	1.25	1.25	1.25	1.25
Ge	*Occ*	$4s^2$	$4p^2$	$4d^0$	$4f^0$
	r	1.89	2.19	2.78	2.19

Table 3.1: Specific details for the generation of the pseudopotentials. *Occ*=Occupation, *r*=cutoff radii (Bohr).

The wide range of experimental techniques used to construct these models suggests that they represent a more precise description of the atomic structure of the phase under study than the previous model of Xu *et al.* However, it is interesting to elucidate which one among the models proposed by Torrellas *et al.* is energetically the best solution to the phase. This has prompted the present first-principles density functional theory calculations. These results will allow a further theoretical analysis in order to reveal the nature of the C_{60}-substrate interaction as well as its electronic properties.

Experimental results concerning the electronic structure of this phase, i.e., STM and photoemission measurements, have been used to compare with those from our calculations.

3.2 Computational Details

We work within the local-density approximation (LDA) using the exchange-correlation potential of Ceperley and Adler [7] as parametrized by Perdew and Zunger [6]. The pseudopotential configuration and cutoff radii (no core corrections were used), generated according to the Troullier-Martins scheme [23], in the Kleinman-Bylander [25] separable form, used along this work are collected in Table 3.1.

We have used a split-valence double-ζ basis set with a single shell of polarization orbitals, as obtained with an energy shift of 0.02 Ry and a split-norm of 15% [16]. The energy cutoff of the real space integration mesh was 260 Ry. This cutoff was tested against well converged values and it represents an optimal value to describe both systems separately, i.e, the bulk Ge and the C_{60} molecule.

In order to describe the bulk Ge, its Brillouin zone was sampled using a grid of $(9 \times 9 \times 9)$ k points [41]. Again, convergence tests were done to obtain a well converged k-point grid. Under these conditions we obtain an equilibrium lattice constant of 5.59 Å, which is in good agreement with the experimental value of 5.66 Å having in mind that LDA systematically underestimates this parameter. In Fig.

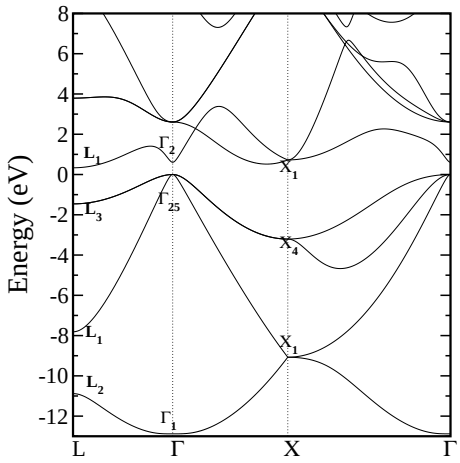

Figure 3.6: Energy band structure of germanium calculated at the theoretical equilibrium lattice constant. The energy origin is the uppermost valence band at the point ($\Gamma_{25'}$).

Ge	Γ_1	$\Gamma_{2'}$	X_1	X_4	X_1	$L_{2'}$	L_1	$L_{3'}$	L_1
SIESTA	-12.88	0.61	-9.1	-3.2	0.733	-10.88	-7.81	-1.46	0.33
Expt.	-12.9±0.2	0.89	-9.3±0.2	-3.5±0.2	1.3±0.2	-10.6±0.5	-7.7±0.2	-1.4±0.3	0.84

Table 3.2: Eigenvalues of the Kohn-Sham equations evaluated at the theoretical equilibrium lattice constant. Experimental values taken from [73, 74, 75]. The eigenvalue at point ($\Gamma_{25'}$) is the energy origin.

3.6 we have included the electronic band structure of bulk Ge evaluated at this equilibrium lattice. The corresponding eigenvalues of the Kohn-Sham equations as well as the experimental ones are collected in Table 3.2. When comparing the eigenvalues it is worth noting that LDA functional underestimates the band gaps in semiconductors. Hence, form our calculation we get an indirect gap ($\Gamma \rightarrow L$) of 0.33 eV (exp. 0.84 eV [73, 74, 75]) and the direct gap is around 0.61 eV (exp. 0.89 eV).

The simulations involving C_{60} on a Ge(111) surface were done in a periodic slab model in a supercell geometry. We have worked with slabs of five bilayers of Ge(111) of width plus the C_{60} molecule, see Fig. 3.7. All the initial atomic positions were those proposed by Torrelles *et al.* from the fitting of the x-ray diffraction data. A layer of hydrogen atoms was included in order to saturate the germanium dangling bonds in the lower bilayer of the slab, see Fig. 3.7. The Ge-H binding distance atoms was 1.5297 Å obtained from a previous calculation on a germanium hydride molecule, GeH_4. Thus, our unit cells include 198 atoms (one less in the geometries

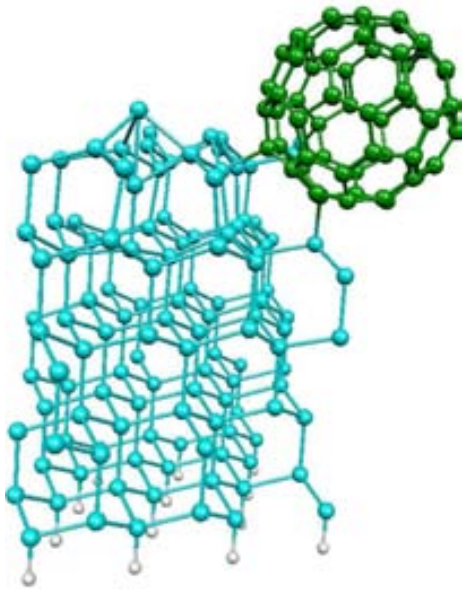

Figure 3.7: Side view with perspective of a slab model. There are five Ge bilayers (in cyan color), one bottom layer of hydrogen atoms (white spheres), and the C_{60}. We can see the adatom on the top surface binding three germanium atoms just below.

without adatom).

The original experimental lattice vectors $\boldsymbol{a}$ and $\boldsymbol{b}$ of the hexagonal cell have a magnitude of 14.422 Å. This magnitude is related with the Ge bulk lattice constant a_{bulk} by the equation $|\boldsymbol{a}| = |\boldsymbol{b}| = \sqrt{13} * (a_{bulk}/\sqrt{2})$. Since our equilibrium Ge bulk lattice constant is smaller than the experimental one, in our simulations the magnitude of the $\boldsymbol{a}$ and $\boldsymbol{b}$ vectors change to 14.246 Å, implying a scaling of the initial experimental coordinates. In this way we have avoided any possible strain in the direction perpendicular to the surface, which would compress the slab in a fictitious way. The magnitude of the unit cell in the perpendicular direction to the surface was 36 Å, of which around 7 Å represent the vacuum. The hexagonal Brillouin zone of these slabs was sampled by a $(2 \times 2 \times 1)$ Monkhorst-Pack mesh.

3.2.1 Optimization of Coordinates

The equilibrium structures for the four different *models* were obtained using the standard conjugate-gradients technique [76]. We restricted the positions of the lowest bilayer of germanium, together with the hydrogen atoms, to their initial values. In this way we simulate a bulk-like environment, this is, the atomic positions change little as we move away of the surface, into the solid.

As all experimental atomic positions satisfy the *p3* symmetry, an important

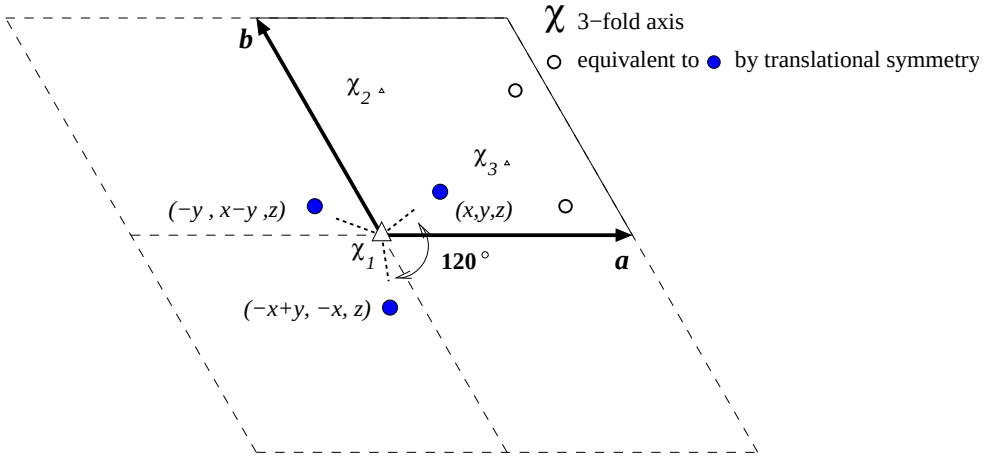

Figure 3.8: Rotation operation. Full circles: atoms related by a rotation of 120° around a χ 3-fold axis. Open circles are the equivalent ones inside the unit cell.

issue in our calculations was to verify that the relaxed coordinates of each model satisfy in the same way this constrain. In the *p3* symmetry, each atom is related to two other by a rotation operation of 120° around a 3-fold axis perpendicular to the surface. This can be translated in a simple rule: if there is an atom with fractional coordinates (x, y, z) (referred to the lattice vectors $\boldsymbol{a}$, $\boldsymbol{b}$ and $\boldsymbol{c}$), Fig. 3.8, then there are two other atoms with coordinates $(-y, x-y, z)$ and $(-x+y, -x, z)$, respectively. The maximum atomic deviation, in angstroms, from the position given by the former rule, was used as a criterion of symmetry conservation of a geometry at each relaxation step.

Fig. 3.9(a) shows how the symmetry evolves along the relaxation process for *model I*, with adatom (blue solid line) and without it (red dotted line). Fig 3.9(b) shows the corresponding results for *model II*. Both graphs represent in a logarithmic scale the maximum symmetry deviation found among all atoms in the cell after each relaxation step.

In Fig. 3.9(a) we see how in the systems named *models I*, despite small numerical fluctuations, their structures conserve the *p3* symmetry along all the relaxation process, irrespective of whether the adatom is included. The picture is rather different in the relaxation process of the *models II*. The maximum deviation value of both systems is around 1 Å at the end of the optimization process. This can not be considered anymore as numerical fluctuations, but a loss of the initial *p3* symmetry. In such manner the initial proposed models *model II*, characterized by a 60° rotation of C_{60} with respect to models *model I*, have to be discarded because they are no longer compatibles with the experimental evidence.

In spite of these results, we wondered whether the preservation of the *p3* sym-

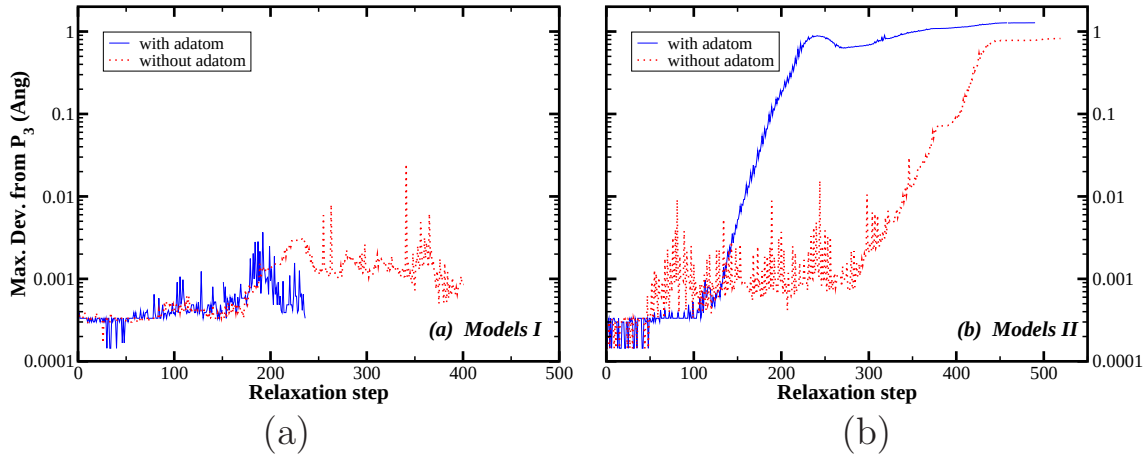

Figure 3.9: Symmetry analysis: (a) maximum atom deviation by relaxation step to *models I*. (b) The corresponding to *models II*.

metry in the *models I* would be a consequence of being trapped in a local minimum in the phase space. As a test we carried out a small molecular dynamics simulations with a constant temperature of 500°K for the *models I*. Thus, the systems were heated up to reach a maximum symmetry deviation around 0.1 Å; doing this we introduce a small loss of symmetry in the systems, taking them into a point energetically higher in the configuration phase space. A final relaxation process on the disturbed system allows us, in a rough way, to evaluate if another near and more energetically favorable state could exist in the configuration phase space. The results show that the systems recovered the *p3* symmetry, with energy values very similar to the previous ones.

3.2.2 Energetic Analysis

We carried out a comparative analysis of the energy between the models under study. However, it is relevant to point out that there is a different number of atoms in the unit cell depending on whether the adatom is considered or not. Therefore, it is not possible to compare directly the final total energies between all these models. However, we can compare directly *models I* and *models II* with the same number of atoms. From the results collected in Table 3.3, we conclude that *models I* are more stable than the *models II*. This confirms the above conclusion of the rejection of *models II* based on the symmetry analysis in relation to the experimental observation of the *p3* symmetry of this phase.

The relative stability between both *models I* (with and without the adatom) can be analyzed with the help of the germanium chemical potential. Taking this into

Including adatom		
	Model I	***Model II***
Relative energy (eV)	0.0	0.88

Without adatom		
	Model I	***Model II***
Relative energy (eV)	0.0	0.52

Table 3.3: Relative energies between *models I* and *models II* with the same number of atoms. The energy of *models I* was taken as a reference, in each case.

	Model I including adatom	***Model I without adtom***
Relative energy (eV)	0.0	0.38

Table 3.4: Relative energies between *models I* taking into account the Ge chemical potential.

account in an energy analysis we can figure out if it is more favorable energetically for the system to locate the adatom in the surface than to retain it in the bulk. We have taken the energy per atom of germanium in its bulk form as a suitable selection of its chemical potential. Our calculations, see Table 3.4, show a preference of the system for having a localized adatom on the surface. However, due to the small difference in energy it is difficult to confirm without doubt this prediction.

In summary, from a symmetry and energetic analysis the *models II* have been discarded. In addition, we can not definitively decide which one between both *models I* is the most probable structural model for the $\sqrt{13} \times \sqrt{13}\, R14^\circ$ phase, although the model with adatom is more likely, since it has a slightly lower energy. The agreement between these optimized *models I* with the diffraction data was calculated by the Crystallography and X-ray diffraction group at the ICMAB. Both sets of final atomic coordinates were the initial proposals for a Modulus Sum Function (MSF) algorithm [77]. They concluded that, although our geometries do not give the best agreement to the X-ray reflections, their degree of confidence, given by a Chi-square statistical analysis, allow to accept both as valid models.

3.2.3 Electronic Properties

Band Structure

The band structure of the surface for the *models I* is shown in Fig. 3.10. The shaded zones come from a calculation of the Projected Band Structure (PBS) of the bulk Ge on the Brillouin zone of the (111) surface. The dashed lines represent the bands of the finite slabs used calculated between Γ, K, and M special points of

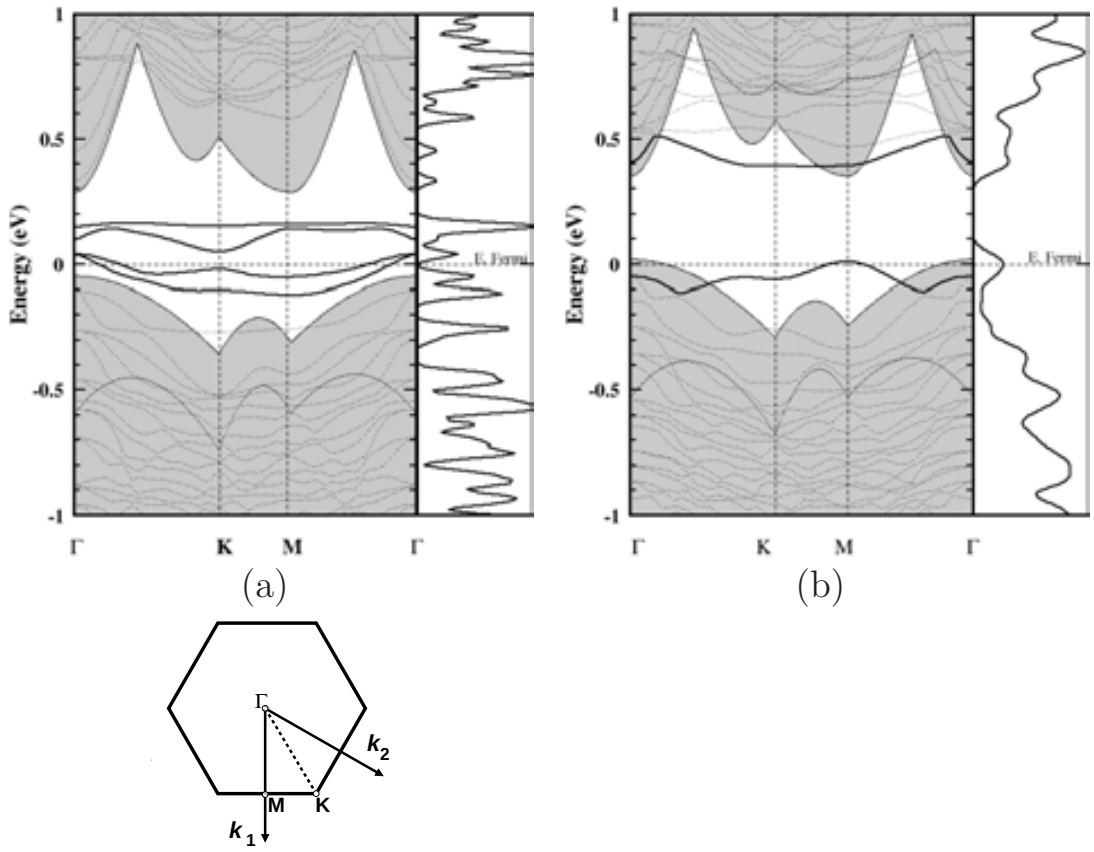

Figure 3.10: a) Electronic structure of the *model I* with adatom. b) *Model I* without the adatom. The shaded zone indicates the corresponding projected band structure of the germanium in bulk. Right panel, the density of states. Inset: The surface Brillouin zone scheme

the hexagonal surface Brillouin zone (see scheme in inset). In both graphs the PBS have been adjusted to that of the slab, by shifting its eigenvalues by an amount, $\delta\epsilon$. We have obtained this value from the comparison between the average total electrostatic potential calculated on the Ge bilayer in the center of the slab with the corresponding one calculated in the bulk [78]. A detailed description of the method can be found in ref. [79].

There is a remarkable characteristic coming from this specific C_{60}/Ge(111) phase. Both systems with and without adatom have an odd number of electrons per unit cell despite the number of Ge layers used. Therefore, in the absence of further distortions or other electronic instabilities (such as magnetic ordering or others), this reconstruction should have a metallic behavior, due to partially filled bands

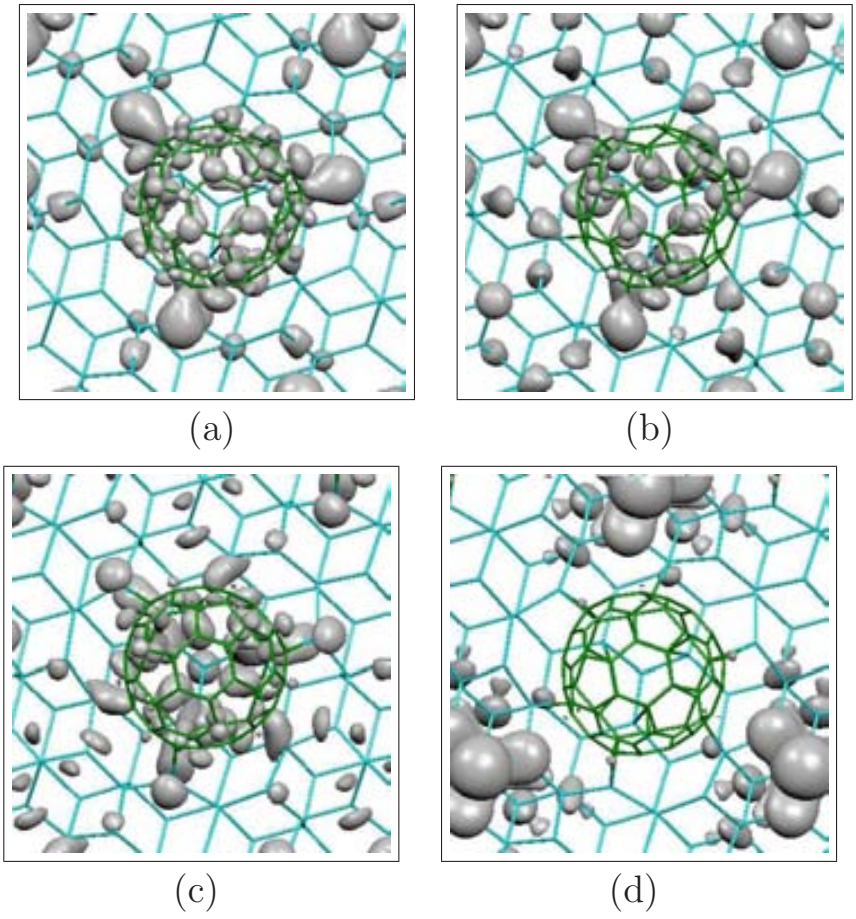

Figure 3.11: Modulus of wave functions around the Fermi level, at the K point of the surface Brillouin zone for the *model I* with adatom. See band diagram 3.10(a).

crossing the Fermi level. Indeed, we see that the system with adatom, Fig. 3.10(a), has four bands inside the band gap of the bulk Ge, with the Fermi level crossing two of these bands. On the other hand, the system without adatom, Fig. 3.10(b) has two bands inside the band gap of the bulk Ge with the Fermi level crossing only one.

The energy separation between the last partially filled band and the lowest unoccupied band is rather small for the surface with adatom, Fig. 3.10(a). On the other hand, the system without adatom, Fig. 3.10(b) has an energy gap, of around 0.4 eV, between the last partially filled band and the lowest unoccupied band.

The nature of these bands can be revealed by the visualization of the wave functions in real space. In Fig. 3.11 we show the charge density of the four states inside the band gap of the bulk for the *model I*, calculated at the K point of the surface Brillouin zone. These are sorted from the state with lowest energy, Fig.

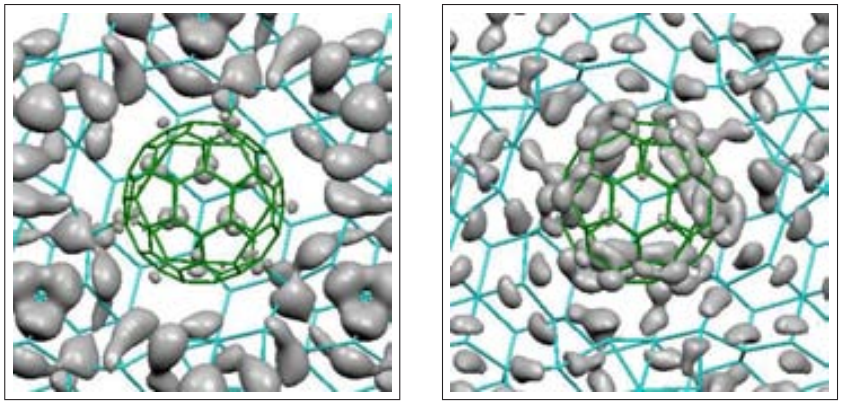

(a) (b)

Figure 3.12: *Model I* without adatom. a) Last surface state and b) first surface state, below and above the Fermi level, respectively. Images at the K point of the surface Brillouin zone

3.11(a) to the higher, Fig. 3.11(d). These images show that these states can not be identified with pure C_{60} molecular states. Rather, three of them, Fig. 3.11(a-c), are related mainly with the bonding between C_{60} and substrate. In contrast, the fourth state in the bulk band gap, Fig 3.11(d), is strongly localized at the adatom.

The corresponding images for the system with adatom are displayed in Fig. 3.12. The charge density of the state in Fig. 3.12(a) (associated to lower band inside the band gap of the bulk Ge) is delocalized in all the surface except in the C_{60} molecules. Meanwhile, the next surface state (Fig. 3.12(b)) from the first unoccupied band spreads along the whole surface, including the fullerene.

Bonding Analysis

We give here a description of the bond between germanium atoms in the surface and the C_{60} for both structural models. First, we looked for a possible charge transfer which would be a proof of an ionic bonding. We have used the Voronoi Deformation Density (VDD) method [80]. This method "..calculates the amount of electronic density that flows to or from a certain atom due to bond formation by spatial integration of the deformation density over the atomic Voronoi cell". We decided to use this method instead of the usual Mulliken Population analysis, because the latter has a strong dependency with the basis set used.

The Voronoi analysis in the *model I* shows a total charge in the whole fullerene of -0.27 *e*. However, the majority of this charge is located in the atoms at the lower hemisphere, actually, in those nearer to Ge atoms. Meanwhile, in the system without adatom the charge transferred from the surface to the molecule is half lower, -0.14

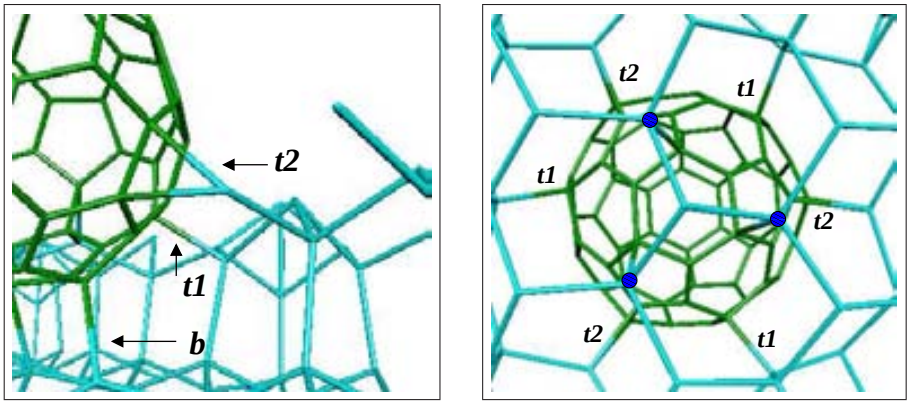

(a) (b)

Figure 3.13: C_{60}-Ge bond structure for the model with adatom. a) Side view showing three different class of bonds. b) Bottom view of two bilayers and the C_{60}. The blue circles indicate a b bond type.

e. These values are very small and therefore we conclude that there is no significant ionic bonding between the C_{60} and the surface Ge atoms.

From the analysis of the geometry of the *model I* with adatom we have identified all the possible directional bonds between carbon and germanium atoms, see Fig. 3.13(a). We have classified them in three groups. To the first group belong the bonds labeled t_1. This type of bond involves a germanium atom in the topmost bilayer with a carbon atom. The distance between both atoms is 2.05 Å. The second group is formed by the t_2 bonds. The Ge atom in this type of bond is localized 2.03 Å from the closest C atom, however the next C atom is only at 2.2 Å. Therefore, there is a possible chemical bond between this Ge atom and both C atoms. In the last group we found the b bonds. They are between a Ge atom in the second bilayer and a C atom, with a Ge-C separation of 2.16 Å. Fig. 3.13(b) shows a view of this surface from a point below the second bilayer. This image shows that each C_{60} is attached to the substrate by three t_1, three t_2 and three b bonds (for clarity, b type bonds have been marked by solid blue circles).

We have done a similar analysis for the model without adatom, Fig. 3.14. In this structure there are only two groups of bonds. The first group includes the t bonds, i.e, those in which the Ge atom is in the topmost bilayer, with a bond length of 2.1 Å. The second group are made from b type bonds. In this bond the Ge atom is located in the second bilayer and its link length is 2.07 Å. In Fig. 3.14(b) we can observe that there are six Ge-C_{60} bonds (3 t and 3 b).

It is relevant to point out that these descriptions have been done from the analysis of structural representations in which the atomic bond is established by the proximity between atoms.

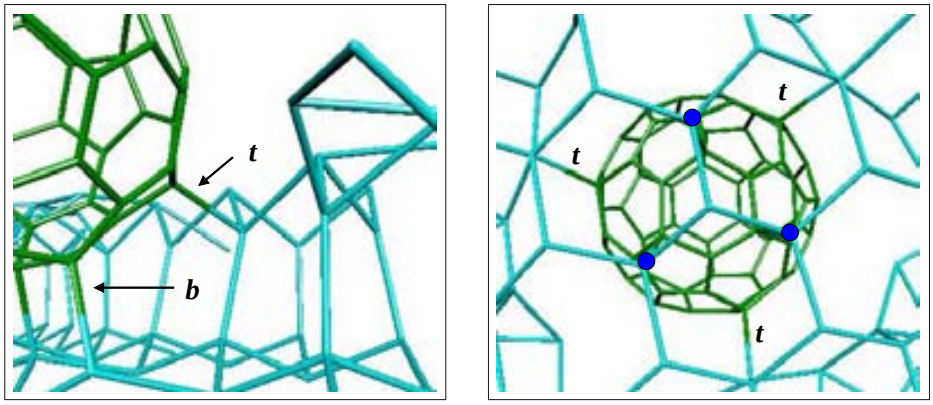

Figure 3.14: C_{60}-Ge bond structure for the model without adatom. a) Side view. b) Bottom view of two bilayers and the C_{60}. The blue circles indicate a b bond type.

We carried out a more rigorous analysis of bonding based on electron charge density. For this we drew isosurfaces of the charge density difference, $\delta\rho(\boldsymbol{r}) = \rho(\boldsymbol{r}) - \rho_{atoms}(\boldsymbol{r})$. This is the valence pseudocharge density minus the sum of atomic valence pseudocharge densities, and hence it is a measure of the change in charge density induced by the chemical bond. This is more clear if we see the contour surface for three close germanium atoms in the bulk, Fig. 3.15(a), where the Ge first neighbors distance is 2.4 Å. The contour graphs are drawn from -0.03 to 0.065 $e/\text{Å}^3$, in steps of 0.05 $e/\text{Å}^3$. The dashed red lines indicate regions with depleted charge, while solid blue lines correspond regions where the charge has accumulated (relative to unperturbed atoms). The presence of a localized charge between two germanium atoms is characteristic of directional covalent bonds. The same situation can be seen in a C_{60} hexagonal ring between first neighbor carbons, Fig. 3.15(b).

Now we show in Fig. 3.16 the contour for the t_1, t_2 and b bonds. The contours for the t_1 bonds (Fig. 3.16(a)) and b bonds (Fig. 3.16(c)) show a clear directional covalent character, with the charge density slightly displaced towards carbon. This is in agreement with the former Voronoi analysis and with the fact that carbon has an electronegativity about 27 % higher than germanium, in the Pauling scale [81]. The conclusions are not so clear when we see the contour graph for t_2 bonds, Fig. 3.16(b). In this figure we show an analogous view to the Fig. 3.13(b) in such a way that the lower C atom at the left side is closer to Ge surface than the upper C atom. The charge is located mainly in the region between the Ge atom and the upper C atom, but not exactly in the line joining both atoms. Meanwhile, it is clear that, in spite of the short length of 2.2 Å between the lower carbon and the germanium atom, there is no bonding charge, thus no bond between them. This, of course, is in contradiction with the representation in Fig. 3.13(a) which is based only in the

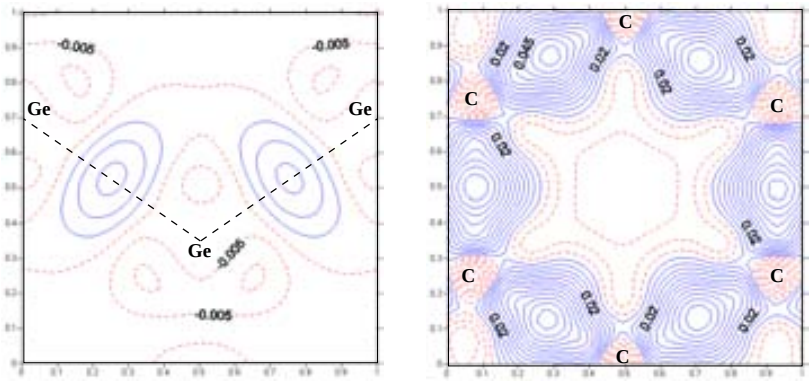

(a) (b)

Figure 3.15: Charge density difference, $\delta\rho(\boldsymbol{r}) = \rho(\boldsymbol{r}) - \rho_{ions}(\boldsymbol{r})$. The contour graphs are in the range (-0.03, 0.065 $e/\text{Å}^3$), and each line correspond to a step of 0.05 $e/\text{Å}^3$. Dashed red a solid blue lines correspond to a negative a positive values, respectively. a) Germanium bonding in the diamond phase. The size of the square side is 3.97 Å. b) A C_{60} hexagonal ring, square side size 2.9 Å.

distance between atoms.

Contours for the system without adatom, Fig. 3.17, show how both bonds t and b have the same directional covalent character seen for the former t_1 and b in Fig. 3.16. In summary, these graphs show evidence of a strong covalent interaction between the C_{60} and the substrate, especially in the case with adatom, in wich there is an extra bond respect to the model without the adatom. Thus, we can talk of chemisorption of C_{60} on the germanium substrate.

Photoemission Spectra

Our next step was to calculate the photoemission spectra for both geometries and to compare them with the experimental ones from the *Surface and Interface Science Group* at ESRF [72]. An important aspect was to decide the contributions from which atoms we should consider in the expression for the photoemission spectrum intensity. Because of the low energy source used in the photoemission experiment (resonance line He I (21.22 eV)), we decided to include only the most superficial germanium atoms in the slab and C_{60} carbon atoms. In low energy photoemission experiments, photons penetrate only few angstroms into the surface and there is a high probability that the electrons coming from deeper layers will be absorbed and will not leave the sample. As a result, the shape of these spectra will be dominated by the electronic properties of the fullerene and the top Ge layers.

In an angle-integrated (PES) experiment, electrons are collected ideally over all

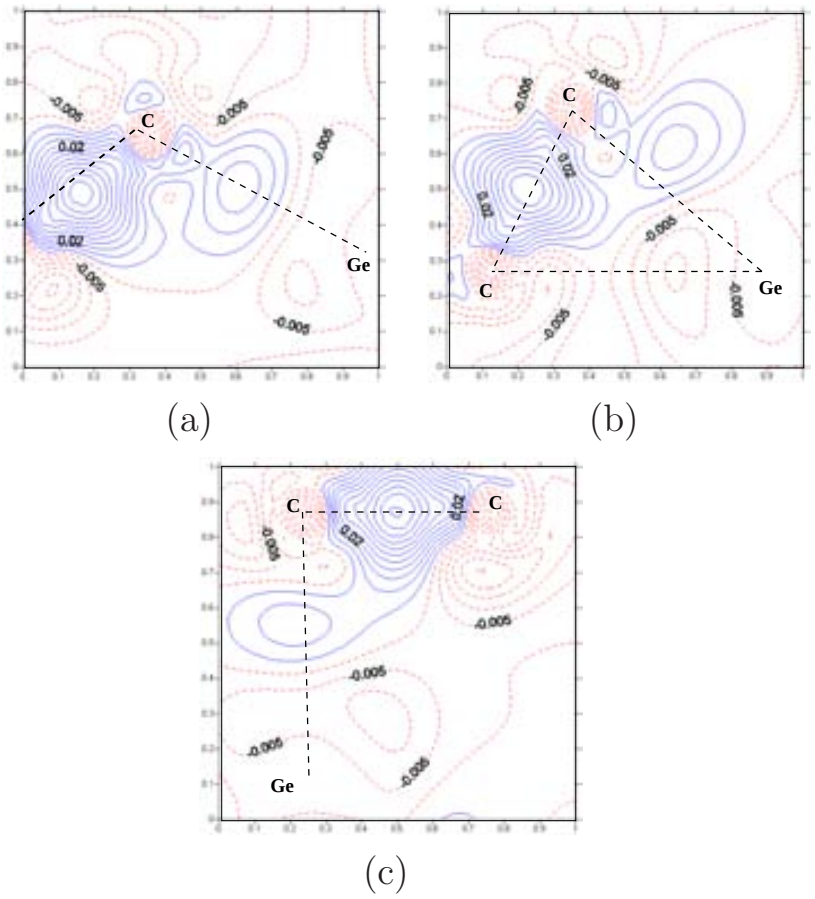

Figure 3.16: Charge density difference contours for *model I*. (a) t_1, (b) t_2 and (c) b bond in Fig. 3.13. The size of the plotted region is 2.9 Å each side.

emission directions, then the photoelectron energy distribution is (neglecting matrix element effects) proportional to the electron density of states (DOS). If matrix elements are taken into account in the simplest way, the photoemission spectrum intensity can be roughly approximated as

$$I(E) = \sum_{i=1}^{N} PDOS(i, E) * \sigma(i) \tag{3.1}$$

where i runs over each atomic basis orbital in the system, PDOS is the projected density of states on the i orbital at an energy value of E, and $\sigma(i)$ is the photoemission cross-section for the corresponding orbital. The cross-section values were taken from reference [82].

The approximation 3.1 to the intensity implies an adiabatic approximation in which the electron is assumed to leave the system slowly so that the electrons from

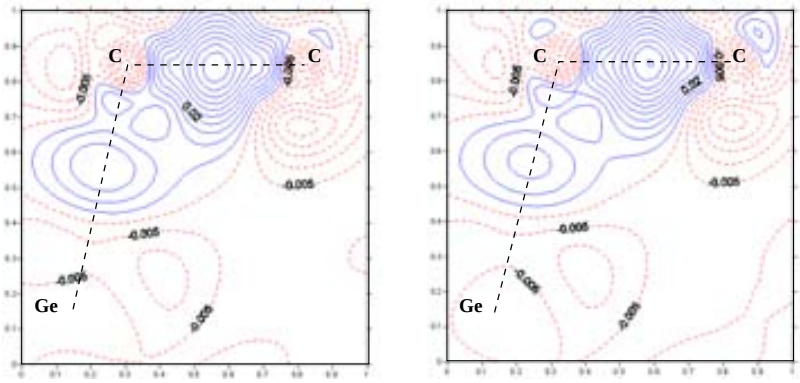

(a) (b)

Figure 3.17: Charge density difference contours for *model I*-without adatom. a) For the t bond Fig. 3.14. b) For the b bond. The square side size is 2.9 Å

or near the excited atom change their energy by slowly adjusting to the effective atomic potential in a self-consistent way. Thus, at any time, the system is in a state of equilibrium [83]. Thus, the approximation 3.1 is only valid for low kinetic energy of photoelectrons.

Figures 3.18(a) and 3.18(b) are the simulated spectra of both *models I*. Due to the reduced number of k points, the simulated photoemission spectrum calculated from the approximation 3.1 has been convoluted with a Gaussian of width 0.23 eV.

By a direct comparison of these spectra with the corresponding spectrum for a film of C_{60} (see Fig. 3.19(a)), it is possible to relate the features labeled $\boldsymbol{A}$, $\boldsymbol{-1}$ and $\boldsymbol{-2}$ with the first three peaks (starting from lower binding energy) in the C_{60} spectrum. Therefore, from the Fig. 3.19(b) the feature $\boldsymbol{A}$ is associated with the C_{60} HOMO (with $6h_u$ symmetry), the $\boldsymbol{-1}$ peak with the molecular orbitals $10h_g$ and $6g_g$, and finally, $\boldsymbol{-2}$ peak with the $6t_{2u}$, $9h_g$, $5h_u$ and $6g_u$ C_{60} states.

The shoulder-like observed $\boldsymbol{B}$ feature is the contribution of Ge surface atoms to the spectra. The dotted lines in Fig. 3.18(a) and 3.18(b) are the calculated photoemission spectra for the system with and without adatom, respectively, but without taking into account the Ge atoms. As a result we find that this shoulder practically disappears in both geometries.

The experimental Angle Resolved Ultraviolet Photoelectron Spectrum (ARUPS) is shown in Fig. 3.18(c). It was obtained by Zegenhagen and collaborators [72] using a conventional He discharge lamp ($h\nu = 21.22$ eV). The reported angles are relative to the emission normal to the surface plane. We see that the main peaks do not suffer any dispersion with the angle, only a decrease of relative intensity of the peak $\boldsymbol{A}$ from 0^0 angle. This behavior could be an indication of localized bonds between the C_{60} atoms and the substrate atoms. The low dispersion implies

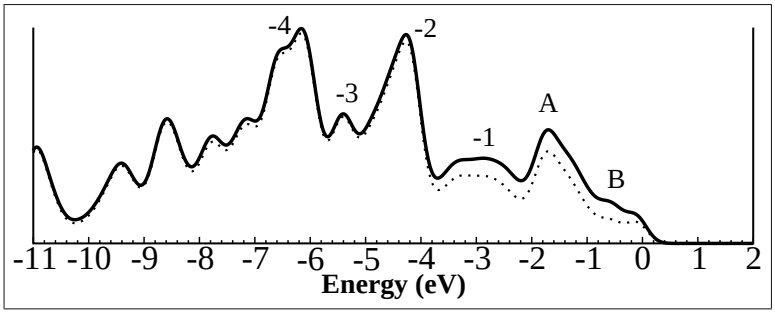

(a)

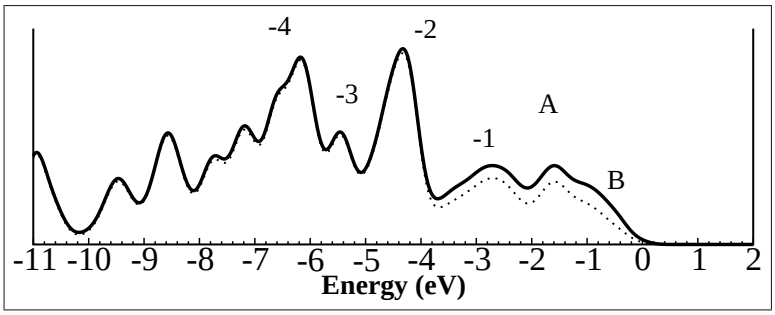

(b)

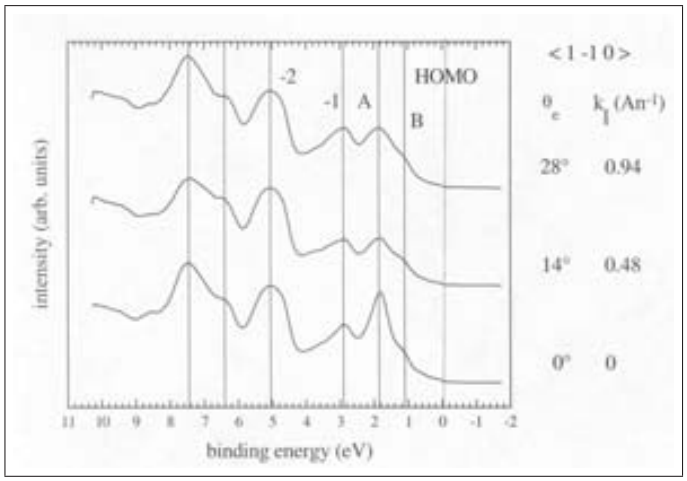

(c)

Figure 3.18: (a) Calculated photoemission spectrum for the *model I* with adatom. (b) Without adatom. (c) Experimental Angle Resolved Ultraviolet Photoelectron Spectroscopy (ARUPS) spectrum of the C_{60}/Ge(111) $\sqrt{13} \times \sqrt{13}\,R14°$ surface. The dotted lines correspond to a calculated photoemission spectrum without taking into account the Ge atoms.

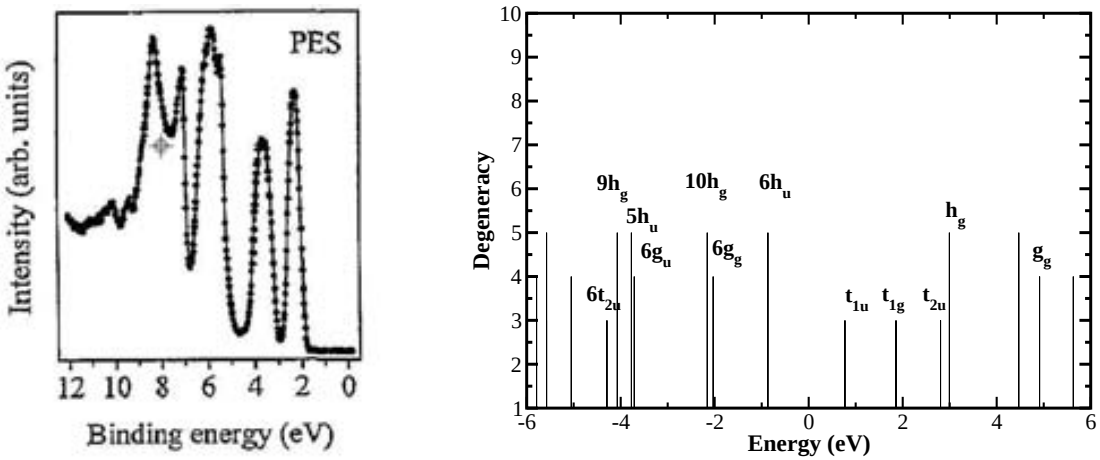

(a) (b)

Figure 3.19: (a)Photoemission spectrum of a film of C_{60} at $h\nu$=21.22 eV from [84]. (b) Electronic energy levels of the C_{60}

that we can make a direct comparison to our simulated spectra calculated in an angle-integrated approximation. These comparisons show that the calculated and experimental $\boldsymbol{A}$ and $\boldsymbol{-1}$ features agree well but that the calculations locate the feature $\boldsymbol{-2}$ about 0.5 eV lower than in the experimental. Nevertheless we have also observed this discrepancy in the simulated spectrum of a isolated C_{60}(results not shown). In summary, both simulated spectra for *models I* are in good agreement with the experimental ones. Hence, from this analysis we conclude again that both structural models are equally probable.

STM Simulation

Finally, we have simulated the constant-current STM images of the optimized models, and then, we have made a comparison with the experimental ones [70, 72]. These simulated images were calculated using the Tersoff-Hamann approximation [85] in which the tunneling current is proportional to the local density of states integrated from the Fermi level to the bias voltage. The experimental images are displayed in Fig. 3.20(a), 3.21(a) and 3.22(a) with a bias voltage applied on the sample of -2, $+1$ and $+2$ eV, respectively.

Our calculated STM images for *model I* including the adatom are presented in Fig. 3.20(b), 3.21(b) and 3.22(b). Those for *model I* without the adatom are displayed in Fig. 3.20(c), 3.21(c) and 3.22(c). These images were calculated at the same experimental voltage.

As a measure of the agreement between simulated and experimental STM images,

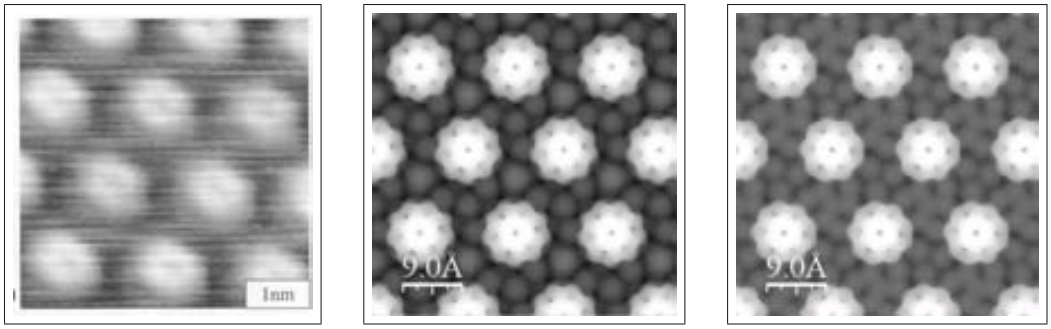

Figure 3.20: a) STM experimental image at -2.0 eV. b) Simulated image in the *Model I* with adatom. c) For the *Model I* without adatom. Isovalue 3.2×10^{-4}.

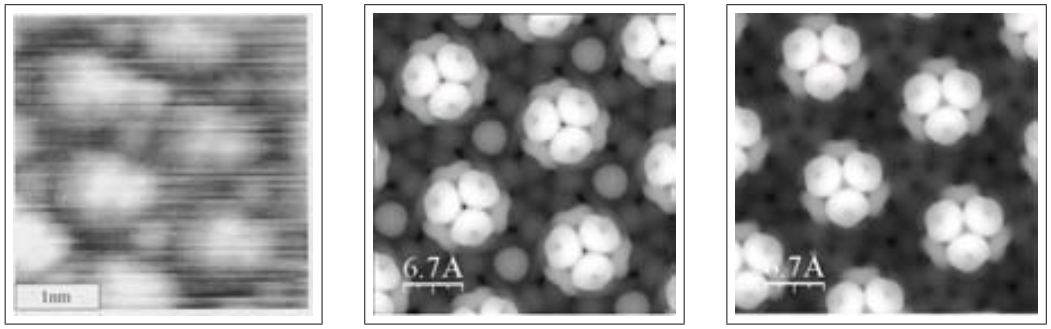

Figure 3.21: a) STM experimental image at +1 eV. b) Simulated image in the *Model I* with adatom. c) For the *Model I* without adatom. Isosurfaces corresponding to the charge density $\rho = 1.5 \times 10^{-4}$ e/Å^2.

we considered mainly the overall shape. In all the images high values of the charge density correspond to white values. A first observation is that the shape of C_{60} in the simulated images is in good agreement with the experimental ones, no matter the presence of the adatom. At -2 eV we can see that there is practically no contribution of the adatom to the simulated image (Fig. 3.20(b)). In the same manner, there is no evidence of its presence in the experimental image (Fig. 3.20(a)) . On the other hand, at positive voltage value it is evident the contribution of the adatom states to the local density of states (Fig. 3.21(c) and 3.22(c)), being this contribution larger at +1 eV (Fig. 3.21(c)). In fact, the presence of this adatom is only observed experimentally at this voltage 3.21(a). Therefore, from this STM analysis the *model I* including the adatom looks better compared to the experimental one.

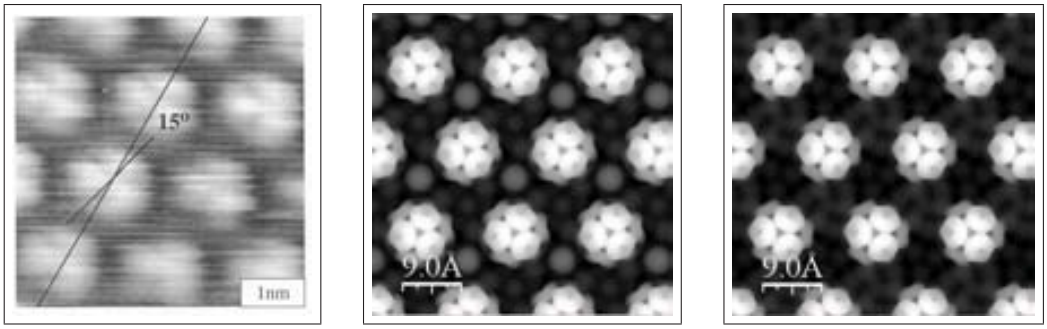

Figure 3.22: a) STM experimental image at +2.0 eV. b) Simulated image in the *Model I* with adatom. c) For the *Model I* without adatom. Isovalue 3.2×10^{-4}.

3.3 Concluding Remarks

The adsorption of C_{60} molecules on a clean Ge(111)-c(2×8) surfaces leads to the formation of a $\sqrt{13} \times \sqrt{13}\,R14°$ phase upon annealing at 550°C. From the analysis of STM, LEED, SXRD data four structural models of this phase were proposed by Torrelles *et al.* The common characteristic in these models is the position of the C_{60} in a hole of the Ge substrate, where six atoms have been removed. All models are consistent with the experimentally observed *p3* symmetry. Each model is characterized by the specific rotation of C_{60} around a 3-fold rotation axis perpendicular to the surface and whether a Ge adatom is located at the (1/3,2/3) axis saturating the dangling bonds of three germanium atoms. The inclusion of this was done based mainly on the analysis of the STM images.

In this work we have validated by first-principles electronic structure calculations these proposed structural models. From a symmetry and energetic analysis the experimentally proposed *models II* have been discarded. In addition, we were not able to decide which of the *models I* is the most probable structural model for the $\sqrt{13} \times \sqrt{13}\,R14°$ phase, although the model with adatom is more likely, since it has a slightly lower energy.

By electron counting arguments all the models considered have a metallic character. Moreover the presence or not of the adatom in the *models I* introduces changes in the electronic structure of the system around the Fermi level. The presence of the adatom generates a set of surface bands inside the band gap of germanium in bulk with small energy differences among them. From an analysis of the wave functions at different k-points it was revealed that the partially filled bands crossing the Fermi level, are made of states localized at those carbon and germanium atoms in contact. However, in the band structure of the system without adatom, the energy difference between the first unoccupied band orbital and the last partially filled band is around

the gap energy value of germanium in bulk. This latter partially filled band is made of only germanium surface states. From a Voronoi charge analysis we concluded that there is a small total charge transfer to carbon from neighbour germanium atoms. This transfer was -0.27 and -0.15 e for the system with and without adatom, respectively. The analysis of electron charge density contours reveals that C_{60} forms nine directional covalent bonds with the substrate. Three of them are with the Ge atoms in the second bilayer. For the case without adatom the number of bonds decreases to six, with also three of them with the Ge atoms in the second bilayer.

The simulated photoemission spectra and STM images of the *models I* reproduce with good agreement the main features and characteristics of the experimental ones. However, the agreement between theoretical and experimental STM images at +1 eV is better when the adatom is included.

In summary, we found that the *model I* with adatom is slightly most stable and in addition it has the best agreement with the experimental evidence. However, the presence of the adatom is still an open question. Further investigations are needed to elucidate the presence and role of this adatom in the $\sqrt{13} \times \sqrt{13}\,R14°$ phase.

Chapter 4

Analysis of STM Experiments on the Charge Density Wave Phase in Quasi-one-dimensional $Rb_{0.3}MoO_3$

This chapter is devoted to analyze recent experimental scanning tunneling microscopy (STM) images of the rubidium blue bronze, $Rb_{0.3}MoO_3$, in the charge density wave phase (CDW) by means of first-principles calculations.

4.1 Introduction and Motivation

The ternary compounds with stoichiometry formula A_xTO_n, in which T is a transition metal, belong to the general group of *bronzes*. In the specific case in which A is an alkali metal and the transition metal T is molybdenum, there is whole series of interesting low-dimensional materials. Among the most interesting ones, we will consider here the so called blue bronzes, with general formula $A_{0.3}MoO_3$ (A = K, Rb, Tl) [86]. This group has structures which result in unique physical properties such as highly anisotropic electronic transport properties. The discovery of non lineal transport due to sliding of charge density waves (CDW) launched an enormous interest on the physics of these materials. Here we are specially interested on this CDW state, which induces a metal-to-semiconductor transition at 180°K.

The layered structural character of these materials has prompted many efforts to try to observe this CDW state on their cleaved surfaces through microscopy techniques. The characterization of the CDW state in the bulk [87] revealed that the main structural distortions are along the plane of each layer. Therefore, in principle this state could be imaged by scanning tunneling microscopy (STM) of the surface. In spite of this and after many attempts, observation of this surface CDW in these materials has been elusive. Several interpretations were advanced to explain

why this state was not seen in STM experiments. However, very recently in the *Laboratoire of Photonique et Nanostructures-CNRS*, successful high resolution STM images of an *in situ* cleaved $(\bar{2}01)$ surface of the rubidium blue bronze, $Rb_{0.3}MoO_3$, have been obtained at low temperature and in ultra-high vacuum (UHV) by Brun *et al.* [88]. In these images it has been possible to observe simultaneously both the surface unit cell and the CDW superlattice at temperatures well below the metal-to-semiconductor transition temperature.

Comparison of these images with previous first-principles Density Functional Theory (DFT) calculations for the bulk [89], as well as with experimental information of the bulk structure of the modulated phase [87], is quite puzzling. The first problem concerns the behavior of the order parameter at the sample surface, i.e., what is the effect of the loss of crystal periodicity at the surface on the CDW wave vector. Due to the weak coupling between the layers of the blue bronze and the fact that the main effects of the CDW state are localized in each layer, it is to be expected that the surface CDW wave vector will have the same magnitude as in the bulk. This is essentially what Brun *et al.* [88] observe in their experiments. However, they also realized that the CDW modulation can present deviations around the bulk value depending on the plateaux probed. A detailed description of this experimental observation will be given in Section 4.5.2. Another experimental matter which compels an analysis has been the interpretation of the features observed in these STM images. In particular, the most intense features of the images showing a modulation associated to the CDW state have been associated, without any doubt, with the Mo_IO_6 octahedra (Fig. 4.1 and 4.2). However, these octahedra are only weakly involved in the CDW distortions according to previous superlattice structural studies in the bulk [87]. Furthermore, the Mo_I orbitals have a minor contribution to the states near the Fermi level according to the first-principles calculations [89], and these states are those that are mainly probed in STM experiments. The understanding of these observations has been the motivation of the study presented here.

Our way to proceed was to calculate and compare the electronic structure for the $Rb_{0.3}MoO_3$ crystal and the surface system, focusing the surface calculations on the role of the alkali atoms at the surface. We have found that this is a key issue in the resulting surface CDW state in low-dimensional blue bronzes, because the surface cation concentration can affect the surface nesting vector and, hence, the nature of the modulation observed by STM. In addition, we have simulated the STM images of the $Rb_{0.3}MoO_3$ CDW state in order to understand the features observed in the experimental ones.

Before describing and discussing the work carried out for this compound, it is necessary to give a brief summary of its crystal structure. This will be useful to have a whole understanding of the problem.

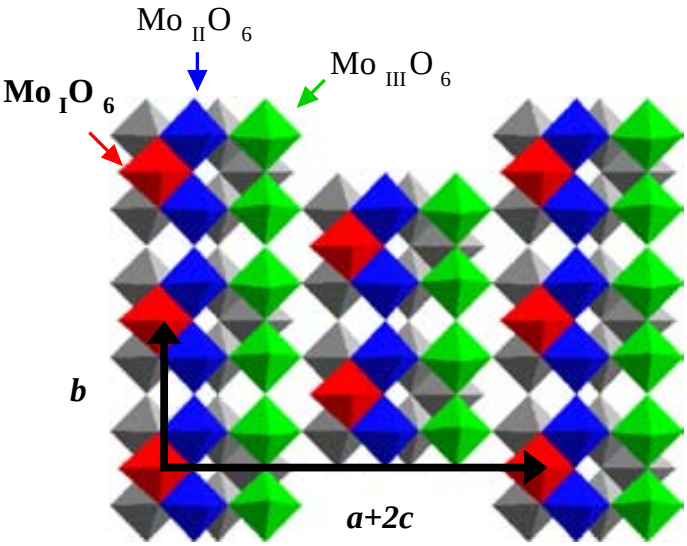

Figure 4.1: An idealized surface structure of $Rb_{0.3}MoO_3$ in the $(\bar{2}01)$ plane. The red, blue and green units are in the first MoO_6 sublayer.

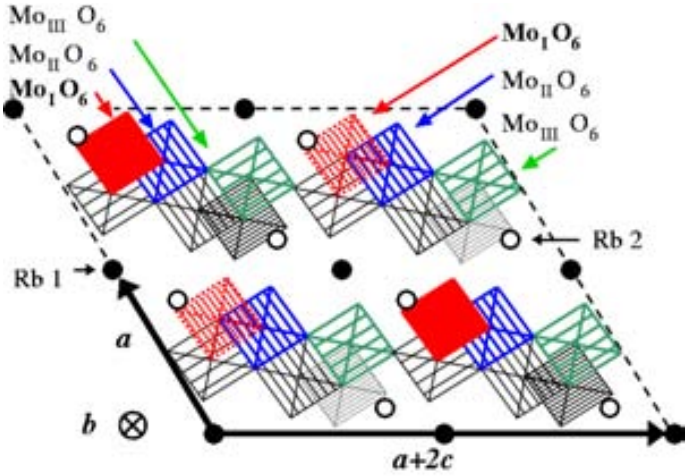

Figure 4.2: Idealized sideview of the room temperature $Rb_{0.3}MoO_3$ structure projected onto the plane perpendicular to the ***b*** axis. Each square represents a MoO_6 octahedron with the Mo located at the center of the oxygen octahedron. Closed circles are Rb atoms at the uppermost positions of the surface (labeled 1) and empty circles are Rb atoms 1.2 Å below (labeled 2). The three highest octahedra with respect to the "surface" are the dashed squares indicated by the arrows. Their centers lie at levels 1.8, 2.4 and 3.5 Å below the surface.

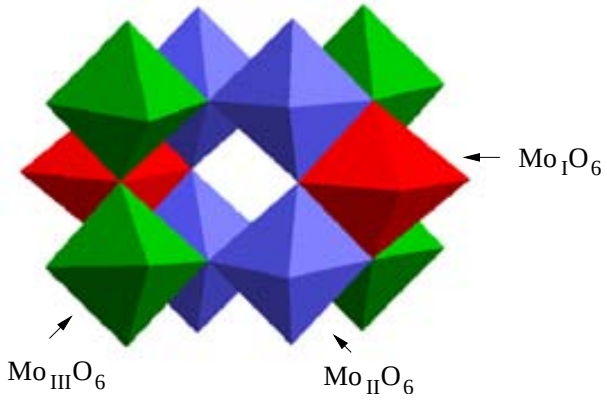

Figure 4.3: The $Mo_{10}O_{30}$ cluster

4.2 Crystal Structure

The blue bronzes $K_{0.3}MoO_3$ and $Rb_{0.3}MoO_3$ exhibit the same crystal structure and similar properties. The first determination of the crystal structure, in the non modulated phase, for these compounds was made by Graham and Wadsley [90]. They have monoclinic symmetry, belonging to the space group $C2/m$, with 20 formula units per unit cell. The lattice parameters of $Rb_{0.3}MoO_3$ for the simple monoclinic cell commonly used in the literature are those from of Graham and Wadsley, i.e., $\boldsymbol{a}$ =18.94 Å, $\boldsymbol{b}$ =7.560 Å, $\boldsymbol{c}$ =10.04 Å and $\gamma = 118.83°$. Nevertheless, for our specific case of Rubidium-based blue bronze we work with the more recently refined values obtained by Guedira *et al.* [91] from a x-ray diffraction experiment; these are $\boldsymbol{a}$ =18.6354 Å, $\boldsymbol{b}$ =7.555 Å, $\boldsymbol{c}$ =10.094 Å and $\gamma = 118.842°$.

The structure is built of infinite layers of distorted MoO_6 octahedra (Fig. 4.1 and 4.2) which are parallel to the $(\bar{2}01)$ plane. It is possible to see from Fig. 4.1, how these layers can be described in terms of a periodic rigid unit. These units are made by clustering ten distorted MoO_6 octahedra (Fig. 4.3) which share their edges or corners. There are three types of octahedra in each cluster, namely, two Mo_IO_6, four $Mo_{II}O_6$ and four $Mo_{III}O_6$ (red, blue and green respectively in Fig. 4.3). These clusters are linked together along $\boldsymbol{b}$, the [010] direction, to form chains by sharing four corners, two from $Mo_{II}O_6$ and two from $Mo_{III}O_6$ octahedra. The chains are then linked together to form the layers by sharing corners of the $Mo_{III}O_6$ octahedra along the [102] direction. Finally the layers are held together by the Rb cations between them (Fig. 4.2). Due to this structural character of the layers, the conductivity along $\boldsymbol{b}$ is larger by several orders of magnitude than along the [102] and the perpendicular directions [86]. For this reason $Rb_{0.3}MoO_3$ is considered a pseudo 1D conductor along $\boldsymbol{b}$.

An important point at this moment is to emphasize that the Mo_IO_6 octahedra are structurally very different from the $Mo_{II}O_6$ and $Mo_{III}O_6$ octahedra, i.e, they do not form continuous chains along the $\boldsymbol{b}$ direction and the octahedral distortions are considerably larger. This will be key in the analysis of the experimental STM images.

We carried out band structure calculations for $Rb_{0.3}MoO_3$ both before and after the Peierls transition. The structural information of the $Rb_{0.3}MoO_3$ in the modulated phase for the bulk was determined, by x-ray diffraction at 100°K, by Schutte and De Boer [87]. They obtained a wavevector $\boldsymbol{q} = \boldsymbol{a}^* + 0.748\boldsymbol{b}^* + \frac{1}{2}\boldsymbol{c}^*$. This particular fraction value of $\boldsymbol{b}^*$ indicates that the modulated superstructure is incommensurate with the initial lattice periodicity at this temperature (see Section 4.4). The model used by us for the modulated phase was constructed using the amplitude for each atom displacement measured by Schutte. However, we had to assume a commensurate value (0.75) for the $\boldsymbol{b}^*$ component of the modulation vector in order to be able to use the supercell approach to describe this system.

4.3 Computational Details

Due to the large number of atoms included in the simulation box, especially in the modulated case, we decided to use a single-ζ basis set including polarization orbitals for Mo atoms, as obtained with an energy shift of 0.02 Ry [13]. We verified that the electronic description of the bulk bands for this bronzes using this basis size, especially around the Fermi level, is essentially the same as when using a split-valence double-ζ basis set including polarization for all atoms. Comparison of our electronic description with the previous DFT calculations, with a DZP basis set by Mozos *et al.* [89] show that the present calculations keep the essential aspects of the electronic structure near the Fermi level. We have worked within the generalized gradient approximation to DFT and, in particular, the functional of Perdew, Burke, and Ernzerhof [8].

The atomic configuration, cutoff radii and core corrections of the pseudopotentials, generated according to the Troullier-Martins scheme [23] in the Kleinman-Bylander [25] separable form are collected in Table 4.1. The energy cutoff of the real space integration mesh was 300 Ry. The Brillouin zone (BZ) was sampled using grids of $(2 \times 21 \times 1)$ and $(2 \times 21 \times 6)$ k points for the slabs and the bulk, respectively [41]. The energy cutoff and k points values were tested against well converged values.

		valence structure				core correction
O	*Occ*	$2s^2$	$2p^4$	$3d^0$	$4f^0$	
	r	1.15	1.15	1.15	1.15	-
Rb	*Occ*	$4p^6$	$5s^1$	$4d^0$	$4f^0$	
	r	4.5	1.8	2.5	3.0	-
Mo	*Occ*	$4d^5$	$5s^1$	$5p^0$	$4f^0$	
	r	2.1	2.5	3.1	2.2	0.9

Table 4.1: Specific details for the generation of the pseudopotentials. *Occ*=Occupation, r=cutoff radii (Bohr).

4.4 Bulk Band Structure

The centered crystal structure of this material allows the use of a repeat unit half in size with respect to the monoclinic cell. This fact facilitates the band calculations as well as their interpretation. The cell vectors defining the new unit cell in terms of the original ones are $\boldsymbol{a'} = \frac{1}{2}(-\boldsymbol{a}+\boldsymbol{b}+\boldsymbol{c})$, $\boldsymbol{b'} = \boldsymbol{b}$ and $\boldsymbol{c'} = \boldsymbol{c}$. We show in Fig. 4.4(a) the band structure around the Fermi level for the bulk $Rb_{0.3}MoO_3$ calculated in the nonmodulated state, i.e., above the Peierls transition. Its general characteristics are in a good agreement with previous DFT calculations done for the $K_{0.3}MoO_3$ (see [89, 92]). We can see two partially filled quasi-one-dimensional bands crossing the Fermi level. These bands are non-degenerate. The lower band is cut by the Fermi level at $\sim 91\%$ of $\pi/\boldsymbol{b}$ and the upper band is cut at $\sim 59\%$ of $\pi/\boldsymbol{b}$, whereas the values given by the most recent photoemission studies [93] are 90% and 59% respectively (values measured for $K_{0.3}MoO_3$).

The nature of the bands crossing the Fermi level is governed mainly by the Mo $4d$ orbitals from the Mo_{II} and Mo_{III} type atoms, which mix in a small amount O p orbitals [94, 89]. This bands are partially filled by the valence electrons transferred from the cation atoms (K, Rb). In this way the cations act essentially like electron donors to the MoO_3 layers, and, in fact, their orbitals do not contribute to the occupied states of the system. This explains why the band structure of the potassium and the rubidium blue bronzes are so similar.

As shown in Fig 4.4(a) the dispersion of the bands along the interlayer direction ($\Gamma - Z'$) is very small. This circumstance allows us to plot the Fermi surface of the blue bronzes only in the ($\boldsymbol{a'^*}$, $\boldsymbol{b'^*}$) plane of the Brillouin zone (see Fig. 4.4(b) adapted from [89]). The two bands cut by the Fermi level lead to pairs of slightly warped lines, as expected for a quasi 1D system. Since the warping is small, we can consider than only a single nesting vector will lead to the destruction of the complete Fermi surface. In other words, we show in Fig. 4.4(b) how the upper and lower Fermi lines from the first band nearly match the lower and upper Fermi lines of the second band via a translation by exactly the same vector $\boldsymbol{q}$. Therefore the

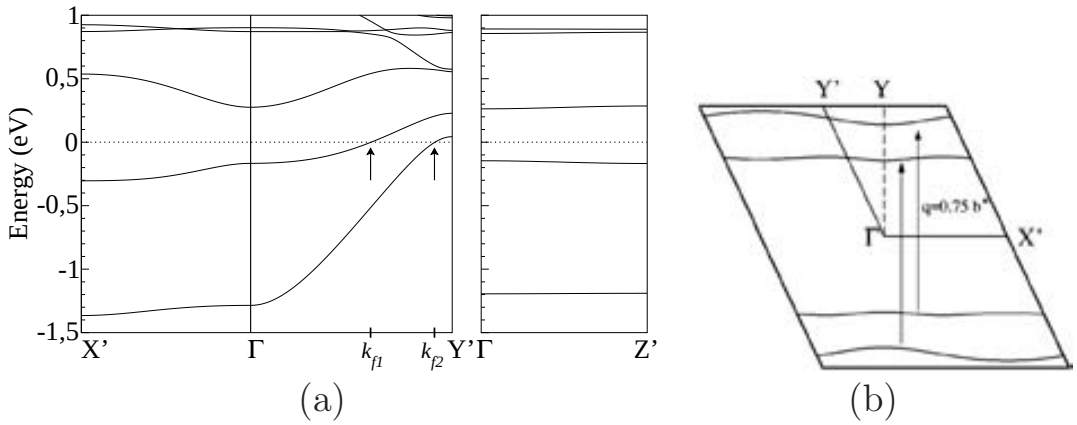

Figure 4.4: (a) Bulk bands for $K_{0.3}MoO_3$ showing the Fermi wave vector of each band. (b) The (a'^*, b'^*) plane of the Fermi surface. $\Gamma = (0,0,0)$, $X' = (\frac{a'^*}{2}, 0, 0)$, $Y'=(0, \frac{b'^*}{2}, 0)$, $Z'=(0, 0, \frac{c'^*}{2})$ and $Y = (0, \frac{b^*}{2}, 0)$, from [89].

charge density wave vector, $\boldsymbol{q_{CDW}}$, is given by the simplest expression $\boldsymbol{k_{f1} + k_{f2}}$ where $\boldsymbol{k_{fi}}$ is the Fermi wave vector of band $\boldsymbol{i}$ [95, 94, 96].

Because of the one dimensional character of the Fermi surface, the value of this $\boldsymbol{q_{CDW}}$ vector is theoretically defined by the degree of filling of the bands crossing the Fermi level. If there is a complete charge transfer from the cations to the MoO_3 layers, there will be three conduction electrons per formulae unit filling these two bands. This then represents a filling of three-quarters of the bands crossing the Fermi level. Consequently, an interband nesting mechanism must be associated with the $0.75\boldsymbol{b^*}$ value. This value of $\boldsymbol{q_{CDW}}=\boldsymbol{k_{f1}}+\boldsymbol{k_{f2}}=0.75$ along $\boldsymbol{b^*}$ indeed was observed at low temperature [97], but is slightly different from the one found at the transition temperature. Although it is not the goal of this study, it is interesting to mention this point. Various experimental results have indicated the temperature dependence of the nesting vector. Its value at the transition temperature of 180°K is $0.72\boldsymbol{b^*}$, i.e., an incommensurate[1] value with the crystal lattice. With the decrease of the temperature it approaches the commensurate value $0.75\boldsymbol{b^*}$ around the 100°K. This behavior has deserved much attention and is still an open topic. The interest on this subject is emphasized by the fact that the first empty band lies at an energy value, with respect to the last partially filled band, which it does not allow to consider a occupation of it via thermal activation. Therefore it is difficult to explain a mechanism which changes the degree of filling of the bands crossing the Fermi

[1]A distortion is commensurate with the lattice when the ratio between the new unit cell and the old one is a rational number. In the incommensurate case, no unit cell can contain the exact period of both the distortion and the underlying crystal

level and thus the nesting vector.

As it was mentioned before, the bulk $\boldsymbol{q_{CDW}}$ vector has also components in other directions than $\boldsymbol{b^*}$. Experimentally, Brun *et al.* [88] found that the projection of $\boldsymbol{q_{CDW}}$ perpendicular to the $\boldsymbol{b^*}$ axis is close to $(\boldsymbol{a}^* + 2\boldsymbol{c}^*)$. The occurence of this component is due to the electrostatic interaction between CDWs in adjacent rows, and does not have a direct relationship with any feature of the Fermi surface. Moreover, Brun *et al.* observed that, on the surface, this value is constant without any dependence on the plateaux probed. Hence, this component of the CDW vector will not be taken into account from now on in our discussion.

4.5 Surface Structure

4.5.1 Electronic Properties

Before trying to gain insight about the experimental STM images of the blue bronze we had first to understand the role of the cations on the electronic properties after sample cleavage.

As mentioned, the layers can be described, independently of the cell vectors chosen, in term of clusters of ten chemical units. This results in three rubidium atoms per repeat unit of a layer. We can classify them by their position with respect to the octahedral layer. Two of them, named type-2, (empty circles in Fig. 4.2), are very near the surface of the layers. The third one, named type-1 (full circles in Fig. 4.2) is equidistant to both layers.

We must point out that the position of the cations will play a key role in understanding the STM image of Blue Bronze. After cleaving the sample, along the $(\bar{2}01)$ plane, we expect that only the type-2 Rb atoms closest to the surface and the type-1 Rb atoms may remain at the surface. However, due to their position exactly in between the layers, type-1 Rb atoms have in average only 0.5 probability to remain at the surface after cleavage. This implies that a reliable study of this surface must include different distributions and concentrations of surface rubidium atoms.

For this specific part of our study the geometric model of the surface was based on the structure of $Rb_{0.3}MoO_3$ before the transition. We have employed periodic slab models with different number of octahedral (and rubidium) layers parallel to the $(\bar{2}01)$ plane. In this way our simulations are in a supercell geometry, i.e, the slabs are periodic in the $(\bar{2}01)$ plane and the vacuum between slabs is large enough to avoid direct interactions between periodic images. Clearly, this approach implies taking into account the presence of two surfaces (one on each side of the slab). On the other hand, to be able to compare the bulk states and surface states, we made calculations using slabs with different thickness. Since the surface rubidium atoms

are expected to relax from their bulk crystallographic position after the cleavage, we carried out full optimizations of their position with the rest of atoms fixed. These positions were the basis for all remaining calculations.

The first conclusion from our calculations was that the number of octahedral layers used in the computations is irrelevant, in the sense that the bands from both surface layers are unaffected by the thickness of the slab considered. Nevertheless, since we need to correctly place the bulk states with respect to the states from the surface layers for different cation distributions, in the following analysis we used a slab model with three layer of thickness.

Shown in Fig. 4.5(b) is the band structure for a surface which preserves the stoichiometry of the bulk. Specifically, we are concerned about preserving the number of rubidium atoms per repeat unit of a layer, i.e., three. To fulfill this restriction, it would be necessary to locate 1.5 Rb atoms on each surface per repeat unit. From these 1.5 Rb atoms one must be a type-2 Rb atom, and the remaining half will be of type-1 Rb atom. Therefore, in the stochiometric composition, one of each two type-1 Rb atoms should be missing. We have represented this situation using the simplest possible configuration, in which we assume that the positions of the type-1 Rb atoms are alternatively occupied and empty, producing a structure with a translation vector along $\boldsymbol{b}$ twice the one of the original unit cell. The supercell has, therefore, three Rb atoms on each surface of the slab: two of type-2 and one of type-1. As a consequence, the BZ of the supercell is folded with respect to the original one. This is clearly seen comparing the band structure of the bulk, Fig. 4.5(a), and the slab, 4.5(b). The partially filled bands, despite the folding, are nearly identical. The physical meaning of this is that a $(\bar{2}01)$ surface of $Rb_{0.3}MoO_3$ with this cation concentration will suffer a structural distortion with the same periodicity as the bulk.

We have a very different panorama when the repeat unit of the cell at the surface is covered by just one Rb atom. This means a charge 0.5 smaller than in the stoichiometric case. The band structure (Fig. 4.5(c)) looks different around the Fermi level respect to those in the bulk. This change of the superficial cation distribution raises the quasi degeneracy and the corresponding bands for the most superficial layers are shifted upward with respect to those of the bulk. The opposite situation, i.e., an excess of Rb atoms with respect to the stoichiometric situation led to a band shift in the opposite direction.

After carrying out computations for several surface Rb concentration, we conclude that different concentrations of Rb atoms at the surface generate a nearly rigid energy shift of the surface bands with respect to those of the bulk. Therefore, at the surface, we have new values for the Fermi wave vectors $\boldsymbol{k_f}$ of these bands. This result has the important implication that the nesting vector at the surface, and hence the periodicity of the modulation after the transition, must change with the Rb content at the surface.

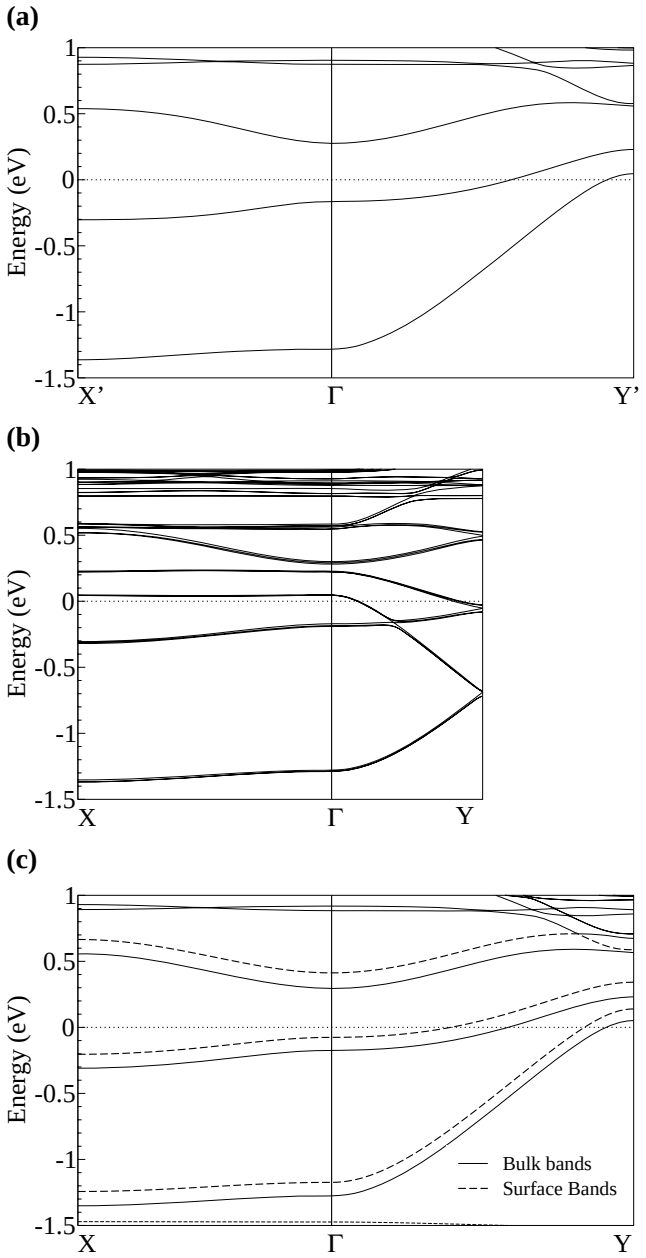

Figure 4.5: The band structure for (a) bulk $Rb_{0.3}MoO_3$; (b) a slab preserving the bulk stoichiometry at the surface, and (c) a slab with a defect of Rb atoms (one every three) at the surface. In (a) $\Gamma = (0, 0, 0)$, $X' = (\frac{1}{2}, 0, 0)$ and $Y' = (0, \frac{1}{2}, 0)$ in units of the $\boldsymbol{a'^*}$, $\boldsymbol{b'^*}$ and $\boldsymbol{c'^*}$ reciprocal lattice vectors [89]. In (b) and (c) $\Gamma = (0, 0)$, $X = (\frac{1}{2}, 0)$, and $Y = (0, \frac{1}{2})$ in units of the corresponding oblique reciprocal lattice vectors.

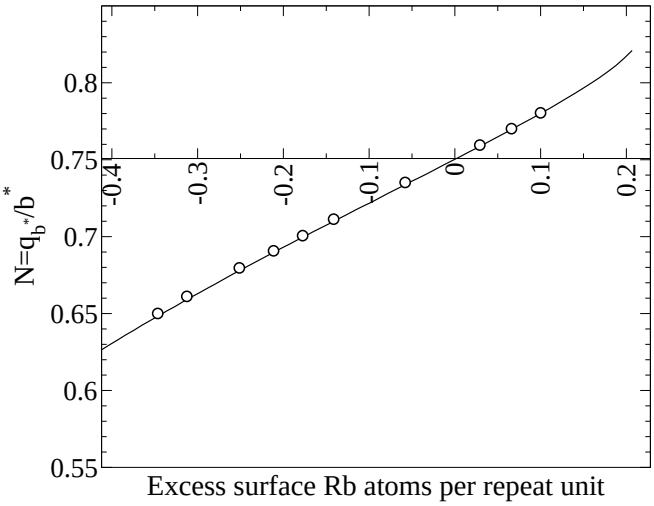

Figure 4.6: The $\boldsymbol{b^*}$ component of the surface nesting vector of the $(\bar{2}01)$ surface of rubidium blue bronze versus the density of alkali atoms at the surface. The horizontal axis indicates the number of excess Rb atoms at the surface per unit cell, with the zero corresponding to the stoichiometric Rb composition. The continuous line corresponds to the calculated values. The empty circles refer to the experimental values of $\boldsymbol{q^*}$ probed by STM (See text).

In the next section we will show experimental evidence which confirms the existence of inhomogeneities of $\boldsymbol{b^*}$ surface component of the wave vector of the modulation probed by STM. Our results therefore suggest that this variation can be interpreted in terms of the variation in the surface concentration of Rb atoms.

4.5.2 Experimental Evidence

This experimental work was carried out by C. Brun, J. C. Girard and Z. Z. Wang at the *Laboratoire de Photonique et de Nanotructures, CNRS, Marcoussis, France.* A detailed description of the experimental setup can be found in the Ref. [88, 98].

For clarity of this Section we introduce the quantity N, defined as the ratio $N = q_{b^*}/b^*$, where q_{b^*}, is the component of $\boldsymbol{q_{CDW}}$ in the direction of $\boldsymbol{b^*}$. Thus $N = 0.75$ corresponds to the commensurate value of the bulk reported at low temperature. In a STM experiment the periodicity of the new superlattice is directly extracted from the analysis of the two-dimensional (2D) Fourier transform of each image, and this is given in terms of the $1 - N$ value.

In their first paper on this material Brun *et al.* [88] claim to have measured by careful STM experiments the nearly commensurate value of the projection of the $\boldsymbol{q_{CDW}}$ onto the $(\bar{2}01)$ plane. However, it was mentioned that, on some optically flat

terraces, $1-N$ was found to deviate from the commensurate 0.25 value, yielding inhomogeneities for $\boldsymbol{q_{b^*}}$. We report here their experimental results concerning these inhomogeneities of $\boldsymbol{q_{b^*}}$ measured by STM in the rubidium blue bronze.

Their measurements consisted of constant current mode topographical images and were performed at 77°K or at 63°K, well below the transition temperature (T_c=180°K). The typical experimental conditions were ±450 mV for the applied bias voltage and from 50 to 150 pA for the tunneling current. With the objective of getting accurate measurements of $1-N$ they scanned areas ranging from $20\times20\text{nm}^2$ to $50\times50\text{nm}^2$. Their images, with typical sizes of 512×512 pixels, achieve molecular resolution and CDW resolution. The main features of the STM images described hereafter as well as the extracted CDW wave vector are found to be independent of bias voltage polarity in the above mentioned energy range.

It is found that optically distinct plateaux (of at least several 100 μm^2 area) could yield distinct values of $1-N$ significantly different from the 0.25 bulk value. Moreover, on the same plateau, different locations estimated to be at least several μm from each other yielded differences in $1-N$ values that were much greater than the typical error bar for a single location $1-N$ measurement, leading to clear deviations of the surface $\boldsymbol{q_{CDW}}$ wave vector with respect to the bulk one projected onto the $(\bar{2}01)$ surface. On the contrary, displacements along $\boldsymbol{b}$ or $\boldsymbol{a}+\boldsymbol{2c}$ on the scale of tens of nanometers from a given position of measurement, did not lead to noticeable changes of $\boldsymbol{q_{b^*}}$. This shows that all measurements were performed far enough from CDW domain boundaries. On the same plateau the greatest change in $1-N$ value ranged from 0.21 to 0.32. Figure 4.7 illustrates this situation for STM measurements performed on two different samples with similar imaging conditions: in (a) $N=0.75$, the bulk value and in (c) $N=0.70$.

As a result of this study all $1-N$ values were found in the range 0.21 to 0.35, as indicated by the empty circles in Fig. 4.6 for the N value.

4.5.3 Discussion

According to our calculations these inhomogeneities would correspond to a variation of surface alkali atoms from the stoichiometric value ranging from about 0.1 to −0.35 Rb atoms per repeat unit. These predictions would then be consistent with the hypothesis that the distribution of type-1 alkali atoms is mainly responsible for the experimental deviations observed in the CDW wave vector value at the surface. The effect on the electronic properties induced by losing surface alkali atoms has been studied by photoemission combined with Ne ions sputtering [99]. It was found that alkali desorption decreases the electronic spectral weight around the Fermi level and shifts away from the Fermi level the onset of the valence band. Our experimental and theoretical studies are consistent with these observations. On the other hand the present experimental results could seem in disagreement with angu-

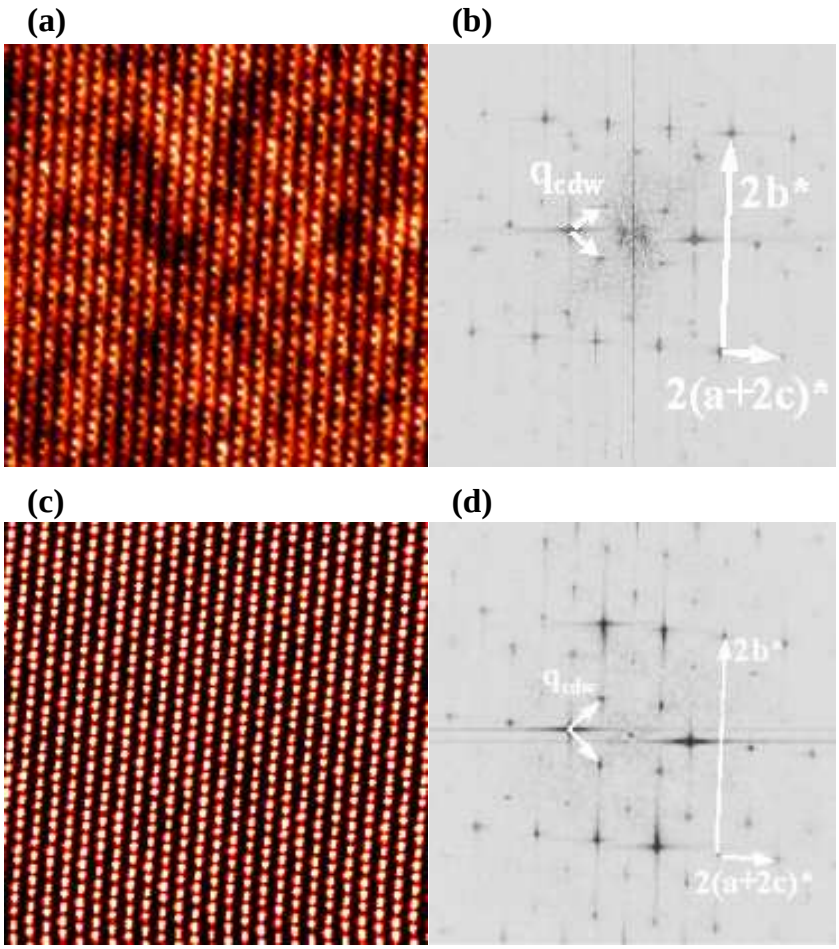

Figure 4.7: (a) The constant current STM image of about 30×30 nm^2 of an *in situ* cleaved $(\bar{2}01)$ surface of $Rb_{0.3}MoO_3$ in the CDW ground state at 63°K with molecular and CDW resolution. The tunneling conditions are Vbias= +420 mV and $I_t = 110$ pA. (b) A 2D Fourier transform of (a) showing surface lattice spots indicated by vectors $2\boldsymbol{b}^*$ and $\boldsymbol{2(a+2c)}^*$ and CDW superlattice spots around each lattice spot indicated by $\boldsymbol{q_{CDW}}$ short white arrows. In this scanned zone the $\boldsymbol{b}^*$ component of $\boldsymbol{q_{CDW}}$ equals the 0.25 bulk value. (c) The constant current STM image with similar parameters as indicated in (a) but measured on another sample. (d) A 2D Fourier transform of (c) showing the same spots as those appearing in (b) but with the $\boldsymbol{b}^*$ component of $\boldsymbol{q_{CDW}}$ equals 0.30, showing significant clear deviation from the 0.25 bulk value.

lar resolved photoemission spectroscopy (ARPES) and grazing x-ray diffraction,both showing that N almost equals 0.75 under 100°K [100, 101]. This is because STM probes $\boldsymbol{q_{CDW}}$ only at the uppermost layer of the compound and very locally at

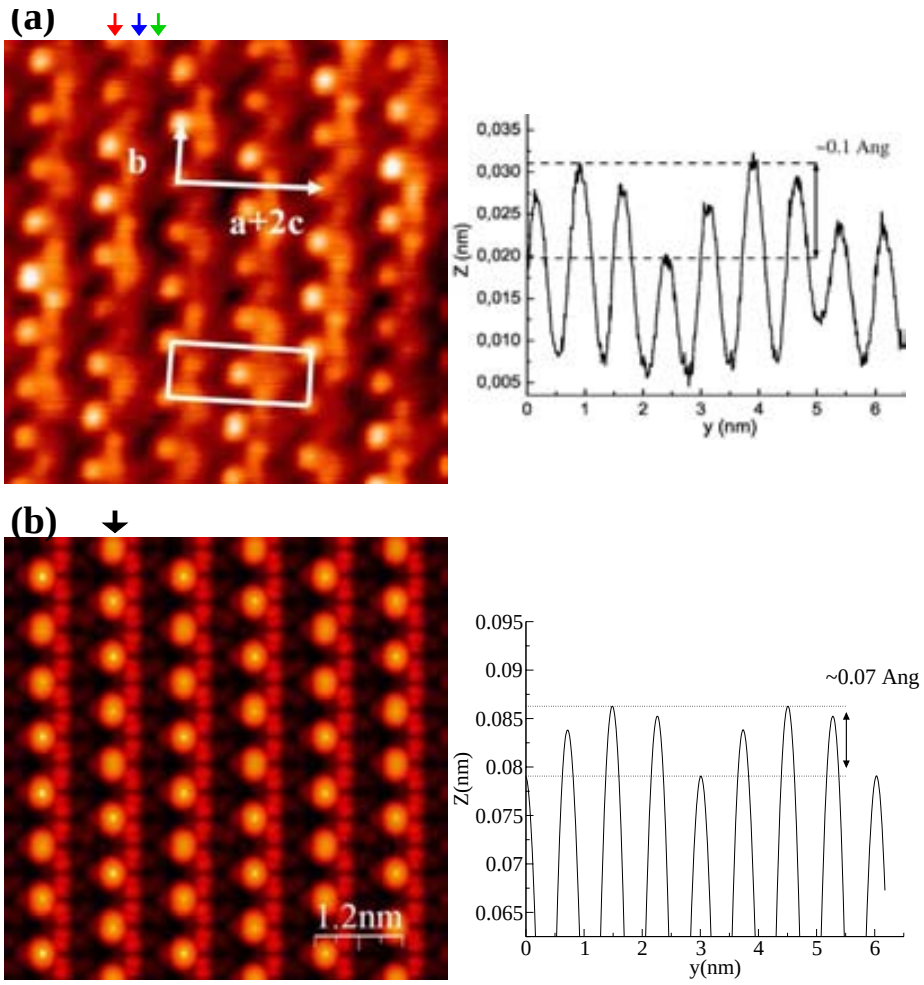

Figure 4.8: (a) The constant current mode topographical image of 6.2×6.2 nm^2 on $(\bar{2}01)$ plane of $Rb_{0.3}MoO_3$ at 63°K (raw data image). The bias voltage applied on the sample is +420 mV and the set-up tunneling current is 110 pA. Molecular lattice and CDW superlattice coexist in the image. The three arrows indicate (from left to right), respectively, the observed type I, II MoO_6 octahedra, and the expected position of the $Mo_{III}O_6$ octahedra. An associated profile along Mo_IO_6 octahedra indicated by the left arrow (from Ref. [88]). (b) The calculated image and associated profile along the Mo_IO_6 octahedra for the modulated phase of $Rb_{0.3}MoO_3$.

the nanometer scale inside a single CDW domain. Both x-ray and ARPES experiments probe $\boldsymbol{q_{CDW}}$ over a macroscopic in-plane scale and over deeper layers (for x-ray), which remain unaffected by the inhomogeneities present in the first layer, according to our present calculations. This leads to an averaged value of $\boldsymbol{q_{CDW}}$ in a macroscopic volume showing no surface inhomogeneities.

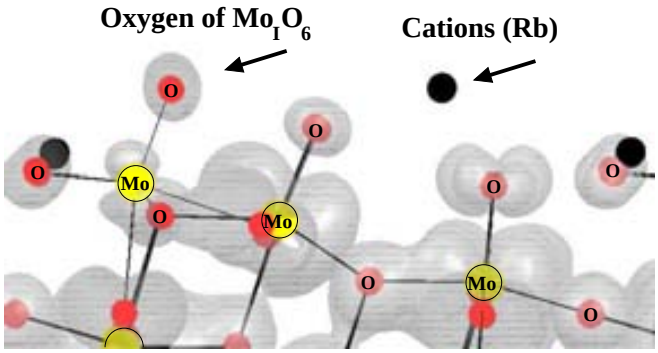

Figure 4.9: The isosurface of the charge density, represented as the gray surface, (side view as in Fig. 4.2) integrated from the Fermi level to 0.5 eV above. All the relevant atoms have been labeled. In the image the Rb, Mo, and O atoms are shown as black, yellow and red balls, respectively.

4.6 Analysis of the Simulated STM Images

We now turn to the analysis of the main features of the STM images for the modulated phase of $Rb_{0.3}MoO_3$ in stoichiometric conditions. As it was stated before, the structure after the transition used in our study is based in the x-ray resolution by Schutte and De Boer [87], with modulation vector value of $\boldsymbol{q}^*$=0.75. Our simulated images were calculated using the Tersoff-Hamann approximation [85] in which the tunneling current is proportional to the local density of states integrated from the Fermi level to the bias voltage. The bias voltages in our calculations were $\pm 0.5eV$ (as the experimental range). However, as for the experimental case, the integrated density of states in this energy range was found to be independent upon de bias voltage.

As shown in Fig. 4.8, where the chains along $\boldsymbol{b}$ are readily visible, there is a very good agreement between the experimental and calculated images. The observed STM pattern inside the surface elementary unit cell consists of one well defined ball next to a more elongated continuous pattern along $\boldsymbol{b}$, attributed to the Mo_IO_6 and $Mo_{II}O_6$ octahedra respectively.

In order to better understand these images we report in Fig. 4.9 a plot of an isosurface of the charge density integrated from the Fermi level to 0.5 eV above. Two features must be noted. First, there is essentially no contribution of the Rb atoms. This provides computational support for the suggestion that the STM measurement is not sensitive to them [102]. Second, the density is noticeable around the outer O atom of the Mo_IO_6 octahedra. These O atoms are the uppermost part of a $(\bar{2}01)$ surface, those of the $Mo_{II}O_6$ octahedra staying approximately 0.6 Å below. These two facts together easily explain why the brightest spots originate from the outer O

atom of the Mo_IO_6 octahedra, even if these participate weakly in the bands crossing the Fermi level, and in the CDW distortion. In addition, the amplitude of the bulk vertical displacement of the outer O atom of the Mo_IO_6 octahedra in the modulated structure used in the calculation is between three and four times smaller than the amplitude of the calculated density profile along the Mo_IO_6 octahedra [Fig. 4.8(b)]. This means that the STM experiment is mainly measuring the differences in the local density of states (LDOS) associated with these O atoms, as a result of the existence of the CDW and not the differences in height of these atoms. The above mentioned apparent contradiction with previous works is solved by the results of Fig. 4.9. Around 42.5% of the charge density in this figure is associated to Mo_{II}, 22.1% to Mo_{III}, 1.9% to Mo_I and 1.2% to the outer O of the Mo_IO_6. Consequently, the CDW modulation mostly affects the Mo_{II} and Mo_{III} atoms. However, because of the nonnegligible participation of the outer O atoms of the Mo_IO_6 octahedra, as a result of the strong hybridization between the Mo and O orbitals, the orbital mixing associated with the CDW modulation affects the LDOS of these atoms, leading to the differences in the profile of Fig. 4.8. According to the present results the more continuous path must originate not only from the outer O atoms of the $Mo_{II}O_6$ octahedra, but also from the Mo_{II} atoms which strongly participate in the wave function. However, the difference in height with respect to the uppermost part of the surface leads to the considerably less intense signal. Finally, the $Mo_{III}O_6$ octahedra, which lie considerably deeper (i.e., approximatly 1.7 Å lower than the Mo_IO_6 octahedra) are not visible at all in the STM image, even though the CDW modulation strongly affects them.

4.7 Concluding Remarks

In summary, a combined theoretical-experimental approach has led to an in-depth understanding of the scanning tunneling microscopy observation for the charge density wave phase in quasi-one-dimensional blue bronze. Thus, from electronic structure calculations of the bulk and surface we have shown that a CDW phase can exist at the surface because the bands crossing the Fermi level are not sensitive to the loss of crystal periodicity at the surface. However, the magnitude of the nesting vector $\boldsymbol{q_{CDW}}$ defining the modulation of the surface CDW phase is sensitive to the concentration of rubidium atoms at the surface. Only when the surface preserves the stoichiometry of the bulk, with respect to the number of rubidium atoms per repeat unit, the CDW probed by STM will have the same modulation as the bulk. Hence, the observed inhomogeneities on the surface CDW vector have been explained in terms of the surface Rb concentration.

Finally, the discrepancy between how the CDW reveals in STM and x-ray experiments has been understood. Although the modulation amplitude in the CDW phase

along the Mo_IO_6 octahedra is very small compared to the $Mo_{II}O_6$ and $Mo_{III}O_6$, the brightest spots in the STM image were associated to them. Our calculations show that the participation of the outer oxygen atom of Mo_IO_6 octahedra to the integrated density of states is considerably smaller than that associated with Mo_{II} and Mo_{III}, but nonnegligible. However, these oxygen atoms are localized in the uppermost part of the $(\bar{2}01)$ surface. This, together with fact that STM experiments measure differences in the local density states instead of the atomic distortion, explain the experimental observations.

Chapter 5

Layered III-VI Semiconductors under Pressure

This chapter deals with the simulations carried out in order to get insight into the structural and electronic properties of the group of III-VI semiconducting compounds under hydrostatic pressure.

5.1 Introduction and Motivation

The InSe, GaSe, GaS and GaTe compounds belong to the family of layered III-VI semiconductors[1]. They have shown their technological potential in different fields, e.g. nonlinear optics [106, 107], solar energy conversion [108], and solid-state batteries [109, 110]. The properties of this family have been widely investigated by pressure techniques. These experiments are a tool of great value to investigate the electronic properties and the nature of the chemical bonds in these semiconductors. At the same time, it has been observed the emergence with pressure application of some interesting properties: a large anisotropy and non-linearity of the elastic properties [111, 112], nonlinearities in the pressure dependence of the phonon frequencies [112, 113, 114, 115] and electronic transitions [112, 116, 117, 118, 119], etc.

At ambient conditions, these compounds are characterized by an anisotropic layered crystalline structure. Each layer is formed by two sublayers of hexagonal symmetry, Figs. 5.1(a) and 5.1(b), with strong covalent interactions between the atoms. In contrast, the interaction between two adjacent covalent layers is weaker and, in fact, is formally recognized as of van der Waals (vdW) type.

From the experimental point of view, there is a considerable lack of knowledge about the structural evolution of these materials under pressure. The main reason

[1]InTe and InS do not have a layered character at ambient conditions [103, 104]. However, at high pressure and high temperature InS has a layered phase [105].

is the difficulty to have pure single-crystalline samples in which x-ray diffraction techniques can be used. This is a consequence of their layered character, which introduces stacking faults or twinned planes in the sample [120]. Furthermore each grain in the sample looks like a platelet which orientates parallel to the other with the application of pressure, introducing preferential orientations in the powder. This problem prevents having a good description of the physical properties in terms of its structure.

The consequences of the different character between the intra-layer and inter-layer interactions is a highly anisotropic behavior under application of hydrostatic pressure. These two facts, the presence of two successive regions characterized by different types of interaction between the atoms, and the different evolution followed by each region under pressure, makes these compounds a challenging case for theoretical studies based on the Density Functional Theory. DFT calculations can not give us an accurate description for layered materials. Because none of the exchange-correlation functionals commonly used include explicitly the vdW interaction. In other words, DFT calculations can not reproduce the well known R^6 behavior of the vdW interaction at large distances. There have been, in the last years, efforts in order to design correlation functionals [121, 122] which include this interaction. However, it will be still necessary a strong testing process of these nonlocal functionals, as well as their numerical implementation and optimization, before they can be applied in theoretical investigations of layered materials.

Our goal is to study the evolution of the structural properties of different III-VI polytypes from an *ab-initio* point of view, and from this, to have a description of the evolution of its band structure. There are some previous studies, especially on γ-InSe [123, 124] and ε-GaSe [125]. In spite of this, we want to have a comparative view of the effect of the pressure on these polytypes, having in mind their similarities either in physical structure or in chemical composition. To reach this, we will succesively study the γ-InSe polytype, its isomorphic γ-GaSe containing a different cation, the ε-GaSe polytype which has the same chemical composition but different stacking of the layers, and finally the β-GaS polytype, with still a different polytype and a different anion with respect to the others. This study has been carried out in collaboration with the experimental group of Professor A. Segura from the *Institut de Ciència dels Materials* in the *Universitat de València*. In this work we present their experimental data for these compounds together with our calculations, in an attempt to understand the structural and electronic properties of these materials under pressure.

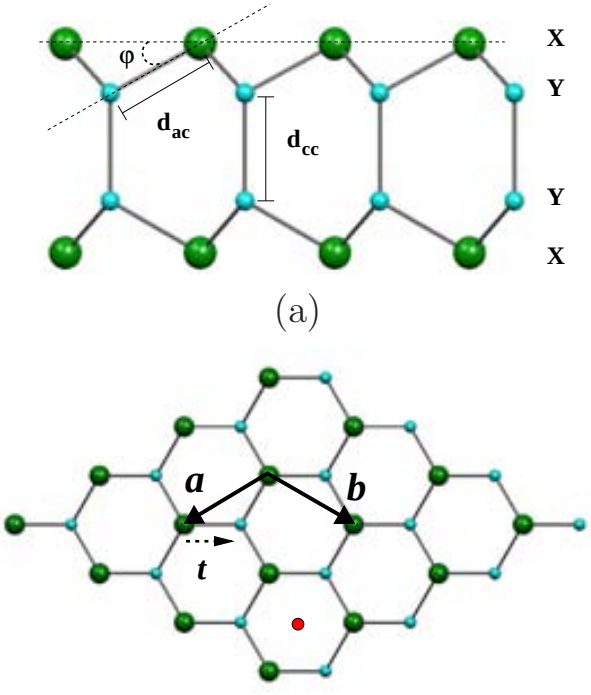

Figure 5.1: (a) Idealized sideview of the intralayer structure. (b) Idealized view of one layer in the $(\boldsymbol{a}, \boldsymbol{b})$ plane perpendicular to the stacking direction. The red point indicates the stacking π rotation axis (see text). Green balls are anion atoms (group VI), blue balls are cation atoms (group III)

5.2 Crystal Structure

We will first give a description of the structure of the III-VI semiconductors considered here. At ambient pressure, all polytypes of this family exhibit the same type of layers, with the striking exceptions of GaTe.

The intralayer stacking of these compounds follows a X-Y-Y-X scheme, X being the anion (S, Se) and Y the cation (Ga, In), Fig. 5.1(a). Each X (or Y) atomic plane makes an hexagonal network by atomic translations along $\boldsymbol{a}$ and $\boldsymbol{b}$, Fig. 5.1(b). Two adjacent networks, X and Y, are related among them by a translation vector with two components, one along the $(\boldsymbol{a}, \boldsymbol{b})$ hexagonal plane and one along the stacking direction $\boldsymbol{c}$. In Fig. 5.1(b), it is possible to see that the displacement of the Y network, in the hexagonal plane, respect to a X one, is given by the vector $\boldsymbol{t} = (\boldsymbol{b} - \boldsymbol{a})/3$. For the stacking direction $\boldsymbol{c}$, the magnitude of displacement of the Y network is $d_{ac}sin(\varphi)$, where d_{ac} is the length of the anion-cation bond, and φ is the angle made by this directional bond and the X network (see Fig. 5.1(a)). These two

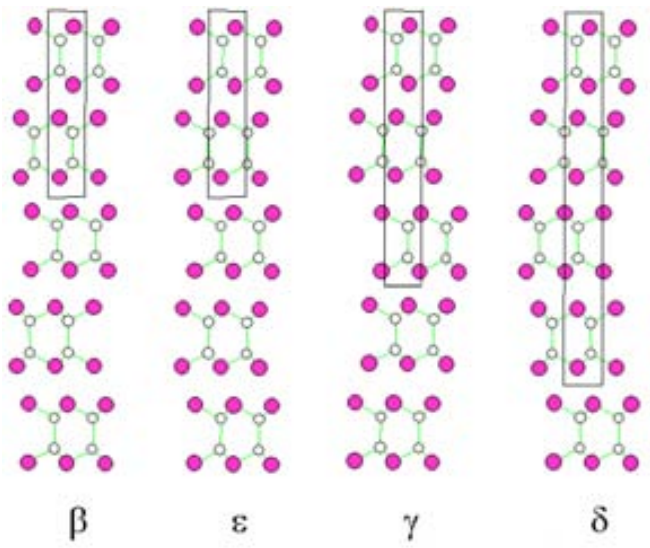

Figure 5.2: Stacking scheme of the different polytypes. Magenta balls are anion atoms and white balls are cations atoms. From [126].

adjacent networks, X and Y, make a sublayer. Finally, one layer is made by two of these sublayers related between them by a mirror operation with respect to the plane intersecting the cation-cation bond d_{cc} (the Y-Y distance). This description is valid as far as we consider an isolated layer. The mirror symmetry between the two sublayers may disappear when the stacking of successive layers giving the different polytypes is considered

The stacking sequence between successive layers defines a polytype. The existence of different polytypes is a simple consequence of the weaker bonding between these layers. The vdW interactions allow the adoption of different stacking sequences depending on the growth conditions. Four different ways of stacking successive layers have been found (see Fig. 5.2): the so called β, ε, γ, and δ polytypes. The stacking in each polytype can be characterized by the set of operations carried out on one layer to generate the correct periodicity. In addition to the translation operation along $\boldsymbol{c}$ axis, each stack sequence can be characterized on the basis of the operations carried out on each layer in the $(\boldsymbol{a}, \boldsymbol{b})$ plane. These operations are translations $\boldsymbol{t}$, $-\boldsymbol{t}$ along the $(\boldsymbol{a}, \boldsymbol{b})$ plane (as it is defined in Fig. 5.1(b)) and rotations $\boldsymbol{R}$ (by π) around an axis perpendicular to this plane and crossing it through the center of an hexagon in the plane (red point in Fig. 5.1(b)). Thus, for example, the β polytype, with the stack sequence A-B-A.., is generated by two consecutive π rotations. The sets of operations to generate these polytypes, without including the translation operation along $\boldsymbol{c}$ axis, are included in Table 5.1.

Polytipe	Stack sequence	Operations
β	A-B-A..	$\{R, R\}$
ε	A-B-A..	$\{\boldsymbol{t}, -\boldsymbol{t}\}$
γ	A-B-C-A..	$\{\boldsymbol{t}, \boldsymbol{t}, \boldsymbol{t}\}$
δ	A-B-C-D-A..	$\{\boldsymbol{t}, R, -\boldsymbol{t}, R\}$

Table 5.1: Operations defining the different polytypes. The obvious translation operation parallel to the axis of rotation is not included.

5.3 Computational Details

All calculations were carried out using a split-valence double-ζ plus polarization basis set (DZP). We have treated these compounds within the local density approximation to the exchange-correlation potencial, as parametrised by Perdew and Zunger [6]. The atomic configuration, cutoff radii and core corrections of the pseudopotentials for each species, generated according to the Troullier-Martins scheme [23], in the Kleinman-Bylander [25] separable form, are collected in Table 5.2.

Because of the different nature of these polytypes, we give now some specific details of the calculations carried out for each of them:

- γ-InSe
  Our simulations have been done using the rhombohedral representation of the primitive cell because in this way the number of atoms in the repeat unit reduces to two Se and two In. The range of the numerical (pseudo-) atomic orbitals for the split-valence double-ζ plus polarization basis set, were obtained by application of the variational optimization method proposed by Anglada *et al.* [18] at the fictitious pressure of 0.1 GPa. The sampling of the Brillouin zone was carried out with a regular grid of $7 \times 7 \times 7$ k points [41]. The energy cutoff which determines the real space integration mesh was 500 Ry.

- γ-GaSe
  Since the staking pattern is the same as in γ-InSe, we have worked with the same primitive cell of four atoms. The ranges of the basis orbitals were obtained with an energy shift of 0.02 Ry. The k grid used was $8 \times 8 \times 8$ and the energy cutoff was 650 Ry.

- ε-GaSe
  In the hexagonal primitive cell of this polytype four unit chemical formulae must be considered. The energy shift and energy cutoff were the same as for γ-GaSe. The k grid was $8 \times 8 \times 8$.

- β-GaS
  As for ε-GaSe its primitive cell is hexagonal, with four unit chemical formulae.

		valence structure				core correction
S	*Occ*	$3s^1$	$3p^{3.75}$	$3d^{0.25}$	$4f^0$	
	r	1.45	1.45	1.45	1.45	-
Ga	*Occ*	$3d^{10}$	$4s^2$	$4p^1$	$4f^0$	
	r	1.1	2.07	2.29	2.0	0.5
Se	*Occ*	$4s^2$	$4p^4$	$4d^0$	$4f^0$	
	r	1.4	1.6	2.0	2.0	1.235
In	*Occ*	$4f^0$	$5s^2$	$5p^1$	$5d^0$	
	r	3.0	2.5	2.75	3.0	1.9

Table 5.2: Details of the pseudopotentials generation. *Occ*=Occupation, *r*=cutoff radii (Bohr).

We used an energy shift of 0.01 Ry, an $11 \times 11 \times 4$ k-grid sampling and an energy cutoff of 1200 Ry.

We checked that the total energy is well converged with respect to both the k-grid and energy cutoff values for each polytype. We have also checked the possible influence on the calculated energies of the use of the same k-grid for all pressures. We found that our calculations are indeed also well converged in that respect for all polytypes.

We have used the usual conjugate gradients algorithm, implemented in the SIESTA code to optimize the coordinates of the atoms in the unit cell by the force relaxation. The coordinates were relaxed to forces smaller than 0.03 eV/Å. In the same manner, SIESTA gives the possibility to optimize the cell vectors to a desired hydrostatic pressure by the stress relaxation. This gives us some degrees of freedom in our simulations. Firstly, it is possible to optimize only the internal coordinates of the atoms at a given cell volume, which can be, for example, the experimental one. Second, we can keep the internal relationship between coordinates of the atoms, by an appropriate scalar definition of them, and the cell vectors are optimized to a target pressure. Finally, it is possible to carry out a full optimization, i.e., the forces on the atoms will be minimized while the cell vectors are changing.

In spite of the knowledge of some experimentally determined lattice vectors with pressure, we decided to make full optimizations for each compound to a desired target pressure, having as the starting point the well known ambient pressure crystal structure. Working in this way, we can obtain a general description of the effects of pressure on the structures for which there is not enough experimental information, as for instance, γ-GaSe. Additionally, we can explore a wider range of pressures.

Finally, let us point out the question of the band gap. It is well known that the Local Density Approximation LDA to the exchange and correlation functional underestimates the band gaps in semiconductors. This problem can not be overcome

by the use of the Generalized Gradient Approximation. However, it is usual to correct this by the application of the so called 'Scissors operator', i.e., a rigid shift of all the conduction band to the right experimental value. We did not use this technique in our study. To begin with, the experimental value is not always available. In addition we are not interested here in the quantitative determination of these band gap energies but rather on a qualitative description of the changes in the valence and conduction bands with pressure.

5.4 Results and Discussion

In this section we report the results of our study of the pressure evolution of the crystal and electronic structures for γ-InSe, γ-GaSe, ε-GaSe and β-GaS. The main conclusions of our study will be summarized in Section 5.5.

5.4.1 γ-InSe

At ambient conditions, γ-InSe belongs to the spatial group $R3m$ (C_{3v}^5). This group allows two alternative descriptions. In the first one the primitive unit cell extends over one layer and is rhombohedral; in the second the unit cell is hexagonal extending over three layers and the volume is three times larger. The latter cell is depicted in the Fig. 5.2. The crystal parameters in the hexagonal representation at ambient pressure are $\boldsymbol{a} = 4.002$ Å and $\boldsymbol{c} = 24.946$ Å[127].

The effect of pressure on the structural an electronic properties of γ-InSe has been studied with *ab-initio* methods by different authors. Manjon *et al.* [128] performed the analysis of the band structure taking the experimental lattice parameters and atomic positions inside the cell from a model based on experimental data. Afterwards, Olguin *et al.* [124] carried out a plane wave study including spin-orbit coupling to get the optimized internal atom positions but in the experimental volume [129]. The first full internal structure and pressure relaxation study was done by Ferlat *et al.* [123] using three different methods. Among these, two of them used the pseudopotential approximation and either the linear combination of atomic orbitals method used in SIESTA [13] or a plane wave expansion for the basis set, and the third is a full potential linearized augmented plane wave (FLAPW) method. They reported the evolution of the distance between the Se and In atoms, the cell parameters, as well the variations in the band structure for pressures ranging from 0 to 8 GPa.

In spite of the very complete study by Ferlat *et al.* [123], and, although we applied a similar methodology, in this section we are going to report our own results on γ-InSe because our main interest is in developing a consistent set of data for the different members of this family.

Structural Evolution under Pressure for γ-InSe

The experimental evolution of the $\boldsymbol{a}$ and $\boldsymbol{c}$ lattice parameters of the hexagonal cell under pressure were measured by x-ray diffraction [129] and by Angle Dispersive X-ray Diffraction (ADXRD) [130, 131]. As we mentioned before, it is difficult to have a direct determination of the whole internal structure. Nevertheless, a direct determination of the change of the In-Se bond length d_{InSe} is possible. These values, obtained by Extended X-ray Absorption Fine Structure experiments (EXAFS) [132], are depicted in Fig. 5.3(a).

The knowledge of the evolution of the cell parameters and the d_{InSe} distances, allows the suggestion of a plausible model for all the internal unknown distances. This was done by Pellicer *et al.* [132]. In order to accomplish this, Pellicer *et al.* had to make two physical assumptions:

- The trigonal symmetry of the Se atoms in the layer plane and the perpendicularity of the In-In bonds with respect to the Se planes are maintained with pressure. Therefore, the angle φ (see Fig. 5.1(a)) may be found from the relation between the known values $\boldsymbol{a}$ and d_{InSe},

$$\boldsymbol{a}/2 = d_{InSe} cos(\varphi) cos30^{\circ} \tag{5.1}$$

- The d_{InSe} and d_{InIn} bond lengths have the same relative behavior under pressure.

The resulting d_{InIn} and d_{InSe}, interlayer and intralayer distances calculated with this model are depicted as continuous lines in the Fig. 5.3(b). Something which must be emphasized in this model is the slight increase of the intralayer distance, i.e., the width of the layer, with pressure as well as the strong decrease of the interlayer distance. These were found to be in contradiction with previously proposed models [112]. We have plotted the evolution of distances in this model up to 10 GPa, although the experimental evidence shows that around 6 GPa this polytype starts a transition towards a high pressure phase which is completed at 10 GPa, e.g., see the variation of d_{InSe} in Fig. 5.3(a). This high pressure phase was identified as a rock-salt phase by Schwarz *et al.* [129].

Let us now consider the results of our theoretical study. We report in Fig. 5.3(a) a comparison of the calculated and experimental results for the evolution with pressure of the average d_{InSe} in γ-InSe. We have also included our predictions for this distance in a rock-salt phase at pressures higher than 8 GPa. Let us note that we did not observe the expected transition of the γ-InSe to the high pressure phase in our calculations. We must take in consideration that this transition is experimentally observed at room temperature, while our calculations are done at T=0 and with a restricted number of atoms in the simulation cell. The constraints

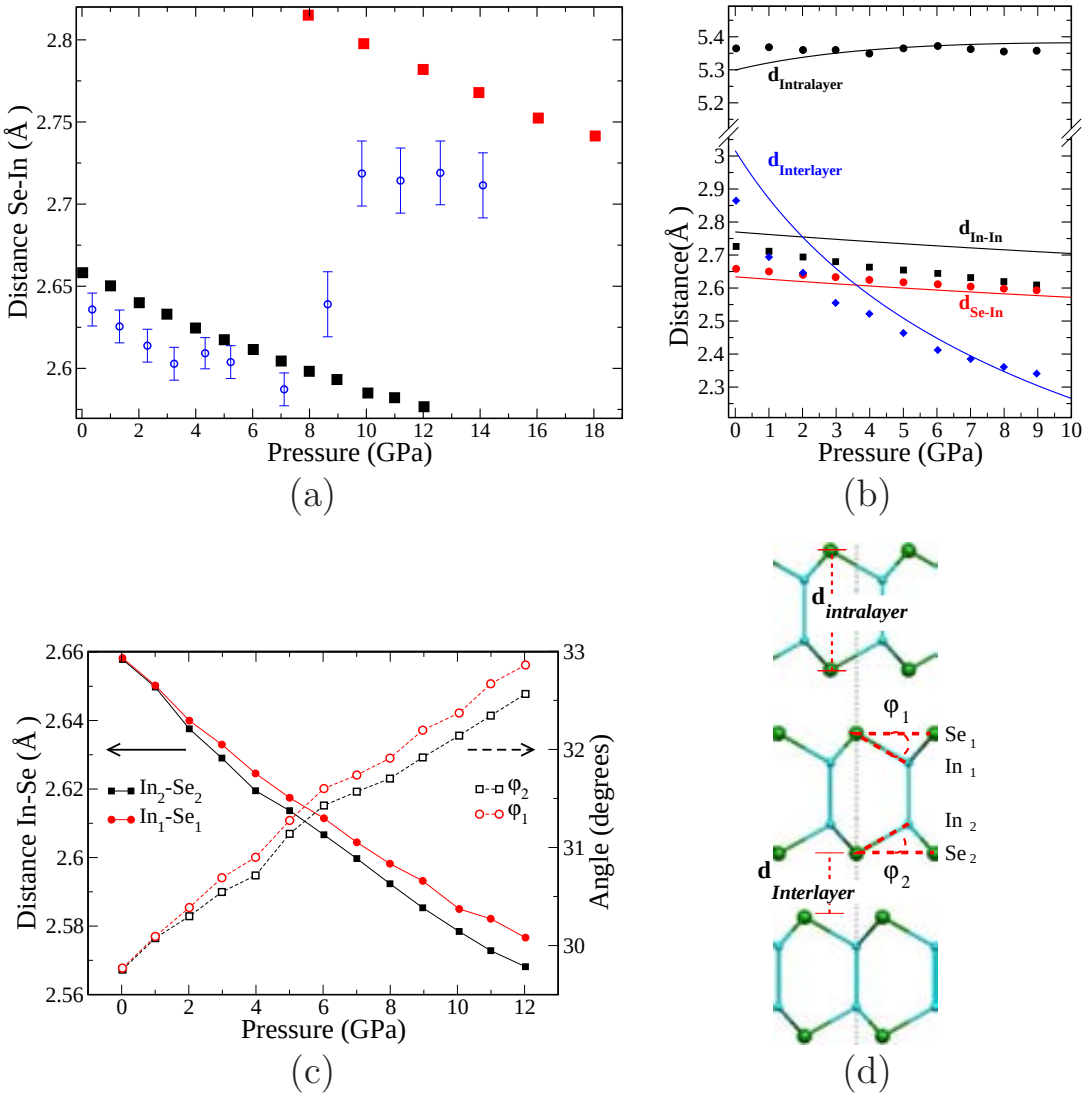

Figure 5.3: (a) Evolution of the In-Se distance with pressure in the γ-InSe polytype. Blue circles are experimental data from Ref. [132]. Squares: DFT calculations for γ-InSe (black) and rock-salt phase (red). (b) Evolution under pressure of the intralayer, interlayer, In-In, and In-Se distances. The continuous lines are the variations according to the hypothesis of Pellicer *et al.* [132] and the dots are results of the DFT calculations. (c) Calculated values for the two different In-Se intralayer distances as well as the φ_1 and the φ_2 angles defined in (d). (d) View of three successive layers showing that there is no symmetry plane through the midpoint of the In-In bonds.

in our calculation keep the system in a given state, not allowing it to transit to other more stable phases.

Something striking in Fig. 5.3(a) is the somewhat overestimated value, at low pressure, of the d_{InSe} bond in contrast with the natural behavior of LDA. This could be a consequence of the neglect of the vdW interaction in our calculations, something which is emphasized at low pressure. In spite of this, up to 8 GPa, the evolution follows a behavior similar to the experimental one. With respect to the distances for the rock-salt phase, our calculated values are quite overestimated when compared with the experimental ones; however it is important to remind the experimental difficulties to get accurate values at these pressures and for this phase. From the theoretical side, let us note that this is a three-dimensional structure and thus our results should not suffer form the incorrect treatment of the vdW forces.

If we compare our results for the layered phase with those of the model of Pellicer *et al.*, Fig. 5.3(b), we have some clear differences. First, for the interlayer distance we obtain smaller values than the model almost up to 8 GPa, although this is more accentuated in the range between 0 and 3 GPa. Where our values are higher than those of Pellicer *et al.* model. At pressures higher than 3 GPa, there is a close agreement between the calculated distances and those predicted by the model. Second, the calculated bond distances between the cations, In-In, are smaller than those predicted by the model. Quite probably the length of this internal bond has been underestimated by the LDA functional. Finally, the evolution of the calculated d_{InSe} and d_{InIn} distances do not follow, strictly speaking, the same relative behavior under pressure, as it was assumed in the model of Pellicer *et al.*. If we take the whole range between 0 and 10 GPa, the d_{InIn} decreases around 4.6%, which is slightly larger than the change in the average value for d_{InSe}, $\sim$ 2.87%. Our calculated ambient pressure value for d_{InIn} is 2.73 Å (expt. $\sim$ 2.77 Å) and for the d_{InSe} is 2.66 Å (expt. $\sim$ 2.64 Å).

Now, let us consider more in depth the structure of this γ polytype. In each layer there are two non equivalent anion positions; in Fig. 5.3(d) the atoms have been labeled as Se_1 and Se_2. This becomes more clear if we follow the atoms along the dotted line in that scheme. Every Se_2 atom is located in front of an indium atom from the lower layer, while this is not the case for the Se_1 atoms. This structural feature has some influence on the variation of the bond distance d_{InSe} and angle φ as a function of pressure. We see in the Fig. 5.3(c), how the distance between the In_1 and Se_1 and the angle φ_1 are larger for pressures greater than 0 GPa, than the distance between In_2 and Se_2 and the angle φ_2. Both differences increase with pressure, and this behavior is in fact a verification than it is not a numerical error. As a result, the difference between the two crystallographic pairs of atoms increases at hight pressures.

Another important feature is the behavior of the intralayer distance, i.e., the width of the layer, as a function of pressure. This width remains nearly constant

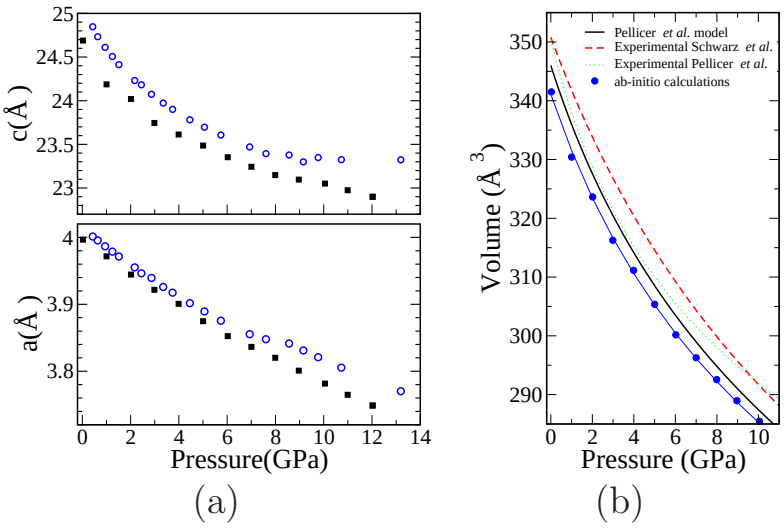

Figure 5.4: (a) γ-InSe crystal cell parameters as a function of pressure. Blue circles: Experimental data from Ref. [130, 131]. The black squares are DFT values. (b) VP equation of state. Blue circles are the results of the DFT calculations and the blue continuous line is the fit to a Murnaghan equation of state. The experimental values of Schwarz *et al.* [129], Pellicer *et al.* [130] and the values from the Pellicer *et al.* model [132] are also shown.

with pressure despite the mentioned decrease in the internal distances. This can be understood when noting the increase of both angles φ and the decrease of the cell parameter $\boldsymbol{a}$ (Fig. 5.4(a)). In this way, our results for each angle φ, the corresponding d_{InSe} and the cell parameter $\boldsymbol{a}$ fulfill the equation 5.1 which takes into account the invariant character of the trigonal symmetry with pressure.

In Fig. 5.4(a), we plot the experimental lattice parameters from ADXRD experiments [130] together with our theoretical values. The calculated values for $\boldsymbol{a}$ and $\boldsymbol{c}$ are smaller than the experimental ones, especially for $\boldsymbol{c}$, which is the stacking direction. Our calculated value for $\boldsymbol{a}$ at P=0 GPa is 3.996 Å (expt. a=4.0013 Å), with a relative change of -5.38 % from 0 to 10 GPa. The calculated value for $\boldsymbol{c}$ at P=0 GPa is 24.69 Å (expt. 24.946 Å) and the relative change in the same range is -6.63 %. From the results in Fig. 5.3(b) the larger change along the stacking direction $\boldsymbol{c}$ is due to the strong reduction of the interlayer distance, which is around -18% at P=10 GPa.

The values for the volume and its evolution with pressure are detailed in Fig. 5.4(b). We have included the corresponding fits to a Murnaghan equation for the experimental values of references [129] and [130]. We have also included the calcu-

Origin	Volumen at P=0 GPa ($Å^3$)	Bulk modulus B_o(GPa)	Pressure derivative B'_o (GPa)
Experimental Schwarz [129]	350.8	36.5±0.1	4.05±0.3
Pellicer model [132]	346.01	31.74	5.28
Experimental Pellicer [130]	350.4±0.2	24±3	8.6±0.8
ab-initio calculations (P>3 GPa)	340.01	34.65	5.26

Table 5.3: Parameters of the Murnaghan equation of state for the volume of γ-InSe.

lated volume and its fit according to the Pellicer *et al.* model [132]. The parameters associated with these fits have been included in Table 5.3. The fit for the calculated values has been carried out considering only values for pressures greater than 3 GPa, for which our results for the bulk modulus, in spite of the lower volume due to the underestimation of the In-In distance, are in good agreement with the experimental ones. Of course, if we have in mind that the transition to the rock-salt starts around 6 GPa, we do not have a very wide range of pressures to compare. However, despite the problems noted, we believe that the calculated geometries in this range allow to get a reliable picture of the electronic structure.

Band Structure Evolution for γ-InSe under Pressure

Figure 5.5 shows the evolution of the band structure around the Fermi level for γ-InSe on the basis of the fully relaxed structures. As we pointed out before, this evolution has been already studied in our group (see Manjon *et al.* [128]). In a qualitative way, the present results are very similar to the previous ones. These were obtained using experimental lattice parameters and atomic positions inside the cell from the model of Pellicer *et al.* However, there are quantitative differences in the pressure dependence of the electronic transitions, due to our use of fully relaxed structures.

At ambient pressure the Valence Band Maximum (VBM) and the Conduction Band Minimum (CBM) occur at the Z point, i.e., there is a direct gap E_{dg} at the zone boundary in a direction perpendicular to the layers. Our calculated value for it in the fully relaxed structure at P=0 GPa is around 0.42 eV, while the experimental one is 1.25 eV. [128]. In addition to the CBM at Z, there are two extra minima at points B and A, which are located somewhat higher in energy with respect to the CBM at Z. The value of the indirect gaps E_{Z-A} and E_{Z-B} are around 0.98 eV in both cases. Under pressure, both minima shift down in energy, but the A minimum remains always lower than the B minimum. The calculated pressure coefficients (for P>2 GPa) are -9.8 meV/GPa and -4.6 meV/GPa, respectively. This is a difference with respect to the previous study of Manjon *et al.* [128] where the lower indirect gap was found to be associated with the B minimum. This change in

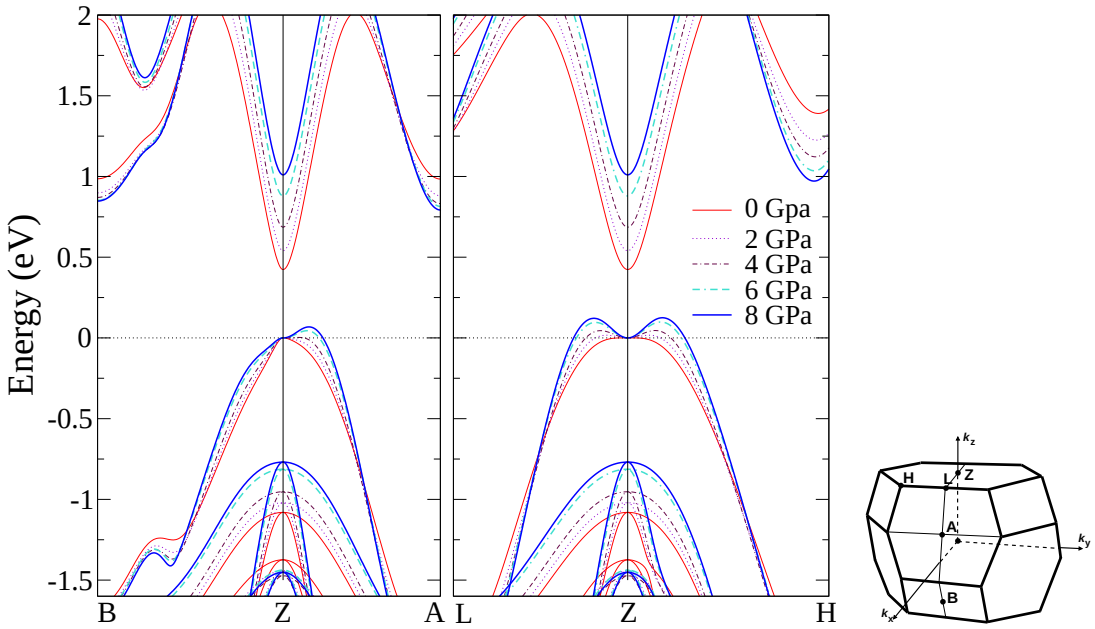

Figure 5.5: Energy band structure of γ-InSe at different pressures. For all the structures the energy origin is the uppermost valence band at the Z point. The Brillouin zone with the high symmetry points is included.

the nature of the lower indirect gap was already observed by Ferlat *et al.* [123] in their study using also fully relaxed structures. We found that this transition has a lower value than the direct gap at pressures around 6 GPa, and that the calculated pressure coefficient of the energy difference between the Z to A indirect transition and the Z direct transition (for P>2 GPa) is -86.1 meV/GPa, which is close to the experimental value of Z-I_2 energy difference (-76 ± 10 meV/GPa, see Fig. 5.6(a)). We conclude that the I_2 experimental indirect gap, Fig. 5.6(c), must be associated with an indirect transition between Z and A.

A very interesting effect of the pressure on the band structure is the shift of the VBM location from the Z point at 0 GPa into a nearby k state. As shown in the Fig. 5.5 this feature of the VBM around Z appears in the directions Z-H, Z-L and Z-A. Segura *et al.* [133] have shown that this feature has a quasi cylindrical symmetry with respect to the Γ-Z direction, i.e, the $\boldsymbol{c}$-axis, in such a way that the constant energy surface looks as ring shaped. This is also the case in our calculations. This effect, theoretically observed for the first time by Manjon *et al.* [128, 133] in a non spin-orbit calculation, has been also observed by Olguin *et al.* [124] in a GGA full-potential augmented-plane wave calculation including spin-orbit corrections and splittings. The distance of this feature in reciprocal space with respect to the Z point

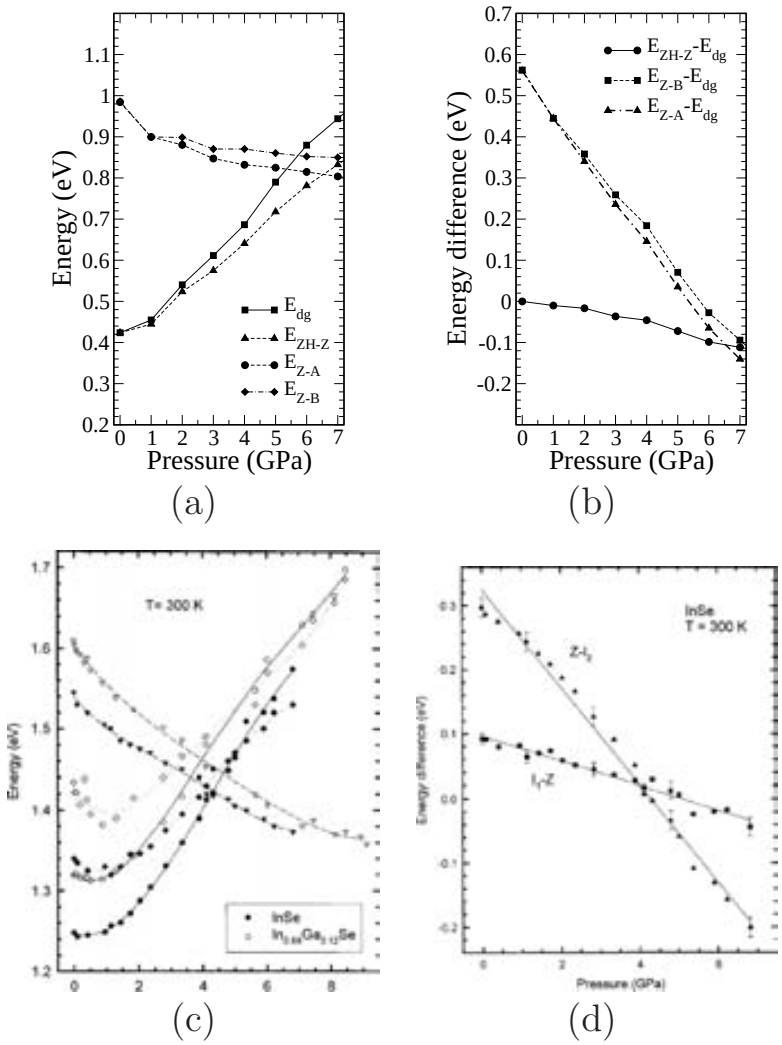

Figure 5.6: (a) Different band gaps calculated for γ-InSe at different pressures. (b) Calculated pressure dependence of the different indirect energy gaps with respect to the Z direct gap (E_{dg}). (c) Experimental pressure dependence of the direct and indirect gaps in InSe (filled symbols) and $In_{0.88}Ga_{0.12}Se$ (hollow symbols). The direct gap position at the Z point of the BZ is represented by circles, the I_1 indirect edge by rhombohedrons and the I_2 indirect edge is symbolized by triangles. (d) Experimental pressure dependence of the energy separation between the I_1 (squares) and I_2 (triangles) indirect edges with respect to the Z direct gap. Solid lines are the fits of the data to linear equations on pressure taken from Ref. [128].

constantly increases with pressure. The calculated gap between this new VBM under pressure and the CBM at Z is lower than the calculated direct gap at Z (see Fig. 5.6(a)). In fact, according to our results this occurs at any applied pressure, but the differences are so small that they can not be considered significant until $\sim$ 3 GPa. Therefore, it must be identified as the experimental direct gap in Fig. 5.6(c), for pressures higher than 3 GPa. The calculated pressure coefficient (for P>2 GPa) of the energy difference between the indirect transition from this new feature of the valence band, which we will label as ZH, to Z of the conduction band, and the Z direct transition, is -17.6 meV/GPa. This value is in good agreement with the experimental value of the I_1-Z energy difference (-19 ± 5 meV/GPa, see Fig. 5.6(d).)

As far as the experimental results of Figure 5.6(c) are concerned, we note that the three transitions (one direct and two indirect) show non linear pressure dependence at low pressures and almost linear behavior above 2 GPa. The non linear behavior at low pressures in not well described by the present DFT calculations. This is probably related to the inability of the local-density approximation to describe correctly essentially non local interactions, such as vdW interactions, which dominate in the low-pressure range of compression. In contrast, the present calculations describe the almost linear behavior for pressures higher than 2 GPa as well as the almost linear pressure dependence of the energy difference between the two indirect gaps with respect to the Z direct gap (see Figs. 5.6).

5.4.2 γ-GaSe and ε-GaSe

The goal of this section is to analyze the effect of changing the cation in these layered semiconductors, i.e., the replacement of an indium by a gallium atom. We first focused our study in the description of γ-GaSe because it can give us insight about the nature of the electronic structure changes observed for γ-InSe. We have completed our study considering ε-GaSe because of the extensive amount of experimental information about this phase, which allows us a comparison with our calculated values.

At ambient conditions, γ-GaSe (as γ-InSe) belongs to the spatial group $R3m$ (C_{3v}^5), which can be described either with a rhombohedral or an hexagonal cell. The crystal parameters in the hexagonal representation are $\boldsymbol{a} = 3.3739$ Å and $\boldsymbol{c} = 23.862$ Å according to Kuhn *et al.* [134]. However, the quantitative accuracy of these values is questionable because of the pour quality of the experimental data. Consequently, we have estimated the unit cell of γ-GaSe to be used as the initial guess in our geometry optimization assuming the same interlayer structure and the same interlayer separation as found in more recent studies for ε-GaSe [120], and then generating the crystal structure with the appropriate symmetry for the γ polytype. In that way, the crystal structure is defined by the cell parameter $\boldsymbol{a} = 3.743$ Å and $\boldsymbol{c} = 23.8785$ Å and the atoms Ga_1, Ga_2, Se_1 and Se_2 are in 3(a) positions, with

Z values of 0.0, 0.1001, 0.8167 and 0.6165, respectively. As for InSe we used the rhombohedral cell for the calculations of the γ-GaSe. It is relevant to point out the large difference between our initial guest for the $\boldsymbol{a}$ parameter and that reported by Kuhn *et al.* , i.e. around 0.4 Å.

On the other hand, ε-GaSe belongs to the symmetry group $P\bar{6}m2$ (C_{3h}^1) and the experimental lattice parameters for its hexagonal unit cell at ambient pressure, reported by Pellicer *et al.* [120], are: $\boldsymbol{a}$=3.743 Å and $\boldsymbol{c}$=15.919 Å. From the best of our knowledge, there have been only three theoretical studies of the pressure effect on ε-GaSe. The first pressure-dependent calculation of the band structure was carried out in our group [135]. Since at the time we did not dispose of direct experimental data for the structure evolution with pressure, we estimated the $\boldsymbol{a}$ and $\boldsymbol{c}$ parameters form the data in references [136] and [112], respectively. The atomic positions inside the cell were those proposed by Pellicer *et al.* [120] using a similar model than that for γ-InSe (see Section 5.4.1). Recently, Schwarz *et al.* [125], have measured simultaneously both lattice parameters, i.e. $\boldsymbol{a}$ and $\boldsymbol{c}$ up to high pressures from a powder x-ray diffraction study. In addition, due to the difficulty of a direct determination of the internal structure, they carried out plane waves calculations, including spin-orbit coupling, in order to optimize the internal structure. In their calculations they fixed the unit cell constants to the experimental values. Also very recently, Zhang *et al.* [137] have carried out plane waves plus local orbital calculations on the elastic constants of ε-GaSe. However, these calculations suffered from several geometrical assumptions and were limited to pressures below 5 GPa. The evolution of the band structure was not considered, neither. Despite these studies, up to now there is no full relaxation calculation of the internal structure and cell vectors on the ε and γ-GaSe polytypes.

Structural Evolution under Pressure for γ-GaSe

As far as we know there is no experimental data about the evolution of this phase with pressure. However, it is interesting to compare first the calculated structural changes with our previous results for γ-InSe, and later with the data for ε-GaSe. These calculations will also allow us to obtain the band structure of this GaSe polytype and to see if it also exhibits the unexpected ring-shaped feature of the valence band in γ-InSe. Our main results are summarized in Figs. 5.7 and 5.8. The first noticeable fact is the smaller cation-cation distance at ambient pressure (a 11%) with respect to γ-InSe, which is the natural consequence of the smaller extension of the valence electrons in gallium with respect to indium. The calculated Ga-Ga distance is 2.43 Å, which is very similar to the optimized value in the ε polytype (2.44 Å) obtained by Schwarz *et al.* [125]. The experimental value is not known but in the ε polytype is estimated to be 2.39 Å [120]. On the other hand, the average bond distance between cation and anion for γ-GaSe ($\sim$ 2.45 Å) is, at

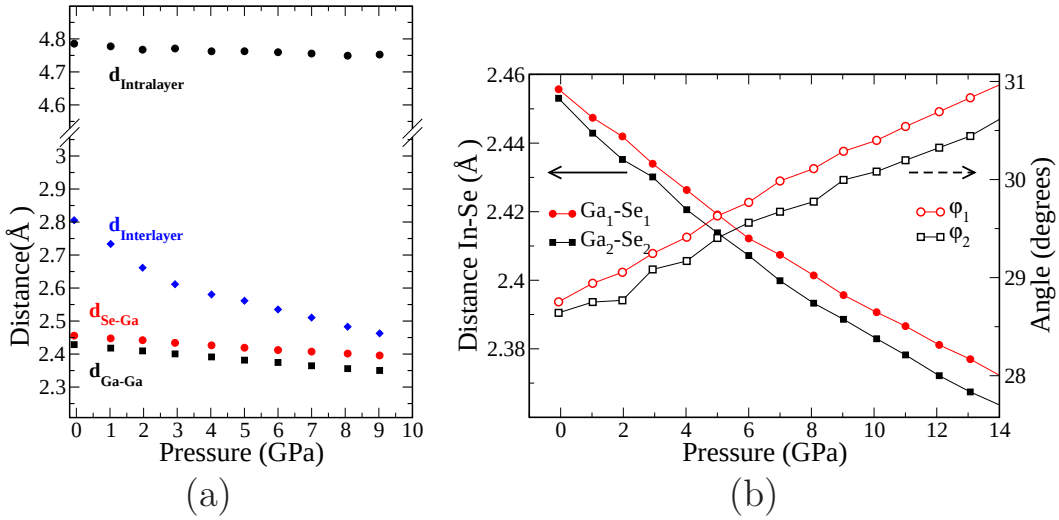

Figure 5.7: (a) Evolution under pressure of the intralayer, interlayer, Ga-Ga, and Se-Ga distances in the γ-GaSe polytype. (b) Calculated values for the two different Ga-Se intralayer distances as well as the φ_1 and the φ_2 angles defined before in Fig. 5.3(d).

ambient pressure, 8% smaller than in γ-InSe. Again, there is no experimental value for this distance, but in the ε polytype is estimated to be 2.47 Å and the optimized value according to Schwarz *et al.* is also 2.47 Å [125]. This leads to a layer in which, at low pressure, d_{Ga-Se} is quite similar to d_{Ga-Ga}. However, in contrast with the γ-InSe case, here the cation-cation distance at 0 GPa is smaller than the cation-anion distance. Due to the difference in compressibility (-3.52% for d_{Ga-Ga} and around -2.76% for d_{Ga-Se} calculated between 0 and 10 GPa), this difference is moderately accentuated with pressure.

With respect to the intralayer distance, the layers of this compound also maintain a nearly constant width, although with a slight constant decrease (-0.8% at P=10 GPa). The interlayer distance has a relative change of -13% in the range between 0 an 10 GPa which is smaller than that observed for InSe in the same range.

In a similar way to γ-InSe, there are two inequivalent selenium atoms in each layer, and therefore for each selenium the d_{Ga-Se} distance, and its angle, follow a different evolution depending on its position in front or not of a gallium atom in the neighbor layer (see Fig. 5.7(b)). The values plotted in Fig. 5.7(a) are of course average values.

Our calculated values at ambient pressure for $\boldsymbol{a}$ and $\boldsymbol{c}$ (see Fig. 5.8(a)) in the hexagonal representation are 3.73 Å and 22.77 Å. Thus, this calculated $\boldsymbol{a}$ value provides support for our initial guest based on ε-GaSe and confirms the suspicion

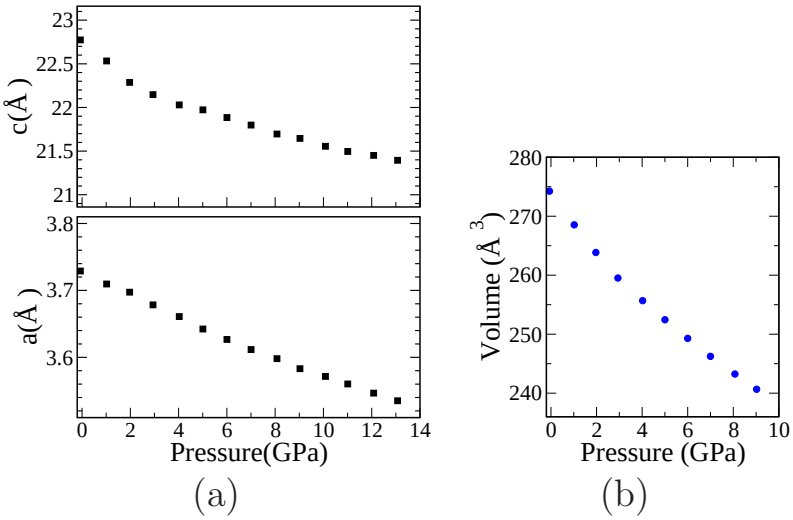

Figure 5.8: a) Theoretical γ-GaSe crystal cell parameters as a function of pressure. b) Theoretical volume as a function of pressure

that the value of Kuhn *et al.* [134] was not reliable. The compressibility of the $\boldsymbol{a}$ and $\boldsymbol{c}$ axes at 10 GPa are -4.2 % and -5.34%, respectively, which are smaller than the calculated values for γ-InSe at the same pressure (-5.38% and -6.63%). It would be interesting to have experimental values for the cell parameters evolution under pressure.

Band Structure Evolution under Pressure for γ-GaSe

Figure 5.9 shows the evolution of the band structure for γ-GaSe along the same lines in the Brillouin zone as for γ-InSe in Fig. 5.5. The first observation is that the lower energy gap at ambient pressure is not a direct gap between the VBM at Z and the Z point in the conduction band, as in γ-InSe. The smallest gap is between Z at the valence band and the A point in the conduction band, although the difference with the corresponding value between Z and B is almost inappreciable for any pressure (see Fig. 5.10). In comparison with γ-InSe both of these transitions change more strongly with pressure. At very high pressures, between 14 and 20 GPa, the lowest energy gap is associated with an indirect transition between the VBM at Z and a local minima in the conduction band located between Z and H (see Fig. 5.10).

In figure 5.9 we have included results for pressures up to 20 GPa. This is because the effect of pressure on the VBM, i.e the appearance of the new maximum away from Z, now is only present for pressures around 8 GPa and its rise with pressures is very slow. As for γ-InSe, this feature exhibits a cylindrical symmetry with respect

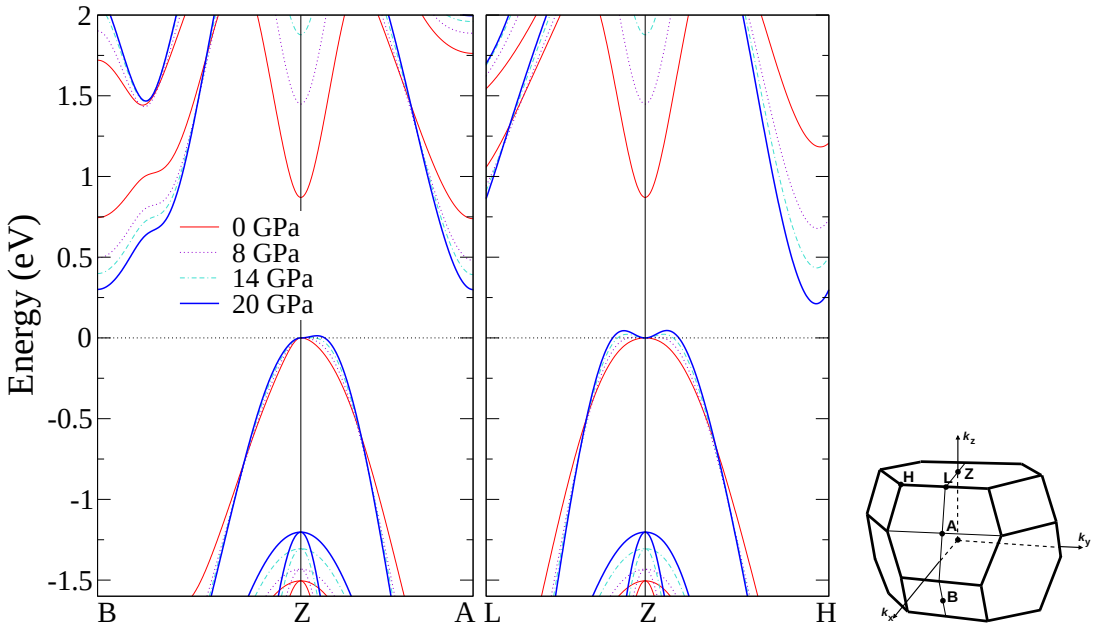

Figure 5.9: Energy band structure of γ-GaSe at different pressures. For all the structures the energy origin is the uppermost valence band at the Z point. The Brillouin zone with the high symmetry points is included.

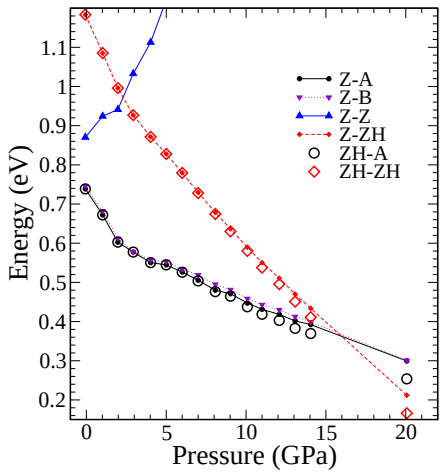

Figure 5.10: Energy gaps calculated of γ-GaSe at different pressures.

to the Γ-Z direction with a k-shift towards the Z-H direction when the pressure increases. As we have discussed before, in γ-InSe the new maximum in the valence band has considerably developed at 8 GPa and is associated with the lowest energy

gap. This is not the case here. In fact, even at very high pressures this feature is not very important and consequently, it is not expected that it can play any important role in the optical behavior of this compound.

In conclusion, the replacement of In by Ga in the γ polytype affects both the direct and all indirect gaps. Although we are not aware of a detailed optical study of γ-GaSe, such study as well as the comparison with γ-InSe would be very interesting.

Structural Evolution under Pressure for ε-GaSe

The effect of pressure on the ε-GaSe cell, up to around 30 GPa, has been recently studied using x-ray-absorption experiments by Schwarz *et al.* [125]. In these experiments a high pressure transition to a possible rock-salt type phase was observed around 20 GPa. With respect to the internal structure, there is a previous (EXAFS) experiment in which the bond length between Ga and Se (d_{GaSe}) was measured as a function of pressure by Pellicer *et al.* [120]. The experimental and the average calculated d_{GaSe} values are depicted in Fig.5.11(a). We have also included the Murnaghan fit carried out by Pellicer *et al.* to their data up to 15 GPa,[2] with the parameters $B_0 = 92 \pm 6$ GPa, $B_0' = 5$ and an ambient pressure distance of 2.470 Å. Our average calculated values of d_{GaSe} and d_{GaGa} at ambient pressure are 2.455 and 2.42 Å respectively. In contrast to InSe, the DFT results for this compound slightly underestimate the value for the cation-anion distance in the whole range. The d_{GaSe} value has a relative change of $\sim -2.63\%$ at 10 GPa, which is very similar to the value for γ-GaSe ($\sim -2.76\%$), and around -6% at 30 GPa. We have also compared the results for d_{GaGa}, the intralayer and interlayer distances (Fig. 5.11(b)), with those for γ-GaSe (Fig. 5.7(a)) and we find that in general terms they follow a similar behavior in both phases.

The evolution of the intralayer distances from the Pellicer *et al.* model are displayed in Fig. 5.11(b). The agreement with the calculated values is very close if we take into account that this model is supposed to be valid only up to 15 GPa.[3]) The width of the layer in both the Pellicer *et al.* model and our calculations clearly has an essentially constant value for the whole range, in contrast with γ-InSe at low pressure. This is evidence of the lower compressibility of the layers for the GaSe compounds. With respect to the interlayer distance, we have an almost constant difference between the calculated values and those from the model, although this difference is larger at ambient pressure.

[2]Pellicer *et al.* [120] obtained d_{GaSe} values from independent EXAFS fits for Ga K edge and Se K edge experiments. They observed that d_{GaSe} is essentially the same for both experiments up to 15 GPa allowing a common Murnaghan fit.

[3]At higher pressures than 15 GPa the d_{GaSe} values from Ga K edge and Se K edge EXAFS fits have clear different behaviors. For that reason their proposed model for the atomic positions is only valid up to this pressure.

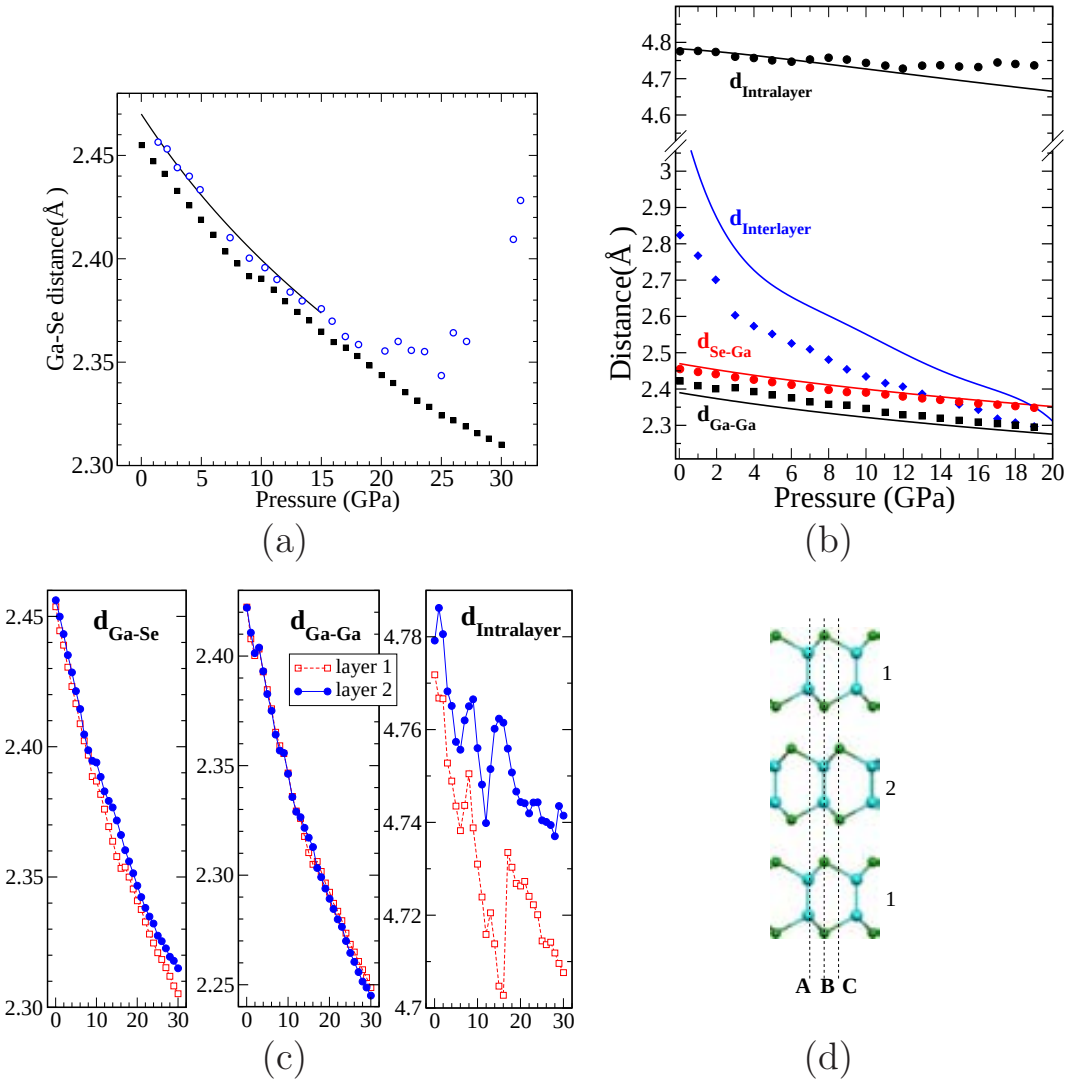

Figure 5.11: (a) Evolution of the Ga-Se distance with pressure in the ε-GaSe polytype. Blue circles are experimental values [120] (from an EXAFS fit for Ga K edge) and solid line is its Murnaghan fit. Squares are the average Ga-Se distance from DFT calculations. (b) Evolution under pressure of the intralayer, interlayer, Ga-Ga, and Ga-Se distances. The continuous lines are the variations according to the hypothesis of Pellicer *et al.* [120] and the dots are theoretical results. (c) Evolution of the calculated d_{GaSe}, d_{GaGa} and intralayer distances with pressure for layers 1 or 2 defined in scheme (d). (d) Structural scheme for ε-GaSe. The inequivalent layers are labeled as 1 and 2.

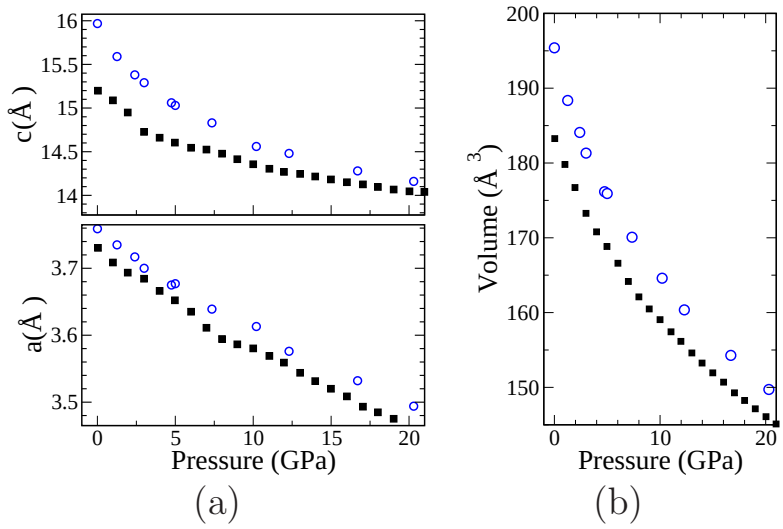

Figure 5.12: (a) ε-GaSe crystal cell parameters as a function of pressure. (b) Volume variation with pressure. The black squares are DFT values. The blue circles are experimental values from Ref. [125].

In spite of the similarities in the evolution of the internal coordinates for the γ-GaSe and ε-GaSe, there is an important difference. In the ε polytype, the hexagonal primitive cell has two inequivalent layers. There is a different environment for each pair of cations (or anions) in one layer with respect to those in the neighbor layer. This is more clear if we see the scheme in Fig. 5.11(d). Consequently, the values plotted in Fig. 5.11(b) are average values. As shown in Fig. 5.11(c), the d_{GaSe} and d_{GaGa} distances are practically identical in the two layers. However, there are noticeable differences in the $d_{intralayer}$. This means that the layers react to the different interlayer environments by flattening in a different way the Ga-Se sublayers while keeping the bond lengths unchanged.

Our calculated values at ambient pressure for $\boldsymbol{a}$ and $\boldsymbol{c}$ (see Fig. 5.12(a)) are 3.73 Å and 15.2 Å (expt. 3.759 and 15.97 Å, respectively [125]). The compressibility of the $\boldsymbol{a}$ and $\boldsymbol{c}$ axes at 10 GPa are -4.03 % and -5.54%, respectively, which are very similar to those calculated for γ-GaSe at the same pressure (-4.2% and -5.34%). Thus, we can conclude that up to 10 GPa our calculations predict a similar behavior of both phases under pressure [4]. At 20 GPa, the compressibilities of the $\boldsymbol{a}$ and $\boldsymbol{c}$ axes for ε-GaSe, respect to the ambient pressure structure, are -7.12% and 7.58%, respectively. At this pressure there is a close agreement between the experimental and calculated value for the $\boldsymbol{c}$ value (14.16 vs 14.05 Å).

[4]Recent experimental work on this phase seems to confirm this conclusion [138]

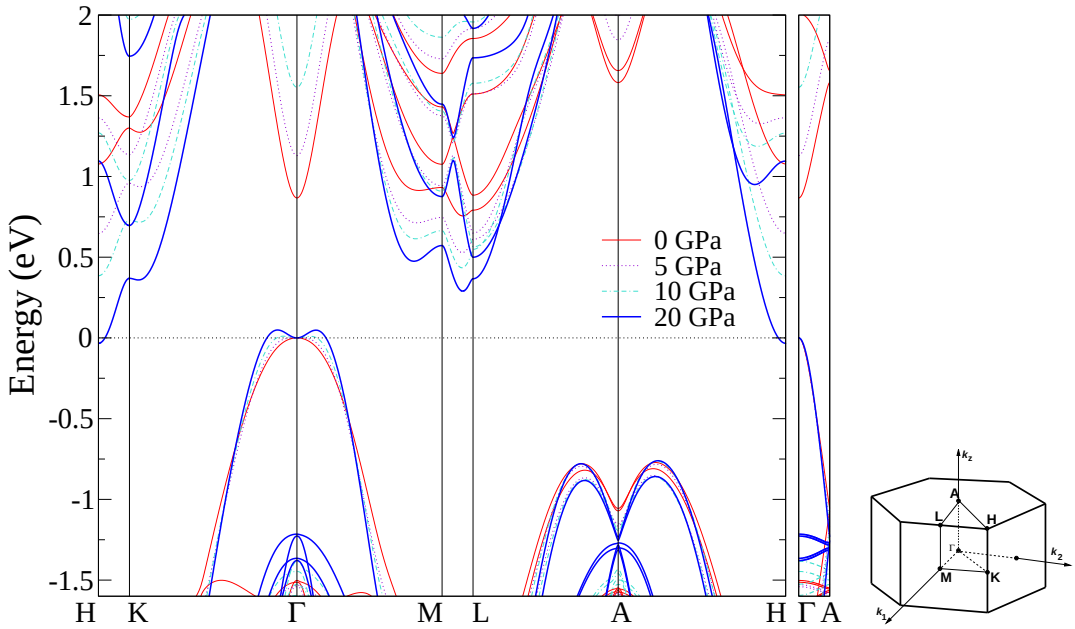

Figure 5.13: Energy band structure of ε-GaSe at different pressures. For all the structures the energy origin is the uppermost valence band at the Γ point. The Brillouin zone with the high symmetry points is included.

Band Structure Evolution under Pressure for ε-GaSe

In Fig. 5.13 we show the evolution of the band structure for ε-GaSe near the band gap. Since its primitive cell is hexagonal, we must be careful in comparing the band structure with the previous γ-polytypes. The hexagonal cell contains two GaSe layers and the $\boldsymbol{c}$ direction is perpendicular to the layers. The ΓA axis (see Fig. 5.13) is parallel to $\boldsymbol{c}$ and therefore is equivalent to the ΓZ axis in the Brillouin zone for the γ-polytype. The band structure of ε-GaSe at ambient pressure along this direction can be seen as the result of folding of the band structure of γ-GaSe along the ΓZ direction. The maximum of the valence band is thus now at the Γ point and the plane containing the Γ, K and M points (see Fig. 5.13) is the plane of the Brillouin zone to be studied in looking for the new ring shaped maximum of the valence band.

At ambient pressure, the VBM is located at the Γ point. As for the γ-GaSe, the lowest transition is not associated with a direct gap. The CBM is located at some point in the path between L and M. The direct gap is larger by almost 0.1 eV. At ambient pressure we see another local minimum in the conduction band at the H point, which lies at ~ 0.3 eV with respect to the CBM.

A shift of the VBM with pressure is observed in the KΓM plane with almost a

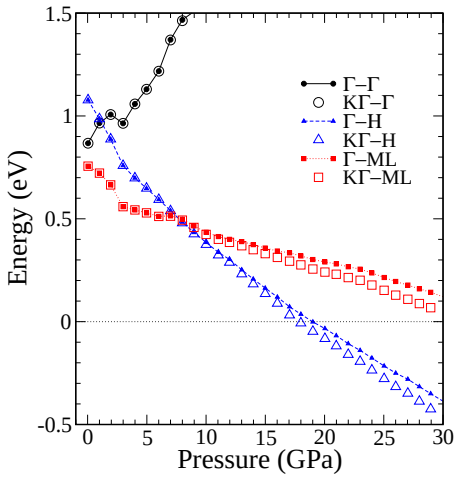

Figure 5.14: Energy gaps calculated for ε-GaSe at different pressures.

cylindrical symmetry with respect to the Γ point. However, as in γ-GaSe, this effect rises only at relatively high pressures, $\sim$ 10 GPa and it is only $\sim$ 0.05 eV higher than the Γ point at 20 GPa. Consequently, this effect is not expected to have any important role in the optical properties of the ε-GaSe.

The Γ-ML and Γ-H transitions have a negative relative change with pressure, unlike the direct $\Gamma - \Gamma$ transition (Fig. 5.14). The smaller gap is between Γ-ML up to 8 GPa, and from there, between Γ-H.

Experimentally, ε-GaSe was found to be an indirect gap semiconductor, although the difference with the direct gap should be only around 10 meV [112]. It was also found that there is a change of sign in the evolution of the direct band gap with pressure at around 2 GPa. The indirect gap was found to decrease with pressure in a continuous way. It should be pointed out that only above 3 GPa the values of the indirect gap could be obtained directly [112]. The present results are only partially in agreement with the experimental results. We are uncomfortable with the results below 2 GPa. In a previous study of our group in which we used the experimentally derived $\boldsymbol{a}$ and $\boldsymbol{c}$ cell constants and the Pellicer *et al.* model for the internal structure, we obtained the correct behavior for the direct gap pressure evolution, unlike the behavior found here. Thus, we suspect that the results at very low pressures (below 2 GPa) may be contaminated by the already noted problems of DFT in handling the vdW forces. It is possible that by fixing the $\boldsymbol{c}$ parameter to a more realistic value, the results for the model calculation may be in fact better at low pressures. If the region between 0 and 2 GPa of Fig. 5.14 is thus incorrect, the comparison with the experimental results would be relatively satisfactory.

Let us note that in a recent theoretical study using plane waves [125] it was

claimed that ε-GaSe is a direct gap semiconductor with the CBM and VBM at Γ. However, the authors did not consider the band dispersion along the M to L line, which is what makes ε an indirect gap semiconductor. Also, in that study the structural relaxation was carried out using experimental cell parameters. The two studies share a number of features like the change in the nature of the lowest indirect gap to one associated with a minimum of the conduction band at H. Thus, we believe that the two studies would be essentially similar if carried out with the same geometrical conditions.

These results point out the need for further work (both theoretical and experimental) in order to more clearly understand the optical properties of ε-GaSe. In particular, the role of the different indirect gaps at high pressures and the question of the direct versus indirect nature of the lowest gap at ambient pressure are questions which deserve further attention. What is, however, quite clear is that, whatever it is the polytype, the replacement of Ga by In in these layered materials strongly affects the nature of the optical transitions.

5.4.3 GaS

The next logical step in this study was to replace the anion. For this we choose to replace selenium by sulphur because the character of the layers, as described in Section 5.2, is not altered as it is the case of GaTe. At ambient conditions, gallium sulfide crystallizes in a β polytype and belongs to the spatial group $P6_3/mmm$, with the lattice parameters for the hexagonal cell being $\boldsymbol{a}$=3.585 and $\boldsymbol{c}$=15.53 [139]. As for ε-GaSe this cell contains four pairs of atoms (i.e. two layers).

The structural changes in this compound at low pressures have been studied by several authors [139, 140, 141]. It has been found to exhibit a transition to a new layered phase, GaS-II, between 0.3 and 3 GPa. In a recent angle dispersive x-ray diffraction experiment it has been possible to obtain a more exact knowledge about the pressure at which this transition takes place. Pellicer *et al.* [130] have determined a pressure of 2.7 ± 0.3 GPa for this transition. Additionally, they did not observe any clear sign below 35 GPa of another transition to a rock-salt phase, as it occurs for InSe and GaSe. The internal structure of this high pressure phase around 3 GPa was previously determined by d´Amour *et al.* [139]. It has the same space group as the β-GaS but the Ga atoms change their position from the $4(f)$ site (2/3,1/3,z) to the $4(e)$ site (0,0,z). This represents a shift of one layer with respect to the adjacent ones as shown in Fig. 5.15.

We decided to carry out a study of the effect of pressure on the structure and electronic properties of both gallium sulfide phases. Although for pressures higher than 2.7 GPa only the GaS-II phase occurs, we have also studied the β-GaS phase at high pressures in order to compare the electronic structure evolution of two slightly different interlayer situations.

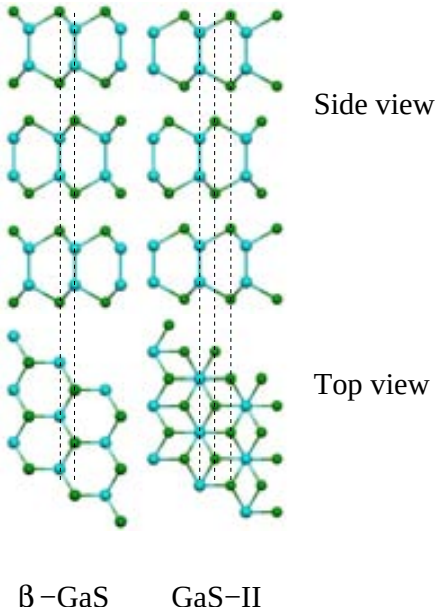

Figure 5.15: Schematic representation of the crystal structure of β-GaS and GaS-II. Green balls are anion atoms (S), blue balls are cations atoms (Ga).

Structural Evolution under Pressure for β-GaS and GaS-II

Our DFT results for d_{GaGa} and d_{GaS}, and the interlayer and intralayer distances for both phases are reported in figures 5.16(a) and 5.16(b), and the evolution of the cell constants is reported in Fig. 5.17(a). Let us note that the two phases have practically the same enthalpy for a large pressure range so that we are unable to reproduce the transition from β-GaS to GaS-II at around 3 GPa. As shown in Fig. 5.17(b), the GaS-II phase is associated with a smaller volume for all pressures. The calculated value of volume change between the β-GaS and GaS-II phases at 3 GPa is $\sim 1.5\%$, which compares well with the experimental value, 0.8% [130]. The change in the cell parameters for the high pressure phase, GaS-II, between 3 and 20 GPa are: -4.4% for $\boldsymbol{a}$, -7.0% for $\boldsymbol{c}$ and -14.9% for the volume.

β-GaS has an almost constant value for the intralayer distance, ~ 4.63 Å, in the studied range. However, GaS-II presents a relative change of ~ -2.5 % between 3 and 27 GPa. This is a clear difference with GaSe and InSe. As shown in Fig. 5.16 this change is mainly due to the decrease in the Ga-Ga bond length. The calculated Ga-Ga distances in the β-GaS (ambient pressure) and GaS-II (3 GPa) phases, 2.430 and 2.414 Å, are in good agreement with the experimental values, 2.44 and 2.42 Å, respectively [139].

There is also a clear difference in the interlayer distance. It is around 1 Å smaller at pressures higher than 1 GPa in GaS-II than in β-GaS. This is a consequence of

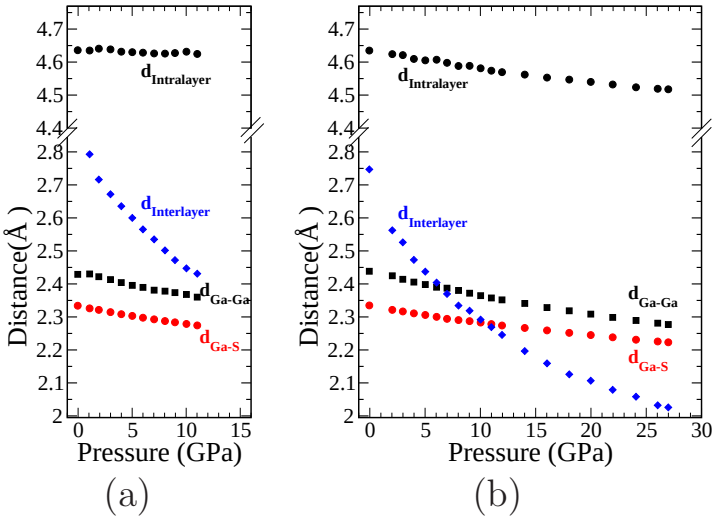

Figure 5.16: Evolution under pressure of the intralayer, interlayer, Ga-Ga, and S-Ga distances of (a) β-GaS and (b) GaS-II.

the array of the two neighboring layers. In β-GaS both anions in one layer are in the same axis as both cations in the next one. In the GaS-II the cations in neighboring layers are in the same axis, but there is a mismatch between its anions.

In both compounds the cation-anion distance is smaller than the cation-cation distance (see Fig. 5.16) and is practically the same in both phases. For instance, at 3 GPa, where the transition occurs, it is 2.321 Å for β-GaS and 2.316 Å for GaS-II. The relative change with pressure of the Ga-Ga distance is larger than that of the Ga-S distance. This fact is emphasized in the GaS-II phase. Let us note that in the β-polytype, as well as in the GaS-II phase, the two layers are in fact identical.

Band Structure Evolution under Pressure for β-GaS and GaS-II

Figures 5.18 and 5.19 show the evolution of the band structure near the band gap, for β-GaS and GaS-II, respectively. Independently of the compound, the VBM at ambient pressure occurs at the Γ point and, for the range of pressure studied, we did not find any change in the position for this maximum. This is in contrast with our results for selenides. However, there are clear differences on the CBM and in its evolution with pressure. At ambient pressure the CBM of β-GaS is at the M point; however, a second minimum very close in energy appears at K. This minimum in K becomes the CBM at pressures above 2 GPa. Both transitions have a negative relative change with pressure (see Fig. 5.20(a)). The direct gap, as for all polytypes so far analyzed, increases in magnitude with pressure.

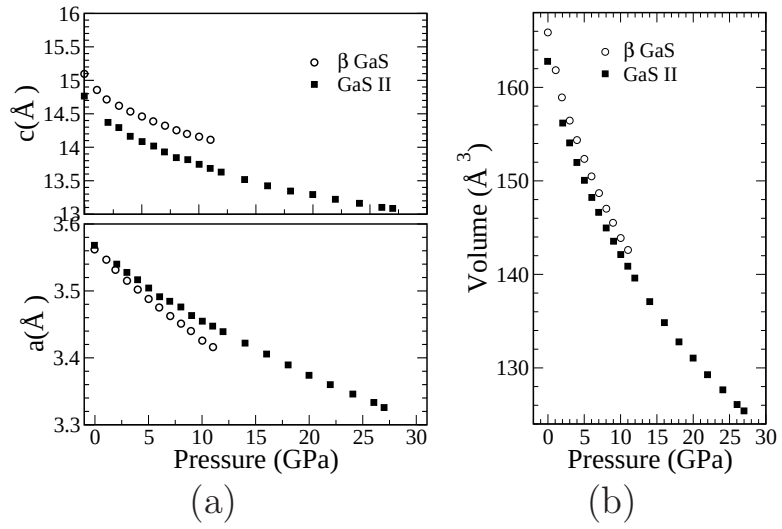

Figure 5.17: Calculated β-GaS and GaS-II (a) crystal cell parameters and (b) volume as a function of pressure.

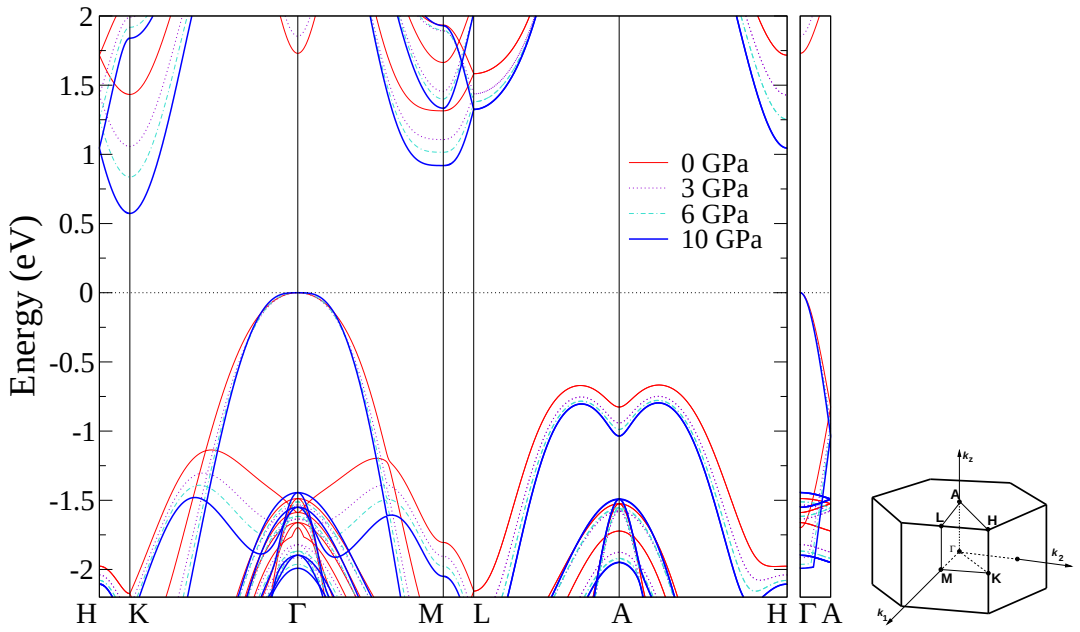

Figure 5.18: Energy band structure of β-GaS at different pressures. For all the structures the energy origin is the uppermost valence band at the Γ point. The Brillouin zone with the high symmetry points is included.

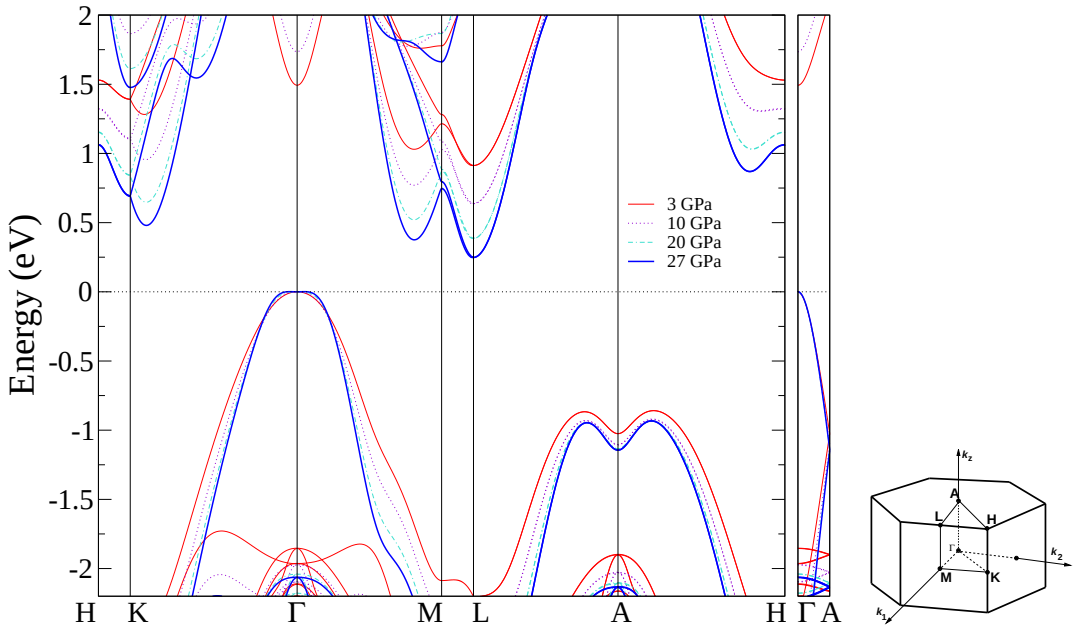

Figure 5.19: Energy band structure of GaS-II at different pressures. For all the structures the energy reference is the uppermost valence band at the Γ point. The Brillouin zone with the high symmetry points is included.

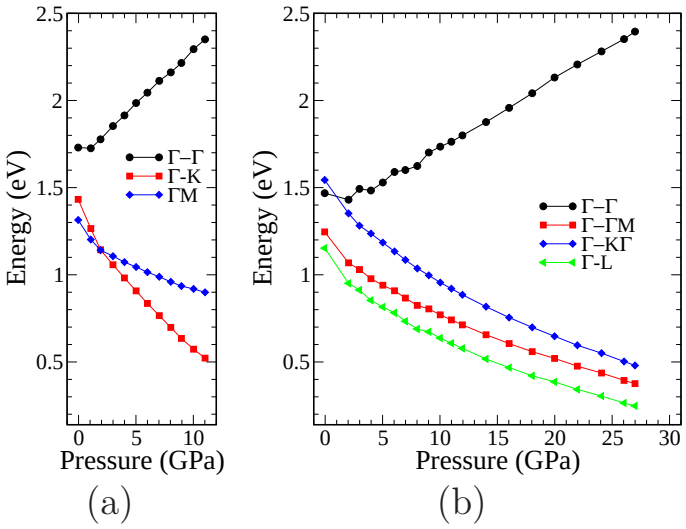

Figure 5.20: Evolution of the calculated energy gaps of β-GaS (a) and GaS-II (b) with pressure.

For GaS-II, the CBM occurs at L. There are two additional minima in the LΓM plane, one close to K an another close to M. With pressure these three indirect gaps evolve in a similar way, the ΓL transition being always the lowest one. Thus, it is very interesting to see how a slight shift between the layers can noticeably affect the optical properties. In the present case, the lowest indirect gap in the high-pressure phase is different from the two indirect gaps of the low-pressure phase.

5.5 Concluding Remarks

The main goal of this chapter was to provide a consistent set of results, based on *ab-initio* calculations and without imposing geometrical constrains, on the structural and electronic structures of layered III-VI semiconductors. The effect of pressure on the electronic structure of this family of compounds is an intriguing one. However, the theoretical study of this effect is complex because of the non existence of detailed structures under pressure. An important step in this direction has been the development of models describing the pressure evolution of the crystal structure of γ-InSe [132] and ε-GaSe [120]. It was using these models that the initial studies of our group were possible [128, 133, 135]. As for any model, it is important to dispose of a consistent of set of structural results which can be used as a test of the main points in which these models are based. This was another of the initial purposes of this study. In addition, let us note that even if the III-VI semiconductors which we have considered here possess the same type of layers, in some polytypes (for instance the ε) the layers must not be identical by symmetry. Even if there is only one type of layer in other polytypes (for instance the γ), there are two different, even if very similar, cations and anions as a result of the different interlayer environments. Obviously, these minor structural features can not enter into the models developed to give a hint of the structural evolution under pressure. Thus, we thought that examination of these aspects was important. Although it is quite obvious that from the structural viewpoint they will only give minor corrections, it is not that clear how much these corrections may affect the subsequent band structure studies. In the preceding pages we have reported results concerning all these points which we hope may be important for future work in this area.

From the viewpoint of the electronic structure, the more surprising feature of these compounds is probably the development of the ring shaped new maximum of the valence band under pressure initially discovered in γ-InSe [128]. The appearance on this new maximum with pressure is important to explain satisfactorily the direct to indirect gap crossover in γ-InSe, some features of the photoluminescence at low excitation energy as well as the Hall effect and resistivity measurements at high pressure in this material. Thus, it was important to study if a similar behavior of the conduction band was also possible for other members of this family. As has been

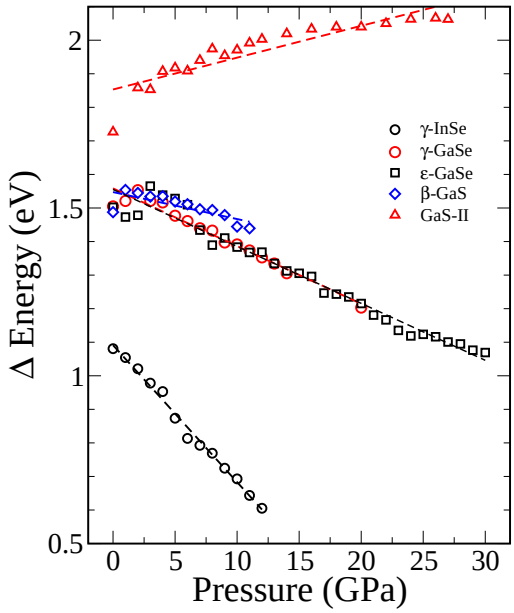

Figure 5.21: Change with pressure of the energy difference of the top of the highest occupied band and next occupied band for the different systems studied.

clearly shown in Section 5.4 it turns out that γ-InSe is the only of the five different systems studied which presents this feature. This fact seems to agree with the observation of very different behavior of γ-InSe and ε-GaSe concerning the variation of the hole concentration and mobility with pressure which can be accounted for on the basis of the existence or absence of the ring shaped feature [135]. The origin of this ring shaped feature of the valence band at high pressures can be discussed in great detail in the frame of the $k \cdot p$ model [133, 135]. However, the driving force for its appearance can be traced back to the mixing into the highest occupied band (which is mostly Se p_z in character) of the next occupied bands (which are mostly Se p_x and p_y in character). This mixing is more favourable when the energy difference between the two types of bands is smaller. As it can be seen in Fig. 5.21 where we have plotted the difference between the top of the highest occupied band and the next one, for γ-InSe both the energy difference is the smaller and the decrease with pressure is the stronger. The two polytypes of GaSe, γ and ε, although when they are considered closely exhibit some differences, they exhibit a very similar behavior, having a larger ambient pressure energy difference and a decrease with pressure which is almost half that of the γ-InSe. Thus, the tendency to the formation of the ring shaped feature is severely decreased and only at very high pressure can really occur. For the high pressure form of GaS the situation is even worse. We believe that the main structural factor behind the unique behavior of γ-InSe is the larger

and more compressible nature of the In-In bond with respect to the Ga-Ga bond. The shorter separation between the two sublayers of the XSe layer for X = Ga leads to a larger initial separation between the Se p_z and Se $p_{x,y}$ bands and of course to a more mitigated variation with pressure.

At this point it is worth noting the large difference in terms of electronic structure between the low- and high-pressure forms of β-GaS. The difference is clearly related with the difference in interactions along the interlayer direction. The high pressure form being more compact as far as the interlayer region is concerned, it leads to the appearance of extra minima in the conduction band. This observation is just a reminder that even if the interactions along the interlayer region are much weaker than the intralayer interaction, they strongly dominate the nature of the energy gaps between the valence and conduction band so that, if possible to prepare with enough purity, the optical properties of different polytypes of the same compound can exhibit notable differences.

Let us consider the question of the type of structural relaxation appropriate in studies of the pressure effect on the structure of the layered III-VI semiconductors. The use of full geometrical relaxation is a powerful tool because it leads to a very detailed knowledge of the structural details. We believe that this is really important when subsequent studies of fine details of the electronic structure are needed. These calculations have now become perfectly affordable for systems of this size and thus there is no reason to carry out studies under geometrical constrains. However, as commented several times along Section 5.4, the layered nature of these materials leads consistently to an underestimation of the cell volume which is mostly due to the underestimation of the cell axis along the interlayer direction. This is due to the well known problems of DFT to deal with the vdW forces which have a decisive role along the interlayer space. Thus, it seems to us that in future studies of the pressure effect on these materials, and until reliable DFT functionals able to describe vdW interactions are available, the better approach would be the use of full relaxation except for the cell axis along the interlayer direction, which should be kept at the experimental value. In that way, the problems of DFT with the vdW component of the interlayer interaction would be in some way obviated. Since the pressure evolution of the cell axis is easier to determine than the internal structure, this would not limit the applicability of the theoretical approach.

How do the simple models developed previously for γ-InSe and ε-GaSe compare with the fully relaxed structures? The two main assumptions of these models were that (i) the local trigonal symmetry of the Se atoms in the layer plane and the perpendicularity of the X-X (X=In, Ga) bonds with respect to the X planes are maintained with pressure, and (ii) the In-Se and In-In bond lengths have the same relative behaviour under pressure. Analysis of our data shows that indeed the first assumption is fulfilled and the second is partially followed. In general, the X-X bond shrinks faster than the X-Se bonds according to the DFT calculations. However,

the differences generated with respect to those predicted by the model are not very important. From the data reported in Section 5.4 it clearly appears that from the structural viewpoint these models can be considered as very satisfactory. Let us mention, however, that at the beginning of our study we used the model to generate the crystal structures for ε-GaSe under pressure when calculating the pressure evolution of the band structure of this compound. In contrast with the results obtained using the fully relaxed geometries, i.e. the top of the Se p_z and Se p_x and p_y bands approach although more slowly than in γ-InSe, we found that the top of the two types of bands separate form each other. Although from a physical viewpoint the important result in both calculations is the same, i.e. the ring shaped feature of the valence band only develops at considerably higher pressures and becomes irrelevant, this fact clearly points out that some subtle aspects of the band structure may be very strongly dependent of the structural details. In the present case the difference is easily understood because, as analyzed above, the separation between the top of the Se p_z and Se p_x and p_x bands depends critically of the X-X (X = In, Ga) distance, which is precisely the structural parameter for which we noted differences in the evolution with respect to what is assumed in the model. Although these differences are not that significant for the structural description they have some influence on one of the important aspects of the electronic structure. Thus, we believe that use of a fully relaxed structure may be more satisfying in this type of studies.

Chapter 6

A Tetragonal Phase of InSe

In this chapter we analyze the changes with pressure of the electronic and structural properties of monoclinic InSe. We present experimental and theoretical evidence concerning a second order phase transition towards a new tetragonal phase.

6.1 Introduction and Motivation

As we point out before in Chapter 5, there is high interest on the III-VI semiconductors family due to its potential application in solar energy conversion devices [108], solid-state batteries [109, 110], and nonlinear optics [106, 107]. The layered character of these compounds determines an anisotropic behavior of their properties with pressure, for this reason it is very important to understand their structural and electronic evolution with this parameter. In particular the effect of pressure at room temperature on the indium selenide (InSe) has been widely studied [129, 132]. However, in the last years there has also been very much interest in taking into account the temperature effects, and to improve the knowledge about the pressure-temperature phase diagram of InSe [142, 105].

The pressure-temperature phase diagrama recently constructed by Errandonea *et al.* [105], based on their own work as well as in previous studies [129, 143, 142], is shown in Fig. 6.1. It is mainly characterized by three solid phases. At ambient conditions InSe crystallizes in a rhombohedral layered phase, belonging to the γ-polytype (from now on InSe-I) and with the space group $R3m$ (C_{3v}^5). At high-pressure (around 6 GPa) and room-temperature (RT) γ-InSe starts a phase transition towards a metallic NaCl-like cubic phase (from now on InSe-III) which is completed at 10 GPa [129]. At high pressure and high temperature the layered γ-InSe transforms into a monoclinic (MC) phase (from now on InSe-II) with space group symmetry P2/m(C_{2h}^1) [144].

The monoclinic InSe-II phase was reported for the first time by Vezzoli *et al.*

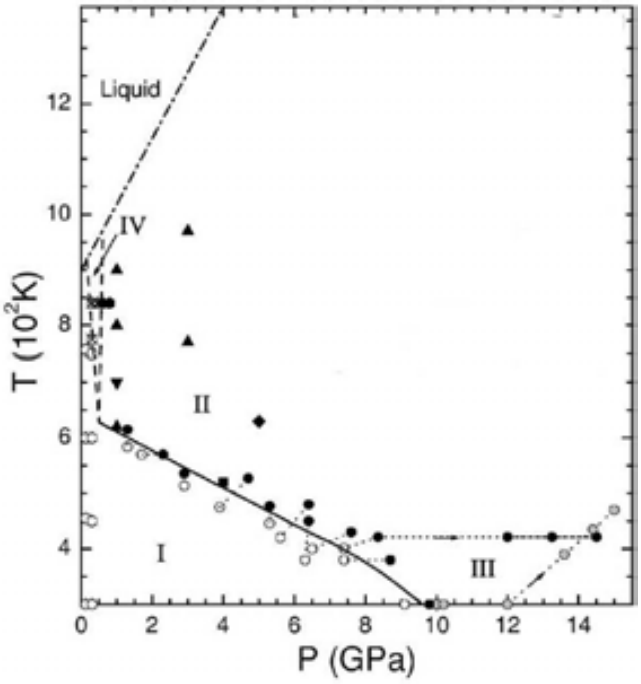

Figure 6.1: Pressure-temperature phase diagram of InSe from Ref. [105]. Solid (empty) circles indicate the stability of InSe-II (InSe-I), and gray circles the stability of InSe-III. The solid line indicates the Phase I→Phase II transition line. The dashed lines are postulated phase boundaries. The dashed-dotted line is the melting curve of InSe [142]. The dotted lines connect data points measured in the same sample. Black diamond: InSe-II from Iwasaki *et al.* [144], square: InSe-II from Vezzoli *et al.* [145], up triangles: InSe-II from Ferlat *et al.* [142], down triangle: InSe-II from Errandonea *et al.* [105], and gray diamond: InSe-III from Schwarz *et al.* [129]. The hexagons correspond to the results obtained from the resistivity measurements from Ref. [105]. Empty hexagons: InSe-I, solid hexagons: InSe-II, and crossed hexagons: InSe-IV.

[145]. Apparently, the authors of the first physical studies of this phase did not realize the layered character of this system [144, 146]. However, in the recent study by Errandonea *et al.* [105] its layered character was taken into account. As can be seen in Fig. 6.2, InSe-II has four molecular units in the unit cell and it is built up from In-Se layers. The difference with the γ-polytype lies in the fact that, whereas in the monoclinic structure the In-In bonds are parallel to the layers, in the γ-polytype (see Fig. 5.3(d)) they are perpendicular to the layers.

In their work, Errandonea *et al.* [105] also reported a band structure calculation of this monoclinic layered phase. These calculations provide the first description of the electronic structure of InSe-II. They were carried out using the more recent

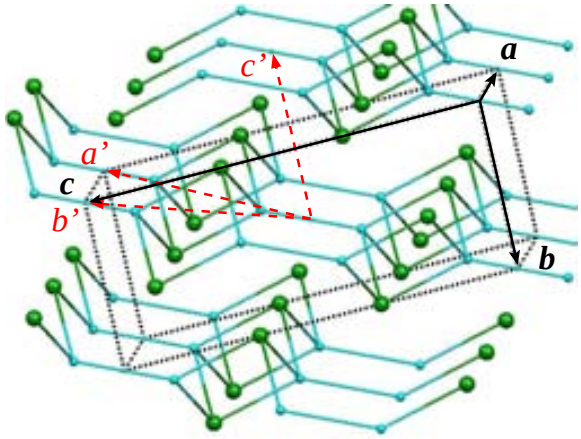

Figure 6.2: Perspective view of the crystalline structure of InSe-II. Indium and selenium atoms are cyan and green balls, respectively.

experimental cell parameters at low pressure and the atomic positions determined by Watanabe *et al.* [146].

Although in their work Errandonea *et al.* [105] studied the effect of pressure on the optical properties of InSe-II, they did not investigate the structural pressure effects. In order to study the evolution of structure with pressure, recent angle-dispersive powder diffraction (ADXRD) experiments on InSe-II have been carried out up to pressures close to 30 GPa. This work is a collaboration between the *Grupo de Semiconductores y Fibras Opticas (Universitat de València)*, the *Laboratoire de Physicochimie de la Matière Condensée (Universite de Montpellier II)* and the *IMPMC (Universite de Paris VI)*. Gradual changes in the diffraction pattern of the InSe-II have been observed with pressure application up to 19.4 GPa. At this pressure some low angle peaks of monoclinic InSe disappear. These changes are fully reversible upon decompression of the sample. This evidence, together with a cell volume change without discontinuity, allow to propose a second order phase transition for monoclinic InSe into a new high pressure phase. As this transition is very slow, it is possible to expect still a layered character of this new phase. However, it is well known that some layered III-VI semiconductors suffer a first order transition to a three dimensional phase, e.g., the rock-salt phase. Thus, it is very interesting to study what is the actual structure of this new high pressure phase.

We report here our theoretical work concerning this problem, which is the result of a collaboration with the experimental groups mentioned above, in order to provide some understanding of the internal structure of this new phase. We propose a structural transition of the monoclinic phase to the calomel type structure which has already been observed as the high pressure phase of indium sulphide. The subsequent fits of the diffraction patterns at high pressure considering this crystal structure

	Wy	x	y	Z
In(1)	2m	0	-1/8	3/26
In(2)	2n	1/2	5/8	10/26
Se(1)	2m	0	0	9/26
Se(2)	2n	1/2	1/2	4/26

Table 6.1: Atomic Wyckoff positions for InSe-II in the space group P2/m(C_{2h}^1) [146].

have confirmed our suggestion. Additionally, some current Raman spectroscopy measurements under pressure also seem to be in agreement with this proposal.

6.2 Computational Details

The computational details are similar to those used for the layered III-VI semiconductors (see Section 5.3). The basis set used was a split-valence double-ζ plus polarization (DZP) and the range of its numerical (pseudo-) atomic orbitals are those obtained by application of a variational optimization method [18] at the fictitious pressure of 0.1 GPa. We have worked within the local density approximation as parametrised by Perdew and Zunger [6].

The optimization of atomic coordinates and/or cell were done using a unit cell of eight atoms, while for the band structure calculation we used the primitive representation (further details in Section 6.3). For these cells we use a grid of $4 \times 4 \times 4$ and $7 \times 7 \times 7$ k points for sampling the Brillouin zones of the nonprimitive and primitive cells, respectively. The energy cutoff for the real space integration mesh was 500 Ry. It is worth emphasizing that we checked the total energy convergence with respect to these parameters. The atomic configuration, cutoff radii and core corrections of the pseudopotentials generation for the indium and selenium atoms are those summarized in Table 5.2.

6.3 The Monoclinic Phase of InSe

We present first our results for InSe-II at ambient pressure. In Table 6.1 we show the crystal parameters used for the independent atoms in the P2/m(C_{2h}^1) space group. These were reported by Watanabe *et al.* [146] and were determined on a sample obtained at high temperature and pressures of 40 and 50 kbar and by quenching at ambient conditions. Let us note that the initial P2/m space group of this InSe phase was revised by Cenzual *et al.* [147]. They concluded that the more symmetric representation C2/m(C_{2h}^3) is a better description of the crystal structure. In this representation the cell parameters are defined with respect to those of Watanabe *et*

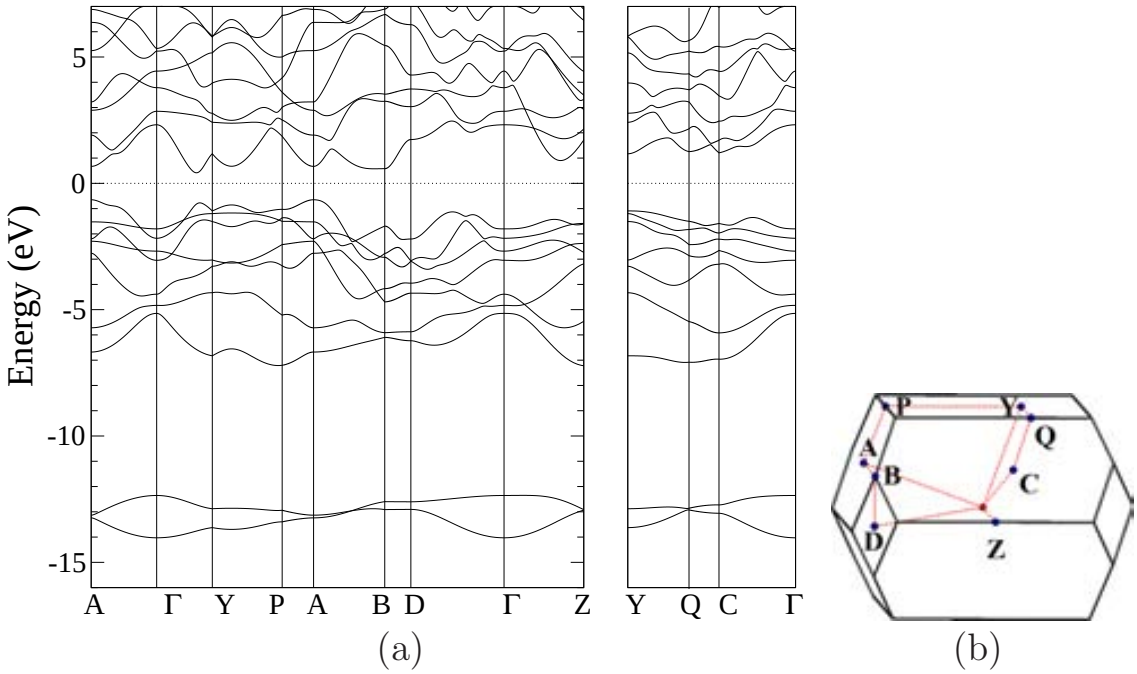

Figure 6.3: (a) Band structure of the non optimized monoclinic InSe-II structure at 0 GPa. The energy origin corresponds to the Fermi level. (b) Brillouin zone of InSe-II. For a reference of the orientation the high symmetry A point is at $\vec{c'}^*/2$ (with $\vec{c'}^* = 2\pi(\vec{a'} \times \vec{b'})/[\vec{a'} \cdot (\vec{b'} \times \vec{c'})]$ (see Fig. 6.2)).

al. by the vector base transformation $(\boldsymbol{b} - \boldsymbol{c}, \boldsymbol{a}, -\boldsymbol{b})$, and the independent In [Se] atoms are located at the Wyckoff positions: 4i (0.160,0,0.142)[4i (0.384,0,0.505)]. In spite of this, there are no structural differences between both representations.

Errandonea *et al.* observed that indeed the monoclinic unit cell of InSe-II is a nonprimitive unit cell. As shown in Fig. 6.2, the primitive unit cell can be constructed using the vector base transformation:

$$\vec{a'} = \frac{\vec{a}-\vec{b}+\vec{c}}{2}, \quad \vec{b'} = \frac{-\vec{a}-\vec{b}+\vec{c}}{2} \quad \text{and } \vec{c'} = -\vec{b},$$

where $\vec{a'}, \vec{b'}, \vec{c'}$ is the vector base of the primitive unit cell, and $\vec{a}, \vec{b}, \vec{c}$ is the vector base of the conventional unit cell of the P2/m structure. Thus, the primitive unit cell only has two molecular units instead of four. This fact has great importance in the correct assignment of the Raman lines and in the electronic band representation. For consistency with the previous discussion of the physical properties of InSe-II we will use the structural description of Errandonea *et al.*

The band structure of the monoclinic phase of InSe calculated along the high symmetry directions of its Brillouin zone is shown in Fig. 6.3. In generating this

figure we have used the experimental cell parameters obtained by Errandonea *et al.* [105], i.e., $\boldsymbol{a}$=4.088 Å, $\boldsymbol{b}$=4.655 Å, $\boldsymbol{c}$=10.981 and $\alpha = 86.85°$ and the atomic positions from Watanabe *et al.* The Γ-A direction in the Brillouin zone is parallel to the axis perpendicular to the layer plane in the InSe-II (see Fig. 6.2); thus the Γ-Z and Γ-Y are perpendicular and parallel to the In-In bonds. The calculation using relaxed atomic coordinates within the experimental cell leads to a band structure which is almost identical.

The main characteristics of the band structure of Figure 6.3(a) are: (a) the two lowest lying bands have mainly Se *s* character, (b) the next upper band has predominant In *s* character and corresponds to the In-In covalent bond (molecular bonding σ orbitals), (c) the following six bands have predominant Se *p* character, (d) the upper valence band has, in most of the Brillouin zone, predominant Se p_z character and mainly corresponds to the electon pair responsable for the interlayer interactions, (e) the In character dominates in the lowest conduction band (with a stronger participation of *s* orbitals), although there is also a very sizeable contribution of the Se *p* orbitals (i.e., antibonding In-Se σ orbitals). Further details concerning the nature of the bonding will be given in Section 6.5.

This band structure was previously calculated in our group and reported in Ref. [105]. However, in that work some high symmetry points of the Brillouin were erroneously determined. Thus, the nature of the direct vs. indirect lower energy gaps must be reexamined. In the present calculation the valence-band maximum (VBM) occurs in the high symmetry point A, i.e., a point in the direction of the intralayer interactions, and not in the P-Y line as reported before. The conduction-band minimum (CBM) is located at some point along the Γ-Y line (the In-In bond direction). Thus, InSe-II is an indirect semiconductor. However, it must be realized that the direct gaps at A and at the point in between the Γ and Y where the minimum of the CBM occurs, are only 0.25 and 0.12 eV larger. In addition, the indirect gap between the maximum in between Γ and Y at the valence band and A in the conduction band is 0.38 eV larger. Thus, it is clear that at least one indirect and one direct gaps are relatively close. Let us note, however, that when using relaxed atomic coordinates within the experimental cell, the difference between the two closest gaps increases from 0.12 eV to 0.24 eV.

6.4 High Pressure Structure and Phase Transition

In order to study the pressure behavior of the monoclinic phase we carried out, in a first step, full optimizations of the structure for different pressures. In this optimization scheme the forces on the atoms were minimized while the cell vectors

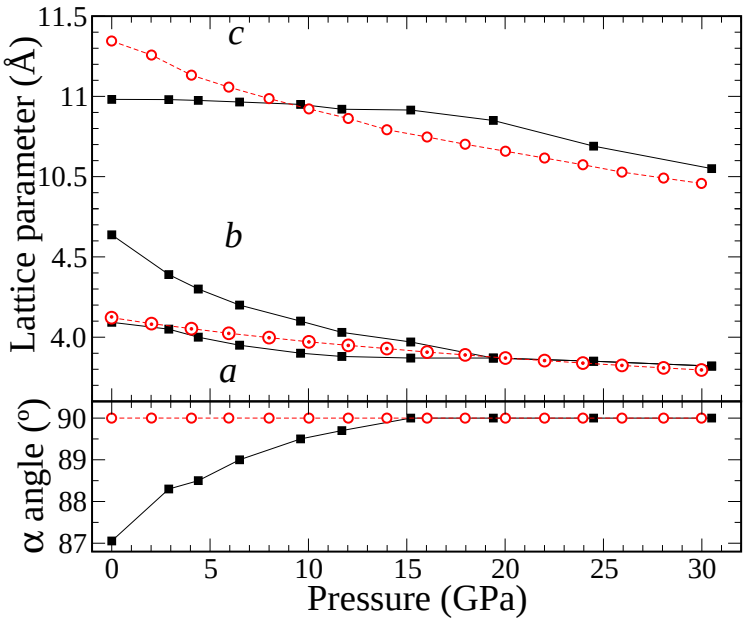

Figure 6.4: Pressure evolution of the structural parameters of monoclinic - tetragonal InSe. Squares are experimental data, circles are theoretical calculations.

were changed to reach a target pressure. The initial experimental cell parameters were those reported in Ref. [105], i.e., $\boldsymbol{a}$=4.088 Å, $\boldsymbol{b}$=4.655 Å $\boldsymbol{c}$=10.981 and α = 86.85° and the internal positions were taken from the Ref. [146] (see the Table 6.1).

The results for the $\boldsymbol{a}$, $\boldsymbol{b}$, $\boldsymbol{c}$ and α parameters, together with the experimental ones, are plotted in Fig. 6.4.[1] Concerning the experimental parameters we can see that the $\boldsymbol{c}$ parameter is reduced by less than 1% in the range between 0 and 15.2 GPa, while $\boldsymbol{a}$ and $\boldsymbol{b}$ are reduced by 6% and 14%, respectively. Moreover, the change in lattice parameter along the $\boldsymbol{c}$ axis varies almost linearly with pressure, whereas the other two axes exhibit a non-linear dependence on pressure. At 19 GPa both parameters $\boldsymbol{a}$ and $\boldsymbol{b}$ reach the same value. On the other hand, it can be also seen that the monoclinic angle α gradually increases upon compression from its value at 0 GPa, 86.85°, to 90° around 15.2 GPa. From 19 GPa $\boldsymbol{a}$ and $\boldsymbol{c}$ follow a linear behavior. The smaller compressibility rate of $\boldsymbol{c}$ with respect to $\boldsymbol{a}$ and $\boldsymbol{b}$ below 19 GPa can be understood if we note that the In-In bonds, which are stronger than the In-Se bonds, are nearly parallel to the $\boldsymbol{c}$ axis (at 0 GPa the In-In bond is tilted by $\sim$ 25° from the $\boldsymbol{c}$ axis, see Fig. 6.2). On the other hand, the $\boldsymbol{b}$ axis is almost oriented along the interlayer direction, and therefore it suffers a large change under

[1]The x-ray diffraction patterns up to 15.2 GPa were fitted with the POWDER CELL program [148] considering the monoclinic InSe-II structure. The unit cell parameters at high pressure were extracted by a Le Bail analysis [149].

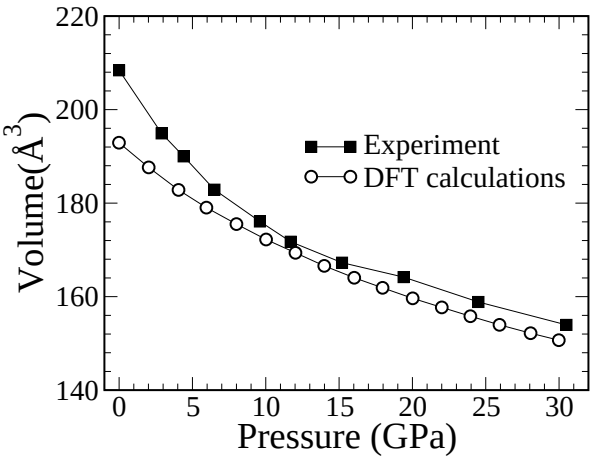

Figure 6.5: Pressure dependence of the volume of monoclinic - tetragonal InSe. Squares are experimental data, empty circles are theoretical calculations.

pressure.

In contrast, the fully optimized cell suffers a spontaneous transformation from the monoclinic cell to a more symmetric cell at low pressures. In fact our calculated $\boldsymbol{a}$ and $\boldsymbol{b}$ parameters are practically equal even at 0 GPa while α is $\sim 90°$. Thus, in our calculations the more stable phase at 0 GPa is a tetragonal one. The calculated $\boldsymbol{c}$ parameter is larger than the experimental one at 0 GPa, and it follows, as it does $\boldsymbol{a}$, a linear compression with pressure. Near 19 GPa the calculated and the experimental $\boldsymbol{a}$ parameters are in close agreement. The calculated pressure coefficient for P>19 GPa of the $\boldsymbol{a}$ and $\boldsymbol{c}$ lattice parameters are -0.0075 Å/GPa and -0.02 Å/GPa respectively, while the experimental ones are -0.0045 Å/GPa and -0.027 Å/GPa respectively. Above 19 GPa both calculated lattice parameters are smaller than the experimental ones, something which can be explained in terms of the underestimation on the bonding distances in LDA. The pressure dependence of the volume of the monoclinic and tetragonal InSe is shown in Fig. 6.5. Above 19 GPa both the calculated and the experimental volumes exhibit the same linear behavior with pressure.

Let us now consider the internal structure of the tetragonal phase as obtained from the full optimization. In Fig. 6.6 we present a schematic view of its crystalline structure. The first observation is that this structure is not a layered structure anymore and therefore it does not have a vdW gap. Each In atom is bonded to another In atom, as in InSe-II, but each In atom is now bonded also to five Se atoms, four of them are in the same plane while the fifth Se atom is in the adjacent plane. Consequently, every In atom exhibits an octahedral environment with five Se and one In atoms. We can describe this structure as made by layers of the rock-salt structure linked by the In-In bonds. From our analysis this structure belongs to

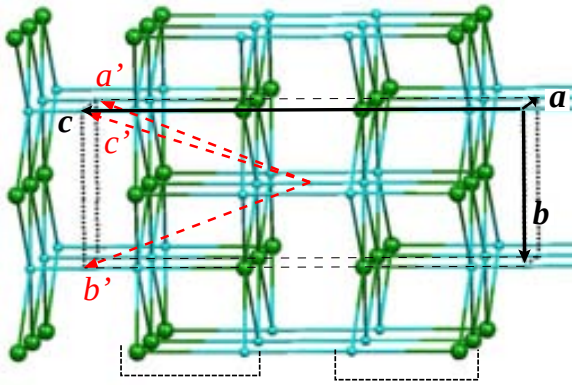

Figure 6.6: Perspective view of crystalline structure of tetragonal InSe. Indium and selenium atoms are cyan and green balls respectively.

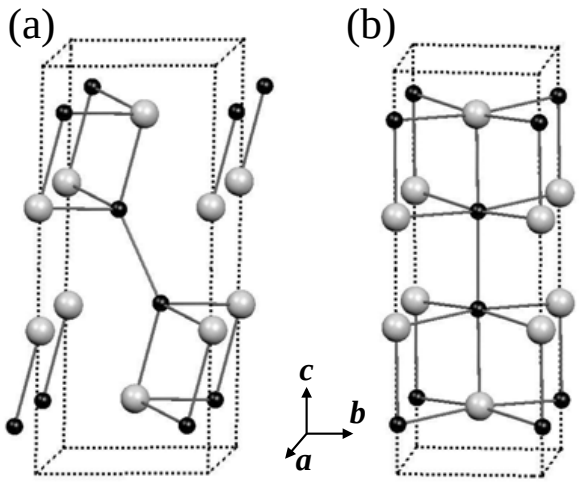

Figure 6.7: Schematic view of the crystal structure of (a) monoclinic InSe and (b) tetragonal InSe. In atoms (black), Se atoms (grey). The first neighbors interatomic bonds are shown.

the space group *I4/mmm* with the independent In [Se] described by the Wyckoff positions 4e (0.0,0.0,0.122002) [4e (0.0,0.0,0.36595]. In fact this structure, which is the calomel one, has been reported before for indium sulphide (InS) [150]. At ambient conditions, InS has a orthorhombic cell and its crystal structure is not layered [103] although it is structurally related with monoclinic InSe. At 13 GPa and in the 293-573°K temperature range, Kabalkine *et al.* [150] observed a reversible phase transition to a tetragonal phase with calomel type structure and space group *I4/mmm*. However, they did not report the positions of the independent atoms.

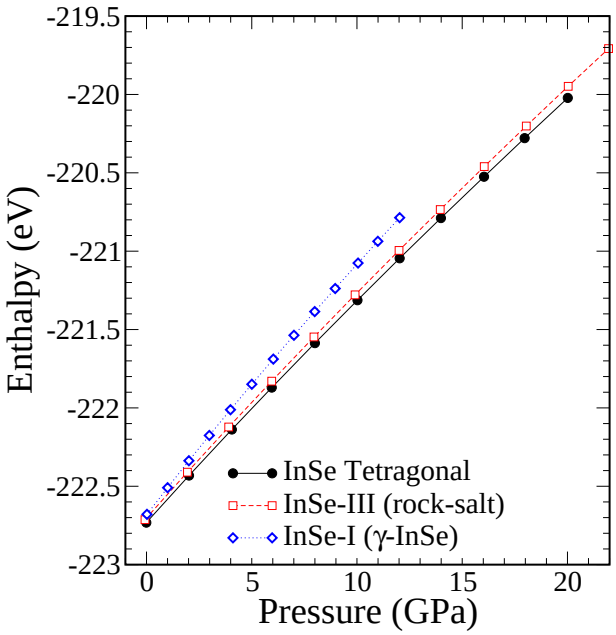

Figure 6.8: Pressure dependence of the calculated enthalpy for the InSe-I, InSe-III and InSe-II→InSe-tetragonal transition.

Although the previous description of the monoclinic and tetragonal InSe phases may suggest that they are structurally very different, this is not the case. In fact, InSe monoclinic is very well 'prepared' to led to InSe tetragonal as schematically shown in Fig. 6.7. It can be seen that tetragonal InSe is a symmetrized and compressed version of the monoclinic InSe obtained basically by a displacement of the In atoms. In the monoclinic InSe each In atom is bonded to three Se atoms and one In atom. As a result of the pressure application, the angle between the In-In bond and the $\boldsymbol{c}$ axis ($\sim 25°$ in the InSe-II) is reduced so that, at the end, the In-In bond is totally parallel to $\boldsymbol{c}$, each In acquiring the previously mentioned octahedral coordination with five Se atoms and one In atom.

The striking difference between the calculated and the experimental results, i.e the failure of the DFT calculations to obtain the correct phase at low pressure, can be explained in terms of the intrinsic problems of DFT in handling the vdW forces as well as in the second order nature of this transition. Systems with vdW gaps are relatively badly described by DFT with respect to those without them, so that, the layered systems are treated in a unfavorable way with respect to three dimensional ones. In addition, if the transition between them is a second order one, then the transition barrier between both phases may be very small, or even may not exist, i.e., the high pressure phase may be a metastable phase in the same potential well of the low pressure phase or may be the more stable structure. In this

way it can occur that the layered structure is not located by the DFT calculation if there are no constraints in the optimization process, as for example fixing the cell volume. We plot in Fig. 6.8 the theoretical enthalpy versus pressure for layered γ-InSe (InSe-I), InSe rock-salt phase (InSe-III), and for InSe-tetragonal system. As we pointed out before, γ-InSe has a transition to a rock-salt phase above 10 GPa at ambient temperature. However, the DFT calculated enthalpy for γ-InSe is higher than the rock-salt enthalpy for any pressure, even at 0 GPa, i.e., we also describe relatively badly this layered phase with respect to the 3D rock-salt phase. In spite of this, in our previous calculations for γ-InSe we did not have a transition at 0 GPa because of the high activation barrier between both phases. The limitations in the simulation, e.g., the temperature and cell volume, did not allow to observe the first order transition with pressure application. It is interesting to notice that, according to our calculations, the tetragonal phase is always more stable than the rock-salt one below 20 GPa (see Fig. 6.8). Since both structures are three-dimensional and very similar, DFT should correctly predict the relative stability between them. The greater stability of the tetragonal phase can be reasonably attributed to the existence of strong In-In covalent bonds along the $\boldsymbol{c}$ axis, in between the double planes of the rock-salt structure. Experimentally, both phases appear to be stable between 20 and 30 GPa and no transition has been observed between them. Once the rock-salt phase (tetragonal) is attained from rhombohedral (monoclinic) InSe, further heating of the sample does not induce a transition to the tetragonal (rock-salt) phase. This suggests the existence of a very large kinetic barrier between both phases.

Having in mind the above mentioned problems of DFT to correctly describe the relative stability between the low pressure layered and high pressure three-dimensional phase we wondered about the validity of the internal structure identified so far for the high pressure tetragonal cell. In other words, it might be possible that another internal structure exists in the tetragonal cell which can not be determined because of the way in which we carried out the calculations. In order to overcome the problem, the structure of the monoclinic phase at different pressures was calculated by imposing the experimental values of the unit cell parameters and optimizing only the internal atomic coordinates. This atomic optimization of the crystal structure at 0 GPa kept the layered structure of the monoclinic phase. However, the relaxed structure at 5 GPa has already the topology observed before from the full optimization scheme, and finally, at 19.4 GPa it has the same symmetry and internal structure described by the space group *I4/mmm*.

In a further step to fully characterize the high pressure phase, our structure was used to reconsider the experimental high pressure diffraction pattern. In Fig. 6.9 we show the fit obtained for the diffraction pattern collected at 19.4 GPa taking as a model our calculated atomic positions for the *I4/mmm* structure. The residual of the structural refinement is also shown in Fig. 6.9. Alternative refinements considering the orthorhombic *Pmcm* and cubic rock-salt type structures gave larger residuals.

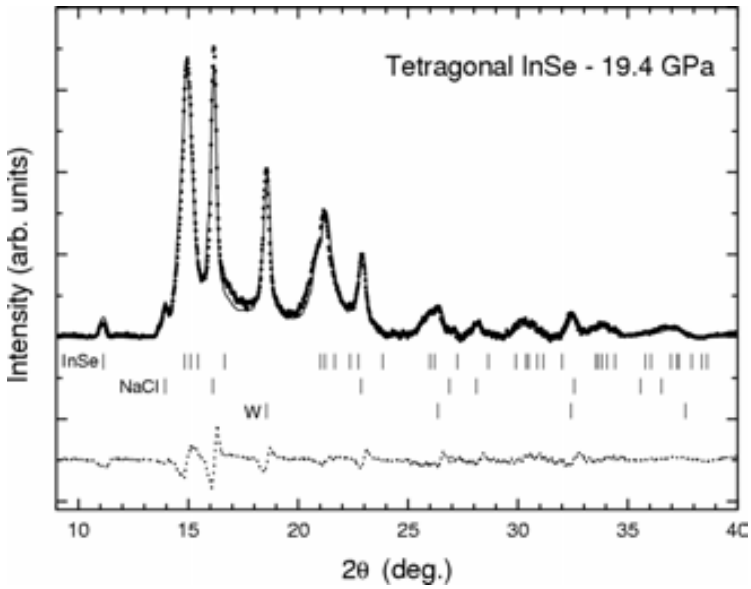

Figure 6.9: Powder diffraction pattern of tetragonal InSe at 19.4 GPa. Solid line: refined model, and dotted line residual. The position of the Bragg reflections of tetragonal InSe, NaCl (pressure-transmitting medium), and W (gasket) are indicated.

Consequently, we conclude that the theoretically proposed *I4/mmm* structure provides the best agreement with the experimental data for this new high pressure structure.

6.5 Electronic Structure of the Tetragonal InSe High Pressure Phase

We discuss now the electronic structure of the tetragonal InSe phase and briefly compare it with that of the monoclinic phase. The calculations were carried out on the basis of the relaxed atomic positions in the cell defined by the experimental lattice parameters in both cases. As mentioned before, the results for the monoclinic InSe calculated on this basis are practically undistinguishable from those in Fig. 6.3 and consequently are not reported again. The calculated band structure for the tetragonal structure at 19.4 GPa is shown in Fig. 6.10. In this diagram the Γ-M line is parallel to the In-In bonds, and therefore is perpendicular to the rock-salt layers. In this band diagram we see that tetragonal InSe does not have a clear semiconductor gap, as the monoclinic InSe does. The close relationship between the Brillouin Zones of the monoclinic and tetragonal structures (see Figs. 6.3(b) and

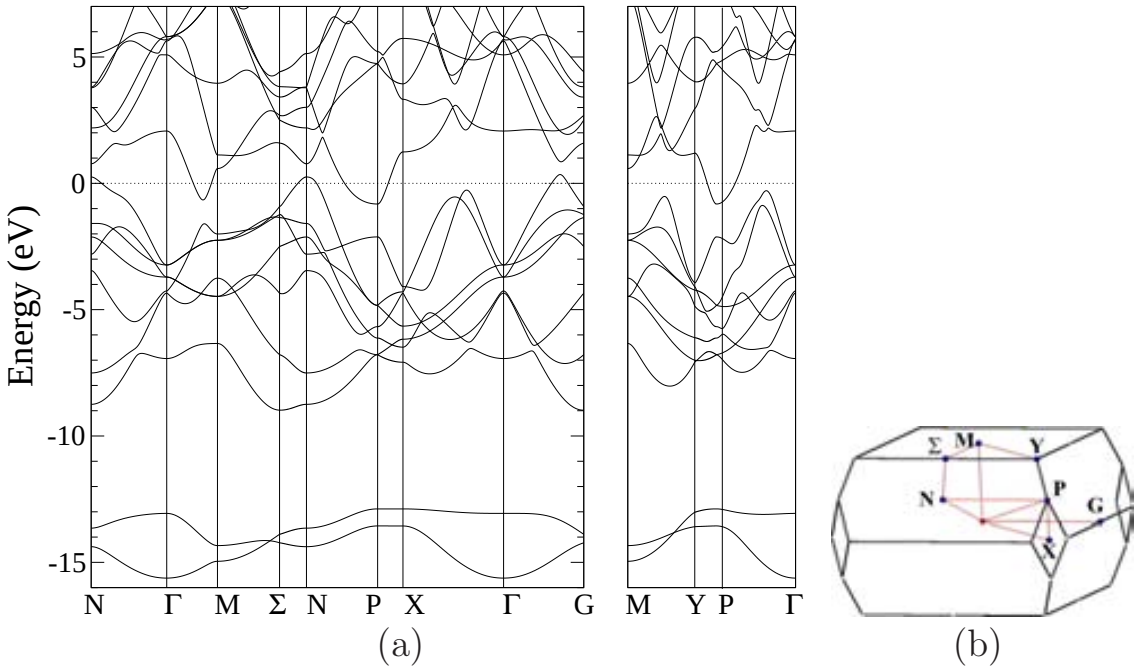

Figure 6.10: (a) Band structure of tetragonal InSe in the experimental cell at 19.4 GPa. The energy origin corresponds to the Fermi level. (b) Brillouin zone for the centered tetragonal cell.

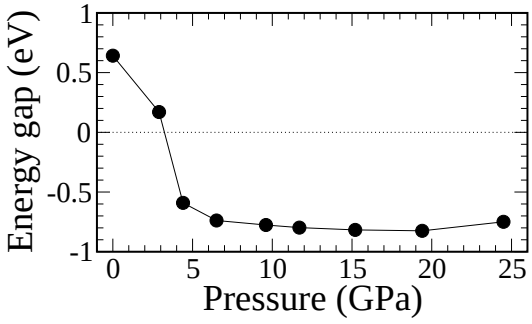

Figure 6.11: Pressure dependence of the calculated energy gap for the optimized atomic coordinates at the experimental cell volume.

6.10(b)) allows a direct comparison of the two band structures. In fact most of the bands in the two systems can be correlated since the general shape is kept for most lines. As expected, the close structural relationship between the two structures is also associated with a clear relationship between the electronic structures. However, the band dispersions are larger in the tetragonal structure as a result of the greater

delocalization inherent with the rock-salt layers. The most remarkable consequence of this feature is that the band gap disappears in the tetragonal phase. At the Fermi level there is a band overlap of the first conduction band with the upper valence band. However, given the DFT band gap underestimation, it is difficult to conclude if the tetragonal InSe is a metal or a low gap semiconductor. As a matter of fact, for monoclinic InSe the underestimation of the bandgap is between 0.7-1.0 eV according to our calculations. This is of the same order as the calculated band overlap in tetragonal InSe so that it is difficult to give a reliable answer to the gap existence. The calculated overlap at different pressures is reported in Fig. 6.11. We see that below 3 GPa there is still a semiconductor gap, however above this pressure the overlapping is almost constant. Let us note that in the cell constrained optimizations on which the results of Fig. 6.11 are based, the structures above 3 GPa correspond to the tetragonal structure whereas those at 3 GPa and lower pressures correspond to the monoclinic structure. Errandonea *et al.* [105] have observed a negative pressure coefficient of the band gap in the monoclinic InSe from measurements up to 10 GPa (below the transition) which seems to be in agreement with the low pressure part of Fig 6.11. The semiconductor or metallic character of the tetragonal phase is consequently an open question.

It is interesting to compare the structure and bonding in the two phases (see Fig. 6.12). Let us remind that all the data discussed in this section correspond to the optimized structures with fixed experimental cell parameters. As mentioned, in the monoclinic phase the In atoms are implicated in three In-Se bonds with distances 2.680, 2.731 and 2.731 Å and one In-In bond of 2.738 Å. In addition, two Se atoms of the nearest layer are at 3.558 Å and these are the two Se atoms which will become bonded to the In atom to complete the octahedral coordination. In the tetrahedral structure, the apical In-Se distance is 2.616 Å, the four basal In-Se distances are 2.740 Å and the In-In distance is 2.642 Å. Thus, in the monoclinic to tetrahedral transformation, the In-In distance shortens, one of the already existing In-Se bonds shortens, two of the already existing In-Se bonds slightly lengthen and two new In-Se bonds are created.

In order to compare the bonding, it is useful to look at the calculated Mulliken overlap populations associated with the different pairs of interacting atoms. Despite its well know shortcomings, these overlap populations provide a useful measure of the strength of a given type of bond in different structures. The calculated overlap populations for In-In and the three In-Se bonds in the monoclinic structure are 0.363, 0.276, 0.276 and 0.307, respectively (see Fig. 6.12). It is very interesting to note that the overlap populations associated with the two Se atoms which will become bonded in the tetragonal structure are positive and far from negligible (0.067 for each of the interactions). This means that the structure is very well prepared, both structurally and electronically, to evolve toward the tetragonal structure and that the interlayer interactions are very strong.

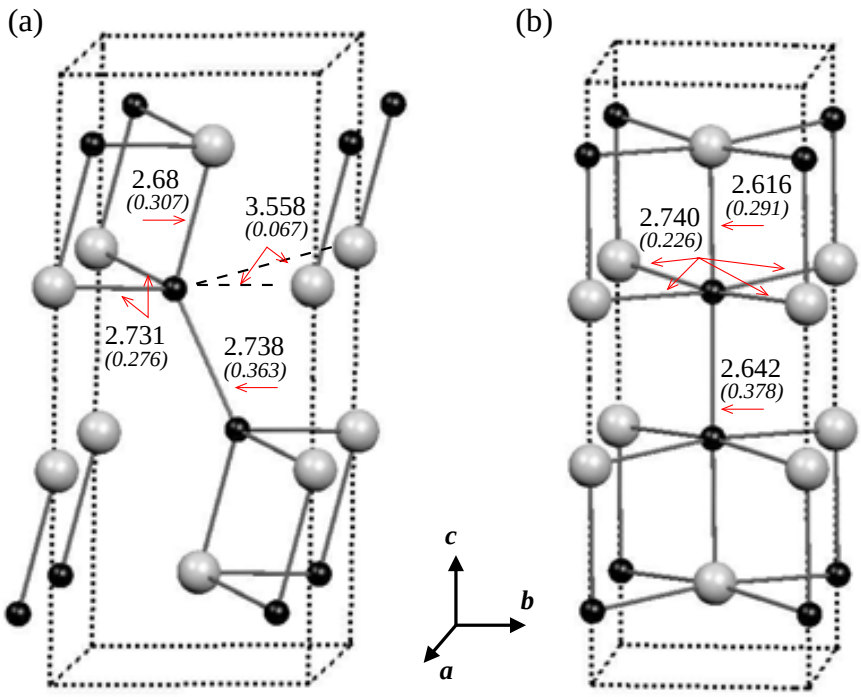

Figure 6.12: First neighbors interatomic distances in Angstroms (and their associated *Mulliken overlap population*) for the optimized structures with fixed experimental cell parameters for (a) monoclinic InSe at 0 GPa and (b) tetragonal InSe at 19.4 GPa. In atoms (black), Se atoms (grey).

In the tetragonal structure, the In-In, apical In-Se and basal In-Se overlap populations are 0.378, 0.291 and 0.226, respectively. In this way, the total overlap population implicating one In atom is 0.993 in the monoclinic structure and 1.195 in the tetragonal structure. Thus, it is clear that along the monoclinic to tetragonal transformation there is a slight reinforcement of the In-In bonds (from 0.363 to 0.378) and a decrease of the strength of the already existing In-Se bonds (from 0.859 to 0.743 per In atom) which is more than compensated by the reinforcement of the In-Se bonding associated with the two new In-Se bonds (from 0.134 to 0.452). The tetrahedral structure is favored in terms of both the covalent bonding and coulombic interactions (the charges are larger and more favorably distributed in this structure). Therefore, we conclude that the stability of the monoclinic structure must be associated with strong favorable interlayer interactions which are underestimated in our calculations.

6.6 Concluding Remarks

Recent experiments have shown that there is a pressure induced second order transition of the layered monoclinic InSe to a tetragonal phase at around 19 GPa. We have carried out full relaxations at different pressures from the initial experimental monoclinic cell and found a spontaneous transition to a tetragonal phase even at 0 GPa. This phase crystallizes in the space group *I4/mmm* and corresponds to the calomel type structure. The disagreement with the experiments concerning the pressure of the transition may be explained in terms of the implicit problem in DFT to describe layered systems with vdW interactions, because whereas the monoclinic structure is layered, the tetragonal structure is three-dimensional. Furthermore this problem is specially important when describing second order transitions between them. When constrained calculations have been carried out in which the experimental cell constants are imposed, the change from the monoclinic to the tetragonal structure occurs between 3 and 4 GPa.

The theoretical study described here has allowed to unravel the nature of the new tetragonal phase of InSe. Both new fits of the diffraction pattern and analysis of the Raman spectra under pressure have been successfully conducted on the basis of the proposed calomel type structure, opening the way to a more in depth physical characterization of this phase.

The *I4/mmm* calomel type structure has also been observed as a high pressure phase of InS. The orthorhombic InS $\rightarrow$ tetragonal InS transition is apparently reversible. This prompts the question about a possible new orthorhombic phase for indium selenite.

Chapter 7

Electronic Structure of Cubic GaS: Metallic versus Insulating Phases

In this chapter we discuss the possible structure of a semiconducting metastable cubic form of gallium sulphide (GaS) experimentally grown either by Chemical Vapor Deposition (CVD) or Molecular Beam epitaxy (MBE). We present a way to understand the experimental results in terms of a hydrogen insertion in the cubic structure.

7.1 Introduction and Motivation

In the course of our investigation on the III-VI semiconductors under pressure, we have found experimental reports from the 1990s about the growth of a metastable and semiconductor face centered cubic (fcc) phase of gallium sulphide (GaS) [151, 152, 153, 154, 155, 156, 157, 158]. The films were grown at atmospheric pressure conditions by chemical vapor deposition or molecular beam epitaxy methods. The characterization of thin films of this material by X-ray photoelectron analysis (XPS), Rutherford backscattering (RBS), and energy-dispersive X-ray (EDX) analysis have shown that its chemical composition is Ga:S (1:1). Initially, this attracted our interest because it is commonly accepted that layered III-VI semiconductors certainly suffer a transition towards a metallic cubic rock-salt (NaCl -type) structure [129, 159, 160, 120], but at pressures higher than 8 GPa. Furthermore, by going in the direction of decreasing pressure, this high-pressure modification becomes amorphous at P=0 GPa [160]. Thus, these III-VI NaCl -type phases are inherently unstable at ambient conditions, as we will also see later from a theoretical point of view.

The first experimental report about this cubic form of GaS was published by the group of Andrew Barron at Rice University [151] in 1992. In that report they posed

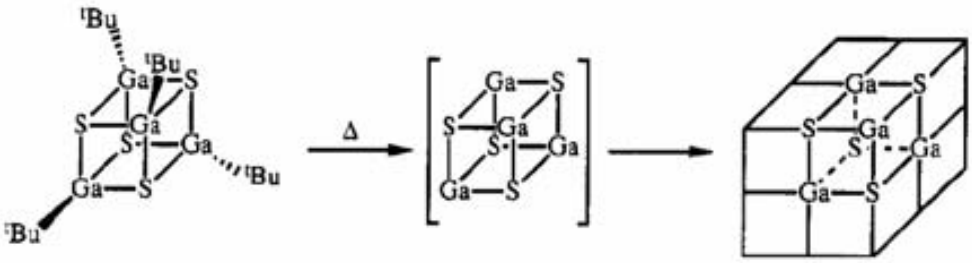

Figure 7.1: Schematic representation of the structural relationship between the precursor and the cubic GaS phase, from [151].

this question: *Does the molecular structure of the precursor* (in a CVD process) *control the crystal structure of a solid state product?*. Their answer was positive, giving as proof their experience using the single precursor tertiary-butyl-galliumsulfide cubane $[(\text{t-Bu})\text{GaS}]_4$.

The general process, hypothesized by Barron, for the formation of cubic gallium sulfide thin films by a metal-organic chemical vapor deposition (MOCVD) at 400°C, is schematized in Fig. 7.1. The core of the precursor molecule is a pseudo-cubic unit[1] of Ga_4S_4, where each gallium carries a tert-butyl group. They confirmed that this core remains intact under the typical conditions employed for vapor transport during the MOCVD. The main idea of Barron´s hyphotesis is that the bare $[GaS]_4$ clusters, after losing the tert-butyl groups, are the assembling blocks of the deposited thin film. These distorted core units relax in the deposited film and rearrange to a cubic lattice at the grown temperature of 380-420°C. From the analysis of the electron diffraction pattern, the authors attributed a rock-salt (NaCl -type) structure to their films, with a lattice parameter $\boldsymbol{a}$=5.37 Å, see Table 7.1. In the cases where the deposition temperature was different, the resulting films acquired an amorphous structure. However, in a succeeding paper [153], the same authors assigned the zinc-blende structure to their fcc GaS films, based on the relative intensity of 111 and 002 x-ray diffraction peaks (Table 7.1). They stated that, although the core of the precursor is retained during the deposition and the films may initially grow as shown in scheme 7.1, there is a NaCl to zinc-blende transformation on the surface of the growing film. The lattice parameter of this zinc-blende phase is increased from 5.4 to 5.5 Å by thermal annealing of the deposited film at 450°C. It is interesting to point out that the authors showed that the so called cubic GaS could be grown on a variety of substrates, including GaAs, borosilicate glass, Si, KBr an Mo.

Independently of what is the internal structure in the cubic phase, the authors reported the semiconductor character of the film grown under these conditions (see

[1]By electron diffraction in gas phase this core was found to be distorted from a regular cubic geometry; the Ga-S-Ga angle is decreased to 82.3° and the S-Ga-S angle is increased to 97.3°[157].

	Ref. [151]	Ref. [152]	Ref. [153]	Ref. [158]
Structure	RS	RS/GaAs	ZB/KBr	ZB/GaAs
$\boldsymbol{a}$(Å)	5.37	5.63	5.4-5.5	5.33
d_{111}(Å)	3.11		3.11-3.19	3.08
d_{002}(Å)	2.70	2.803	2.70-2.79	2.67
d_{022}(Å)	1.83		1.83-1.88	1.88
d_{113}(Å)	1.64		1.64-1.68	
d_{222}(Å)	1.56		1.56-1.59	
d_{004}(Å)	1.37	1.409	1.37-1.40	

Table 7.1: Experimental lattice parameter $\boldsymbol{a}$(Å) and d_{hkl} spacings (Å) reported in literature for cubic gallium sulfide thin films. RS (rock-salt), ZB (zinc-blende), GaAS (gallium arsenide substrate) and KBr (potassium bromide substrate).

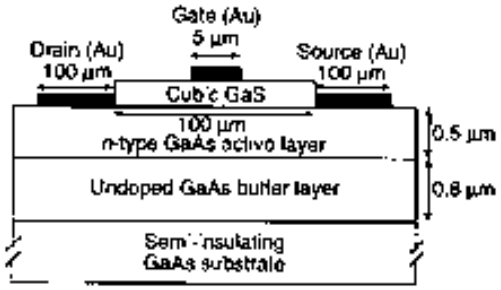

Figure 7.2: Schematic diagram of a GaS-GaAs field-effect transistor, from [155].

for example Ref. [152, 154]). Their films exhibit a large band gap (> 3.5 eV), which is basically independent of the substrate in which they were grown. This property and its lattice parameter, which nearly matches that of GaAs, have allowed its use in the passivation of the surface states of GaAs. In fact, they successfully realized a GaS/GaAs field-effect transistor (FET), Fig. 7.2. The cubic GaS film plays the role of an insulating sulfide hetero-junction in the resulting metal-insulator-semiconductor field effect transistor (MISFET) device [155]. Despite this, the critical temperature at which GaS has to be grown (380-400°C) is higher than would be desirable for some of the fabrication steps in certain device applications.

In 1999 Okamoto and Tanaka [158], working independently and using the same precursor in molecular beam epitaxy experiments, grew cubic GaS films on GaAs at 500°C. From their transmission electron microscope (TEM) analysis, they also proposed the zinc-blende structure for their crystalline structure of the GaS, but with a lattice parameter $\boldsymbol{a}$=5.33 Å, see Table 7.1.

The interest in this cubic phase, and its ability to passivate GaAs surfaces, practi-

Structure	**Crystal packing**	**Lattice parameter (Å)**	**Ga-S (Å)**	**Ga-Ga (Å)**	**Ga-H (Å)**	**S-H (Å)**
β-GaS	Hexagonal	$\boldsymbol{a}$=$\boldsymbol{b}$=3.57, $\boldsymbol{c}$=14.3	2.32	2.434		
Rock-Salt	fcc	5.19	2.595			
Zinc-blende	fcc	5.73	2.481			
Cubane based zinc-blende	fcc	14.328	2.340	2.413		
Rock-Salt with H	fcc	5.35	2.675		2.317	2.317
Zinc-blende with H	fcc	5.47	2.369		2.369	2.735
Simple Cubic $[HGaS]_4$	SC	5.75	2.366, 3.397		1.553	

Table 7.2: Main details of the optimized structures for the different phases studied

cally disappeared as a consequence of the great advances that the silicon technology has experienced in the last years. The reason for this comes basically from GaAs: its poor hole mobility as well as the low heat dissipation capacity makes it unable to compete with silicon based technology.

Nevertheless, from the basic science point of view, it is interesting to understand some aspects of this cubic phase. We must remind that the thermodynamically stable structure of GaS corresponds to a layered phase with D_{6h} hexagonal symmetry [161]. This phase is an indirect semiconductor with a bandgap of 2.5 eV [117]. If we consider that the deposited film adopts a NaCl structure then the lattice parameter proposed for the cubic unit cell, i.e., $\boldsymbol{a}$=5.37 Å, implies an unreasonably large Ga-S bond ($\boldsymbol{a}/2$=2.83 Å) compared with the value of 2.33 Å in the stable hexagonal symmetry. However, this will not be the case for the zinc-blende structure. But most interesting is the analysis of the electronic properties. Based only on elementary band theory considerations, the experimental reports on insulating cubic phases of GaS are puzzling. Cubic GaS with rock-salt or zinc-blende structure must necessarily be a metal as both phases contain a single GaS group per unit cell and, consequently, an odd number of valence electrons. This basic prediction is confirmed by high-pressure experiments on rock-salt polymorphs of InSe and GaSe. Optical and transport measurements under pressure establish without ambiguity the metallic character of rock-salt InSe at pressures above 10 GPa [129, 162] and rock-salt GaSe at pressures above 20 - 25 GPa [136, 120, 163]. One possibility to overcome this constraint is to assume that an increase in the size of the unit cell followed by a structural distortion, as it occurs for instance in a typical Peierls distortion, can lead the system into a non metallic state (see the discussion at the end of Section 7.3.1). However, strictly speaking, this new structure can not be described as a rock-salt or zinc-blende anymore. Additionally, resulting gaps from Peierls distortion usually are much smaller than the observed 3.5 eV. Hence, it is surprising that these unrealistic proposals were not questioned from the beginning. We decided to study different

		valence structure				core correction
H	*Occ*	$1s^1$	$1p^0$			
	r	1.49	1.25			-
S	*Occ*	$3s^1$	$3p^{3.75}$	$3d^{0.25}$	$4f^0$	
	r	1.45	1.45	1.45	1.45	-
Ga	*Occ*	$3d^{10}$	$4s^2$	$4p^1$	$4f^0$	
	r	1.1	2.07	2.29	2.0	0.5

Table 7.3: Specific details for the generation of the pseudopotentials. *Occ*=Occupation, *r*=cutoff radii (Bohr).

cubic polymorphs of GaS by first-principles band structure calculations with the goal of finding an appropriated description of the nature of the semiconducting cubic GaS. All the phases considered along our work are compiled in Table 7.2.

7.2 Computational Details

Our calculations use the exchange-correlation functional of Ceperley-Alder [7] within the local density approximation as parametrised by Perdew and Zunger [6]. We have used a split-valence double-ζ basis set with a single shell of polarization orbitals, as obtained with an energy shift of 0.02 Ry and a split-norm of 15% [16]. The 3d electrons of gallium were treated as valence electrons. The selected value for the mesh cutoff, which defines the grid in real space, was 1000 Ry (which changes slightly with the volume of the unit cell). A regular grid of $18 \times 18 \times 18$ k-points [41] was used to sample the Brillouin zone of β-GaS, the rock-salt and the zinc-blende (with and without hydrogen atoms) structures. For the simple cubic packing of $[HGaS]_4$ cubanes and the cubane-based zinc-blende, grids of $5 \times 5 \times 5$ and $6 \times 6 \times 6$ k points were used, respectively. The atomic configuration, cutoff radii and core corrections of the pseudopotentials for each species, generated according to the Troullier-Martins scheme [23] in the Kleinman-Bylander [25] separable form, are collected in Table 7.3.

7.3 Results and Discussion

Here we report the analysis of the stability and electronic structure of a series of structures which may shed light on the nature of the semiconducting cubic GaS phase. We must point out that both restrictions, the face centered cubic nature of the phase and the small value of the lattice parameter, leave a small number of structures which can be considered. For each of the systems considered we have

calculated both the band structure and density of states at the equilibrium structure.

7.3.1 Rock-salt and Zinc-blende Structures

The rock-salt and zinc-blende structures are shown in Figs. 7.3(b) and 7.4(b). The optimized value of the $\boldsymbol{a}$ lattice parameter for the GaS rock-salt and zinc-blende structures is 5.19 and 5.73 Å leading to Ga-S distances of 2.595 and 2.481 Å, respectively. The rock-salt structure is found to be more stable by 0.745 eV per GaS unit. As expected, the room temperature β-GaS structure is calculated to be more stable than the rock-salt one by 0.219 eV per GaS unit, although this energy difference is probably slightly underestimated because of the well-known problems of DFT in dealing with layered systems where van der Waals forces play a role. In fact, layered GaS is a very stable structure. Recent x-ray diffraction experiments [130] under high pressure show that, apart from a reversible change of the layer sequence [139] occurring at 1.2 GPa, the layered structure is maintained up to 35 GPa. The calculated Ga-S and Ga-Ga bond lengths in β-GaS (2.320 and 2.434 Å, respectively) are in good agreement with the experimental values (2.333 and 2.441 Å, respectively).

The calculated band structures for the rock-salt and zinc-blende structures of GaS are shown in Figs. 7.3(a) and 7.4(a), respectively. The antibonding character of the upper, partially filled, band in both the rock-salt and zinc-blende structures is clear when comparing the calculated overlap populations in these structures with those in the β-GaS or the [(alkylsubstituted)-GaS]$_4$ cubanes. The Mulliken overlap population [164], which may be interpreted as a kind of chemical bond order, is one of the most useful and widely used indicators of the strength of a bond. Although, as in any population analysis, there is some degree of arbitrariness in its own definition, it has been shown to be extremely valuable when comparing the strength of a given type of bond in different structures. The Ga-S overlap populations in the rock-salt (0.200) and zinc-blende (0.257) GaS structures are clearly smaller than those in β-GaS (0.378 for Ga-S and 0.395 for the Ga-Ga overlap population) and the [(Me)-GaS]$_4$ cubane (0.379). Keeping in mind that every atom is involved in six nearest-neighbor interactions in the rock-salt structure but only in four in the zinc-blende one, the improved stability of the rock-salt structure is understandable because the total overlap population per repeat unit is larger (1.200 vs 1.028) in this structural alternative. In addition, the rock-salt structure is also favored from the viewpoint of the Coulomb interactions.

Occupation of antibonding levels in the rock-salt or zinc-blende GaS leads to an inherent instability of the structures. In contrast, the rock-salt and zinc-blende structures are commonly found for systems with one electron less per chemical unit as, for instance, GaP (zinc-blende) or CdO (rock-salt). The instability of the GaS rock-salt or zinc-blende structures may be overcome either through pressure (and

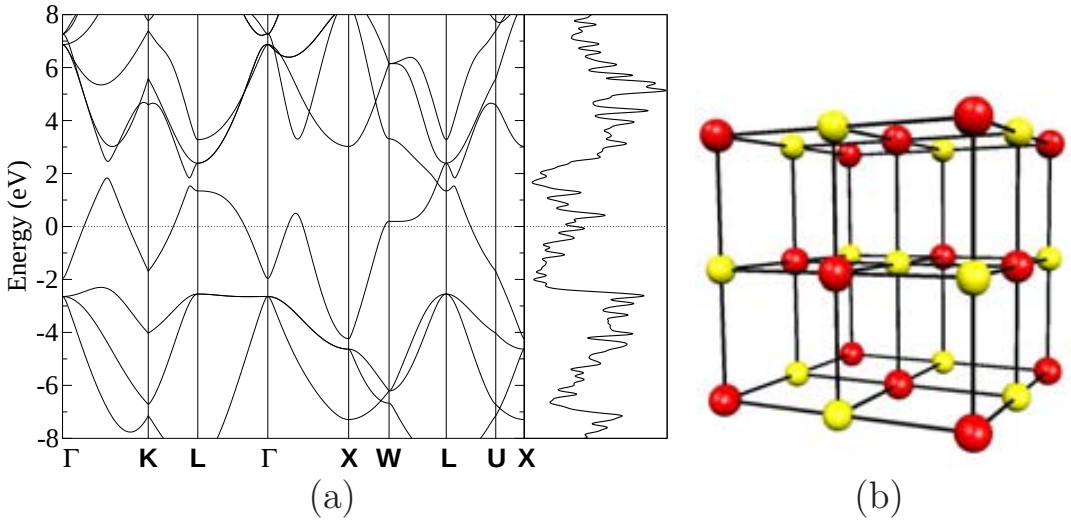

Figure 7.3: Rock-salt GaS: (a) band structure and density of states; (b) structure. Red balls are gallium atoms, yellow balls are sulfur atoms.

then the more stable alternative, i.e., the rock-salt structure, probably could be stabilized) or through partially breaking the structure and relocating these formally antibonding electrons in nonbonding, lone-pair, levels [165]. As a matter of fact this provides a conceptual model to understand the structure of layered GaS. Since there is one electron in excess per GaS unit, formally one bond every two GaS units should be broken. The double layers of β-GaS can be described as resulting from the condensation of two As-type layers derived from the zinc-blende structure in such a way that there are seven bonds (and two lone-pairs) associated with every two GaS units as required by the electron counting.

Note that, in the band structures shown in the Figs. 7.3(a) and 7.4(a), there is a low-lying valence band not shown in these figures. Thus, with nine valence electrons per repeat unit there are four completely filled bands and partially filled bands in both cases. These partially filled bands have a large dispersion and the metallic character of the structures is very clear. Consequently, we conclude that the semiconducting metastable cubic form of GaS reported by several authors cannot adopt the previously proposed rock-salt or zinc-blende structures.

In addition to this calculations, we have also considered distorted cubic structures based on the rock-salt and zinc-blende networks, i.e., using a simple cubic cell with four formula units as the repeat unit, in order to test if some local distortion could open a band gap in these structures, but no stable structure with a band gap was

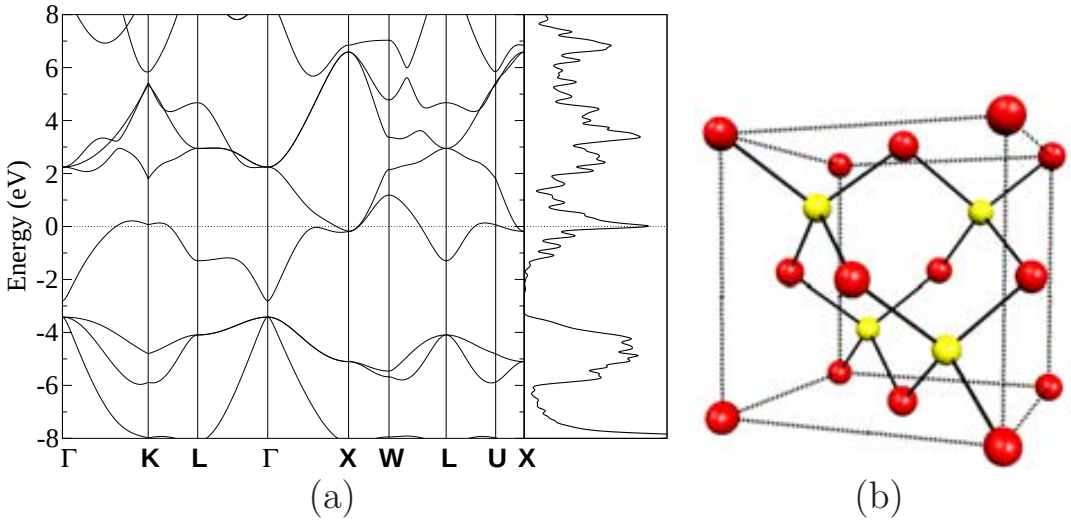

Figure 7.4: Zinc-blende GaS: (a) band structure and density of states; (b) structure. Red balls are gallium atoms, yellow balls are sulfur atoms.

found.

7.3.2 A Zinc-blende Structure based on Cubane

One of the arguments underlying the proposal of a fcc rock-salt structure for cubic GaS by McInnes *et al.* [151] was that the molecular structure of the precursor may control the crystal structure of the solid state product. An interesting possibility arises when trying to build an fcc cubic structure for GaS taking into account this remark and the tetrahedral structure of the $[GaS]_4$ cubane unit from the precursor molecule: that of a zinc-blende network of such cubane units (Fig. 7.5(b)). Although in principle this phase would have a too large $\boldsymbol{a}$ lattice parameter we decided to briefly explore its structural and electronic features. In fact, this structure is interesting in itself, as a new variety of 'host' structure, with a large proportion of open space, like clathrates or zeolites and with possible applications to catalysis, ionic conduction, etc. As shown in the band structure of Fig. 7.5(a), this solid would exhibit a band gap of the same order of magnitude as those reported for the cubic metastable GaS phase. The optimized structure of this material (see Table 7.2) is associated with a cubic cell constant of 14.328 Å as well as Ga-Ga and Ga-S distances of 2.413 Å and 2.340 Å, respectively which are very similar to

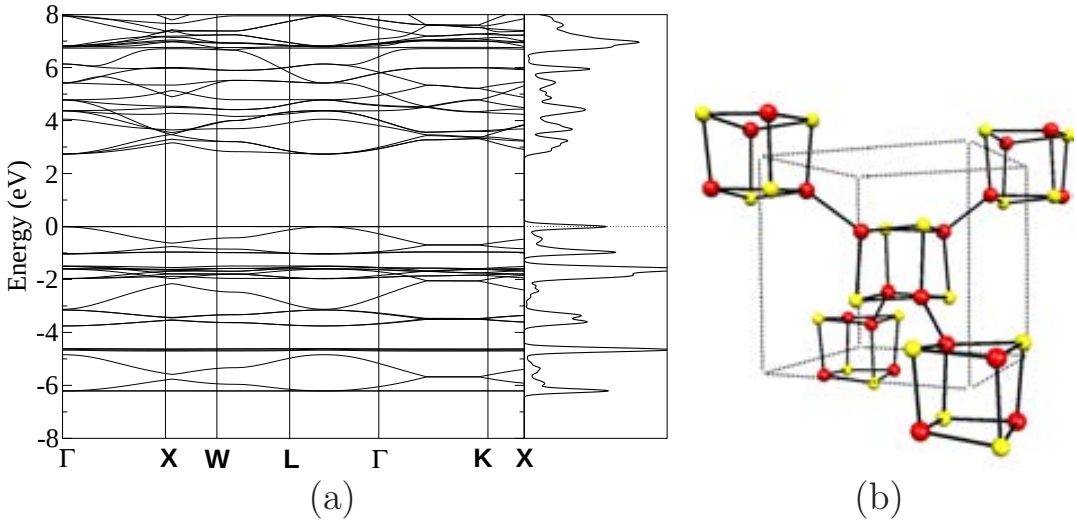

Figure 7.5: Zinc-blende network of $[GaS]_4$ cubane units: (a) band structure and density of states; (b) structure. Red balls are gallium atoms, yellow balls are sulfur atoms.

those calculated for β-GaS. The cubane unit is of course distorted, while keeping the tetrahedral symmetry, with S-Ga-S angles of 96.7° and Ga-S-Ga angles of 83.0°. These values are very similar to those observed in cubanes like $[(t\text{-Bu})GaS]_4$, 97.3° and 82.3°, respectively [157].

When comparing this structure with the layered β-GaS structure, it is noticeable that the number and type of bonds per GaS unit are the same in both structures, i.e. three Ga-S and one-half Ga-Ga bonds. In fact, by using the calculated overlap populations, it is found that the values for the present structure ($3 \times 0.366 + 1/2 \times 0.423 = 1.3095$) and β-GaS ($3 \times 0.378 + 1/2 \times 0.395 = 1.3315$) are quite similar. In spite of this, the calculated energy per GaS unit for this structure is 0.982 eV less stable than that of β-GaS. This preference for the β-GaS can be explained in terms of the slightly stronger Ga-S bonds in the layered structure in comparison with the zinc-blende structure based on cubane. In the latter structure, the relative weakness of the Ga-S bonds, which is the result of the inherent strain in the cubane unit destabilizing the zinc-blende network of cubanes, is partially compensated by somewhat stronger Ga-Ga bonds. However, the main feature destabilizing this structure is its very open character which makes this structural alternative less favorable from the viewpoint of the Coulomb interactions. In addition to the large $\boldsymbol{a}$ value, the calculated diffraction pattern (see Table 7.4) for this structure is too different from those reported for the cubic phase of GaS so that it cannot be taken as a likely possibility for the structural description of this phase. However, it is interesting to point out that stable extended structures based on cubane units

	Experiment				**Theory**					
	Ref. [151]	Ref. [152]	Ref. [153]	Ref. [158]	This work					
Structure	RS	RS/GaAs	ZB/KBr	ZB/GaAs	RS-GaS	ZB-GaS	ZB-$[GaS]_4$	RS-GaSH	ZB-GaSH	SC-$[HGaS]_4$
$\boldsymbol{a}$(Å)	5.37	5.63	5.4-5.5	5.33	5.19	5.73	14.33	5.35	5.47	5.75
d_{111}(Å)	3.11		3.11-3.19	3.08	3.00	3.31	8.27	3.09	3.16	3.32
d_{002}(Å)	2.70	2.803	2.70-2.79	2.67	2.60	2.87	7.17	2.68	2.74	2.88
d_{022}(Å)	1.83		1.83-1.88	1.88	1.83	2.03	5.07	1.89	1.93	2.03
d_{113}(Å)	1.64		1.64-1.68		1.56	1.73	4.32	1.61	1.65	1.73
d_{222}(Å)	1.56		1.56-1.59		1.50	1.65	4.14	1.54	1.58	1.66
d_{004}(Å)	1.37	1.409	1.37-1.40		1.30	1.43	3.58	1.34	1.37	1.44

Table 7.4: Comparison of the experimental structural data reported in literature to those of the structures studied here. RS (rock-salt), ZB (zinc-blende), SC (simple cubic), GaAS (gallium arsenide substrate) and KBr (potassium bromide substrate).

can be envisioned (a cubane-based wurtzite network is another possibility).

7.3.3 Hydrogen-containing Phases

The fcc nature of the structure and the small values of the $\boldsymbol{a}$ lattice parameter found from different authors (5.3-5.7 Å) drastically limit the possible structures for the metastable GaS cubic phase. The previous results show that there is a clear inconsistency between the possibility of rock-salt or zinc-blende structures and the existence of a sizeable band gap. A search for alternative and chemically meaningful structural choices[2] free from such inconsistency leads to structures either with too large lattice parameters or with diffraction patterns in disagreement with the reported ones, as for instance for the cubane-based zinc-blende lattice. Consequently, one is led to the conclusion that some key aspect is still lacking in the present view of the nature of the cubic structure of GaS. At this point it is interesting to remark that the thin layers of this cubic phase are grown in a very hydrogen-rich medium. The diffraction measurements used to characterize the chemical composition (XPS and EDX) of the films can not detect less heavy atoms ($z < 3$ and $z < 11$ respectively), like hydrogen. On the other hand, Rutherford backscattering (RB) technique actu-

[2]For instance, the TlNa cubic structure is made of two interpenetrated diamond fcc latices. However, careful consideration of the structure shows that it is unlikely for GaS. In fact, a structural optimization of GaS starting with a TlNa type structure led to the rock-salt structure.

ally can give an estimation of the hydrogen concentration versus depth at surfaces, within a 5 % accuracy, but only if a specific modification of the setup is done, the so called Hydrogen Forward Scattering analysis (HFS). Thus, the possibility that hydrogen is incorporated into the phase deserves some attention.

We first considered a rock-salt-based HGaS phase containing a hydrogen atom in the center of half of the cubes (occupation of all the centers would lead to a H_2GaS stoichiometry and, consequently, to an odd number of electrons per repeat unit). The calculated $\boldsymbol{a}$ lattice parameter for this fcc structure increases from 5.19 Å in hydrogen-free GaS rock-salt (see Table 7.2) to 5.35 Å. The calculated band structure and density of states are shown in Fig. 7.6. Although the symmetry in this phase is lower with respect to that of the host rock-salt structure, the fifth and sixth bands still overlap (as in Fig. 7.3, here there is also a low-lying valence band not shown in the Figure) and consequently, the metallic character is kept. The calculated overlap populations for the Ga-H and S-H contacts are positive, 0.082 and 0.030, respectively, clearly indicating the existence of bonding interactions even if the distances are relatively long (see Table 7.2). However, the overlap populations for the Ga-S bonds are even smaller (0.181 vs 0.200) than those for the hydrogen-free GaS rock-salt. Together, these two facts clearly show that the hydrogen cannot be formally described as a hydride (as naively could have been expected) thus acquiring the electron residing in the antibonding levels of the parent GaS rock-salt and conferring stability to the structure as well as opening a gap. Although the calculated lattice parameter fits very well with the known experimental data, the calculated metallic character of the system fails to fulfill one of the essential requirements of the structure. Other hydrogen positions than the center of the cubes were also considered with the same result, namely a metallic character of the system.

Our next step was to consider a zinc-blende HGaS phase. The more stable position for a hydrogen atom within the zinc-blende structure (see Fig. 7.7) is found to be at the center of the tetrahedral unit formed by four gallium atoms (and consequently at the center of an octahedron of sulfur atoms). The calculated $\boldsymbol{a}$ lattice parameter for this fcc structure decreases from 5.73 Å in hydrogen-free GaS zinc-blende (see Table 7.2) to 5.47 Å. Consequently, the Ga-S bond length decreases from 2.481 to 2.369 Å so that introduction of hydrogen in this network can be considered as a kind of "chemical pressure". This is in contrast with the situation in the rock-salt alternative where the parent network expands after hydrogen introduction. This structure is calculated to be 0.638 eV per HGaS unit more stable than the previous rock-salt alternative. The Ga-H distance is 2.369 Å, i.e., somewhat larger than in the rock-salt-based structure but the overlap population is nevertheless stronger (0.095). The important observation is that the overlap population of the Ga-S bonds, 0.312, has now considerably increased with respect to that of the parent zinc-blende GaS, 0.257. These two features clearly show the difference with the case of the HGaS rock-salt alternative. When introduced, hydrogen is an active

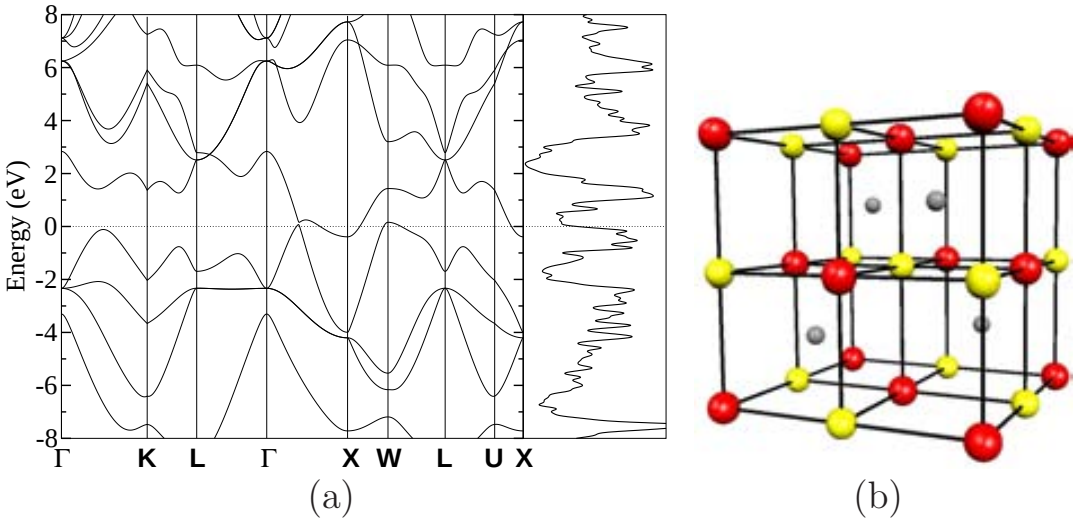

Figure 7.6: Rock-salt based HGaS: (a) band structure and density of states; (b) structure. Red balls are gallium atoms, yellow balls are sulfur atoms.

partner in an extended structure while considerably removing the inherently destabilizing driving force associated with the occupation of antibonding Ga-S states in the parent GaS zinc-blende. In addition, as shown in the band structure reported in Fig. 7.7, there is a band gap of approximately 0.9 eV. This is in good agreement with the experimental information given that DFT usually underestimates the band gap of semiconductors. For instance, whereas the calculated band gap for β-GaS is 0.89 eV the experimental one is 2.5 eV [117]. The origin of this band gap lies in the stabilization of the fifth band of the GaS zinc-blende structure, which crosses the Fermi level (remember that there is a low-lying valence band not shown in the band structures of Figs. 7.4 and 7.7) as a result of the bonding Ga-H interactions developed in HGaS structure and the concomitant decrease of the Ga-S antibonding character of this band, as clearly shown by the above-mentioned overlap populations. Consequently, zinc-blende-based HGaS seems to be a material which fits well with the structural information (i.e., the cubic $\boldsymbol{a}$ lattice parameter and diffraction pattern, see Tables 7.2 and 7.4) as well as with its semiconducting nature. We suggest that this is a likely form for the metastable cubic GaS polymorph, repeatedly reported in the literature since the initial study by McInnes *et al* [151], until now not characterized structurally. In this direction, the sensitivity of the lattice parameter to thermal annealing at relatively low temperature [151, 153, 152] supports our suggestion, as it is expected that the layers will lose some proportion of hydrogen by annealing. As hydrogen stabilizes the zinc-blende structure, hydrogen loss should lead to an increase of the lattice parameter, as actually reported [151, 153, 152].

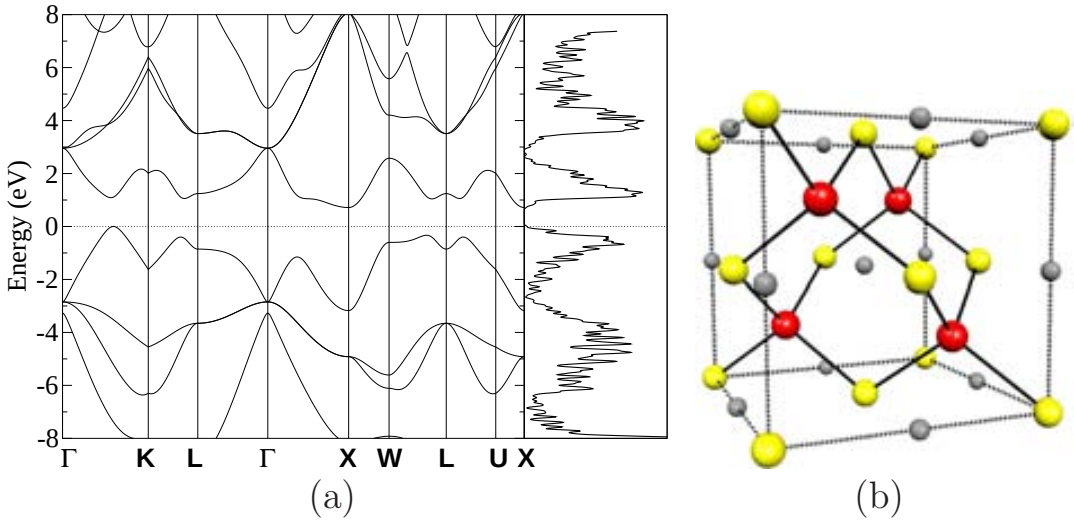

Figure 7.7: Zinc-blende based HGaS: (a) band structure and density of states; (b) structure. Red balls are gallium atoms, yellow balls are sulfur atoms.

Finally, we would like to comment on a very interesting cubic HGaS phase which we have located in the course of this work. Although it has a simple cubic structure and thus does not rank as a likely candidate for the material under consideration, we believe that it is an interesting phase deserving experimental attention. Stimulated by the remark of McInnes *et al.* [151] concerning the possibility of generating solids in which the cubane basic unit was preserved, we noticed that the interesting structure based on a simple cubic packing of $[HGaS]_4$ cubanes shown in Fig. 7.8 was possible. At first sight this structure looks like a molecular solid in which every hydrogen atom of the Ga-H bonds is involved in a hydrogen bonding interaction with the sulfur atom of another cubane. However, a closer look at the structure shows that in trying to establish such hydrogen bonds the cubanes must come quite close together and then all Ga and S atoms of adjacent clusters are involved in relatively short contacts. The result is that, if we disregard the hydrogen atoms, the structure looks as a distorted GaS rock-salt structure in which every atom is involved in three nearly orthogonal series of alternating short and long Ga-S series of bonds. We carried out a structural optimization of this cubic structure and we found that this phase is even considerably more stable (1.019 eV per HGaS unit) than the hydrogen-centered zinc-blende structure. The calculated Ga-H bond length is 1.553 Å which is in very reasonable agreement with typical Ga-H distances in molecular systems [166]. As a matter of fact, the above-mentioned hydrogen bonds implicating the sulfur atoms finally do not play any sizeable role in stabilizing the structure since in the final optimized structure the S-H distances are long, 4.321 Å and the

corresponding overlap populations are nil.

The hydrogen atoms in this structure play a very different role than in the zinc-blende- or rock-salt-based alternatives since here they are implicated in fundamentally localized bonds. However, by creating these localized bonds and making possible the right electron count for the cubane units they also allow the packing of these cubane units in such a way that both from the Coulombic and covalent viewpoints the intercubanes interactions are very favorable. For instance, the intra- and intercubane Ga-S overlap populations are 0.321 and 0.052, respectively. Since there are the same number of inter- and intracluster Ga-S interactions we can say that the total Ga-S overlap population per HGaS unit is 0.373. The Ga-H overlap population is 0.391. These values give a hint of why this structure is so stable. The total Ga-S overlap is considerably larger than found in the HGaS zinc-blende alternative (0.321) and, as a matter of fact, practically identical to that calculated for β-GaS (0.378). This is due to the fact that by creating the localized Ga-H bonds antibonding levels are not occupied at all whereas in zinc-blende HGaS there is still some memory of the occupation of antibonding levels in the parent structure. In addition, the strength of the H-Ga interactions is considerably larger here (one Ga-H bond with overlap population of 0.391 versus two H-Ga interactions per HGaS unit with overlap population of 0.095 in zinc-blende-based HGaS).

The calculated band structure (see Fig. 7.8) exhibits a band gap of approximately 2.5 eV and the calculated $\boldsymbol{a}$ lattice parameter, 5.75 Å, is of the right order of magnitude to fit into the presently available information concerning the cubic GaS phase. However, as expected from the simple cubic nature of the structure, the simulated diffraction pattern of the structure (see Table 7.4) does not agree with the experimental reported ones. Nevertheless, because of its stability, this phase would be an interesting target for future experimental work.

7.4 Concluding Remarks

In this study we have clearly shown that the commonly accepted rock-salt or zinc-blende structure for the metastable semiconducting phase of GaS cannot be correct. According to the present study a likely situation is that the phase should be formulated as HGaS with hydrogen occupying the gallium tetrahedral holes of the zinc-blende structure. It would be necessary to carry out further experimental work to test the presence of hydrogen in this phase, for example, an hydrogen forward scattering (HFS) analysis. This kind of experiments would be very important in order to unravel the nature of this ubiquitous phase. Another interesting possibility is to make an experimental infrared analysis of the film in order to compare with the calculated phonon spectra of the bulk material. In principle, some vibrational modes from the hydrogen can be discerned in the phonon spectra and then its footprint in

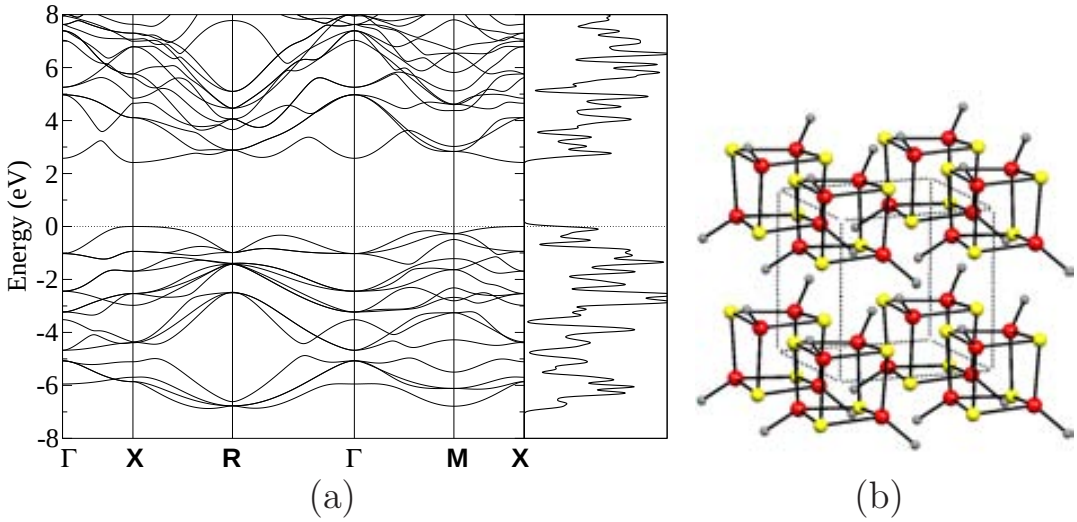

Figure 7.8: Simple Cubic (SC) packing of $[HGaS]_4$ cubanes: (a) band structure and density of states; (b) structure. Red balls are gallium atoms, yellow balls are sulfur atoms.

the infrared spectra may be examined.

Appendix A

Articles and Patents

We list here the articles and patents written and submitted along the development of this doctoral thesis.

A.1 Articles and Proceedings

A.1.1 Directly related with the Present Thesis

- D. Errandonea, D. Martínez-García, A. Segura, J. Haines, E. Machado-Charry, E. Canadell, J.C. Chervin and A. Chevy. *X-ray diffraction, Raman spectroscopy, and theoretical studies of the high-pressure structure and phase transitions in monoclinic InSe.* In preparation.

- E. Machado, M. Kaczmarski, B. Braida, P. Ordejón, D. Garg, J. Norman and H. Cheng. *Interaction of copper organometallic precursors with barrier layers of Ti, Ta and W and their nitrides: a first-principles molecular dynamics study.* Journal of Molecular Modeling **13**, 861,(2007)

- E. Machado-Charry, E. Canadell, and A. Segura. *First-principles study of the electronic structure of cubic GaS : Metallic versus insulating polymorphs.* Physical Review B **75**, 045206 (2007).

- J. Pellicer-Porres, E. Machado-Charry, A. Segura, S. Gilliland, E. Canadell, P. Ordejón, A. Polian, P. Munsch, A. Chevy and N. Guignot. *GaS and InSe equations of state from single crystal diffraction* Physica Status Solidi B-Basic Solid State Physics **244**, 169, (2007).

- E. Machado-Charry, P. Ordejón, E. Canadell, C. Brun and Z. Z. Wang. *Analysis of scanning tunneling microscopy images of the charge-density-wave phase in quasi-one-dimensional* $Rb_{0.3}MoO_3$. Physical Review B **74**, 155123 (2006).

- C. Brun, E. Machado-Charry, P. Ordejón, E. Canadell and Z. Z. Wang. *Inhomogenities of the CDW vector at the (-201) surface of Quasi-1D blue bronze* $Rb_{0.3}MoO_3$. Journal of Physics: Conference Series **61**, 140 (2006).
- M. Cobian, E. Machado, M. Kaczmarski, B. Braida, P. Ordejon, D. Garg, J. Norman and H. Cheng. *Simulation of the Growth of Copper Films for Micro and Nano-Electronics.* Advances in Science and Technology **51**, 167, (2006).
- D. Errandonea, A. Segura, F.j. Manjón, A. Chevy, E. Machado, G. Tobias, P. Ordejón, and E. Canadell. *Crystal symmetry and pressure effects on the valence band structure of γ-InSe and ϵ-GaSe: Transport measurements and electronic structure calculations.* Physical Review B, **71**, 125206 (2005)
- E. Machado, M. Kaczmarski, P. Ordejón, D. Garg, H. Cheng. *First-principles analyses and predictions on the reactivity of barrier layers of Ta and TaN toward organometallic precursors for deposition of copper films.* Langmuir **21**, 7608 (2005).
- Torrelles X., Rius J., Bikondoa O., Ordejón P., Machado E., Lee T.L., Zegenhagen J. *The Structure of Ge(111):C_{60}-($13^{1/2} \times 13^{1/2}$).* ESRF Newsletter **39**, 17-18 (2004)

A.1.2 Not directly related with this Work

- C. Brun, Z. Z. Wang, P. Monceau, E. Machado-Charry and E. Canadell. *Charge density waves modulation in different chains of $NbSe_3$: STM experiments and theoretical intepretation.* In preparation.
- J.L. Mozos, E. Machado, E. Hernández and Pablo Ordejón. *Nanotubes and nanowires: the effect of impurities and defects on their electronic properties.* International Journal of Nanotechnology **2**, 114 (2005).

A.2 Patents

In association with Air Products And Chemicals, INC.

- Title: US20040219369A1: Diffusion barrier layers and methods comprising same for depositing metal films by CVD or ALD processes Priority Number: 2003-05-02 US2003000428447
- Title: US20040234704A1: Diffusion barrier layers and methods comprising for depositing metal films by CVD or ALD processes Priority Number: 2004-04-09 US2004000820864

List of Tables

2.1 Pseudopotentials configurations. *Occ*=Occupation, r=cutoff radii (Bohr). 17

2.2 Adsorption energies (in eV) for a Cu atom on different sites of the Ta(001) and TaN(111) surfaces 25

3.1 Specific details for the generation of the pseudopotentials. *Occ*=Occupation, r=cutoff radii (Bohr). 38

3.2 Eigenvalues of the Kohn-Sham equations evaluated at the theoretical equilibrium lattice constant. Experimental values taken from [73, 74, 75]. The eigenvalue at point ($\Gamma_{25'}$) is the energy origin. 39

3.3 Relative energies between *models I* and *models II* with the same number of atoms. The energy of *models I* was taken as a reference, in each case. 43

3.4 Relative energies between *models I* taking into account the Ge chemical potential. 43

4.1 Specific details for the generation of the pseudopotentials. *Occ*=Occupation, r=cutoff radii (Bohr). 62

5.1 Operations defining the different polytypes. The obvious translation operation parallel to the axis of rotation is not included. 79

5.2 Details of the pseudopotentials generation. *Occ*=Occupation, r=cutoff radii (Bohr). 80

5.3 Parameters of the Murnaghan equation of state for the volume of γ-InSe. 86

6.1 Atomic Wyckoff positions for InSe-II in the space group P2/m(C_{2h}^1) [146]. 112

7.1 Experimental lattice parameter $\boldsymbol{a}$(Å) and d_{hkl} spacings (Å) reported in literature for cubic gallium sulfide thin films. RS (rock-salt), ZB (zinc-blende), GaAS (gallium arsenide substrate) and KBr (potassium bromide substrate). 127
7.2 Main details of the optimized structures for the different phases studied 128
7.3 Specific details for the generation of the pseudopotentials. *Occ*=Occupation, r=cutoff radii (Bohr). 129
7.4 Comparison of the experimental structural data reported in literature to those of the structures studied here. RS (rock-salt), ZB (zinc-blende), SC (simple cubic), GaAS (gallium arsenide substrate) and KBr (potassium bromide substrate). 134

List of Figures

2.1 Disproportionation reaction 15
2.2 Relaxed structures of Cu(hfac)(tvms), $Cu(hfac)_2$, and (tvms) in left, center, and right panels, respectively. In the image the H, C, O, F, Si and Cu atoms are shown as white, brown, red, gray, cyan and yellow balls, respectively 20
2.3 View of the initial (left) and final (right) structures for two simulations (up and down) of the $\cdot CF_3$ decomposition on a Ta (001) surface. . . . 21
2.4 View of the initial (left) and final (right) structure for two simulations (up and down) of the adsorption of N_2 on a Ta(001) surface. 22
2.5 View of the initial (left) and final (right) structure for two simulations (up and down) of the adsorption of $\cdot CF_3$ on a TaN(001) surface. . . . 23
2.6 View of the initial (left) and final (right) structure for two simulations (up and down) of the adsorption of N_2 on a TaN(001) surface. 24
2.7 View of the final structures for two simulations of the adsorption of $\cdot CF_3$ on a TaN(111) surface. 25
2.8 Snapshots of four configurations during a MD simulation on the decomposition of Cu(hfac)(tmvs) on a Ta (001) surface. 27
2.9 Snapshots of four configurations during a MD simulation on the deposition of Cu(hfac)(tmvs) on a TaN (111) surface. 28
2.10 Configuration at 1 ps from MD simulations of the interaction of: (a) Cu(hfac)(tmvs) with W(001) and (b) Cu(hfac)(tmvs) with a hexagonal-WN(100) 29

3.1 a) Top view of the clean Ge(111)-c(2×8) reconstruction. Shaded circles represent Ge adatoms. b) the $\sqrt{13} \times \sqrt{13}\,R14^\circ$ model from Xu *et al.* [66]. The C_{60} molecules are represented by 10 Å large open circles scaled in proportion to the Ge(111) bilayer, shown in small open and solid circles in descending order. Image taken from Ref. [66]. 35
3.2 Left side: Two bilayers of Ge substrate. Orange spheres indicate the adatom and green first Ge bilayer. Right side: Including the C_{60}. Image designed by X. Torrelles. 36

3.3 Top view of the C_{60} molecule, from each of the symmetry axes. 36
3.4 The two possible C_{60} orientations respect to the surface unit cell. a) *Model I* and b) *model II*. For clarity, only one hemisphere of C_{60} is shown. 37
3.5 a) A constant current STM image of about 10×10 nm^2 of the $\sqrt{13} \times \sqrt{13}\,R14°$ phase, obtained using a sample bias of +1 eV and a constant current of 0.05nA. b) An enlarged image [70, 72] 37
3.6 Energy band structure of germanium calculated at the theoretical equilibrium lattice constant. The energy origin is the uppermost valence band at the point ($\Gamma_{25'}$). 39
3.7 Side view with perspective of a slab model. There are five Ge bilayers (in cyan color), one bottom layer of hydrogen atoms (white spheres), and the C_{60}. We can see the adatom on the top surface binding three germanium atoms just below. 40
3.8 Rotation operation. Full circles: atoms related by a rotation of 120° around a χ 3-fold axis. Open circles are the equivalent ones inside the unit cell. 41
3.9 Symmetry analysis: (a) maximum atom deviation by relaxation step to *models I*. (b) The corresponding to *models II*. 42
3.10 a) Electronic structure of the *model I* with adatom. b) *Model I* without the adatom. The shaded zone indicates the corresponding projected band structure of the germanium in bulk. Right panel, the density of states. Inset: The surface Brillouin zone scheme 44
3.11 Modulus of wave functions around the Fermi level, at the K point of the surface Brillouin zone for the *model I* with adatom. See band diagram 3.10(a). 45
3.12 *Model I* without adatom. a) Last surface state and b) first surface state, below and above the Fermi level, respectively. Images at the K point of the surface Brillouin zone 46
3.13 C_{60}-Ge bond structure for the model with adatom. a) Side view showing three different class of bonds. b) Bottom view of two bilayers and the C_{60}. The blue circles indicate a b bond type. 47
3.14 C_{60}-Ge bond structure for the model without adatom. a) Side view. b) Bottom view of two bilayers and the C_{60}. The blue circles indicate a b bond type. 48
3.15 Charge density difference, $\delta\rho(\boldsymbol{r}) = \rho(\boldsymbol{r}) - \rho_{ions}(\boldsymbol{r})$. The contour graphs are in the range (-0.03, 0.065 e/Å^3), and each line correspond to a step of 0.05 e/Å^3. Dashed red a solid blue lines correspond to a negative a positive values, respectively. a) Germanium bonding in the diamond phase. The size of the square side is 3.97 Å. b) A C_{60} hexagonal ring, square side size 2.9 Å. 49

3.16 Charge density difference contours for *model I*. (a) t_1, (b) t_2 and (c) b bond in Fig. 3.13. The size of the plotted region is 2.9 Å each side. 50

3.17 Charge density difference contours for *model I*-without adatom. a) For the t bond Fig. 3.14. b) For the b bond. The square side size is 2.9 Å 51

3.18 (a) Calculated photoemission spectrum for the *model I* withadatom. (b) Withoutadatom. (c) Experimental Angle Resolved Ultraviolet Photoelectron Spectroscopy (ARUPS) spectrum of the C_{60}/Ge(111) $\sqrt{13}\times\sqrt{13}\,R14^\circ$ surface. The dotted lines correspond to a calculated photoemission spectrum without taking into account the Ge atoms. . 52

3.19 (a)Photoemission spectrum of a film of C_{60} at $h\nu$=21.22 eV from [84]. (b) Electronic energy levels of the C_{60} 53

3.20 a) STM experimental image at -2.0 eV. b) Simulated image in the *Model I* withadatom. c) For the *Model I* withoutadatom. Isovalue 3.2×10^{-4}. 54

3.21 a) STM experimental image at +1 eV. b) Simulated image in the *Model I* withadatom. c) For the *Model I* withoutadatom. Isosurfaces corresponding to the charge density $\rho = 1.5\times10^{-4}$ e/Å^2. 54

3.22 a) STM experimental image at +2.0 eV. b) Simulated image in the *Model I* withadatom. c) For the *Model I* withoutadatom. Isovalue 3.2×10^{-4}. 55

4.1 An idealized surface structure of $Rb_{0.3}MoO_3$ in the $(\bar{2}01)$ plane. The red, blue and green units are in the first MoO_6 sublayer. 59

4.2 Idealized sideview of the room temperature $Rb_{0.3}MoO_3$ structure projected onto the plane perpendicular to the $\boldsymbol{b}$ axis. Each square represents a MoO_6 octahedron with the Mo located at the center of the oxygen octahedron. Closed circles are Rb atoms at the uppermost positions of the surface (labeled 1) and empty circles are Rb atoms 1.2 Å below (labeled 2). The three highest octahedra with respect to the "surface" are the dashed squares indicated by the arrows. Their centers lie at levels 1.8, 2.4 and 3.5 Å below the surface. 59

4.3 The $Mo_{10}O_{30}$ cluster 60

4.4 (a) Bulk bands for $K_{0.3}MoO_3$ showing the Fermi wave vector of each band. (b) The (a'^*, b'^*) plane of the Fermi surface. $\Gamma = (0,0,0)$, $X' = (\frac{a'^*}{2}, 0, 0)$, $Y'=(0, \frac{b'^*}{2}, 0)$, $Z'=(0,0,\frac{c'^*}{2})$ and $Y = (0, \frac{b^*}{2}, 0)$, from [89]. . . 63

4.5 The band structure for (a) bulk $Rb_{0.3}MoO_3$; (b) a slab preserving the bulk stoichiometry at the surface, and (c) a slab with a defect of Rb atoms (one every three) at the surface. In (a) $\Gamma = (0,0,0)$, $X' = (\frac{1}{2},0,0)$ and $Y' = (0,\frac{1}{2},0)$ in units of the $\boldsymbol{a'^*}$, $\boldsymbol{b'^*}$ and $\boldsymbol{c'^*}$ reciprocal lattice vectors [89]. In (b) and (c) $\Gamma = (0,0)$, $X = (\frac{1}{2},0)$, and $Y = (0,\frac{1}{2})$ in units of the corresponding oblique reciprocal lattice vectors. 66

4.6 The $\boldsymbol{b^*}$ component of the surface nesting vector of the $(\bar{2}01)$ surface of rubidium blue bronze versus the density of alkali atoms at the surface. The horizontal axis indicates the number of excess Rb atoms at the surface per unit cell, with the zero corresponding to the stoichiometric Rb composition. The continuous line corresponds to the calculated values. The empty circles refer to the experimental values of $\boldsymbol{q^*}$ probed by STM (See text). 67

4.7 (a) The constant current STM image of about 30×30 nm^2 of an *in situ* cleaved $(\bar{2}01)$ surface of $Rb_{0.3}MoO_3$ in the CDW ground state at 63°K with molecular and CDW resolution. The tunneling conditions are Vbias= +420 mV and $I_t = 110$ pA. (b) A 2D Fourier transform of (a) showing surface lattice spots indicated by vectors $2\boldsymbol{b^*}$ and $\boldsymbol{2(a+2c)^*}$ and CDW superlattice spots around each lattice spot indicated by $\boldsymbol{q_{CDW}}$ short white arrows. In this scanned zone the $\boldsymbol{b^*}$ component of $\boldsymbol{q_{CDW}}$ equals the 0.25 bulk value. (c) The constant current STM image with similar parameters as indicated in (a) but measured on another sample. (d) A 2D Fourier transform of (c) showing the same spots as those appearing in (b) but with the $\boldsymbol{b^*}$ component of $\boldsymbol{q_{CDW}}$ equals 0.30, showing significant clear deviation from the 0.25 bulk value. 69

4.8 (a) The constant current mode topographical image of 6.2×6.2 nm^2 on $(\bar{2}01)$ plane of $Rb_{0.3}MoO_3$ at 63°K (raw data image). The bias voltage applied on the sample is +420 mV and the set-up tunneling current is 110 pA. Molecular lattice and CDW superlattice coexist in the image. The three arrows indicate (from left to right), respectively, the observed type I, II MoO_6 octahedra, and the expected position of the $Mo_{III}O_6$ octahedra. An associated profile along Mo_IO_6 octahedra indicated by the left arrow (from Ref. [88]). (b) The calculated image and associated profile along the Mo_IO_6 octahedra for the modulated phase of $Rb_{0.3}MoO_3$. 70

4.9 The isosurface of the charge density, represented as the gray surface, (side view as in Fig. 4.2) integrated from the Fermi level to 0.5 eV above. All the relevant atoms have been labeled. In the image the Rb, Mo, and O atoms are shown as black, yellow and red balls, respectively. 71

5.1 (a) Idealized sideview of the intralayer structure. (b) Idealized view of one layer in the $(\boldsymbol{a}, \boldsymbol{b})$ plane perpendicular to the stacking direction. The red point indicates the stacking π rotation axis (see text). Green balls are anion atoms (group VI), blue balls are cation atoms (group III) 77

5.2 Stacking scheme of the different polytypes. Magenta balls are anion atoms and white balls are cations atoms. From [126]. 78

5.3 (a) Evolution of the In-Se distance with pressure in the γ-InSe polytype. Blue circles are experimental data from Ref. [132]. Squares: DFT calculations for γ-InSe (black) and rock-salt phase (red). (b) Evolution under pressure of the intralayer, interlayer, In-In, and In-Se distances. The continuous lines are the variations according to the hypothesis of Pellicer *et al.* [132] and the dots are results of the DFT calculations. (c) Calculated values for the two different In-Se intralayer distances as well as the φ_1 and the φ_2 angles defined in (d). (d) View of three successive layers showing that there is no symmetry plane through the midpoint of the In-In bonds. 83

5.4 (a) γ-InSe crystal cell parameters as a function of pressure. Blue circles: Experimental data from Ref. [130, 131]. The black squares are DFT values. (b) VP equation of state. Blue circles are the results of the DFT calculations and the blue continuous line is the fit to a Murnaghan equation of state. The experimental values of Schwarz *et al.* [129], Pellicer *et al.* [130] and the values from the Pellicer *et al.* model [132] are also shown. 85

5.5 Energy band structure of γ-InSe at different pressures. For all the structures the energy origin is the uppermost valence band at the Z point. The Brillouin zone with the high symmetry points is included. 87

5.6 (a) Different band gaps calculated for γ-InSe at different pressures. (b) Calculated pressure dependence of the different indirect energy gaps with respect to the Z direct gap (E_{dg}). (c) Experimental pressure dependence of the direct and indirect gaps in InSe (filled symbols) and $In_{0.88}Ga_{0.12}Se$ (hollow symbols). The direct gap position at the Z point of the BZ is represented by circles, the I_1 indirect edge by rhombohedrons and the I_2 indirect edge is symbolized by triangles. (d) Experimental pressure dependence of the energy separation between the I_1 (squares) and I_2 (triangles) indirect edges with respect to the Z direct gap. Solid lines are the fits of the data to linear equations on pressure taken from Ref. [128]. 88
5.7 (a) Evolution under pressure of the intralayer, interlayer, Ga-Ga, and Se-Ga distances in the γ-GaSe polytype. (b) Calculated values for the two different Ga-Se intralayer distances as well as the φ_1 and the φ_2 angles defined before in Fig. 5.3(d). 91
5.8 a) Theoretical γ-GaSe crystal cell parameters as a function of pressure. b) Theoretical volume as a function of pressure 92
5.9 Energy band structure of γ-GaSe at different pressures. For all the structures the energy origin is the uppermost valence band at the Z point. The Brillouin zone with the high symmetry points is included. 93
5.10 Energy gaps calculated of γ-GaSe at different pressures. 93
5.11 (a) Evolution of the Ga-Se distance with pressure in the ε-GaSe polytype. Blue circles are experimental values [120] (from an EXAFS fit for Ga K edge) and solid line is its Murnaghan fit. Squares are the average Ga-Se distance from DFT calculations. (b) Evolution under pressure of the intralayer, interlayer, Ga-Ga, and Ga-Se distances. The continuous lines are the variations according to the hypothesis of Pellicer *et al.* [120] and the dots are theoretical results. (c) Evolution of the calculated d_{GaSe}, d_{GaGa} and intralayer distances with pressure for layers 1 or 2 defined in scheme (d). (d) Structural scheme for ε-GaSe. The inequivalent layers are labeled as 1 and 2. 95
5.12 (a) ε-GaSe crystal cell parameters as a function of pressure. (b) Volume variation with pressure. The black squares are DFT values. The blue circles are experimental values from Ref. [125]. 96
5.13 Energy band structure of ε-GaSe at different pressures. For all the structures the energy origin is the uppermost valence band at the Γ point. The Brillouin zone with the high symmetry points is included. 97
5.14 Energy gaps calculated for ε-GaSe at different pressures. 98
5.15 Schematic representation of the crystal structure of β-GaS and GaS-II. Green balls are anion atoms (S), blue balls are cations atoms (Ga). 100

5.16 Evolution under pressure of the intralayer, interlayer, Ga-Ga, and S-Ga distances of (a) β-GaS and (b) GaS-II. 101
5.17 Calculated β-GaS and GaS-II (a) crystal cell parameters and (b) volume as a function of pressure. 102
5.18 Energy band structure of β-GaS at different pressures. For all the structures the energy origin is the uppermost valence band at the Γ point. The Brillouin zone with the high symmetry points is included. 102
5.19 Energy band structure of GaS-II at different pressures. For all the structures the energy reference is the uppermost valence band at the Γ point. The Brillouin zone with the high symmetry points is included. 103
5.20 Evolution of the calculated energy gaps of β-GaS (a) and GaS-II (b) with pressure. 103
5.21 Change with pressure of the energy difference of the top of the highest occupied band and next occupied band for the different systems studied. 105

6.1 Pressure-temperature phase diagram of InSe from Ref. [105]. Solid (empty) circles indicate the stability of InSe-II (InSe-I), and gray circles the stability of InSe-III. The solid line indicates the Phase I→Phase II transition line. The dashed lines are postulated phase boundaries. The dashed-dotted line is the melting curve of InSe [142]. The dotted lines connect data points measured in the same sample. Black diamond: InSe-II from Iwasaki *et al.* [144], square: InSe-II from Vezzoli *et al.* [145], up triangles: InSe-II from Ferlat *et al.* [142], down triangle: InSe-II from Errandonea *et al.* [105], and gray diamond: InSe-III from Schwarz *et al.* [129]. The hexagons correspond to the results obtained from the resistivity measurements from Ref. [105]. Empty hexagons: InSe-I, solid hexagons: InSe-II, and crossed hexagons: InSe-IV. 110
6.2 Perspective view of the crystalline structure of InSe-II. Indium and selenium atoms are cyan and green balls, respectively. 111
6.3 (a) Band structure of the non optimized monoclinic InSe-II structure at 0 GPa. The energy origin corresponds to the Fermi level. (b) Brillouin zone of InSe-II. For a reference of the orientation the high symmetry A point is at $\vec{c'}^*/2$ (with $\vec{c'}^* = 2\pi(\vec{a'} \times \vec{b'})/[\vec{a'} \cdot (\vec{b'} \times \vec{c'})]$ (see Fig. 6.2)). 113
6.4 Pressure evolution of the structural parameters of monoclinic - tetragonal InSe. Squares are experimental data, circles are theoretical calculations. 115
6.5 Pressure dependence of the volume of monoclinic - tetragonal InSe. Squares are experimental data, empty circles are theoretical calculations. 116

6.6 Perspective view of crystalline structure of tetragonal InSe. Indium and selenium atoms are cyan and green balls respectively. 117
6.7 Schematic view of the crystal structure of (a) monoclinic InSe and (b) tetragonal InSe. In atoms (black), Se atoms (grey). The first neighbors interatomic bonds are shown. 117
6.8 Pressure dependence of the calculated enthalpy for the InSe-I, InSe-III and InSe-II→InSe-tetragonal transition. 118
6.9 Powder diffraction pattern of tetragonal InSe at 19.4 GPa. Solid line: refined model, and dotted line residual. The position of the Bragg reflections of tetragonal InSe, NaCl (pressure-transmitting medium), and W (gasket) are indicated. 120
6.10 (a) Band structure of tetragonal InSe in the experimental cell at 19.4 GPa. The energy origin corresponds to the Fermi level. (b) Brillouin zone for the centered tetragonal cell. 121
6.11 Pressure dependence of the calculated energy gap for the optimized atomic coordinates at the experimental cell volume. 121
6.12 First neighbors interatomic distances in Angstroms (and their associated *Mulliken overlap population*) for the optimized structures with fixed experimental cell parameters for (a) monoclinic InSe at 0 GPa and (b) tetragonal InSe at 19.4 GPa. In atoms (black), Se atoms (grey). 123

7.1 Schematic representation of the structural relationship between the precursor and the cubic GaS phase, from [151]. 126
7.2 Schematic diagram of a GaS-GaAs field-effect transistor, from [155]. . 127
7.3 Rock-salt GaS: (a) band structure and density of states; (b) structure. Red balls are gallium atoms, yellow balls are sulfur atoms. 131
7.4 Zinc-blende GaS: (a) band structure and density of states; (b) structure. Red balls are gallium atoms, yellow balls are sulfur atoms. . . . 132
7.5 Zinc-blende network of $[GaS]_4$ cubane units: (a) band structure and density of states; (b) structure. Red balls are gallium atoms, yellow balls are sulfur atoms. 133
7.6 Rock-salt based HGaS: (a) band structure and density of states; (b) structure. Red balls are gallium atoms, yellow balls are sulfur atoms. 136
7.7 Zinc-blende based HGaS: (a) band structure and density of states; (b) structure. Red balls are gallium atoms, yellow balls are sulfur atoms. 137
7.8 Simple Cubic (SC) packing of $[HGaS]_4$ cubanes: (a) band structure and density of states; (b) structure. Red balls are gallium atoms, yellow balls are sulfur atoms. 139

Bibliography

[1] R. G. Parr and W. Yang. *Density-Functional Theory of Atoms and Molecules.* Oxford Science Publications, 1989.

[2] Richard M. Martin. *Electronic Structure. Basic Theory and Practical Methods.* Cambridge, 2004.

[3] P. Hohenberg and W. Kohn. Inhomogeneous electron gas. *Phys. Rev.*, 136:B864, 1964.

[4] W. Kohn and L. J. Sham. Self-consistent equations including exchange and correlation effects. *Phys. Rev.*, 140:A1133, 1965.

[5] F Aryasetiawan and O Gunnarsson. The GW method. *Rep. Prog. Phys.*, 61:237, 1998.

[6] J. P. Perdew and A. Zunger. Self-interaction correction to density-functional approximations for many-electron systems. *Phys. Rev. B*, 23:5048, 1981.

[7] D. M. Ceperley and B. J. Alder. Ground-state of the electron-gas by a stochastic method. *Phys. Rev. Lett*, 45:566, 1980.

[8] J. P. Perdew, K. Burke, and M. Ernzerhof. Generalized gradient approximation made simple. *Phys. Rev. Lett.*, 77:3865, 1996.

[9] A. D. Becke. Density-functional thermochemistry .1. the effect of the exchange-only gradient correction. *J Chem. Phys*, 96:2155, 1992.

[10] J. P. Perdew, J. A. Chevary, S. H. Vosko, K. A. Jackson, M. R. Pederson, D. J. Singh, and C. Fiolhais. Atoms, molecules, solids, and surfaces - applications of the generalized gradient approximation for exchange and correlation. *Phys. Rev. B*, 46(11):6671, 1992.

[11] Y. M. Juan and E. Kaxiras. Application of gradient corrections to density-functional theory for atoms and solids. *Phys. Rev. B*, 48:14944, 1993.

[12] Y. M. Juan, E. Kaxiras, and R. G. Gordon. Use of the generalized gradient approximation in pseudopotential calculations of solids. *Phys. Rev. B*, 51:9521, 1995.

[13] J. M. Soler, E. Artacho, J. D. Gale, A. García, J. Junquera, P. Ordejón, and D. Sánchez-Portal. The SIESTA method for ab initio order-N materials simulation. *J. Phys.: Condens. Matter*, 14:2745, 2002.

[14] *www.uam.es/departamentos/ciencias/fismateriac/siesta/.*

[15] P. Ordejón, E. Artacho, and J. M. Soler. Self-consistent order-N density-functional calculations for very large systems. *Phys. Rev. B*, 54:10441, 1996.

[16] E. Artacho, D. Sánchez-Portal, P. Ordejón, A. García, and J. M. Soler. Linear-scaling ab-initio calculations for large and complex systems. *Phys. Status. Solidi. B*, 215:809, 1999.

[17] J. Junquera, Ó. Paz, D. Sánchez-Portal, and E. Artacho. Numerical atomic orbitals for linear-scaling calculations. *Phys. Rev. B*, 64:235111, 2001.

[18] E. Anglada, J. M. Soler, J. Junquera, and E. Artacho. Systematic generation of finite-range atomic basis sets for linear-scaling calculations. *Phys. Rev. B*, 66:205101, 2002.

[19] D. Sánchez-Portal, P. Ordejón, E. Artacho, and J. M. Soler. Density-functional method for very large systems with LCAO basis sets. *Int. J. Quantum Chem.*, 65:453, 1997.

[20] P. Ordejón. Linear scaling ab initio calculations in nanoscale materials with SIESTA. *Phys. Status Solidi B*, 217(335), 2000.

[21] D. Sánchez-Portal, P. Ordejón, and E. Canadell. Computing the properties of materials from first principles with SIESTA. *Struct. Bond.*, 113:103, 2004.

[22] D. R. Hamann, M. Schlüter, and C. Chiang. Norm-conserving pseudopotentials. *Phys. Rev. Lett.*, 43:1494, 1979.

[23] N. Troullier and J. L. Martins. Efficient pseudopotentials for plane-wave calculations. *Phys. Rev. B*, 43:1993, 1991.

[24] S. G. Louie, S. Froyen, and M. L. Cohen. Nonlinear ionic pseudopotentials in spin-density-functional calculations. *Phys. Rev. B*, 26:1738, 1982.

[25] L. Kleinman and D. M. Bylander. Efficacious form for model pseudopotentials. *Phys. Rev. Lett*, 48:1425, 1982.

[26] V. M. Donnelly and M. E. Gross. Copper metalorganic chemical vapor-deposition reactions of hexafluoroacetylacetonate Cu(I) vinyltrimethylsilane and bis (hexafluoroacetylacetonate) Cu(II) adsorbed on titanium nitride. *J. Vac. Sci. Technol. A*, 11:66, 1993.

[27] S. P. Murarka, R. J. Gutmann, A. E. Kaloyeros, and W. A. Lanford. Advanced multilayer metallization schemes with copper as interconnection metal. *Thin Solid Films*, 236:257, 1993.

[28] Y. Arita, N. Awaya, K. Ohno, and M. Sato. CVD copper metallurgy for ULSI interconnections. In *Electron Devices Meeting, 1990. Technical Digest., International*, page 39, San Francisco, CA, 1990. IEEE CNF.

[29] R. C. Weast, editor. *Handbook of Chemistry and Physics*. CRC Press, Boca Raton, Fla, 55 edition, 1975.

[30] J. O. Olowolafe, C. J. Mogab, R. B. Gregory, and M. Kottke. Interdiffusions in Cu/reactive-ion-sputtered TiN, Cu/chemical-vapor-deposited TiN, Cu/TaN, and TaN/Cu/TaN thin-film structures - low-temperature diffusion analyses. *J. Appl. Phys.*, 72:4099, 1992.

[31] A. Satta, G. Beyer, K. Maex, K. Elers, S. Haukka, and A. Vantomme. Properties of TiN thin films deposited by ALCVD as barrier for Cu metallization. *Mater. Res. Soc. Proc.*, 612:D6.5, 2000.

[32] R. U. Claessen, J. T. Welch, P. J. Toscano, K. K. Banger, A. M. Kornilov, E. T. Eisenbraun, and A. E. Kaloyeros. The 2,2,6,6-tetramethyl-2-sila-3,5-heptanedione route to the chemical vapor deposition of copper for gigascale interconnect applications. *Mater. Res. Soc. Proc.*, 612:D6.8, 2000.

[33] B. S. Lim, A. Rahtu, and R. G. Gordon. Atomic layer deposition of transition metals. *Nat. Mater.*, 2:749, 2003.

[34] J.A.T. Norman and B.A. Muratore. Volatile liquid precursors for the chemical vapor deposition of copper. US Patent 5085731, 1992.

[35] C. Cavallotti, V. Gupta, C. Sieber, and K. F. Jensen. Dissociation reactions of Cu-I(hfac)L compounds relevant to the chemical vapor deposition of copper. *Phys. Chem. Chem. Phys.*, 5:2818, 2003.

[36] J. A. T. Norman, B.A. Muratore, PN. Dyer, D.A. Roberts, A.K. Hochberg, and L.H. Dubois. A new metal organic-chemical vapor-deposition process for selective copper metallization. *Mater. Sci. Eng. B-Solid*, 17:87, 1993.

[37] S. Voss, S. Gandikota, L. Y. Chen, R. Tao, D. Cong, A. Duboust, N. Yoshida, and S. Ramaswami. Chemical studies of CVD Cu deposited on Ta and TaN barriers under various process conditions. *Microelectron. Eng.*, 50:501, 2000.

[38] S. Gandikota, S. Voss, R. Tao, A. Duboust, D. Cong, L. Y. Chen, S. Ramaswami, and D. Carl. Adhesion studies of CVD copper metallization. *Microelectron. Eng.*, 50:547, 2000.

[39] S. Nose. A molecular-dynamics method for simulations in the canonical ensemble. *Mol. Phys.*, 52:255, 1984.

[40] S. Nose. A unified formulation of the constant temperature molecular-dynamics methods. *J. Chem. Phys.*, 81:511, 1984.

[41] H. J. Monkhorst and J. D. Pack. Special points for brillouin-zone integrations. *Phys. Rev. B*, 13:5188, 1976.

[42] G. Brauer and K. H. Zapp. Die nitride des tantals. *Z. Anorg. Allg. Chem*, 277:129, 1954.

[43] C. L. Lin, P. S. Chen, and M. C. Chen. Effects of TaN substrate pretreatment by Ar plasma on copper chemical vapor deposition. *J. Electrochem. Soc.*, 149:C237, 2002.

[44] C. L. Lin, P. S. Chen, C. L. Chang, and M. C. Chen. Characteristics of copper films deposited on H-2-plasma-treated TaN substrate by chemical vapor deposition. *J. Vac. Sci. Technol. B*, 20:1947, 2002.

[45] J. Gatterer, G. Dufek, P. Ettmayer, and R. Kieffer. Cubic tantalum mononitride (b1) and its miscibility with isotypic mononitrides and monocarbides of 4A-group and 5A-group metals. *Monatsh. Chem.*, 106:1137, 1975.

[46] G. S. Chen, P. Y. Lee, and S. T. Chen. Phase formation behavior and diffusion barrier property of reactively sputtered tantalum-based thin films used in semiconductor metallization. *Thin Solid Films*, 353:264, 1999.

[47] M. H. Tsai, S. C. Sun, C. E. Tsai, S. H. Chuang, and H. T. Chiu. Comparison of the diffusion barrier properties of chemical-vapor-deposited TaN and sputtered TaN between Cu and Si. *J. Appl. Phys.*, 79:6932, 1996.

[48] A. Titov and W. Moritz. Structure of the clean Ta(100) surface. *Surf. Sci.*, 123:L709, 1982.

[49] N Schoenberg. An X-ray investigation on ternary phases in the Ta-Me-N systems (Me = Ti, Cr, Mn, Fe, Co, Ni). *Acta Chem. Scand.*, 8:213, 1954.

[50] N Schöenberg. Contriburions to the knowledge of the molybdenum-nitrogen and the tungsten-nitrogen systems. *Acta Chem. Scand.*, 8:204, 1954.

[51] H. W. Kroto, J. R. Heath, S. C. Obrien, R. F. Curl, and R. E. Smalley. C_{60} Buckminsterfullerene. *Nature*, 318:162, 1985.

[52] M. J. Rosseinsky, A. P. Ramirez, S. H. Glarum, D. W. Murphy, R. C. Haddon, A. F. Hebard, T. T. M. Palstra, A. R. Kortan, S. M. Zahurak, and A. V. Makhija. Superconductivity at 28 K in Rb_xC_{60}. *Phys. Rev. Lett*, 66:2830, 1991.

[53] Y. Wang. Photoconductivity of fullerene-doped polymers. *Nature*, 356:585, 1992.

[54] M.S. Dresselhaus, G. Dresselhaus, and P.C. Eklund. *Science of Fullerenes and Carbon Nanotubes*. Academic Press, Inc, 1 edition, 1996.

[55] K. M. Kadish and R. S. Rouff, editors. *Fullerenes: Chemistry, Physics, and Technology*. Wiley-Interscience, 1 edition, 2000.

[56] A. J. Maxwell, P. A. Bruhwiler, A. Nilsson, N. Martensson, and P. Rudolf. Photoemission, autoionization, and x-ray-absorption spectroscopy of ultrathin-film C_{60} on Au(110). *Phys. Rev. B*, 49:10717, 1994.

[57] T. Stimpel, M. Schraufstetter, H. Baumgartner, and I. Eisele. STM studies of C_{60} on a Si(111): B surface phase. *Mat. Sci. Eng. B-Solid*, 89:394, 2002.

[58] X. W. Yao, T. G. Ruskell, R. K. Workman, D. Sarid, and D. Chen. Scanning tunneling microscopy and spectroscopy of individual C_{60} molecules on Si(100)-(2×1) surfaces. *Surf. Sci.*, 366:L743, 1996.

[59] D. Chen and D. Sarid. Temperature effects of adsorption of C_{60} molecules on Si(111)-(7×7) surfaces. *Phys. Rev. B*, 49:7612, 1994.

[60] P. Moriarty, M. D. Upward, A. W. Dunn, Y. R. Ma, P. H. Beton, and D. Teehan. C_{60}-terminated si surfaces: Charge transfer, bonding, and chemical passivation. *Phys. Rev. B*, 57:362, 1998.

[61] K. Sakamoto, M. Harada, D. Kondo, A. Kimura, A. Kakizaki, and S. Suto. Bonding state of the C_{60} molecule adsorbed on a Si(111)-(7x7) surface. *Phys. Rev. B*, 58:13951, 1998.

[62] G. Bertoni, C. Cepek, and M. Sancrotti. Temperature-dependent interaction of C_{60} with Ge(111)-c(2×8). *Appl. Surf. Sci.*, 212:52, 2003.

[63] K. R. Wirth and J. Zegenhagen. STM study of the adsorption of single C_{60} molecules on the Ge(111)-c(2×8) surface. *Surf. Sci.*, 351:13, 1996.

[64] A. Goldoni, C. Cepek, M. De Seta, J. Avila, M. C. Asensio, and M. Sancrotii. The electronic structure of the $3\sqrt{3} \times 3\sqrt{3}R30°$-$C_{60}$/Ge(111) system as measured by angle-resolved photoemission. *Surf. Sci.*, 454:514, 2000.

[65] T. Kidd, R. D. Aburano, H. W. Hong, T. Gog, and T. C. Chiang. Structural determination of the C_{60}/Ge(111) interface via x-ray diffraction. *Surf. Sci.*, 397:185, 1998.

[66] H. Xu, D. M. Chen, and W. N. Creager. C_{60}-induced reconstruction of the Ge(111) surface. *Phys. Rev. B*, 50:8454, 1994.

[67] T. Sakurai, X. D. Wang, Q. K. Xue, Y. Hasegawa, T. Hashizume, and H. Shinohara. Scanning tunneling microscopy study of fullerenes. *Prog. Surf. Sci.*, 51:263, 1996.

[68] Y. Z. Li, J. C. Patrin, M. Chander, J. H. Weaver, L. P. F. Chibante, and R. E. Smalley. Ordered overlayers of C_{60} on GaAs(110) studied with scanning tunneling microscopy. *Science*, 252:547, 1991.

[69] N. Takeuchi, A. Selloni, and E. Tosatti. Do we know the true structure of Ge(111)c(2×8). *Phys. Rev. Lett*, 69:648, 1992.

[70] X. Torrelles, J. Rius, O. Bikondoa, P. Ordejón, E. Machado, T.L. Lee, and J. Zegenhagen. The structure of Ge(111):C_{60}-($13^{1/2} \times 13^{1/2}$). *ESRF Newsl.*, 39:17, 2004.

[71] G. Dresselhaus, M. S. Dresselhaus, and P. C. Eklund. Symmetry for lattice modes in C_{60} and alkali-metal-doped C_{60}. *Phys. Rev. B*, 45:6923, 1992.

[72] J. Zegenhagen. Private communication.

[73] M. S. Hybertsen and S. G. Louie. Electron correlation in semiconductors and insulators: Band-gaps and quasi-particle energies. *Phys. Rev. B*, 34:5390, 1986.

[74] R. W. Godby, M. Schluter, and L. J. Sham. Self-energy operators and exchange-correlation potentials in semiconductors. *Phys. Rev. B*, 37:10159, 1988.

[75] F. Gygi and A. Baldereschi. Quasiparticle energies in semiconductors: Self-energy correction to the local-density approximation. *Phys. Rev. Lett*, 62:2160, 1989.

[76] M. C. Payne, M. P. Teter, D. C. Allan, T. A. Arias, and J. D. Joannopoulos. Iterative minimization techniques for abinitio total-energy calculations - molecular-dynamics and conjugate gradients. *Rev. Mod. Phys.*, 64:1045, 1992.

[77] X. Torrelles, J. Rius, C. Miravitlles, and S. Ferrer. Application of the 'direct methods' difference sum function to the solution of reconstructed surfaces. *Surf. Sci.*, 423:338, 1999.

[78] C. Pisani(Ed). *Quantum-Mechanical Ab-initio calculation of the properties of crystalline materials: proceedings of the IV School of Computational Chemistry of the Italian Chemical Society.* Springer, 1994.

[79] L. Colombo, R. Resta, and S. Baroni. Valence-band offsets at strained Si/Ge interfaces. *Phys. Rev. B*, 44:5572, 1991.

[80] C. F. Guerra, J. W. Handgraaf, E. J. Baerends, and F. M. Bickelhaupt. Voronoi deformation density (VDD) charges: Assessment of the Mulliken, Bader, Hirshfeld, Weinhold, and VDD methods for charge analysis. *J. Comput. Chem.*, 25:189, 2004.

[81] L. Pauling. *The Nature of the Chemical Bond.* Cornell Univ., USA, 3rd ed. edition, 1960.

[82] A.C. Thompson and D. Vaughan. X-ray data booklet. Technical report, Center for X-ray Optics, Lawrence Berkeley National Laboratory, January 2001.

[83] Diana Pop. *Photoelectron Spectroscopy on Thin Films of Cu-, Zn-, and Metal-Free Extended Porphyrazines.* PhD thesis, Fachbereich Physik, Freie Universität Berlin, month= February, year= 2003.

[84] M. S. Golden, M. Knupfer, J. Fink, J. F. Armbruster, T. R. Cummins, H. A. Romberg, M. Roth, M. Sing, M. Schmidt, and E. Sohmen. The electronic-structure of fullerenes and fullerene compounds from high-energy spectroscopy. *J. Phys-Condens. Mat.*, 7:8219, 1995.

[85] J. Tersoff and D. R. Hamann. Theory and application for the scanning tunneling microscope. *Phys. Rev. Let*, 50:1998, 1983.

[86] For reviews see *Low Dimensional Electronic Properties of Molybdenum Bronzes and Oxides*, edited by C. Schlenker (Kluwer Publ., Dordrecht, 1989); *Physics and Chemistry of Low Dimensional Inorganic Conductors*, edited by C. Schlenker, J. Dumas, M. Greenblatt, and S. van Smaalen, NATO ASI Series B, Physics: vol **354** (Plenum, New York, 1996); J. Dumas and C. Schlenker, Int. J. Mod. Phys. B. **7**, 4045 (1993).

[87] W. J. Schutte and J. L. De Boer. The incommensurately modulated structures of the blue bronzes $K_{0.3}MoO_3$ and $Rb_{0.3}MoO_3$. *Acta Cryst. B*, 49:579, 1993.

[88] C. Brun, J. C. Girard, Z. Z. Wang, J. Marcus, J. Dumas, and C. Schlenker. Charge-density waves in rubidium blue bronze $Rb_{0.3}MoO_3$ observed by scanning tunneling microscopy. *Phys. Rev. B*, 72:235119, 2005.

[89] J. L. Mozos, P. Ordejón, and E. Canadell. First-principles study of the blue bronze $K_{0.3}MoO_3$. *Phys. Rev. B*, 65:233105, 2002.

[90] J. Graham and A. D. Wadsley. Crystal structure of blue potassium molybdenum bronze $K_{0.28}MoO_3$. *Acta Crystallogr.*, 20:93, 1966.

[91] M. Guedira, J. Chenavas, and M. Marezio. Crystal structure, dimensionality, and $4d$ electron distribuiton in $K_{0.28}MoO_3$ and $Rb_{0.28}MoO_3$. *J. Solid State Chem.*, 57:300, 1985.

[92] U. V. Waghmare, H. Kim, I. J. Park, N. Modine, P. Maragakis, and E. Kaxiras. Hares: an efficient method for first-principles electronic structure calculations of complex systems. *Comput. Phys. Commun*, 137:341, 2001.

[93] G. H. Gweon, J. D. Denlinger, J. W. Allen, R. Claessen, C. G. Olson, H. Höchst, J. Marcus, C. Schlenker, and L. F. Schneemeyer. ARPES line shapes in FL and non-FL quasi-low-dimensional inorganic metals. *J. Electron. Spectrosc.*, 117:481, 2001.

[94] M.-H. Whangbo and L. F. Schneemeyer. Band electronic-structure of the molybdenum blue bronze $A_{0.3}MoO_3$ (A=K,Rb). *Inorg. Chem.*, 25:2424, 1986.

[95] J. P. Pouget, C. Noguera, A. H. Moudden, and J. Moret. Structural study of the charge-density-wave phase-transition of the blue bronze - $K_{0.3}MoO_3$. *J. Phys. (Paris)*, 46:1731, 1985.

[96] G.-H. Gweon, J. W. Allen, R. Claessen, J. A. Clack, D. M. Poirier, P. J. Benning, C. G. Olson, W. P. Ellis, Y-X. Zhang, L. F. Schneemeyer, J. Marcus, and C. Schlenker. Fermi surfaces and single-particle spectral functions of low-dimensional inorganic non-cuprate compounds: The molybdenum bronzes. *J. Phys.: Condens. Matter*, 8:9923, 1996.

[97] J. P. Pouget, S. Kagoshima, S. Schlenker, and C. Marcus. Evidence for a peierls transition in the blue bronzes $K_{0.3}MoO_3$ and $Rb_{0.3}MoO_3$. *J. Phys. Lett.(Paris)*, 44:L113, 1983.

[98] E. Machado-Charry, P. Ordejón, E. Canadell, C. Brun, and Z. Z. Wang. Analysis of scanning tunneling microscopy images of the charge-density-wave phase in quasi-one-dimensional $Rb_{0.28}MoO_3$. *Phys. Rev. B.*, 74:155123, 2006.

[99] K. Breuer, K. E. Smith, M. Greenblatt, and W. McCarroll. Electronic-structure of surface-defects in $K_{0.3}MoO_3$. *J. Vac. Sci. Technol. A*, 12:2196, 1994.

[100] A. V. Fedorov, S. A. Brazovskii, V. N. Muthukumar, P. D. Johnson, J. Xue, L-C. Duda, K. E. Smith, W. H. McCarroll, M. Greenblatt, and S. L. Hulbert. Direct observation of temperature-dependent fermi surface nesting vectors in a quasi-one-dimensional conductor. *J. Phys.: Condens. Matter*, 12:L191, 2000.

[101] X-M. Zhu, R. Moret, H. Zabel, I. K. Robinson, E. Vlieg, and R. M. Fleming. Grazing-incidence x-ray study of the charge-density-wave phase transition in $K_{0.3}MoO_3$. *Phys. Rev. B*, 42:8791, 1990.

[102] U. Walter, R. E. Thomson, B. Burk, M. F. Crommie, A. Zettl, and J. Clarke. Scanning tunneling microscopy of the blue bronzes $(Rb, K)_{0.3}MoO_3$. *Phys. Rev. B*, 45:11474, 1992.

[103] K. Schubert, E. Dorre, and E. Gunzel. Kristallchemische ergebnisse an phasen aus B-elementen. *Naturwissenschaften*, 41:448, 1954.

[104] K. Schubert, E. Dorre, and M. Kluge. Zur kristallchemie der B-metalle .3. kristallstruktur von GaSe und InTe. *Z. Metallkd.*, 46:216, 1955.

[105] D. Errandonea, D. Martínez-García, A. Segura, A. Chevy, G. Tobias, E. Canadell, and P. Ordejón. High-pressure, high-temperature phase diagram of InSe: A comprehensive study of the electronic and structural properties of the monoclinic phase of InSe under high pressure. *Phys. Rev. B*, 73:235202, 2006.

[106] R. S. Putnam and D. G. Lancaster. Continuous-wave laser spectrometer automatically aligned and continuously tuned from 11.8 to 16.1 μm by use of diode-laser-pumped difference-frequency generation in GaSe. *Appl. Opt.*, 38:1513, 1999.

[107] R. A. Kaindl, F. Eickemeyer, M. Woerner, and T. Elsaesser. Broadband phase-matched difference frequency mixing of femtosecond pulses in GaSe: Experiment and theory. *Appl. Phys. Lett.*, 75:1060, 1999.

[108] J. Martínez-Pastor, A. Segura, J. L. Valdés, and A. Chevy. Electrical and photovoltaic properties of indium-tin-oxide/p-InSe/Au solar cells. *J. Appl. Phys.*, 62:1477, 1987.

[109] C. Julien, M. Jouanne, P. A. Burret, and M. Balkanski. Optical studies of the cathode material InSe intercalated with lithium. *Solid State Ionics*, 28-30:1167, 1988.

[110] M. Balkanski, P. Gomes Da Costa, and R. F. Wallis. Electronic energy bands and lattice dynamics of pure and lithium-intercalated InSe. *Phys. Status Solidi B.*, 194:175, 1996.

[111] A. Polian, J. M. Besson, M. Grimsditch, and H. Vogt. Elastic properties of GaS under high-pressure by brillouin-scattering. *Phys. Rev. B*, 25:2767, 1982.

[112] M. Gauthier, A. Polian, J. M. Besson, and A. Chevy. Optical-properties of gallium selenide under high-pressure. *Phys. Rev. B*, 40:3837, 1989.

[113] A. Polian, J. C. Chervin, and J. M. Besson. Phonon modes and stability of GaS up to 200 kilobars. *Phys. Rev. B*, 22:3049, 1980.

[114] N. Kuroda, O. Ueno, and Y. Nishina. Lattice-dynamic and photoelastic properties of GaSe under high-pressures studied by raman-scattering and electronic susceptibility. *Phys. Rev. B*, 35:3860, 1987.

[115] C. Ulrich, M. A. Mroginski, A. R. Goñi, A. Cantarero, U. Schwarz, V. Muñoz, and K. Syassen. Vibrational properties of InSe under pressure: Experiment and theory. *Phys. Status Solidi B*, 198:121, 1996.

[116] J. M. Besson, K. P. Jain, and A. Kuhn. Optical-absorption edge in GaSe under hydrostatic-pressure. *Phys. Rev. Lett.*, 32:936, 1974.

[117] M. Mejatty, A. Segura, R. Letoullec, J. M. Besson, A. Chevy, and H. Fair. Optical-absorption edge of GaS under hydrostatic-pressure. *J. Phys. Chem. Solids*, 39:25, 1978.

[118] N. Kuroda, O. Ueno, and Y. Nishina. Supernonlinear shifts of optical-energy gaps in InSe and GaSe under hydrostatic-pressure. *J. Phys. Soc. Jpn.*, 55:581, 1986.

[119] A. R. Goñi, A. Cantarero, U. Schwarz, K. Syassen, and A. Chevy. Low-temperature exciton absorption in InSe under pressure. *Phys. Rev. B*, 45:4221, 1992.

[120] J. Pellicer-Porres, A. Segura, Ch. Ferrer, V. Muñoz, A. San Miguel, A. Polian, J. P. Itié, M. Gauthier, and S. Pascarelli. High-pressure x-ray-absorption study of GaSe. *Phys. Rev. B*, 65:174103, 2002.

[121] J. F. Dobson and J. Wang. Energy-optimized local exchange-correlation kernel for the electron gas: Application to van der Waals forces. *Phys. Rev. B*, 62:10038, 2000.

[122] M. Dion, H. Rydberg, E. Schroder, D. C. Langreth, and B. I. Lundqvist. Van der Waals density functional for general geometries. *Phys. Rev. Lett*, 92:246401, 2004.

[123] G. Ferlat, H. Xu, V. Timoshevskii, and X. Blase. Ab initio studies of structural and electronic properties of solid indium selenide under pressure. *Phys. Rev. B*, 66:085210, 2002.

[124] D. Olguin, A. Cantarero, C. Ulrich, and K. Syassen. Effect of pressure on structural properties and energy band gaps of γ-InSe. *Phys. Status Solidi B*, 235:456, 2003.

[125] U. Schwarz, D. Olguin, A. Cantarero, M. Hanfland, and K. Syassen. Effect of pressure on the structural properties and electronic band structure of GaSe. *Phys. Status Solidi B*, 244:244, 2007.

[126] J. Pellicer-Porres. *Propiedades ópticas y estructurales de semiconductores III-VI bajo presión*. PhD thesis, Departament de Física Aplicada, Universitat de València, 1999.

[127] J. Rigoult, A. Rimsky, and A. Kuhn. Refinement of the 3R γ-indium monoselenide structure type. *Acta Crystallogr. B*, 36:916, 1980.

[128] F. J. Manjón, D. Errandonea, A. Segura, V. Muñoz, G. Tobias, P. Ordejón, and E. Canadell. Experimental and theoretical study of band structure of InSe and $In_{1-x}Ga_xSe$ under high pressure: Direct to indirect crossovers. *Phys Rev. B*, 63:125330, 2001.

[129] U. Schwarz, A. R Goñi, K. Syassen, A. Cantarero, and A. Chevy. Structural and optical properties of InSe under pressure. *High Press. Res.*, 8:396, 1991.

[130] J. Pellicer-Porres, E. Machado-Charry, A. Segura, S. Gilliland, E. Canadell, P. Ordejón, A. Polian, P. Munsch, A. Chevy, and N. Guignot. GaS and InSe equations of state from single crystal diffraction. *Phys. Status Solidi B*, 244:169, 2006.

[131] J. Pellicer-Porres. γ-InSe equation of state. Private communication, 2007.

[132] J. Pellicer-Porres, A. Segura, V. Muñoz, and A. San Miguel. High-pressure x-ray absorption study of InSe. *Phys. Rev. B*, 60:3757, 1999.

[133] A. Segura, F. J. Manjón, D. Errandonea, J. Pellicer-Porres, V. Muñoz, G. Tobias, P. Ordejón, E. Canadell, A. San Miguel, and D. Sánchez-Portal. Specific features of the electronic structure of III-VI layered semiconductors: recent results on structural and optical measurements under pressure and electronic structure calculations. *Phys. Status Solidi B*, 235:267, 2003.

[134] A. Kuhn, A. Chevy, and R. Chevalier. Crystal-structure and interatomic distances in GaSe. *Phys. Status Solidi A*, 31:469, 1975.

[135] D. Errandonea, A. Segura, F. J. Manjón, A. Chevy, E. Machado, G. Tobias, P. Ordejón, and E. Canadell. Crystal symmetry and pressure effects on the valence band structure of γ-InSe and ε-GaSe: Transport measurements and electronic structure calculations. *Phys. Rev. B*, 71:125206, 2005.

[136] M. Takumi, A. Hirata, T. Ueda, Y. Koshio, H. Nishimura, and K. Nagata. Structural phase transitions of Ga_2Se_3 and GaSe under high pressure. *Phys. Status Solidi B*, 223:423, 2001.

[137] D. W. Zhang, F. T. Jin, and J.M. Yuan. First-principles calculation of static equation of state and elastic constants for GaSe. *Chinese Phys. Lett.*, 23:1876, 2006.

[138] J. Pellicer-Porres. Private communication.

[139] H. d'Amour, W. B. Holzapfel, A. Polian, and A. Chevy. Crystal structure of a new high pressure polymorph of GaS. *Solid State Commun.*, 44:853, 1982.

[140] D. Errandonea, A. Segura, V. Muñoz, and A. Chevy. Effects of pressure and temperature on the dielectric constant of GaS, GaSe, and InSe: Role of the electronic contribution. *Phys. Rev. B*, 60:15866, 1999.

[141] I. Rannou. *Études sous pression de la transition de phase interpolytypique du sulfure de gallium.* PhD thesis, Université de Paris VI, 1986.

[142] G. Ferlat, D. Martínez-García, A. San Miguel, A. Aouizerat, and V. Muñoz Sanjose. High pressure-high temperature phase diagram of InSe. *High. Pressure Res.*, 24:111, 2004.

[143] N. Kuroda, Y. Nishina, H. Iwasaki, and Y. Watanabe. Raman scatterings of layered and non-layered phases of InSe. *Solid State Commun.*, 38:139, 1981.

[144] H. Iwasaki, Y. Watanabe, N. Kuroda, and Y. Nishina. Pressure-induced layer-nonlayer transformation in InSe. *Physica B & C*, 105:314, 1981.

[145] G. C. Vezzoli. Synthesis and properties of a pressure-induced and temperature-induced phase of indium selenide. *Mater. Res. Bull.*, 6:1201, 1971.

[146] Y. Watanabe, H. Iwasaki, N. Kuroda, and Y. Nishina. A pressure-induced non-layered structure of indium monoselenide. *J. Solid State Chem.*, 43:140, 1982.

[147] K. Cenzual, L. M. Gelato, M. Penzo, and E. Parthe. Inorganic structure types with revised space-groups. I. *Acta Crystallogr. B*, 47:433, 1991.

[148] W. Kraus and G. Nolze. POWDER CELL-A program for the representation and manipulation of crystal structures and calculation of the resulting x-ray powder patterns. *J. Appl. Crystallogr.*, 29:301, 1996.

[149] A. LeBail, H. Duroy, and J.L. Fourquet. Abinitio structure determination of $LISbWO_6$ by x-ray-powder diffraction. *Mater. Res. Bull.*, 23:447, 1988.

[150] S. S. Kabalkina, V. G. Losev, and N. M. Gasanly. Polymorphism of InS at high-pressures. *Solid. State. Commun.*, 44:1383, 1982.

[151] A. N. MacInnes, M.B. Power, and A. R. Barron. Chemical vapor-deposition of cubic Gallium Sulfide thin-films: A new metastable phase. *Chem. Mater.*, 4:11, 1992.

[152] A. N. MacInnes, M. B. Power, A. R. Barron, P.P. Jenkins, and A.F Hepp. Enhancement of photoluminescence intensity of GaAs with cubic GaS chemical vapor-deposited using a structurally designed single-source precursor. *Appl. Phys. Lett.*, 62:711, 1993.

[153] A. N. MacInnes, M. B. Power, and A. R. Barron. Chemical vapor deposition of Gallium Sulfide: Phase control by molecular design. *Chem. Matter*, 5:1344, 1993.

[154] M. Tabib-Azar, S. Kang, A. N. MacInnes, M. B. Power, A. R. Barron, P. P. Jenkins, and A. F. Hepp. Electronic passivation of N-type and P-type GaAs using chemical-vapor-deposited GaS. *Appl. Phys. Lett.*, 63:625, 1993.

[155] P. P. Jenkins, A. N. MacInnes, M. Tabib-Azar, and A. R. Barron. Gallium-Arsenide transistors - realization through a molecularly designed insulator. *Science*, 263:1751, 1994.

[156] Y. V. Medvedev. Thermodynamic stability of GaAs sulfur passivation. *Appl. Phys. Lett.*, 64:3458, 1994.

[157] W. N. Cleaver, M. Späth, D. Hnyk, G. McMurdo, M.B. Power, M. Stuke, D. W. H. Rankin, and A. R. Barron. Vapor phase laser photochemistry and determination by electron diffraction of the molecular structure of $[(^{t}Bu)GaS]_4$: Evidence for the retention of the Ga_4S_4 cubane core during the MOCVD growth of cubic GaS. *Organometallics*, 14:690, 1995.

[158] N. Okamoto and H. Tanaka. Characterization of molecular beam epitaxy grown gas film for GaAs surface passivation. *Mat. Sci. Semicon. Proc.*, 2:13, 1999.

[159] J. Pellicer-Porres, A. Segura, V. Muñoz, and A. S. Miguel. High-pressure x-ray absorption study of GaTe including polarization. *Phys. Rev. B*, 61:125, 2000.

[160] U. Schwarz, K. Syassen, and R. Kniep. Structural phase-transition of GaTe at high-pressure. *J. Alloy Compd.*, 224:212, 1995.

[161] F. Lévy, editor. *Structural Chemistry of Layer-Type Phases*. D. Reidel Publishing Company, Dordrecht-Holland/Boston-U.S.A., 1976.

[162] D. Errandonea, A. Segura, J. F. Sánchez-Royo, V. Muñoz, P. Grima, A. Chevy, and C. Ulrich. Investigation of conduction-band structure, electron-scattering mechanisms, and phase transitions in indium selenide by means of transport measurements under pressure. *Phys. Rev. B*, 55:16217, 1997.

[163] K. J. Dunn and F. P. Bundy. Pressure-induced metallic and superconducting state of GaSe. *Appl. Phys. Lett.*, 36:709, 1980.

[164] R. S. Mulliken. Electronic population analysis on LCAO-MO molecular wave functions. I. *J. Chem. Phys.*, 23:1833, 1955.

[165] J. K. Burdett. *Chemical Bonding in Solids*. Oxford University Press: New York, 1995.

[166] H. Schmidbaur and S. D. Nogai. From gallium hydride halides to molecular gallium sulfides. *Z. Anorg. Allg. Chem.*, 630:2218, 2004.